

**Quantification of bacterial growth
within orthopaedic scaffolds and
assessment of the efficacy of
antibacterial surface treatments**



**The University of
Nottingham**

Michał Żurawski

Department of Engineering

University of Nottingham

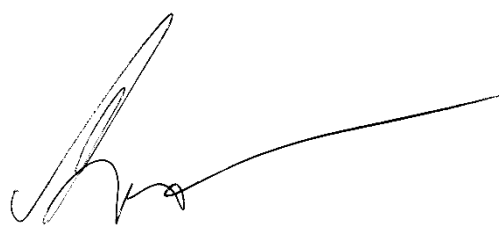
This dissertation is submitted for the degree of

Doctor of Philosophy

This thesis is dedicated to my late mother, Monika Żurawska, and my late grandmother, Barbara Zaremba-Smok; both of whom dedicated their lives to science and attainment of knowledge. They both saw the beginning of this work, though, regrettably, not its conclusion.

Declaration

I hereby declare that except where specific reference is made to the work of others, the contents of this dissertation are original and have not been submitted in whole or in part for consideration for any other degree or qualification in this, or any other University. This dissertation is the result of my own work and includes nothing which is the outcome of work done in collaboration, except where specifically indicated in the text. This dissertation contains fewer than 65,000 words including appendices, bibliography, footnotes, tables and equations and has fewer than 150 figures.

A handwritten signature in black ink, appearing to be 'M. Żurawski', with a long horizontal flourish extending to the right.

Michał Żurawski

2021

Acknowledgements

And I would like to acknowledge the tireless effort and support from my supervisors: Prof. David Grant, Prof. Colin Scotchford, Prof. Steve Atkinson and Dr. Reda Felfel. Each of them was instrumental in shaping the work in this thesis and in instilling my interest in this field across the years.

Further to the above, I'd like to thank Zimmer-Biomet, especially Imran Khan and Elaine Lovelady, for supporting this work both financially and with their expertise, and allowing the use of their commercial samples for the studies mentioned herein.

Final and additional thanks go to Prof. David Grant, who supported me in times of personal difficulty and acted as a stabilising presence to make the completion of this thesis a possibility.

Abstract

This thesis reports on the development of quantifiable methods for the assessment of bacterial bioburden within three-dimensional orthopaedic scaffolds, and the subsequent investigation of the effects of exposure of their surfaces to proteins has on the observed biofouling. The lack of readily available methods for this purpose, and the rising cost (both human and financial) of biofilm infection of orthopaedic devices prompted the need for this research.

Existing methods are identified during the literature review, such as Confocal Laser Scanning Microscopy (CLSM) and Micro-CT which are used in the research field are first investigated for efficacy as they have been used in some studies.

The aim of this study is to develop and validate a new analysis method to provide quantifiable, accurate and reliable results for the measurement of bacterial biofouling on flat and three-dimensional samples alike. This method is then used to measure the bacterial biofouling of samples once inoculated and incubated with *S. aureus* in a protein-rich environment they would be exposed to *in situ* inside a patient.

Analysis using SEM micrographs is adopted as a methodology and refined in this work. The standardised approach which takes readings in triplicate from each sample, and measures bacterial surface coverage of the imaged area through computational image analysis is used to study commercially-available orthopaedic scaffolds (Ta and Ti6Al4V), as well as samples containing elements known for their antibacterial properties (Cu and I).

The reliability of the novel SEM methodology is shown through validation against the research standard of CLSM, which is readily used for analysis of flat, two-dimensional samples. Once validated, the SEM methodology is then used to study the effect a surface which has been pre-conditioned with protein has on bacterial biofouling compared to a clean surface, both when the substrate surface chemistry has known antibacterial properties or not. It is found that the physical shielding of bacterial cells from the antibacterial surface agent by the protein film reduces the antibacterial effect.

The new method developed is of significance as it provides researchers a reliable way to measure biofouling in three-dimensional structures with a protocol made for that very purpose. It is hoped that this method will continue to be refined to further enable research within microbiological assessments within orthopaedic scaffolds which carry a risk of biofilm infection in a clinical setting. The protein conditioning studies go on to explain why samples, even when containing known antibacterial agents, are still susceptible to bacterial infection in a clinical setting.

Contents

Contents xii

List of Figures	xvii
List of Tables	xxiii
Nomenclature	1
Chapter 1 Introduction	5
1.1 Literature review	6
1.1.1 The bacterial cell.....	6
1.1.2 The bacterial biofilm.....	18
1.1.3 Antibiotic Resistance	24
1.1.4 Biomedical Materials	26
1.1.5 The clinical need	30
1.1.6 Bacterial contamination of scaffolds	31
1.1.7 Selection of commercial samples from Zimmer-Biomet.....	33
1.1.8 Possible ways to measure biofilm formation in Zimmer-Biomet scaffolds	35
1.1.9 Aims and Objectives	36
Chapter 2 Characterisation of Sample Composition and Morphology	40
2.1 Materials and Methods	40
2.1.1 Sample Selection.....	40
2.1.2 Scanning Electron Microscopy (SEM)	43
2.1.3 Energy-Dispersive X-Ray Spectroscopy (EDX)	43
2.1.4 X-Ray Photoelectron Spectroscopy (XPS)	44
2.1.5 X-Ray Fluorescence Analysis (XRF)	46
2.1.6 Atomic Force Microscopy (AFM).....	46
2.1.7 Laser Profilometry	47
2.1.8 Water Contact Angle Measurement (WCA).....	47
2.2 Results	48

2.2.1	Scanning Electron Microscopy (SEM)	49
2.2.2	Energy-Dispersive X-Ray Spectroscopy (EDX) and X-Ray Photoelectron Spectroscopy (XPS).....	54
2.2.3	X-Ray Fluorescence Analysis (XRF)	60
2.2.4	Atomic Force Microscopy (AFM) and Laser Profilometry	62
2.2.5	Water Contact Angle Analysis (WCA).....	65
2.3	Discussion	67
2.3.1	Scanning Electron Microscopy (SEM)	67
2.3.2	Energy-Dispersive X-Ray Spectroscopy (EDX) and X-Ray Photoelectron Spectroscopy (XPS).....	70
2.3.3	Atomic Force Microscopy (AFM) and Laser Profilometry	71
2.3.4	X-Ray Fluorescence Analysis (XRF)	73

Chapter 3 Microbiological Assessment On Scaffolds Using Existing Methods 75

3.1	Materials and Methods	79
3.1.1	Bacterial culture	79
3.1.2	Wet weight assessment	80
3.1.3	Dry weight assessment.....	81
3.1.4	Micro-CT assessment.....	82
3.1.5	Confocal Laser Scanning Microscopy (CLSM)	82
3.1.6	Sample Selection.....	83
3.2	Results	84
3.2.1	Wet weight assessment	84
3.2.2	Dry weight assessment.....	88
3.2.3	Micro-CT assessment.....	90
3.2.4	Confocal Laser Scanning Microscopy (CLSM)	91
3.3	Discussion	95
3.3.1	Wet weight assessment	95
3.3.2	Dry weight assessment.....	97
3.3.3	Micro-CT assessment.....	100
3.3.4	Confocal Laser Scanning Microscopy (CLSM)	101
3.4	Conclusion.....	105

Chapter 4 Scanning Electron Microscopy (SEM) Biofilm Formation Analysis Method Development 107

4.1	Materials and Methods	109
4.1.1	Sample Selection.....	109
4.1.2	Bacterial seeding and incubation	110

4.1.3	SEM bacterial growth analysis	112
4.1.4	Confocal Laser Scanning Microscopy (CLSM)	113
4.2	Results	114
4.2.1	Image Processing	114
4.2.2	Method validation	117
4.2.3	Qualitative Scanning Electron Microscope (SEM) micrograph analysis	127
4.3	Discussion	129
4.3.1	Image processing	129
4.3.2	Method Validation	132
Chapter 5 Effect Of A Protein Conditioning Film Upon Substrate Surface On Bacterial Cell Presence		141
5.1	Materials and Methods	143
5.1.1	Characterisation	145
5.1.2	Protein conditioning film establishment	146
5.1.3	Bacterial seeding and incubation	146
5.1.4	SEM microbiological assessment	148
5.2	Results	149
5.2.1	XPS analysis	149
5.2.2	12 hour Bioburden SEM Study.....	151
5.2.3	Iodine Bioburden SEM Study.....	155
5.3	Discussion	166
5.3.1	XPS analysis	166
5.3.2	12 hour Bioburden SEM Study.....	166
5.3.3	Iodine Bioburden SEM Study.....	169
Chapter 6 Metal-Polymer Hybrid Scaffolds		176
6.1	Materials and methods	178
6.1.1	Sample preparation	178
6.1.2	SEM imaging	179
6.2	Results	179
6.3	Discussion	184
Chapter 7 Conclusions, and Future Work.....		188
7.1	Conclusions	188
7.2	Future Work	193
References		197

List of Figures

Figure 1: Simplified bacterial cell showing the major organelles and physical structures of the bacterium.....8

Figure 2: Simple bacterial growth curve. The first, blue, section demonstrates the lag phase. The second, green, section demonstrates the Log phase of rapid division. The penultimate, red, phase shows the stationary phase, during which the colony size remains constant. The final, orange, section shows the death phase, during which two outcomes are considered- a new lower stationary phase or total death of the colony. 12

Figure 3: A simplified diagram of peptide quorum sensing. In Gram-positive quorum sensing bacterial cells, specific ABC transporter proteins (represented as the protein complex in the bacterial membrane) process and subsequently export peptide autoinducers (pheromones) (the precursors of which are depicted as long chains of circles inside the bacterial cell, and the autoinducers as the short chains of circles outside the bacterial cell). Membrane-bound two-component sensor kinase proteins recognise these extracellular pheromones. Upon binding, the sensor complex then autophosphorylate on a histidine residue (H), and transfer a phosphoryl group on to a cognate response regulator. These response regulators are phosphorylated on aspartate residues (D) (this process is denoted by the P in a circle inside the bacterial cell). Once phosphorylated, the response regulator proteins repress or activate the transcription of a specific target gene. 15

Figure 4: A simple diagram of LuxI/LuxR quorum sensing. In Gram-negative quorum sensing bacteria, LuxI autoinducer synthase proteins (blue triangle) produce specific HSL autoinducers (red pentagons). These autoinducers freely diffuse out of the bacterial cell membrane. Once a critical concentration is reached, the autoinducer is bound by its cognate LuxR protein (green circle). The resulting LuxR-HSL autoinducer complex activates transcription of a target gene. 17

Figure 5: Schematic outline diagrams of sample types. A. shows Ti6Al4V and Tantalum 3D scaffolds (Osseo-Ti and Trabecular Bone respectively). B. shows flat samples of the following: polished and grit blasted Tantalum and Ti6Al4V and Tantalum disks, Copper-coated Ti6Al4V disks, anodised and Iodine-treated disks as well as Magnesium and Magnesium-Calcium disks...42

Figure 6: False-colour SEM Micrographs at x100 (left) and x200 (right). Rows A and B show the two scaffold samples (Tantalum (Trabecular Bone) and Titanium (OsseoTi) respectively). Rows C and D show grit-blasted disk

sample surfaces (Tantalum and Titanium respectively). Row E shows a Cu-coated polished Ti disk sample.51

Figure 7: False-colour SEM Micrographs at x100 (left) and x200 (right). Rows A and B show the two scaffold samples (Tantalum (Trabecular Bone) and Titanium (OsseoTi) respectively). Rows C and D show grit-blasted disk sample surfaces (Tantalum and Titanium respectively). Row E shows a Cu-coated polished Ti disk sample.52

Figure 8: Composition of samples, as measured by EDX (inner portion) and XPS (outer portion). The 'Polished' column (left) shows polished disk samples. The 'Grit-Blasted' column contains grit-blasted disk samples. The 'Ta' row shows Tantalum disk samples. The 'Ti' row contains Ti6Al4V disk samples, and the 'Cu-Ti' row shows the polished, Cu-coated Ti6Al4V samples.55

Figure 9: Composition of samples, as measured by EDX (inner portion) and XPS (outer portion). All samples are 3D scaffold samples. The 'Ta' row contains the tantalum 'Trabecular Bone' scaffolds. The 'Ti' row shows the Ti6Al4V scaffolds (Osseo-Ti).58

Figure 10: XPS analysis of the protein conditioning layer (outer) compared to the underlying sample composition obtained by XPS (inner). A) shows a polished Ti6Al4V disk sample which has been conditioned with a protein layer on its surface by immersion in Foetal Bovine Serum (FBS). B) shows a polished Tantalum disk sample which has been conditioned with a protein layer on its surface by immersion in Foetal Bovine Serum (FBS).59

Figure 11: Sample chemistry analysis using XRF on a Ti6Al4V sample which has been surface treated with Iodine by Zimmer-Biomet. Values are given as % of the total composition measured per element. The results confirm the presence of Iodine within the sample, at 0.095 wt%. The remainder of the composition is made up of Titanium (78 wt%), Aluminium (5 wt%), Vanadium (1 wt%), Oxygen (10 wt%) and carbon (6 wt%).61

Figure 12: Surface roughness measurements using AFM (left of break) and laser profilometry (right of break). The y axis shows Ra roughness, and the x axis shows sample type. 3D model rendering images are shown above the samples as a visual example of the measured surface area. CuTi is the polished, cu-coated Ti6Al4V disk sample, PTa and PTi are polished disk samples (Tantalum and Ti6Al4V respectively)(no statistically significant difference). GTa and GTi are grit-blasted disk samples (Tantalum and Ti6Al4V respectively)(no statistically significant difference). 3D Ta and 3D Ti are 3d scaffold samples (Tantalum (Trabecular Bone) and Ti6Al4V (Osseo-Ti) respectively)(p<0.01).64

Figure 13: Water Contact Angle measurements of disk and scaffold samples. 'Polished Ti' is a polished Ti6Al4V disk sample, 'Anodised Ti' is an anodised Ti6Al4V disk sample, and 'Cu coated Ti' is a polished, cu-coated Ti6Al4V disk sample. 'Grit-balsted Ta' is a grit-blasted tantalum disk, and 'Polished-Ta' is a polished tantalum disk sample. 'Ta scaffold' is a tantalum 3D scaffold sample (Trabecular Bone). Measurement was not possible of the 3D Ti6Al4V scaffold sample due to the large size of the pores.66

Figure 14: Weight change over time for wet samples which were incubated in TSB and inoculated with *S. aureus*. Samples at 0 h were incubated TSB, with no inoculation with bacterial culture. ‘PTi’ samples were flat, polished Ti-6Al-4V disks, ‘GTi’ samples were grit-blasted Ti-6Al-4V disks, and ‘Iodine Ti’ samples were iodine-treated polished Ti-6Al-4V disks.....86

Figure 15: Weight change over time for wet scaffold samples (Ti-6Al-4V Osseo-Ti scaffolds) which were incubated in TSB and inoculated with *S. aureus*. Samples at 0 h were incubated TSB, with no inoculation with bacterial culture.87

Figure 16: Weight change over time for freeze-dried samples which were incubated in TSB and inoculated with *S. aureus*. Samples at 0 h were incubated TSB, with no inoculation with bacterial culture. ‘PTi’ samples were flat, polished Ti-6Al-4V disks, ‘GTi’ samples were grit-blasted Ti-6Al-4V disks, and ‘Iodine Ti’ samples were iodine-treated polished Ti-6Al-4V disks. ‘3D Ti’ samples were Osseo-Ti (Ti-6Al-4V) scaffold samples.....89

Figure 17: Micro-CT cross sectional scans of two metal scaffolds 2mm from the top surface (a hydrogel was cast in what would be the bottom half of these cross-sections, though this is not visible in the scans) ; A- Trabecular Bone scaffold (Ta), B- Osseo-Ti scaffold (Ti-6Al-4V). Typically, in CT scans, dark areas are areas of high density, lighter areas are areas of low density, with white denoting voids.90

Figure 18: Biomass as measured by confocal laser microscopy after incubation for 96h in TSB media. Sterile samples were incubated in the media without inoculation with a bacterial culture, otherwise samples were inoculated with *S. aureus* prior to incubation. ‘2D’ marks flat, polished samples of either Ti-6Al-4V or Ta, and ‘3D’ marks scaffold samples (Osseo-Ti in the case of Titanium, and Trabecular Metal in the case of Tantalum.93

Figure 19: Example 3D rendering of confocal scans, measuring fluorescence of the GFP marker. A-D show renderings of the scanned surface of scaffolds at different, randomised locations. A-B were from a Trabecular Metal scaffold, and C-D were from an Osseo-Ti scaffold. E-F show the rendered scans of locations on flat, polished disks (Tantalum and Ti-6Al-4V respectively). Presence of GFP fluorescence is shown as a colour, and this colour changes depending on the relative height of the signal (with red being the lowest and blue being topmost).94

Figure 20: The main image processing steps to achieve a binary image. A shows a raw micrograph as taken using SEM imaging. B shows an image which has had its brightness reduced (pixel devaluation) and subsequently had a mask of bright pixels applied over any location where bacterial cells were present in the image (masking). Image C shows the binary picture which was used to count pixels, once the image has gone through thresholding which left only 2 types of pixels – black and white (values of 0 and 255 respectively).116

Figure 21: Validation of the SEM method against confocal laser scanning microscopy (CLSM) on polished Ti6Al4V disks. *S. aureus* was used to inoculate the media, and the samples were incubated for up to 24h. Graph A shows the biomass as measured by CLSM at 3, 6, 9, 12 and 24h. Graph B

shows pixel counts as measured by the SEM method. Graph C shows how the normalised values from both methods (values were divided by the maximum seen in the cohort) compared at each time point. No statistically significant difference is seen between different methods in graph C at any time point ($p > 0.005$)..... 119

Figure 23: Validation of the SEM method against confocal laser scanning microscopy (CLSM) on polished Ti6Al4V disks. *S. aureus* was used to inoculate the media, and the samples were incubated for 3h in different media. Samples in the FBS cohort were incubated in TSB media with added FBS. Samples in the TSB cohort were incubated in pure TSB media. Samples in the PRE cohort were left in FBS media to obtain a protein conditioning film, then incubated in TSB media. CuTi were copper-coated Ti disks, PTa and PTi were polished Tantalum and Titanium disks respectively. GTa and GTi were grit-blasted Tantalum and Titanium disks respectively Graph A shows the biomass as measured by CLSM at 3h. Graph B shows pixel counts as measured by the SEM method. Graph C shows how the normalised values from both methods (values were divided by the maximum seen in the cohort) compared at each time point. No statistically significant difference is seen between different methods in graph C at any time point ($p > 0.005$) apart from PTi TSB cohorts and GTi FBS cohorts. 126

Figure 24: False-coloured SEM images of multi-layered colonies and single-layered *S. aureus* colonies on surfaces of samples. A is a colony which was incubated for 24h on a polished Ti6Al4V disk surface. The area in blue is the sample surface, and the area in green is the bacterial colony at a magnification of x2584. Image C is the same colony at a magnification of x1292. C is an image of a surface inside a 3D Ti6Al4V scaffold (Osseo-Ti) at a magnification of x3200. The blue area is the sample surface and the bacterial cells are coloured in green. D shows a surface of a strut inside a 3D Tantalum scaffold (Trabecular Metal) at a magnification of x6400. The surface is coloured in purple, and the *S. aureus* cells are coloured in yellow..... 128

Figure 25: Schematic outline diagrams of sample types. A. shows Ti6Al4V and Tantalum 3D scaffolds (Osseo-Ti and Trabecular Bone respectively). B. shows polished Tantalum and Ti6Al4V disks. C shows Ti6Al4V disks coated with Magnesium and Magnesium-Calcium. D shows grit-blasted Tantalum and Ti6Al4V disks. E shows anodised and Iodine-treated Ti6Al4V disks. F shows copper-coated Ti6Al4V disks. 144

Figure 26: Chemical composition as measured by XPS and taken from the surface of disk samples which have been conditioned with protein by immersion in Foetal Bovine Serum. ‘Cu’ is a polished, Cu-coated Ti6Al4V disk. ‘Ta’ is a polished tantalum disk sample. ‘Ti’ is a polished Ti6Al4V disk. 150

Figure 27: Bacterial surface coverage as measured by the SEM analysis method at 3, 9 and 12h timepoints. ‘TSB’ shows the cohort of samples which was incubated in pure TSB media after inoculation with *S. aureus*. ‘PRE’ is a cohort of samples which has been pre-conditioned with protein by immersion in Foetal Bovine Serum prior to inoculation. ‘Cu-Ti’ are polished, Cu-coated Ti6Al4V disks, ‘PTa’ and ‘PTi’ are polished tantalum and Ti6Al4V disks

respectively. 'GTa' and 'GTi' are grit-blasted tantalum and Ti6Al4V disk samples respectively. '3DTi' is a 3D Ti6Al4V scaffold sample (Osseo-Ti). '3DTa' is a 3D tantalum scaffold (Trabecular Bone). The topmost graphs show segmentation by incubation method. The bottom graphs show the bacterial coverage by timepoint. 154

Figure 28: Bacterial surface coverage as measured by the SEM analysis method at 3, 6, 9 and 12h timepoints. 'TSB' shows the cohort of samples which was incubated in pure TSB media after inoculation with *S. aureus*. 'PRE' is a cohort of samples which has been pre-conditioned with protein by immersion in Foetal Bovine Serum prior to inoculation. 'Cu-Ti' are polished, Cu-coated Ti6Al4V disks, 'PTa' and 'PTi' are polished tantalum and Ti6Al4V disks respectively. 'GB Iodine' are grit-blasted disks which have been treated with Iodine. 'MgCa' and 'Mg' samples are Ti6Al4V samples coated with a magnesium-calcium compound and magnesium only, respectively. 'PPS Iodine' are disks which have undergone PPS treatment with iodine. 'GTa' and 'GTi' are grit-blasted tantalum and Ti6Al4V disk samples respectively. '3DTi' is a 3D Ti6Al4V scaffold sample (Osseo-Ti). '3DTa' is a 3D tantalum scaffold (Trabecular Bone). The topmost graphs show segmentation by incubation method. The bottom graphs show the bacterial coverage by timepoint. 159

Figure 29: Bacterial surface coverage as measured by the SEM analysis method at 3 and 6h timepoints. 'PRE' is a cohort of samples which has been pre-conditioned with protein by immersion in Foetal Bovine Serum prior to inoculation. 'Cu-Ti' are polished, Cu-coated Ti6Al4V disks, 'PTa' and 'PTi' are polished tantalum and Ti6Al4V disks respectively. 'GB Iodine' are grit-blasted disks which have been treated with Iodine. 'MgCa' and 'Mg' samples are Ti6Al4V samples coated with a magnesium-calcium compound and magnesium only, respectively. 'PPS Iodine' are disks which have undergone PPS treatment with iodine. 'GTa' and 'GTi' are grit-blasted tantalum and Ti6Al4V disk samples respectively. '3DTi' is a 3D Ti6Al4V scaffold sample (Osseo-Ti). '3DTa' is a 3D tantalum scaffold (Trabecular Bone). 160

Figure 30: Bacterial surface coverage as measured by the SEM analysis method at 9 and 12h timepoints. 'PRE' is a cohort of samples which has been pre-conditioned with protein by immersion in Foetal Bovine Serum prior to inoculation. 'Cu-Ti' are polished, Cu-coated Ti6Al4V disks, 'PTa' and 'PTi' are polished tantalum and Ti6Al4V disks respectively. 'GB Iodine' are grit-blasted disks which have been treated with Iodine. 'MgCa' and 'Mg' samples are Ti6Al4V samples coated with a magnesium-calcium compound and magnesium only, respectively. 'PPS Iodine' are disks which have undergone PPS treatment with iodine. 'GTa' and 'GTi' are grit-blasted tantalum and Ti6Al4V disk samples respectively. '3DTi' is a 3D Ti6Al4V scaffold sample (Osseo-Ti). '3DTa' is a 3D tantalum scaffold (Trabecular Bone). 161

Figure 31: Bacterial surface coverage as measured by the SEM analysis method at 3 and 6h timepoints. 'TSB' is a cohort of samples which has not been pre-conditioned with protein, instead being inoculated with bacteria in pure TSB media. 'Cu-Ti' are polished, Cu-coated Ti6Al4V disks, 'PTa' and 'PTi' are polished tantalum and Ti6Al4V disks respectively. 'GB Iodine' are grit-blasted disks which have been treated with Iodine. 'MgCa' and 'Mg' samples are Ti6Al4V samples coated with a magnesium-calcium compound

and magnesium only, respectively. ‘PPS Iodine’ are disks which have undergone PPS treatment with iodine. ‘GTa’ and ‘GTi’ are grit-blasted tantalum and Ti6Al4V disk samples respectively. ‘3DTi’ is a 3D Ti6Al4V scaffold sample (Osseo-Ti). ‘3DTa’ is a 3D tantalum scaffold (Trabecular Bone)..... 162

Figure 32: Bacterial surface coverage as measured by the SEM analysis method at 9 and 12h timepoints. ‘TSB’ is a cohort of samples which has not been pre-conditioned with protein, instead being inoculated with bacteria in pure TSB media. ‘Cu-Ti’ are polished, Cu-coated Ti6Al4V disks, ‘PTa’ and ‘PTi’ are polished tantalum and Ti6Al4V disks respectively. ‘GB Iodine’ are grit-blasted disks which have been treated with Iodine. ‘MgCa’ and ‘Mg’ samples are Ti6Al4V samples coated with a magnesium-calcium compound and magnesium only, respectively. ‘PPS Iodine’ are disks which have undergone PPS treatment with iodine. ‘GTa’ and ‘GTi’ are grit-blasted tantalum and Ti6Al4V disk samples respectively. ‘3DTi’ is a 3D Ti6Al4V scaffold sample (Osseo-Ti). ‘3DTa’ is a 3D tantalum scaffold (Trabecular Bone)..... 163

Figure 33: False-colour SEM micrographs of chitosan scaffolds which were created within metal scaffolds. Chitosan is coloured in purple and the metal is blue. A is a chitosan scaffold with no metal scaffold. B, C and D are images of chitosan cast within a tantalum scaffold (Trabecular Metal), at 87x, 174x and 695x magnifications respectively. E, F and G are images of chitosan scaffolds within Ti6Al4V scaffolds (Osseo-Ti) at 87x, 174x and 695x magnifications respectively. 181

Figure 34: False-colour SEM micrographs of chitosan scaffolds with Ag nanoparticles which were cast within metal scaffolds. Ag- Chitosan is coloured in yellow and the metal is blue. A is an Ag-chitosan scaffold with no metal scaffold. B, C and D are images of Ag-chitosan cast within a tantalum scaffold (Trabecular Metal), at 92x, 184x and 735x magnifications respectively. E, F and G are images of Ag-chitosan scaffolds within Ti6Al4V scaffolds (Osseo-Ti) at 182x and 365x magnifications respectively. 182

Figure 35: High magnification false-colour SEM images of the chitosan-metal scaffold material interface. Chitosan is purple, Ag-Chitosan is coloured in yellow and the metal is blue. A is a Chitosan-Tantalum material interface at a magnification of 11128x. B and C are Ag-Chitosan-Ti6Al4V material interface at magnifications of 1458x and 2743x respectively. 183

List of Tables

Table 1: Bacterial presence on the surface of flat samples as measured by Confocal Laser Scanning Microscopy (CLSM). CuTi is a Copper-coated, polished Ti6Al4V disk, PTa and PTi are polished Tantalum and Ti6Al4V disks respectively, and GTa and GTi are grit-bladed Tantalum and Ti6Al4V disks respectively. FBS is a cohort of samples incubated in media with added Foetal-Bovine Serum, and inoculated with *S. aureus*. TSB samples were incubated in Tryptic Soy Borth media, and PRE samples were left in pure Foetal Bovine Serum prior to transfer into Tryptic Soy Broth media for inoculation and incubation..... 122

Table 2: Bacterial presence on the surface of flat samples as measured by Scanning Electron Microscopy (SEM) micrograph coverage analysis. CuTi is a Copper-coated, polished Ti6Al4V disk, PTa and PTi are polished Tantalum and Ti6Al4V disks respectively, and GTa and GTi are grit-bladed Tantalum and Ti6Al4V disks respectively. FBS is a cohort of samples incubated in media with added Foetal-Bovine Serum, and inoculated with *S. aureus*. TSB samples were incubated in Tryptic Soy Borth media, and PRE samples were left in pure Foetal Bovine Serum prior to transfer into Tryptic Soy Broth media for inoculation and incubation. 122

Table 3: Bacterial presence on the surface of flat samples as measured by Scanning Electron Microscopy (SEM) micrograph coverage analysis and Confocal Laser Scanning Microscopy (CLSM) normalised (value in each subset is divided by the maximum value in the subset). CuTi is a Copper-coated, polished Ti6Al4V disk, PTa and PTi are polished Tantalum and Ti6Al4V disks respectively, and GTa and GTi are grit-bladed Tantalum and Ti6Al4V disks respectively. FBS is a cohort of samples incubated in media with added Foetal-Bovine Serum, and inoculated with *S. aureus*. TSB samples were incubated in Tryptic Soy Borth media, and PRE samples were left in pure Foetal Bovine Serum prior to transfer into Tryptic Soy Broth media for inoculation and incubation. 124

Table 4: Bacterial presence on the surface of flat samples as measured by Scanning Electron Microscopy (SEM) micrograph coverage analysis. CuTi is a Copper-coated, polished Ti6Al4V disk, PTa and PTi are polished Tantalum and Ti6Al4V disks respectively, and GTa and GTi are grit-bladed Tantalum and Ti6Al4V disks respectively. 3DTa and 3DTi are Trabecular Metal (Tantalum scaffold) and OsseoTi (Ti6Al4V scaffold) respectively. TSB samples were incubated in Tryptic Soy Borth media, and inoculated with *S.*

aureus; and PRE samples were left in pure Foetal Bovine Serum prior to transfer into Tryptic Soy Broth media for inoculation and incubation..... 152

Table 5: Table of bacterial surface coverage as measured by the SEM analysis method at 3, 6, 9 and 12h timepoints. ‘TSB’ is a cohort of samples which has not been pre-conditioned with protein, instead being inoculated with bacteria in pure TSB media. ‘Cu-Ti’ are polished, Cu-coated Ti6Al4V disks, ‘PTa’ and ‘PTi’ are polished tantalum and Ti6Al4V disks respectively. ‘GB Iodine’ are grit-blasted disks which have been treated with Iodine. ‘MgCa’ and ‘Mg’ samples are Ti6Al4V samples coated with a magnesium-calcium compound and magnesium only, respectively. ‘PPS Iodine’ are disks which have undergone PPS treatment with iodine. ‘GTa’ and ‘GTi’ are grit-blasted tantalum and Ti6Al4V disk samples respectively. ‘3DTi’ is a 3D Ti6Al4V scaffold sample (Osseo-Ti). ‘3DTa’ is a 3D tantalum scaffold (Trabecular Bone)..... 164

Table 6: Table of bacterial surface coverage as measured by the SEM analysis method at 3, 6, 9 and 12h timepoints. ‘PRE’ is a cohort of samples which has been pre-conditioned with protein by immersion in Foetal Bovine Serum prior to inoculation. ‘Cu-Ti’ are polished, Cu-coated Ti6Al4V disks, ‘PTa’ and ‘PTi’ are polished tantalum and Ti6Al4V disks respectively. ‘GB Iodine’ are grit-blasted disks which have been treated with Iodine. ‘MgCa’ and ‘Mg’ samples are Ti6Al4V samples coated with a magnesium-calcium compound and magnesium only, respectively. ‘PPS Iodine’ are disks which have undergone PPS treatment with iodine. ‘GTa’ and ‘GTi’ are grit-blasted tantalum and Ti6Al4V disk samples respectively. ‘3DTi’ is a 3D Ti6Al4V scaffold sample (Osseo-Ti). ‘3DTa’ is a 3D tantalum scaffold (Trabecular Bone)..... 165

Nomenclature

°	Degree
°C	Degree Celsius
µg	Microgram
µl	Microlitre
µm	Micrometre
AFM	Atomic Force Microscopy
Ag	Silver
Al	Aluminium
BE	Binding energy
CFU	Colony-Forming Units
CLSM	Confocal Laser Scanning Microscopy
cm	Centimetre
Cm	Chloramphenicol

Cu	Copper
CVD	Chemical Vapour Deposition
dL	Decilitre
EDX	Energy Dispersive X-Ray Analysis
eV	Electronvolt
FBS	Foetal Bovine Serum
g	Gram
GFP	Green Fluorescent Protein
GS	gentamicin sulfate
h	Hour
HA	Hydroxyapatite
$h\nu$	Photon energy
I	Iodine
KE	Kinetic energy
kV	Kilovolts
MAO	Micro-Arc Oxidation
Micro-CT	Micro- computed tomography

ml	Millilitre
mm	Millimetre
MPa	Megapascals
nm	Nanometre
OD ₆₀₀	Optical density (600nm filter)
PVD	Physical Vapour Deposition
QS	Quorum-sensing
s	Second
SE	Secondary Electron
SEM	Scanning Electron Microscopy
SLS	Selective Laser Sintering
Ta	Tantalum
TSB	Tryptic Soy Broth
UHMWPE	Ultra-High Molecular Weight Polyethylene
V	Vanadium
WCA	Water Contact Angle

wt%

Weight-Percent

XPS

X-ray photoelectron spectroscopy

XRF

X-ray fluorescence

Chapter 1 Introduction

This chapter intends to create a foundation of understanding of the key underlying concepts of the work, as well as provide context for the direction in which the studies were taken, as well as the aims and objectives of the research.

Bacterial, and the resulting biofilm, infections are a prevalent problem across all areas of medicine, chief amongst which are infections affecting medical devices; be that a short-term polymer catheter, a medium-term metal fixation plate or a long-term hip replacement. Such infections, apart from the obvious risk to health, also result in the necessary removal and replacement of the affected device, requiring revision surgeries which have many risks associated with them, as well as costing the NHS dearly^[1]. An additional issue with removal and replacement of total joint replacement (TJR) devices is that due to the nature of the procedure and the implants themselves, they have a finite amount of times they can be replaced in a lifetime (around 3 in a young, healthy adult), and bearing in mind the implants themselves have an approximate life-span of 15 years due to wear and tear, using up one of these adversely affects the quality of life for these patients in the future. There were 170,000 TJR procedures in 2019 in the UK, out of which 9,154 resulted in

biofilm infections, affecting as many people and at a cost of approximately £45 million to the NHS^[1].

Biofilm infections are particularly troublesome, because once bacteria adhere to a surface they begin to secrete extracellular polymeric substances- such as gellan, N-acetylglucosamine and hyaluronic acid- which form a protective biofilm around them^[2-4]. This biofilm creates a physical barrier between the bacteria and the immune system and antibiotics, more often than not rendering any treatment useless. When this biofilm forms on a medical implant, treatment is nearly impossible and the implant needs to be replaced.

1.1 Literature review

There is a large body of literature outlining the study of bacterial growth and biofouling, both in general terms and in the medical device context. This literature review aims to build a basis of understanding around the foundational concepts of bacteria, medical devices and their relationship in healthcare, as well as identifying possible methods for the study of bacterial cell behaviour within 3D medical scaffold implants.

1.1.1 The bacterial cell

There are variations in the composition of the bacteria cell wall but their cytoplasmic membranes are comparable to those of eukaryotic cells which are composed of lipids assembled in a bilayer arrangement (see Figure 1). The cell

wall structures themselves are categorised into two classes: Gram-positive and Gram-negative, depending on the reaction of the structure to the Gram staining process, in turn revealing its permeability ^[5]. These differences can influence the type of bacteria considered for a study as different environments (clinical or otherwise) can have differing ratios of Gram-positive and Gram-negative bacterial species present. There are, however, surface features which are common to both Gram-positive and Gram-negative bacteria. Fimbriae are an example of such features (see Figure 1). These serve as adhesive organelles- they are present on the surface of bacteria and play an important role in the interaction between bacterial cells, host cells and other surfaces ^[6]. They allow bacterial cells to aggregate between cells of its own species, co-aggregate with bacterial cells of other strains, attach to non-biological surfaces or interact with host cells ^[7]. Some specialised fimbriae, termed sex pili, are present on Gram-negative bacteria and serve as a way for bacterial cells to transfer genetic material during bacterial mating ^[8]. These are present in lower numbers and appear longer and wider than common fimbriae^[8].

Bacterial DNA is present in two forms in a cell, namely; a chromosome or a plasmid. Chromosomes are different from plasmids in that they contain essential genes, whereas plasmids usually do not ^[9]. They are large,

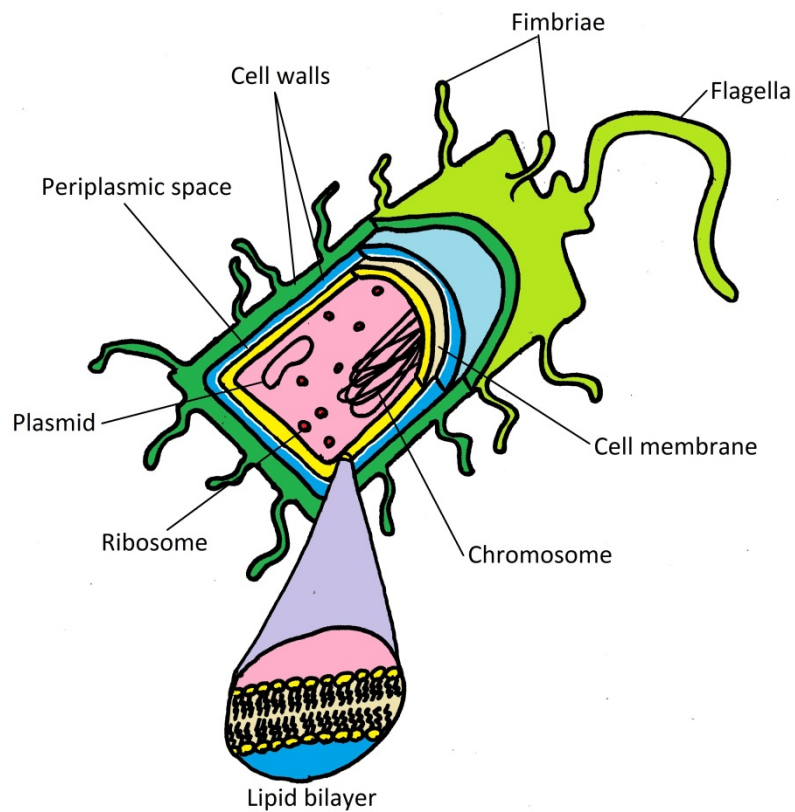


Figure 1: Simplified bacterial cell showing the major organelles and physical structures of the bacterium.

supercoiled loops of DNA. Chromosomes initiate replication once per cell cycle; *ergo* display characteristic cell cycle-linked replication kinetics dissimilar to those of plasmids ^[10]. It is not unusual for prokaryotic bacterial cells to contain more than one chromosome ^[10] although secondary chromosomes usually only contain few essential genes and tend to be much

smaller than the primary chromosomes. In spite of this, some studies have shown that there are exceptions to this rule, such as a study by Mackenzie *et al.* (2001) which showed that *R. sphaeroides* contain two chromosomes with equal weighting of essential genes^[11]. Furthermore, a study by Wood *et al.* (2001) found that the secondary chromosome of *A. tumefaciens* is of rival size to the primary chromosome (2.08Mb as opposed to 2.84Mb, accordingly)^[12].

Plasmids are small loops of DNA (between 1% and 5% of the size of the chromosome), which are present in the cell's cytoplasm and are therefore translated independently of a chromosome. Chromosomes are normally tasked with housing essential genes^[10] whereas plasmids contain genetic information which allow the plasmid to replicate along with genes which impart a selective and/or survival advantage to the cell^[13, 14]. There are several classes of plasmid:

- Resistance factors; these contain genes which allow the cell to resist potentially damaging environmental changes, such as a presence of antibiotics^[15].
- Virulence factors; contain genes which are translated into proteins that have a pathogenic effect on host cells. For example *Salmonella* virulence plasmids (SVPs) increase the bacteria's ability to replicate in extraintestinal organs of infected host animals, leading to death more frequently and rapidly than those infected with strains without SVPs^[16].

- Fertility factors; these plasmids are responsible for holding information vital to the process of conjugation ^[17].
- Bacteriocin; these plasmids encode for the production of bacteriocins, which are released into the environment and kill any bacteria that do not contain a copy of this gene. This results in less competition for resources for the cells which contain this gene ^[18].

Cell growth of bacteria is much faster than that of eukaryotic cells; for example *Clostridium perfringens* are able to double their colony size (generation time) in as little as 6.3 minutes ^[19]. However this time may be much longer for some species, like *Mycobacterium tuberculosis* which has a generation time of between 12 and 16 hours ^[20]. Bacterial cell growth is regulated and influenced by both environmental and internal factors. As a result of the short generation time, a bacterial colony may quickly adapt to changes in its environment, as selection pressures will result in a gene which provides the cell with a selective advantage becoming prevalent in a short amount of time. Such advantageous genes can be passed directly down the genetic line as the cells replicate or during conjugation where an entire plasmid will typically be transferred. Due to the fact that many non-essential advantageous genes are present on plasmids, these can be passed between bacteria via sex pili easily, and with no disturbance to the bacterial cell's chromosome.

Bacterial growth (see Figure 2) can be separated into four distinctive stages. The first stage is the Lag Phase, during which the bacteria adapt to their

environment^[21]. The duration of this stage is dependent on how similar their new environment is to their old one- the higher the similarity, the shorter the time. The second stage, also known as the Log phase represents rapid, normally exponential growth of the culture as a result of an excess of nutrients and the adaptation of the bacteria to their environment during the previous stage^[22]. Over time the bacteria enter the stationary phase, which is initiated by one, or more, of the following factors: the nutrients are limiting the population size, as only so many cells can obtain enough to survive; the concentration of waste product of the bacterial metabolism reaches the bacteria's limit, above which cells cannot survive, or the bacteria have reached their limit of space^[23]. The duration of the stationary phase depends on the amount of nutrients available to the bacteria, and on whether or not the nutrients are replenished^[23]. If the nutrients are not replenished, the bacteria inevitably reach the death phase, during which the bacteria begin to die as a result of a lack of nutrients. This may carry on until all bacterial cells die, or until there is a sufficiently low number of bacteria to be sustained by the low amount of nutrients.

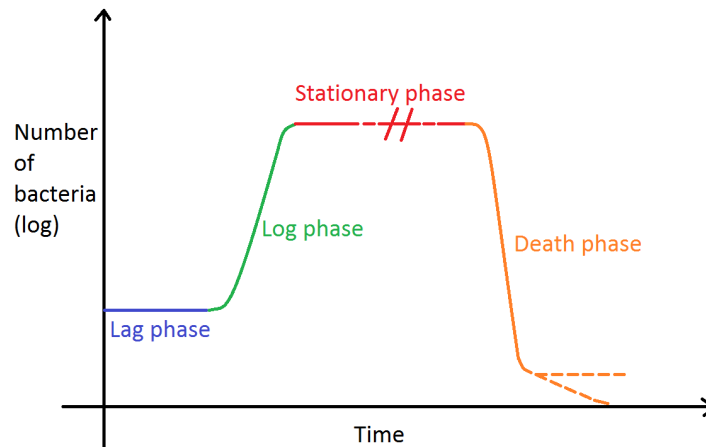


Figure 2: Simple bacterial growth curve. The first, blue, section demonstrates the lag phase. The second, green, section demonstrates the Log phase of rapid division. The penultimate, red, phase shows the stationary phase, during which the colony size remains constant. The final, orange, section shows the death phase, during which two outcomes are considered- a new lower stationary phase or total death of the colony.

Gram-positive bacteria possess a thick protective membrane consisting of peptidoglycans, which protects the cells from changes in the osmotic pressure of their environment, preventing osmotic lysis, as well as an exoskeleton to provide mechanical strength ^[24]. All Gram-positive bacteria also synthesise anionic polymers which are attached to the peptidoglycan layer via covalent bonds or are alternatively tethered to a lipid anchor moiety ^[25, 26]. The Gram-positive classification name arises as the result of the aforementioned Gram staining process, during which a dye (Crystal Violet (CV)) is added and retained by the thick peptidoglycan cell wall, resulting in a purple appearance under a light microscope ^[27].

Gram-negative bacteria have a more complex cell wall system, with a much thinner peptidoglycan membrane. Due to the nature of the outer wall of these cells, the CV dye used in the Gram staining procedure is not retained by the membrane, resulting in the bacteria appearing pink under a light microscope.

The outermost membrane of Gram-negative bacteria is a lipid-protein bilayer, with possible capsules and sheaths present in some organisms. It is composed of phospholipids, lipopolysaccharides (LPSs) and proteins, and it provides a physical barrier between the cell's external environment and the periplasm^[28] (see Figure 1). In some instances bacteria rely on diffusion for removal of waste and the uptake of nutrients and therefore this layer must be permeable to certain substances, otherwise active transport systems have to be present to ensure the required substances are passed across the cell envelope^[28].

Unusually even highly hydrophobic molecules can diffuse through this membrane; such as 3-oxosteroid probes studied by Plésiat *et al.* (1992)^[29].

Quorum-sensing (QS) is the process by which bacteria communicate^[30] to coordinate a population wide response to external challenge. The production, secretion and subsequent detection of extracellular signal molecules allows the bacterial cells to convey information about population density and changes in their environment^[31]. This density-dependent mechanism ensures that above a certain threshold the extra-cellular concentration of the signal molecules triggers gene expression appropriate to the changes in the environment^[32]. The

auto-inducing signal molecules may act on one cell to bring about a change in gene expression, or act on the whole population in order to trigger a co-ordinated population response, which is critical in bringing about the change from the log-phase to the stationary phase of their growth (see Figure 2) ^[33]. QS may trigger a shift in the population from favouring rapid replication and colonisation of the environment, to a slower replication rate by affecting the fertility factors within bacterial cells^[33]. The change results in energy becoming available to be used for other survival strategies such as activation of genes which produce bacteriocins which then reduce competition for resources, or products that interact with the environment to alter it in favour of the bacteria. The latter effects may sometimes be overlooked in laboratory studies, as bacteria are provided with growth substrates which are readily used by bacterial cells, however in nature this effect proves to be instrumental to cell survival in species such as the predatory *Mxyobacteria* which use a ‘wolf pack’ behaviour to lyse their prey organisms by utilizing extracellular enzymes and absorbing the resulting cell contents ^[34]. This behaviour requires the co-ordinated behaviour of the whole colony to work, and would be impossible without the use of QS ^[33].

The quorum-sensing mechanism differs between Gram-positive and Gram-negative bacteria, due to the difference between the permeability of their cell walls (Figure 3 and Figure 4)

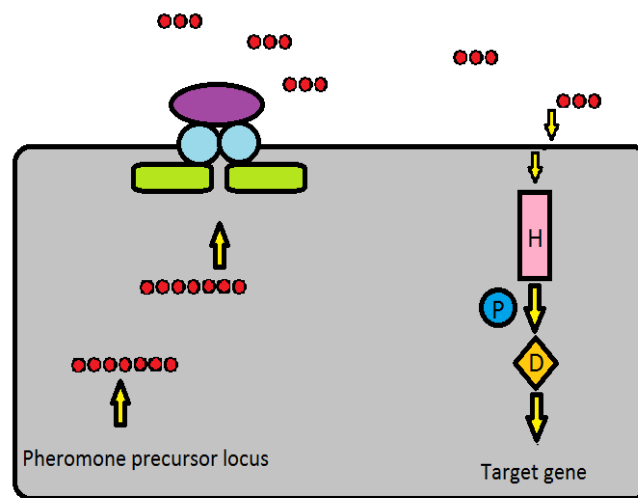


Figure 3: A simplified diagram of peptide quorum sensing. In Gram-positive quorum sensing bacterial cells, specific ABC transporter proteins (represented as the protein complex in the bacterial membrane) process and subsequently export peptide autoinducers (pheromones) (the precursors of which are depicted as long chains of circles inside the bacterial cell, and the autoinducers as the short chains of circles outside the bacterial cell). Membrane-bound two-component sensor kinase proteins recognise these extracellular pheromones. Upon binding, the sensor complex then autophosphorylates on a histidine residue (H), and transfer a phosphoryl group on to a cognate response regulator. These response regulators are phosphorylated on aspartate residues (D) (this process is denoted by the P in a circle inside the bacterial cell). Once phosphorylated, the response regulator proteins repress or activate the transcription of a specific target gene.

Gram-positive bacteria secrete peptide signalling molecules, typically through a dedicated ABC exporter protein (which is an ATP-binding cassette) [35]. These peptides are subsequently recognised by the cognate two-component sensor kinase proteins which combine with response regulator proteins within the cytoplasm. The mechanism of this signal transduction is known as a phosphorelay cascade (see Figure 3) [36]. Gram-positive bacteria adopt a common signalling two-component circuit although the type and complexity of additional regulatory factors vary [37].

Gram-negative bacteria employ a signal-response method of QS for the control of cell-density dependent responses [38]. They use *N*-acylhomoserine lactone (AHL) autoinducer signal molecules, which depends on a LuxI homologue AHL synthase and a LuxR homologue transcription activator protein which is responsible for the detection of cognate AHL and the induction of expression of the appropriate target genes (see Figure 4) [37].

Much like in the QS mechanism of Gram-positive bacteria, typically there exists additional complexity in the mechanism on top of the simple common pathway. For example *Ralstonia solanacearum*, in which QS controls the expression of virulence factors. The research conducted by Schell (1996) and Flavier *et al.* (1997) shows that the expression of the *R. solanacearum* LuxI/LuxR-like (autoinduction) system (SolI/SolR) is regulated by a LysR-like transcriptional regulator (PhcA) which responds to 3-hydroxy-palmitic acid methyl ester. In addition, the SolI/SolR system is also controlled by RpoS- the stationary phase sigma factor [37, 39, 40].

Apart from being involved in population density control, antibiotic resistance, colony behaviour and virulence, QS is also responsible for the motile-sessile transition phenomenon in bacteria which typically occurs in a biofilm. During this process bacterial cells change from a freely moving, motile cells to a surface-bound fixed position bacterial cell or one with limited mobility [41].

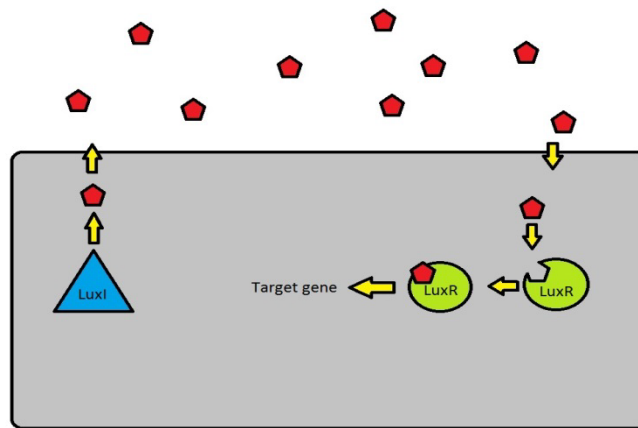


Figure 4: A simple diagram of LuxI/LuxR quorum sensing. In Gram-negative quorum sensing bacteria, LuxI autoinducer synthase proteins (blue triangle) produce specific HSL autoinducers (red pentagons). These autoinducers freely diffuse out of the bacterial cell membrane. Once a critical concentration is reached, the autoinducer is bound by its cognate LuxR protein (green circle). The resulting LuxR-HSL autoinducer complex activates transcription of a target gene.

The fact that bacteria use QS to communicate changes in population density may be exploited to artificially induce a slow growth rate in colonies in an effort to manage infections and/or contaminations. Alternatively, QS molecules may be utilized that cause the pathogenic bacteria to behave in a way detrimental to their own survival. An addition of such molecules to the

surface of medical devices or into drugs may prove to be a promising tool in the fight against pathogenic bacteria. This approach has already been successfully tried for *Candida dubliniensis* and *Candida albicans*^[42]. Work conducted by Ramage *et al.* (2002) shows that the addition of Farnesol, which is a QS molecule utilized by *C. dubliniensis* and *C. albicans* that affects filamentation- an important mechanism in biofilm formation, can completely prevent the cells from producing a biofilm^[42]. Further work by Jabra-Rizk *et al.* (2006) supports these findings as well as studying the effect of the reduced biofilm formation on antibiotic resistance of the colonies. In this case, the approach was conducted on fungal cells with antifungals in the study scope. However, in theory, a similar approach may prove effective for bacterial cells. Due to the fact that biofilms are seen as an important factor in facilitating antibiotic resistance in bacteria, a reduction of biofilm should cause a subsequent susceptibility to antibiotic. The results of this study support this theory, as colonies which had added Farnesol showed increased susceptibility to fluconazole; a common anti-fungal drug used to treat *C. dubliniensis*^[43].

1.1.2 The bacterial biofilm

A biofilm is formed as bacteria which attach to a surface aggregate in a hydrated polymeric matrix which they themselves excrete. The first stage in biofilm formation is the binding of motile bacterial cells to a surface. Initially this is usually via weak Van der Waals, or dipole-dipole forces^[44]. The reversible nature of these bonds allows the bacteria to move across the surface

and replicate freely. Eventually they form irreversible chemical bonds with the surface and enter a sessile stage. Bacterial cells possess numerous proteinaceous structures which they utilise in attachment to surfaces and cell adhesion [44]. These may be anything from simple monomeric proteins to large protein complexes [45], including fimbriae and pili, which consist of multiple appendages, as well as structures such as intimins, invasins, adhesins and curli [45-47]. For example work by Davey *et al.* (2000) showed that *E. coli* and *P. aeruginosa* use both pili and fimbriae during biofilm formation to adhere to surfaces [48], and the utilization of pili of *R. solanacearum* and *A. avenae* as well as afimbrial and fimbrial adhesins of *X. fastidiosa* have been explored by Kang *et al.* (2002), Bahar *et al.* (2009) and Feil *et al.* (2007) respectfully [49-51].

Once a monolayer of the sessile bacteria has formed, they begin to excrete extracellular polysaccharide and as the bacteria replicate within the biofilm, the increased volume creates a diffusion gradient for nutrients and oxygen. This results in the innermost bacteria entering a dormant phase, where their metabolic and replication mechanisms slow down [52]. The matrix is insoluble in water and takes on a slime-like appearance [53]. It is impermeable to most molecules unless they are actively transported through the structure, which proves problematic when attempting to treat a pathogenic bacterial infections which often form as biofilm [54]. Biofilms facilitate a protected setting for growth of a colony in a hostile environment. Their features include channels, through which nutrients can be transported throughout the structure [55], and

bacterial cells of the same species with different patterns of gene expression in different regions of the biofilm ^[56].

The complexity of biofilms has led some to use the analogy of biofilms to tissues of higher organisms ^[53]. Despite the sessile nature of the bacterial cells within the biofilm motile cells arise to promote dispersal. Due to the sessile nature of bacteria within the biofilm, such infections are slow to produce symptoms, which allows the biofilm to mature before any treatment is instigated ^[57]. The host immune system is also ineffective against biofilm-dwelling bacteria even though antigens are released into the host which stimulate the production and release of antibodies. ^[58]. In fact tissues surrounding the biofilm may suffer damage from the immune system response, which leaves the biofilm intact ^[59]. Chronic lung infections in cystic fibrosis patients and periodontitis are both examples of diseases are caused due to biofilm formation ^[60, 61].

Biofilm formation in medical devices is a major clinical problem ^[62] and can affect devices ranging from urinary catheters to intravascular catheters and orthopaedic implants ^[63]. A report conducted by the European Centre for Disease prevention and Control (ECDC) in 2008 estimated that 4,100,000 patients acquire healthcare-associated infections every year in European hospitals; and biofilm infections play a pivotal role in these infections ^[63, 64]. A report by Klevens *et al.* (2007) found that in the United States 13,088 deaths were reported as a result of urinary tract infections and 8,205 deaths due to surgical site infections in 2002 ^[65]; in both types of infections biofilms play a

pivotal role by decreasing the proportion of such infections which can be successfully treated [63]. In the United Kingdom a costing statement released in 2008 by the NHS National Institute for Health and Clinical Excellence (NICE) approximated a national annual cost of £57 million of surgical site infections alone [66].

Current approaches to prevent these infections include addition of antibiotics, nanoparticles (e.g. copper nanoparticles, which have a significantly higher surface area compared to larger particles, and therefore release their bactericidal ions at a higher rate^[67]), antimicrobial coatings and additives to the medical devices to prevent biofilm formation on the surface. All of these methods attempt to inhibit bacterial cell adhesion to the surface, interfere with QS signalling of bacterial cells post-adherence, or disaggregation of the biofilm post-formation [63].

Inhibition of bacterial cell adhesion may be achieved by several approaches, which can be characterised into two distinct groups- physical surface characteristics and chemical surface characteristics.

- Physical surface characteristics: these could be modifications to the surface to make it more hydrophilic, such as the silver nanowire nanostructures developed by Liu et. al (2019), due to the hydrophobic nature of microbial surfaces [68, 69]. The repulsion between the two surfaces may be sufficient to prevent bacterial adhesion altogether. For example, in an effort to reduce adhesion of *S. epidermidis* to silicone

shunts and polyurethane catheters, coatings of poly-N-vinylpyrrolidone and hyaluronic acid, respectively, have proven useful due to their hydrophilic nature ^[70, 71]. Hydrogel coatings have also shown great promise, as in addition to their ability to reduce bacterial cell adhesion, they are also able to take up and release antibiotics as a result of their high water potential ^[72].

Another possible physical surface characteristic modification is the introduction of a negative surface charge to the device. Heparin, for example, reduces fibronectin deposition on vascular catheter surfaces, which makes the surface negatively charged. This, in addition to preventing thrombosis, also reduces bacterial colonisation ^[73]. This effect has been shown both *in vitro* and *in vivo* ^[74]. A randomised clinical trial conducted by Abdelkefi *et al.* (2007) of 246 patients who had either heparin-coated or uncoated central venous catheters further confirmed the antiadhesive property of heparin ^[75].

Some research in this area also focusses on biomimetic structures which have been found to be effective in nature. An example of such a structure is a synthetic version on the surface of a dragonfly wing, studied and manufactured by Ivanova *et al.* (2013) from black Silicon. In effect the surface was manufactured in such a way as to produce nanoprotusions 500 nm in length ^[76]. This surface displayed extensive bactericidal properties, against Gram-positive bacteria, Gram-negative bacteria and fungal spores, by subjecting individual cell walls to

stresses, which in turn lead to cell deformation and eventually bacterial cell death ^[76].

- Chemical surface characteristics: these may include coatings, surface chemistry manipulation or ion-implantation. There are numerous different types of coatings that may be used, both biodegradable (which degrade in the body over time) and non-biodegradable. Degradable coatings offer the opportunity to prevent adhesion in two ways; through adhesion resistance, whereby the surface degrades faster than bacteria can attach to it, as well as the ability to engineer this surface in such a way that it slowly releases molecules which actively kill bacteria. The former effect has been widely studied, and polymers such as poly(ethylene glycol)(PEG) ^[77, 78], polyvinylpyrrolidone (PVP) ^[79, 80] and poly(ethylene oxide) (PEO) ^[81] have shown promise. The latter method; active release of antimicrobial agents, has also been widely investigated, with effective agents including antibiotics ^[82, 83] and metal ions (silver ions ^[84, 85], gallium ions ^[86, 87], copper ions ^[88], zinc ions ^[89]). Nonetheless, the use of antibiotics is decreasing due to the ever-increasing resistance to them, and the negative effect they often have on the human cells ^[90]. Apart from addition of metal ions, the addition of metal nanoparticles to the surface has also been investigated, with silver nanoparticles showing some promise ^[91, 92]. Use of quaternary ammonium compounds has also been widely

researched in a contact-killing surface application ^[93]. The addition of these can be achieved by covalent linking ^[94, 95], grafting ^[96], or self-assembly ^[97]. The aforementioned contact-killing approach is far from perfect as it causes the creation of a layer of dead bacterial cells on the surface. This means that any subsequent bacteria that attach to the surface will not be in direct contact with it, *ergo* reducing the effectiveness of any bactericidal features. In addition to the compromised effectiveness of such a surface after a layer of dead bacteria has formed, the said layer could even trigger an immune response and inflammation in the surrounding tissue ^[98]. A combination of the aforementioned features may be employed to increase the effectiveness of antimicrobial properties of a surface. For example a study by Mi *et al.* (2012) found that when using a switchable polymer system, employing cationic molecules as a contact-killing surface feature, dead bacteria were released after the cationic derivatives were hydrolysed to zwitterionic polymers which have a non-fouling property ^[99].

1.1.3 Antibiotic Resistance

Antibiotic resistance can arise in three ways in bacteria; the bacteria may be naturally resistant, a random mutation occurs in the bacterial DNA or genetic material (usually plasmids) are shared between cells. In most cases the two lattermost mechanisms are the reason as to why a bacterial colony has

developed resistance to an antibiotic; a mutation in a single cell creates the resistance gene, which is then passed on to nearby bacteria by plasmid transference^[100]. This process is exacerbated if the antibiotic dose is increased slowly, or stopped and restarted as this creates selective pressure in the colony, whereby the bacteria containing the gene are at a survival advantage^[101]. Antibiotic resistance has become a serious clinical and public health issue within a very short amount of time, as a result of over-prescription of antibiotics by doctors and patients not finishing the full course of antibiotics^[102]. The latter occurs due to the fact that any bacteria not killed by the course of antibiotics will be exposed to low levels of residual antibiotic in the system— not high enough to kill the bacteria, but enough to exert a selection pressure for resistance genes^[101].

However, during biofilm-associated bacterial infections, the bacteria seldom acquire innate resistance of individual bacterial cells through resistance pathways. Instead, they rely on the multicellular strategy of biofilm excretion of a protective biofilm^[103].

The biofilm allows such effective protection from antibiotics that even doses several thousand times the minimum inhibitory concentration of the bacteria measured in a suspension culture do not eradicate the infection^[104]. Anderl *et al.* (2000) revealed that a β -lactamase-negative strain of *K. pneumoniae* had a minimum inhibitory concentration of 2 $\mu\text{g}/\text{mL}$ of ampicillin when present as a culture suspension but when assessing the same strain grown as a biofilm the colony displayed a 66% survival rate when subjected to a 4 hour treatment

with 5000 µg/mL of ampicillin; a dose which quickly eradicated free-floating bacteria and was 2500 times higher than the minimum inhibitory concentration [105].

1.1.4 Biomedical Materials

Biomedical materials are not solely selected on their antibacterial properties. Another important factor is bioactivity; namely the positive effect the material has on the human cells that interact with it, aiding healing. Medical devices can be manufactured from, coated with, or otherwise treated with materials with these characteristics. For example, Ti6Al4V Titanium alloy is widely used to provide the bulk material to provide required mechanical properties [106], Hydroxyapatite coatings (HA) has been uses as a coating to encourage bone growth^[107], and silver nanoparticles have been embedded in a polymer thin film to prevent surgical site infections^[108]. A combination of these approaches can be adopted to optimise favourable characteristics of several materials. These materials can be metals, polymers, ceramics or composites, and may be naturally occurring or synthetic.

Metals are often used in orthopaedic applications, such as total hip replacement devices, due to their mechanical strength. Stainless steel (316L) has been widely used in the past due to its corrosion resistance^[109], however more recently there has been a shift to Ti6Al4V Titanium alloys and Co-Cr-Mo Cobalt alloys due to their improved bioactivity. The –OH groups present on the surface of Ti6Al4V, present due to the surface oxide layer on the metal,

encourage bone to be formed up to the surface, as osteoblasts (cells which deposit bone) are attracted to them, which improves implant fixation *in vivo* ^[110]. Apart from structural strength, metals may be used as coatings to improve radiopacity of materials. Gold plating, for instance, greatly improves precision with which devices such as stents are placed within the body, by making the device visible *in situ* with aid of an x-ray machine ^[111].

Metal implants are used extensively in fixation and load-bearing applications, mainly due to their high strength and fracture toughness. Whereas the compressive strength of adult femoral cortical bone is ~193 MPa, and tensile strength of ~133 MPa in the longitudinal direction^[112], the compressive strength of a cast Ti6Al4V alloy is ~847 MPa, with the tensile strength of ~976 MPa^[113]. The higher strength allows for the implantation of smaller devices, which results in a slightly lower cost and a smaller displacement of native tissue, without compromising the strength of the device.

However, metal devices tend not be bioresorbable, with the exemption of a few small Mg devices, used in tissue engineering, orthopaedic and cardiovascular applications^[114]. This means that although metal devices will continue to be employed in load-bearing orthopaedic applications, due to their high strength and fracture toughness, they have been replaced by bioresorbable polymers and ceramics in many fixation applications^[114].

Metal implants also have an inherent problem, namely; their Young's Modulus. The Young's modulus of a CoCrMo, 316L Stainless Steel and

Ti6Al4V hip stems is 210 GPa^[115], 200 GPa^[116] and 110 GPa^[115] respectively, which is significantly higher than 19 ± 5 GPa of cortical femoral bone^[117]. This difference in the Young's modulus produces stress shielding of bone surrounding an implant^[118], which in turn causes loss of bone density. This loss of bone density around the device results in eventual implant loosening, which requires a revision surgery to replace it^[119].

Polymers can be used in a wide variety of biomedical applications, from biosensors^[120], to joint replacement sockets^[121] and tissue engineering scaffolds^[122]. When used in biosensors, they provide low-weight biocompatible devices which allow for immobilisation of enzymes. S. Soylemez *et al.* (2014), for instance, successfully immobilised cholesterol oxidase on the surface of a graphene electrode by using 2-(4-fluorophenyl)-4,7-di(thiophene-2-yl)-1H-benzo(d)imidazole as an immobilisation matrix^[120].

In orthopaedics polymers may prove useful in two ways; they may provide biodegradable and bioresorbable fixation devices which degrade over time, allowing for bone to replace them (such as polylactic acid bone screws^[123]), or alternatively provide non-biodegradable components with low coefficients of friction which may be used in applications such as the cup component of a total hip replacement device- an application for which Ultra High Molecular Weight Polyethylene (UHMWPE) is widely used^[124].

As tissue engineering scaffolds, polymers once again provide the opportunity for bioresorbable devices, which are removed over time by the cells of the

tissue that replaces it. Such scaffolds may be synthetic, such as poly(propylene fumarate) scaffolds which aid bone healing and act as a bone defect filler [125], naturally occurring; such as chitosan [122], or naturally derived such as decellularised extracellular matrices [126]. Due to the nature of polymers, signalling molecules and larger proteins can be attached to the surface, in an attempt to increase the rate of healing, and such modification renders the scaffold biomimetic, whereby it acts as a limited extracellular matrix to the cells [127, 128].

Ceramics, such as alumina and zirconia, are often used in total joint replacement devices on articulating surfaces instead of polymers and metals due to their increased wear resistance [129, 130], high compressive strength [131] and low coefficient of friction [132]. They are also used as additives to polymeric and metal devices, due to the fact that ceramic microspheres and coatings can be manufactured from one of the main components of bone- a mineral called hydroxyapatite, which improves osteoconductivity; namely the ability of bone to grow up to the surface of the implant interface, even forming bone of the implant surface itself [133-136].

Bioresorbable and biomimetic ceramics, such as Hydroxyapatite (HA), can be used as coatings or additives to enhance the bioactivity and osteoconductivity of both metal and polymer devices. HA can be used as a coating on orthopaedic metal devices, in order to encourage bone growth up to the surface of the implant, aiding in its fixation *in situ* [137]. Coating with HA is also widely utilised in dental implants, for this very reason [138].

Nanoparticles of HA of varying sizes can be added to polymer scaffolds to produce composite scaffolds with a different *in vivo* degradation or mechanical properties^[139-141]. The addition of HA provides an opportunity to control these properties without compromising the possible bioresorbable nature of the initial scaffold^[142].

1.1.5 The clinical need

In the last two decades, several metallic devices have been developed in order to support biological integration and fixation of orthopaedic implants. The move towards cement-free fixatives, whereby the devices rely on bone ingrowth rather than application of bone cements, has facilitated an improvement in clinical outcomes of patients with these devices. The porous biomaterial field has continued to evolve, and first-generation ingrowth surfaces have given way to metallic foams and scaffolds which present an opportunity to advance cementless technology in all aspects of orthopaedic surgery^[143].

Despite the notable advances in this field, and orthopaedic device field in general, infections resulting from implant placement remain a major complication in modern orthopaedic and trauma surgery^[144]. Despite best practice in surgical management, device placement can lead to infections which negatively impact the clinical outcome of patients and increase healthcare expenditure^[145]. Although pre-operative prophylactic antibiotic administration is mandatory for most orthopaedic procedures, the incidence of

infection following elective surgery is between 0.7% and 4.2%^[146-150]. This rises significantly in trauma cases where the infection rate ranges from *c.a.* 1% after operative fixation of low energy fractures to over 30% in complex tibia fracture fixation^[151, 152]. Current treatment options, such as radical debridement, prolonged antibiotic therapy and revision surgery have a success rate of between 57% and 88%^[153-155]. However these result in significant socioeconomic costs, as well as posing a risk to a life-long functional impairment for patients^[156].

The most prevalent organisms responsible for orthopaedic and trauma device-related infection (ODRI) are Staphylococci, with *Staphylococcus (S.) aureus* alone accounting for between 20% and 30% of infection cases^[157-161].

Considering that the wound may be contaminated by up to 14 different bacterial species in the operating theatre alone, this share of *S. aureus* is very significant^[162]. Recently efforts have also been made to study polymicrobial infections, which account for *c.a.* 10% of cases^[157, 158, 161].

1.1.6 Bacterial contamination of scaffolds

The bacterial^[163] colonisation of orthopaedic scaffolds has not been studied to nearly the same extent as their traditional, solid implant counterparts. Data relating to the bacterial cell behaviour on a device surface is often extrapolated from experiments conducted on flat surfaces (for which studies are numerous)

to be representative of what would happen within a scaffold. The logic behind this is that as the surface chemistry of the device is unchanged, the behaviour of bacteria on it would likewise remain so. However what this approach fails to take into account is that despite the fact that on the nano-, and to some extent micro- geometry of these surfaces is the same, the larger macro-scale features are also an important aspect in the mechanics of infection^[164]. This is due to the 3D geometry of these devices, apart from providing attachment sites for cells such as osteoblasts, also vastly increase the surface area unto which bacterial cells may attach, as well as provide some protection from fluid flow and the immune system^[164]. The difference in fluid dynamics within the scaffold as opposed to a flat surface may also affect the amount of antibiotic reaching bacterial cells further within the scaffold, further reducing the efficacy of such treatments in case of an infection.

A quantifiable assessment of bacterial infection models within scaffolds is particularly challenging, as contemporary methods in microbiology usually focus on flat samples^[165-168]. Methods such as the Japanese Film Method (JIS Z2801), adenosine triphosphate (ATP) bioluminescence assay, or LIVE/DEAD assays are widely used when assessing the bacterial behaviour on flat surfaces^[169-171], and the agar diffusion method is useful in assessing the antibacterial effect of substances eluted by the sample^[172, 173], however they do not facilitate the analysis of 3D porous structures. Imaging of green fluorescent protein (GFP)-tagged bacterial cells with a confocal microscope

allows for better analysis of larger surface structures^[174], but that too does not produce reliable results when faced with porous scaffolds.

A good indication of the infection mechanisms within scaffolds can be obtained by use of animal models, such as rabbits^[175], however it is simply not feasible to use these models at the very early stage of sample screening.

1.1.7 Selection of commercial samples from Zimmer-Biomet

There are a number of metal scaffold orthopaedic devices currently available in a clinical setting, two of which are produced by Zimmer-Biomet; namely: Trabecular Metal and Osseo-Ti devices.

Trabecular Metal scaffolds are produced using a chemical deposition process (Chemical Vapour Deposition/ Infiltration), whereby elemental Tantalum is deposited onto a substrate, creating a structure highly like that of cancellous bone. This allows the scaffold to exhibit high porosity (75%-80%), with highly interconnected pores of regular size^[176]. These features, together with the scaffold's low modulus of elasticity^[177] (which is close to that of cancellous bone), result in the device seeing encouraging results and success clinically^[178, 179].

Osseo-Ti is a Titanium alloy (Ti6Al4V) scaffold manufactured by Selective Laser Sintering (SLS), whereby the bulk powder is sintered together to form the required geometry. In this case, the geometry is based directly on CT scans

of cancellous bone and mimics its structure. The use of the Ti6Al4V alloy is common within orthopaedic devices, therefore well documented^[180-185]. However, despite the widespread use of this alloy, it is not inherently antibacterial^[186, 187], *ergo* infections are common unless treatments are conducted on the bulk material to induce an antibacterial characteristic. Such treatments may include coatings, nano-topography alteration or surface-chemistry modification^[188-191].

As Iodine's antibacterial effect is well documented^[192-194], it provides an opportunity to be combined with a Titanium surface (either by mechanical means, or by chemical deposition) in order to lend those properties to the Titanium device^[195, 196]. This is an approach taken by Zimmer-Biomet, whereby the titanium surface is first anodised and then undergoes micro-arc oxidation (MAO), which produces a surface with numerous micro-channels, upon the conclusion of which Iodine is deposited inside the resulting micro-channels. This Iodine can then, upon placement *in situ*, gradually leach out and provide the surface with antibacterial characteristics.

These samples were chosen owing to the fact that they represent traditional metal alloys used in orthopaedics (Ti6Al4V) as well as more recent advances in the materials in the shape of elemental tantalum devices. They are also already available in the clinic, meaning they provide a direct link to the real-world setting.

1.1.8 Possible ways to measure biofilm formation in Zimmer-Biomet scaffolds

The use of Micro-Computed Tomography (Micro-CT) has shown promise when analysing scaffolds *in vivo* and *in vitro*, aiding in characterisation and with the possibility to analyse bone ingrowth inside these devices^[197-199]. This may pose an opportunity to extrapolate these advances to aid in quantification of bacterial biofilm growth within scaffolds and allow for visualisation of the innermost parts of the samples.

Laser confocal microscopy may also be useful in this assessment, as the computed rendering of resultant images^[200-202] could be modelled in such a way as to account for the varied surface area by modelling. This would allow for standardised and relatively quick testing to be conducted within the pores of scaffolds.

The predominant challenge in measuring the biofilm formation within these scaffolds is the fact that for the measurements to be meaningful, they have to be taken from within the scaffolds themselves, instead of their topmost surface. This has to be done without disturbing the scaffold or the biofilm within, meaning physical and mechanical methods, such as dividing the scaffold and taking measurements from its cross-section would not be appropriate.

1.1.9 Aims and Objectives

The aim of this study is to develop and validate a new analysis method to provide quantifiable, accurate and reliable results for the measurement of bacterial biofouling on flat and three-dimensional samples alike- in this case metal disks of differing surface topographies and 3D metal orthopaedic scaffolds. Methods such as confocal laser-scanning microscopy will be evaluated for suitability in this case. Alternative methods, which haven't been covered in any significance in literature but which may hold promise for this use will also be evaluated- such as micro-CT and weighing methods. This method is then used to measure the bacterial biofouling of samples once inoculated and incubated with *S. aureus* in a protein-rich environment similar to the one they would be exposed to *in situ*.

The objectives of this work are as follows;

- To evaluate currently-available approaches for quantifiable biofouling/ bioburden assessments and their potential use to measure biofilm formation within a metal scaffold.
- If no method present in literature is transferable or suitable to the assessment of bacterial presence within metal scaffolds- to develop and validate a novel methodology for this purpose.
- Evaluate bacterial biofilm growth within orthopaedic scaffolds currently available commercially, in clean media as well as an

environment which scaffold implants would likely be subjected to *in situ*- protein rich media.

- To ascertain what, if any, surface treatments to the aforementioned samples may limit any bacterial biofilm formation.
- To conduct a proof-of-concept evaluation of novel metal-polymer hybrid scaffolds against samples available in clinic in terms of bacterial biofilm formation.

The next chapter outlines and describes the samples studied, as well as their chemical composition and morphology.

The thesis as a whole is divided into 6 chapters. Each chapter is structured in a quasi-paper format, with each containing a materials and methods section, results and discussion sections. This is done so that the reader can access chapters of interest with ease, and have at their disposal all relevant information relating to the studies covered within the chapter. Owing to the large volumes of changing methods throughout the work this structure is intended to bring clarity to the topics covered within each chapter.

The first chapter is a literature review and an overview of the samples provided from a commercial sponsor. It assesses the body of literature

surrounding the subjects of the work, and forms a foundation of subsequent chapters.

Chapter 2 is a characterisation of the samples, in order to study their chemical composition and surface morphology. In addition to this, it forms hypotheses concerning the effect of these characteristics on bacterial growth.

Chapter 3 studies the reliability of existing methods in obtaining quantifiable bacterial biofouling data with the specific use-case of metal 3D scaffolds as its focus. A number of methods are analysed with a view to adopt any which prove effective in this application for the remainder of the work conducted subsequently.

Chapter 4 describes the development of a novel SEM image analysis method to measure bacterial coverage. The method is validated against a well-established analysis method- CLSM- in an application it's well-suited for- flat surfaces. It's then used to conduct proof-of-concept studies using 3D scaffolds.

Chapter 5 describes studies conducted to investigate the effect of protein presence on bacterial coverage and growth upon flat and three-dimensional samples. All microbiological results described herein are obtained using the SEM image analysis method.

Finally, chapter 6 contains proof-of-concept studies concerning hybrid scaffolds (metal-polymer) and their potential in endowing orthopaedic devices with antibacterial properties without compromising their long-term bioactive or mechanical properties. It then follows with conclusions for the entire body of work hitherto described in previous chapters and recommendations for future work.

Chapter 2 Characterisation of Sample Composition and Morphology

This chapter intends to inform about the composition and morphology of samples, as well as form hypotheses regarding the impact this may have on bacterial attachment.

2.1 Materials and Methods

2.1.1 Sample Selection

Samples for this study were supplied by Zimmer-Biomet. They included commercially available surfaces, manufactured from Tantalum and a medical-grade Titanium alloy (Ti6Al4V). All sample disks measured 10 x 2.5 mm (Figure 5). A number of surfaces manufactured from these materials allowed for a simultaneous assessment of surface topography and chemistry effects on bacterial behaviour as well as the suitability of the assessment methodology.

The sample types were as follows: polished disks, grit-blasted disks, 3D additively-manufactured scaffolds (Osseo-Ti: Ti-6Al-4V scaffold manufactured using Selective Laser Sintering (SLS) and Trabecular Metal: Ta scaffold manufactured using Chemical Vapour Deposition (CVD)).

Some polished Ti disk samples were coated with elemental copper through sputtering- a Physical Vapour Deposition (PVD) process whereby a thin film is deposited using ejected materials from a target onto a substrate- in order to be used as positive control in the microbiology studies.

The Trabecular Metal was an open cell highly porous (~80% porosity^[203]) structure, similar in geometry to trabecular bone by being composed of struts ordered in dodecahedron repeats^[204]. In order to achieve this, a vitreous carbon scaffold is used as an internal matrix upon which the Tantalum is later deposited^[205]. The carbon scaffold is then placed in a sealed chamber and the CVD process proceeds using hydrogen and chlorine gases. Evaporated tantalum (as TaCl₂) then deposits Ta molecules onto the underlying carbon scaffold^[206]. A review of available literature suggests that this material exhibits high osteoconductivity, biocompatibility, vascularisation and bone-ingrowth (as observed in *in vitro*, *in vivo* and human studies)^[176, 203, 207-210].

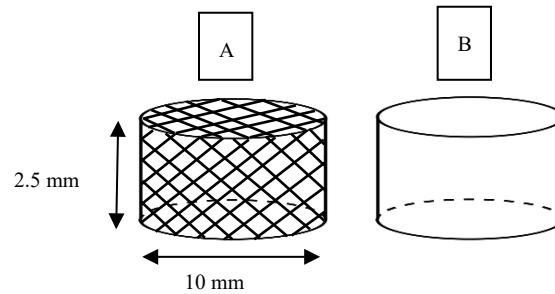


Figure 5: Schematic outline diagrams of sample types. A. shows Ti6Al4V and Tantalum 3D scaffolds (Osseo-Ti and Trabecular Bone respectively). B. shows flat samples of the following: polished and grit blasted Tantalum and Ti6Al4V and Tantalum disks, Copper-coated Ti6Al4V disks, anodised and Iodine-treated disks as well as Magnesium and Magnesium-Calcium disks.

The Osseo-Ti scaffold is manufactured using SLS of Ti-6Al-4V powder, based directly on 3D scans of cancellous bone and exhibits ~70% porosity according to data supplied by Zimmer-Biomet.

The characterisation of samples was undertaken to ascertain the chemical composition and physical topography of their surfaces. To this end, a number of non-destructive approaches and methods were employed. The chemical composition was analysed using Energy-Dispersive X-Ray Spectroscopy (EDX), X-Ray Photoelectron Spectroscopy (XPS) and X-Ray Fluorescence Analysis (XRF). The surface topography was evaluated using a combination of Scanning Electron Microscopy (SEM), Atomic Force Microscopy (AFM) and Laser Profilometry. All of these methods are widely studied and documented in literature for this purpose^[211-218] and are summarised as follows.

2.1.2 Scanning Electron Microscopy (SEM)

SEM in this instance used the detection of Secondary Electrons, whereby a beam of electrons is focussed on the sample surface. When this beam interacts with the surface, the electrons lose energy by repeated scattering and absorption within the interaction volume^[219, 220]. The size of the interaction volume relies upon the atomic number of the elements within the sample, its density and the electron's landing energy^[220]. This energy exchange between the beam and the surface, among other signals, results in the emission of electrons from the surface's constituent atoms. These are Secondary Electrons, and due to their low energy, they are only emitted from the topmost few nanometres of the surface. The brightness of the signal is then dependent upon the number of Secondary Electrons reaching the detector from a specific position^[221, 222].

Surface topography was assessed using SEM imaging in the Secondary Electron (SE) detection setting. Micrographs were obtained using a FEI XL30 Scanning Electron Microscope. A working distance was maintained between 10.0 and 11.0mm utilising a beam energy of 20kV.

2.1.3 Energy-Dispersive X-Ray Spectroscopy (EDX)

EDX relies on the emission of characteristic X-rays from the surface of the sample by focussing a beam of X-Rays on said surface. An electron in the inner shell may be excited by this incident beam and eject itself from it

creating an electron hole in its place^[223]. An electron from a higher-energy outer shell then fills the electron hole, and the difference in energy between the lower inner shell and higher outer shell is released in the form of an X-Ray. These resultant X-Rays emitted from the sample surface are then measured using an energy-dispersive spectrometer, and as the energies of the X-Rays are characteristic of the difference between the higher- and lower-energy shells and of the atomic structure of the surface, EDX allows for the elemental composition of the specimen to be analysed^[223]. The number of the X-Rays of a specific energy are also indicative of the amount of particular element present, *ergo* this information is then used to ascertain the amount of the said element within the sample^[221, 224].

Surface compositional analysis was conducted using an Energy-Dispersive X-ray spectrometer (EDX) (Oxford Instruments) at a beam voltage of 20 kV, a working distance of 10mm and maintaining a min. X-ray count of 150,000.

2.1.4 X-Ray Photoelectron Spectroscopy (XPS)

Unlike EDX analysis, XPS can also be used to determine the molecular composition of the surface, in addition to the elemental presence and quantification. XPS spectra are attained by focussing an X-Ray beam onto the surface and concurrently measuring the kinetic energy of electrons which have been emitted as a result^[225]. A photoelectron spectrum is then recorded by counting the ejected electrons with a range of kinetic energies. As an atom absorbs an X-Ray photon, an electron is ejected. The ejected electron's kinetic

energy depends on the binding energy of the electron and the photon energy^[225]. Measuring the emitted electrons' kinetic energy allows for determination of the binding energy, and therefore the presence of elements and their chemical states. This is because each element in each chemical state has a characteristic and specific binding energy. Further to this, the binding energy also depends upon the orbital from which the electron is ejected, *ergo* this can also be ascertained^[226-228].

The equation allowing for XPS analysis is as follows:^[225]

$$KE = h\nu - BE$$

Where KE = Kinetic Energy, $h\nu$ = Photon Energy and BE = Binding Energy.

X-ray Photoelectron Spectroscopy (XPS) analysis was done using a VGESCALab Mark II X-ray photoelectron spectrometer with a monochromatic Al K α X-ray source incident to the sample surface at 30°. Survey and high-resolution scans were conducted. A measurement of adventitious C 1s was taken for calibration, and consequently the charge was corrected to 284.8 eV. The parameters during acquisition were: number of scans set at 5, step size of 1.0; dwell time 0.2 s (survey scans), and 0.4 s (high-resolution scans). Binding energies were measured over a range of 0–1200 eV. Casa XPS was used for spectrum analysis, constraining the Full Width at Half Maximum to the same value for all de-convoluted spectral peaks of the same element. Samples were sterilised at the Zimmer-Biomet factory and transferred immediately from their sterile packaging to the XPS instrument,

taking care to not handle the surface from which measurements were to be taken.

2.1.5 X-Ray Fluorescence Analysis (XRF)

XRF is similar in principle to EDX and relies on the excitation of the sample surface by a primary high-energy X-Ray. X-Ray Fluorescence is emitted of lower energy than the incident beam, as electrons from inner shells of atoms are excited and emitted, and the space they leave behind is filled by electrons from higher-energy shells^[229]. The characteristic X-Ray Fluorescence diffracted from the element of interest are selectively measured. The energy of the X-Ray Fluorescence is characteristic of each elemental atom, and the intensity of each energy value is proportional to the abundance of the element in the measured surface^[230-232].

The analysis was conducted with a PANalytical Epsilon 3-XL energy dispersive XRF with 6 μ m thick Mylar film. Using the Omnion software. It's a 20-50 kV system, with a 50 μ m Ag target anode.

2.1.6 Atomic Force Microscopy (AFM)

Atomic Force Microscopy utilises a probe at the end of a cantilever in order to measure the height of a surface at a given point^[233]. A tapping mode was used in the procurement of data in this instance. In this mode, the cantilever is made to oscillate at its resonance frequency. As the tip's proximity to the surface decreases, the amplitude of the cantilever's oscillation changes. The tip's

position is moved along the sample surface, and the resulting image is produced by the force of recurrent contact between the tip and the surface.

The surface roughness of scaffold struts was measured using a Dimention ICON AFM (Bruker Nano Surface), working in contact mode. Measurements of 40 μm^2 were taken on the surfaces of individual struts within the scaffold.

2.1.7 Laser Profilometry

Laser profilometry relies on the confocal use of two laser beams, with a detector^[234, 235]. The beams, in order to illuminate a given point on the surface in the sample place need to move up or down depending on the height of the surface feature in question. As the amount by which the lasers are required is known, the physical height of the surface at that point can be ascertained^[236].

The surface roughness of flat samples was measured using an Alicona InfiniteFocus G5 microscope (at 10x magnification and 0.5 μm resolution). The area measured was 2.5 mm^2 . The sample was taken immediately from its sterile packaging in which it was provided by Zimmer-Biomet to the laser microscope using clean gloves to ensure no scratching or other alterations to the surface occurred.

2.1.8 Water Contact Angle Measurement (WCA)

The Water Contact Angle (WCA) is measured by placing a droplet of water onto the surface of the sample and the angle of the interface between the

droplet and the surface is measured optically with the use of a high-resolution camera and imaging software. The WCA can be analysed to give detailed information about the surface free energy, polar and dispersive component determination and hydrogen bond force measurement^[237]. In this instance, the WCA was measured in order to analyse the hydrophilic/hydrophobic nature of the sample surfaces^[238, 239].

The Water Contact Angle was analysed using a Krüss Picoliter Dosing System DSA100M, utilising a ½” CCD-camera with a 20x microscope objective at 500fps. The samples were washed in an ultrasonic cleaner and dried under cover so as to eliminate risk of particles or dust settling on their surface. Once the samples were completely dry, they were transported to the dosing system under cover. At this point, samples were analysed. 3 readings were taken on each surface, and 3 samples were analysed for each sample type.

2.2 Results

Samples were comprehensively characterised in terms of their physical surface morphology as well as their chemical composition (both bulk and surface).

2.2.1 Scanning Electron Microscopy (SEM)

Samples were imaged using Scanning Electron Microscopy (SEM) in order to evaluate the topography and morphology of their surface. Each sample type was measured to provide a series of comparison micrographs. Magnifications of x100, x200, x800 and x25,600 were taken of each surface to assess both macro-level geometry as well as fine surface characteristics.

The geometry of a tantalum scaffold (Figure 6A and Figure 7A) shows a close resemblance to that of trabecular bone, when compared visually to micrographs of each other, upon which it was based ^[203, 240], in the low (x100 and x200) magnification micrographs- though no study was conducted to confirm this similarity. Upon inspection at higher magnification (x800 and x25,600), the roughness of the individual struts becomes apparent. The pores, although somewhat irregular in size and shape, are *c.a.* 300-400 μm in diameter, and the diameter of the lattice struts is 150 μm .

The titanium scaffold (Figure 6B and Figure 7B) has fewer, albeit much larger pores than the aforementioned tantalum scaffold. The pores are not of uniform size; however, have a diameter of over 500 μm . The diameter of individual struts is *circa* 300 μm . At x100 magnification, the size of the pores in this structure is clearly visible. When imaged at x200 magnification, the size of individual struts can be assessed, as well as the microspheres which are present throughout the structure become visible. These microspheres are clearer still at a magnification of x800, and their vastly varied size can be

determined to be between around 5 μm and 45 μm . The integration of the microspheres can be gauged at x25,600 magnification, with some becoming almost entirely integrated and some remaining attached only by small amounts of the metal, much like in the image seen in Figure 7B.

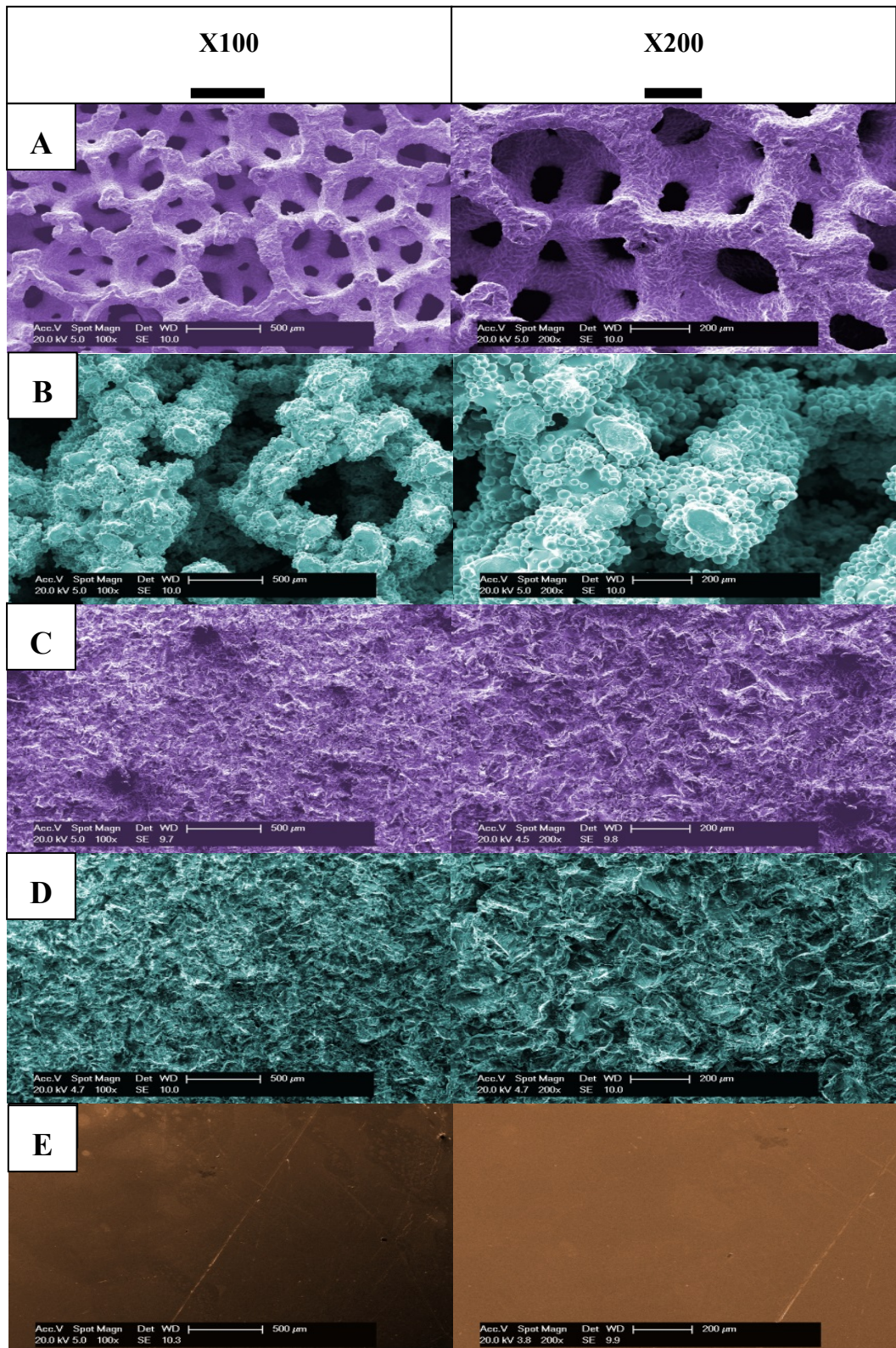


Figure 6: False-colour SEM Micrographs at x100 (left) and x200 (right). Rows A and B show the two scaffold samples (Tantalum (Trabecular Bone) and Titanium (OsseoTi) respectively). Rows C and D show grit-blasted disk sample surfaces (Tantalum and Titanium respectively). Row E shows a Cu-coated polished Ti disk sample.

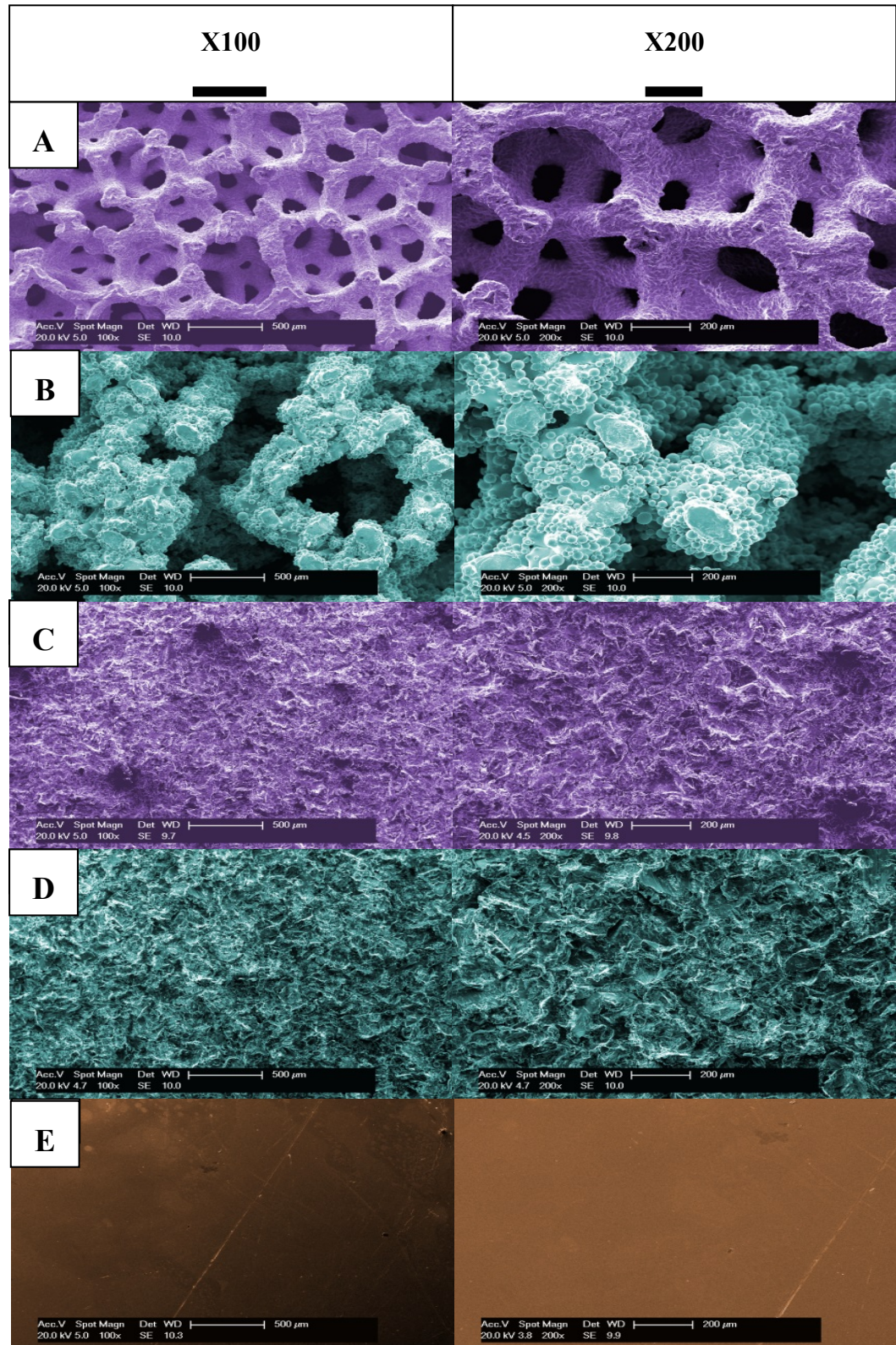


Figure 7: False-colour SEM Micrographs at x100 (left) and x200 (right). Rows A and B show the two scaffold samples (Tantalum (Trabecular Bone) and Titanium (OsseoTi) respectively). Rows C and D show grit-blasted disk sample surfaces (Tantalum and Titanium respectively). Row E shows a Cu-coated polished Ti disk sample.

The grit blasted tantalum and titanium samples (Figure 6C, D and Figure 7 C,D respectively) display identical morphologies. Both have a highly rough surface with large features on the surface as a result of the grit blasting process. No contamination as a result of the processing is apparent in the images.

The polished samples have the same surface morphology as that seen in Figure 6E and Figure 7E, and as such only the copper-coated polished titanium images are given, as representative of themselves, polished titanium and polished tantalum samples. Some superficial, and isolated scratches are present on the surfaces, likely as a result of handling, apart from which the surfaces are flat with no other features.

2.2.2 Energy-Dispersive X-Ray Spectroscopy (EDX) and X-Ray Photoelectron Spectroscopy (XPS)

Energy-dispersive X-Ray spectroscopy (EDX) and X-Ray photoelectron spectroscopy (XPS) were used to study the elemental composition of the samples (Figure 8 and Figure 9). The figures show the XPS measurements as the topmost layer of a composition, and EDX is displayed as the inner portion of the graphical representation. EDX was employed to give the composition up to 2 μm in depth, whereas XPS was used to assess the chemical composition of the topmost 5 nm^[241, 242].

Across all samples the oxygen content, indicative of an oxide layer, is greater in the topmost layer (XPS) than it is in the depth range of EDX. The greatest amount of oxygen on the surface, as measured by XPS (Figure 8) (, is seen on grit-blasted tantalum samples, at 10.09 wt%, followed by grit blasted titanium and scaffold tantalum (7.59 and 6.88 wt% respectively). Titanium samples have a significantly lower oxygen content on the surface, compared to their tantalum counterparts, when measured with EDX and XPS. Copper-coated titanium had an oxygen content of 2.03 wt% when assessed using XPS and 1.48 wt% when measured with EDX.

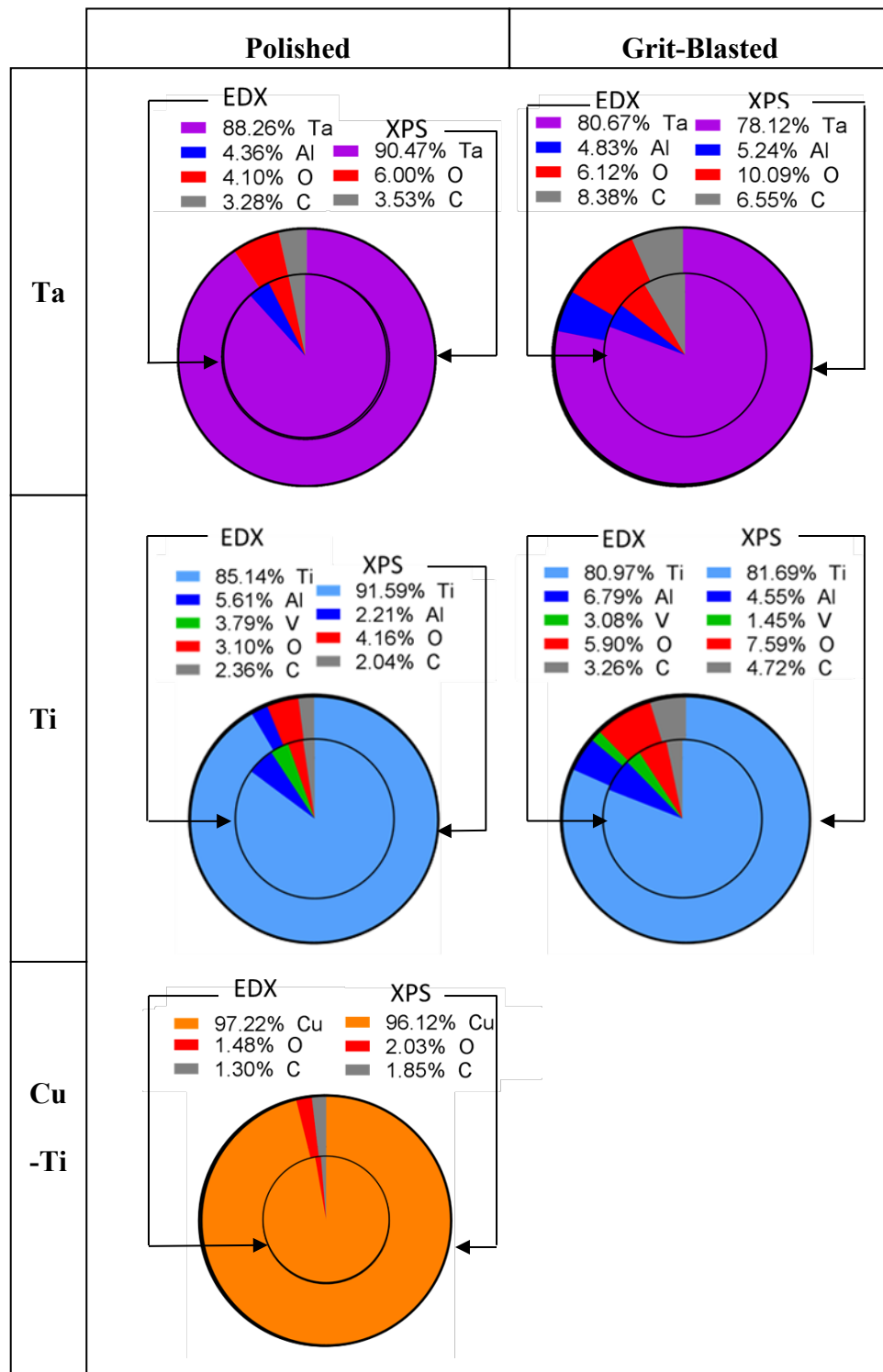


Figure 8: Composition of samples, as measured by EDX (inner portion) and XPS (outer portion). The ‘Polished’ column (left) shows polished disk samples. The ‘Grit-Blasted’ column contains grit-blasted disk samples. The ‘Ta’ row shows Tantalum disk samples. The ‘Ti’ row contains Ti6Al4V disk samples, and the ‘Cu-Ti’ row shows the polished, Cu-coated Ti6Al4V samples.

The oxygen content, as measured with EDX, was highest on grit blasted tantalum (6.12 wt%); followed grit blasted titanium (5.90 wt%). Polished tantalum had a higher oxygen content than polished titanium (4.10 and 3.10 wt% respectively), and the tantalum scaffold (Figure 9) had a higher oxygen content than that of a titanium scaffold (4.90 and 3.40 wt% respectively).

Carbon was seen in varying quantities in all samples. The difference in carbon content measured using EDX and XPS is smallest in polished tantalum (0.25 wt% difference) and polished titanium (0.32 wt% difference) however the content varies significantly between the XPS measurements and EDX in all but the aforementioned samples. The carbon content is greatest in scaffold tantalum (Figure 9), when measured with EDX, at 11.91 wt%, however grit blasted tantalum (Figure 8) shows highest carbon content when measured with XPS. The variation in carbon content measured may be a result of different manufacturing techniques employed in their production.

In titanium samples, vanadium was detected with EDX across all sample types, however it was only seen in grit-blasted titanium using XPS (1.45 wt%). Polished titanium has 3.79 wt% vanadium content, whereas scaffold titanium has 3.62 wt% and grit-blasted has 3.08 wt% when measured with EDX.

Aluminium content in titanium samples was higher when measured with EDX and XPS across all sample types, with the content highest in the grit-blasted

sample, at 6.79 and 4.5 wt% respectively, with little difference between scaffold titanium (5.56 and 1.80 wt% respectively) and polished titanium (5.61 and 2.21 wt% respectively).

Aluminium was detected in polished and grit-blasted tantalum samples (4.36 and 4.83 wt% respectively) using EDX, and the presence of it is measured by XPS in grit-blasted tantalum (5.24 wt%). No aluminium was observed in scaffold tantalum.

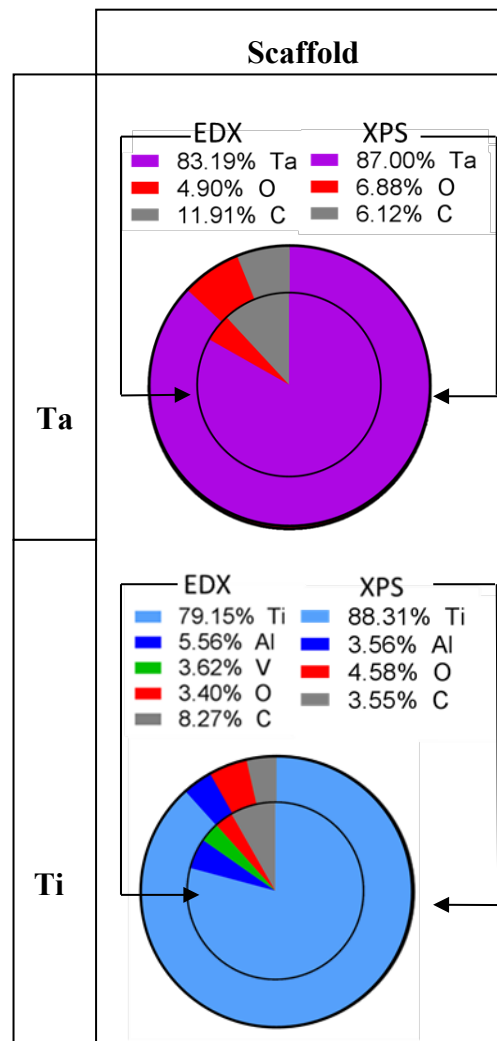


Figure 9: Composition of samples, as measured by EDX (inner portion) and XPS (outer portion). All samples are 3D scaffold samples. The ‘Ta’ row contains the tantalum ‘Trabecular Bone’ scaffolds. The ‘Ti’ row shows the Ti6Al4V scaffolds (Osseo-Ti).

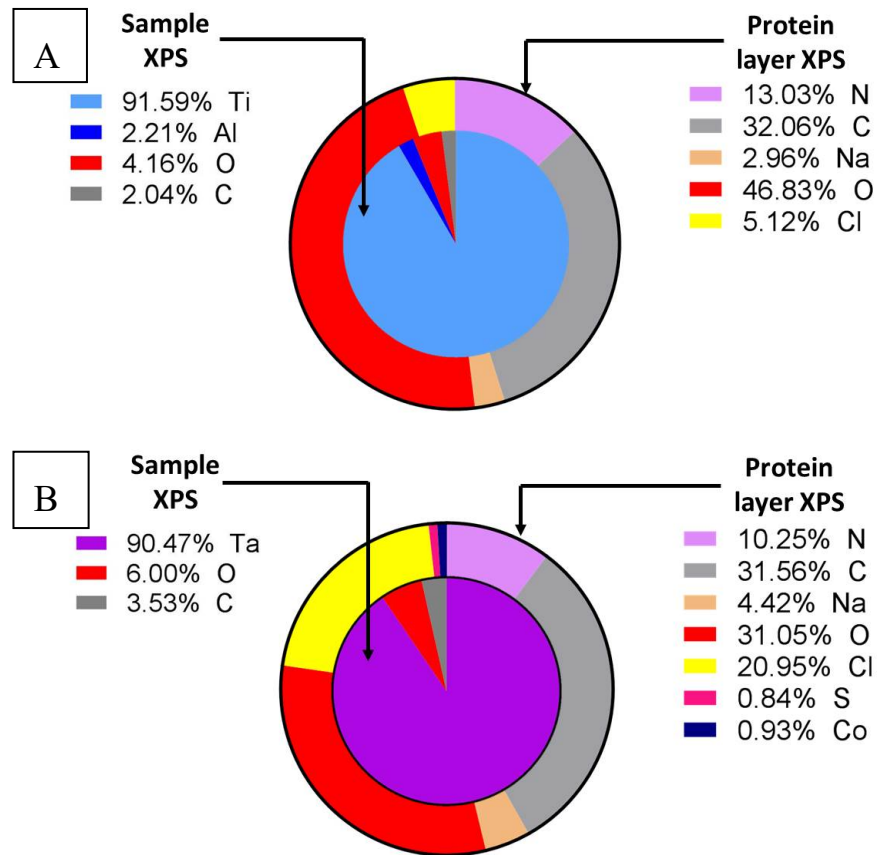


Figure 10: XPS analysis of the protein conditioning layer (outer) compared to the underlying sample composition obtained by XPS (inner). A) shows a polished Ti6Al4V disk sample which has been conditioned with a protein layer on its surface by immersion in Foetal Bovine Serum (FBS). B) shows a polished Tantalum disk sample which has been conditioned with a protein layer on its surface by immersion in Foetal Bovine Serum (FBS).

Composition of the protein conditioning layer varied between a Titanium and Tantalum surface (Figure 10). The protein layer on a Titanium surface showed a higher content of Nitrogen, Carbon and Oxygen than the layer on Tantalum (13, 32 and 47 wt% on Titanium and 10, 32 and 31 wt% on Tantalum respectively), however it had a lower content of Sodium and Chlorine (3 and 5 wt% on Titanium compared to 4 and 21 wt% on Tantalum, respectively). The protein layer on the Tantalum surface also contained Sulphur and Cobalt (both <1 wt%), which the layer upon a Titanium surface did not have.

2.2.3 X-Ray Fluorescence Analysis (XRF)

The presence of Iodine on samples treated with it, which were obtained from Zimmer-Biomet, was confirmed using X-Ray Fluorescence Analysis (XRF) (Figure 11). As Iodine was not successfully identified using EDX or XPS during characterisation alongside other samples, XRF was utilised to confirm whether or not Iodine was present in the chemical composition of the treated samples. Apart from the underlying bulk Ti6Al4V alloy, which constituted 99.9% of the elements detected (78.245 wt% Ti, 4.973 wt% Al, 1.140 wt% V, 9.937 wt% O and 5.742 wt% C), these samples also contained 0.095 wt% Iodine.

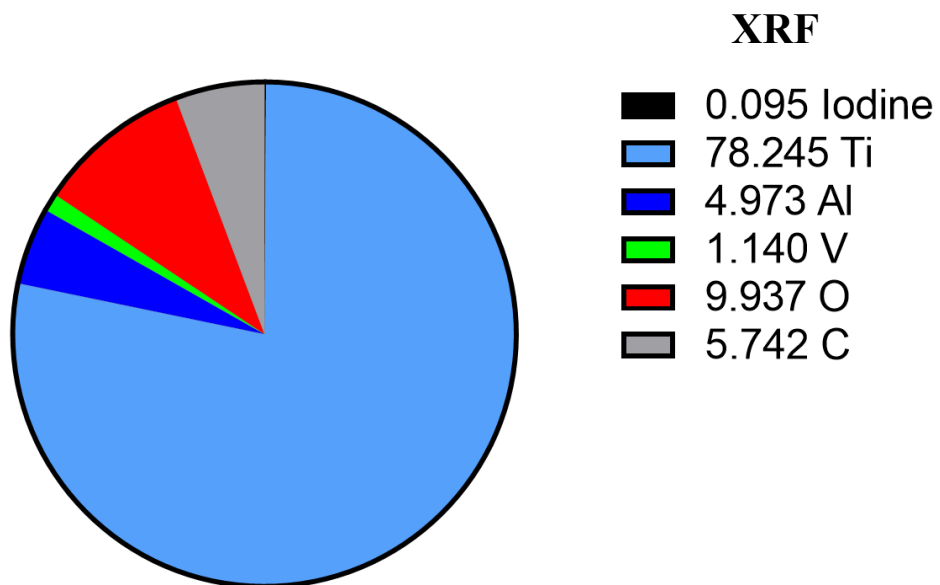


Figure 11: Sample chemistry analysis using XRF on a Ti6Al4V sample which has been surface treated with Iodine by Zimmer-Biomet. Values are given as % of the total composition measured per element. The results confirm the presence of Iodine within the sample, at 0.095 wt%. The remainder of the composition is made up of Titanium (78 wt%), Aluminium (5 wt%), Vanadium (1 wt%), Oxygen (10 wt%) and carbon (6 wt%).

2.2.4 Atomic Force Microscopy (AFM) and Laser

Profilometry

The characterisation of the surface morphology was key in understanding bacterial behaviour. As such, the roughness of all samples was measured using two methods; atomic force microscopy (AFM) was not suitable for taking measurements of the scaffold samples, therefore Laser Profilometry was used in those cases.

Roughness was measured using AFM and laser profilometry (Figure 12).

AFM was employed in assessing scaffolds, and laser profilometry was used for all other samples. The roughness is given as Ra, namely- the arithmetic mean average difference between peaks and valleys on the measured surface, and is given in μm . The formula for Ra is as follows:

$$Ra = \frac{1}{n} \sum_{i=1}^n |y_i|$$

where n is the number of equally spaced, ordered points along the trace of the surface, and y_i is the distance (vertical) from the mean line to the i^{th} data point^[243].

The polished samples have the lowest Ra value- 0.56 ± 0.08 , 0.65 ± 0.06 and $0.64 \pm 0.13 \mu\text{m}$ for copper-coated titanium, polished titanium and polished tantalum respectively. Scaffolds have the next highest Ra value, at 1.90 ± 0.18 and $1.12 \pm 0.24 \mu\text{m}$ for tantalum and titanium scaffolds respectively. Grit blasted samples have the highest roughness, with the Ra value of tantalum at $4.19 \pm 0.63 \mu\text{m}$ and titanium at $4.40 \pm 0.61 \mu\text{m}$.

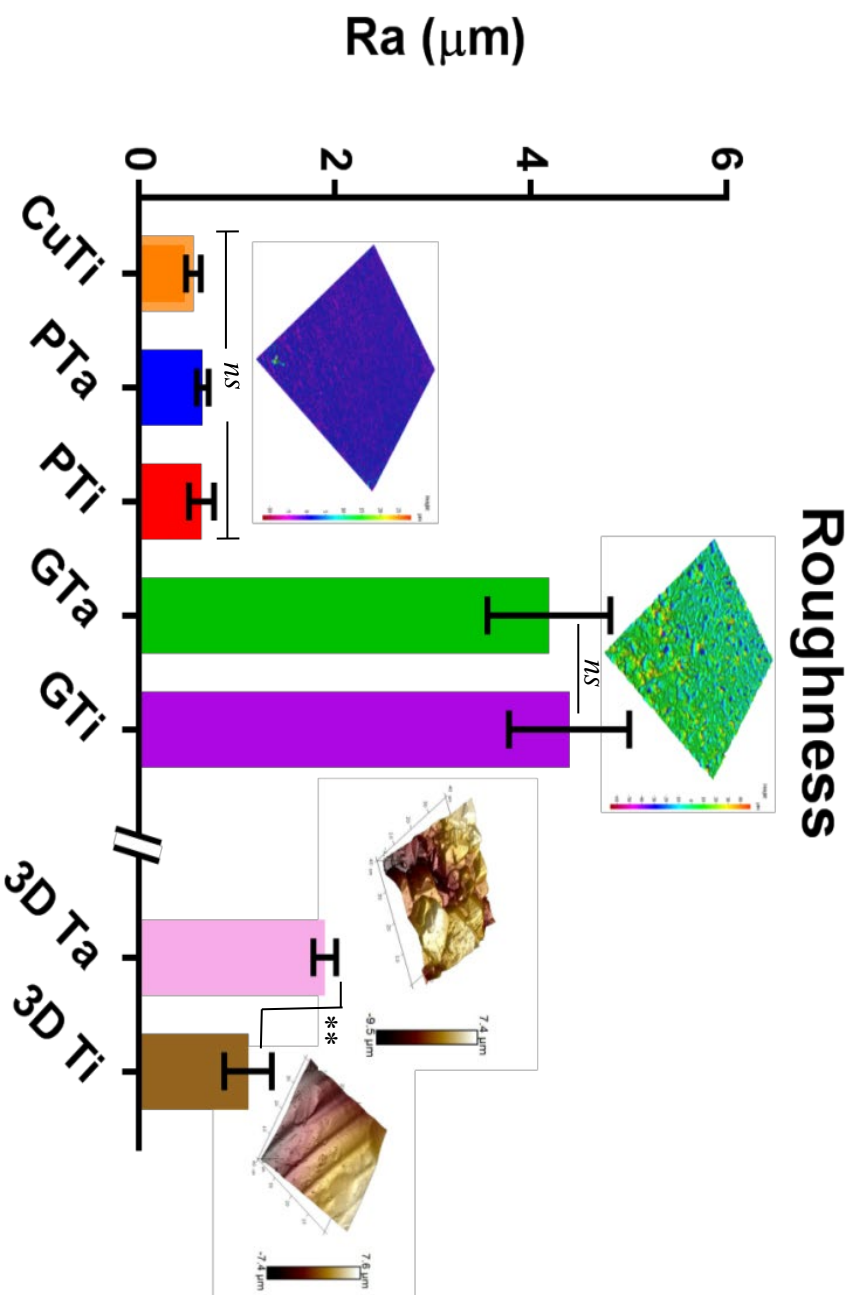


Figure 12: Surface roughness measurements using AFM (left of break) and laser profilometry (right of break). The y axis shows Ra roughness, and the x axis shows sample type. 3D model rendering images are shown above the samples as a visual example of the measured surface area. CuTi is the polished, cu-coated Ti6Al4V disk sample, PTa and PTi are polished disk samples (Tantalum and Ti6Al4V respectively)(no statistically significant difference). GTa and GTi are grit-blasted disk samples (Tantalum and Ti6Al4V respectively)(no statistically significant difference). 3D Ta and 3D Ti are 3d scaffold samples (Tantalum (Trabecular Bone) and Ti6Al4V (Osseo-Ti) respectively)($p < 0.01$).

2.2.5 Water Contact Angle Analysis (WCA)

Surface free energy of a material can have a significant impact of bacterial cell adhesion, and as such this was measured during the characterisation of samples^[244]. The water contact angle below 90° can be considered to be hydrophilic^[245]. The anodised Ti surface (Iodine treated) had the highest water contact angle, at 92.4° ±1.1°, followed by copper-coated Ti disks with 88.3° ±0.8° (see Figure 13)(p<0.01).

Polished Ti and the Ta scaffold had water contact angles of 80.9° ±0.7° and 76.5° ±0.8° respectively(p<0.01).

The lowest water contact angles were observed on polished Ta and grit-blasted Ta surfaces, at 71.9° ±0.3° and 59.7° ±0.6° respectively (p<0.001).

Measurement of the water contact angle on scaffolds was conducted using a water droplet larger than the size of the pores- the pores were on average 0.5µm in diameter, though in the centre of the scaffold this increased to *c.a.* 0.75 µm. Despite this, the pores of a Ti scaffold were too large, allowing water to pass through immediately, *ergo* no measurement was possible on these samples.

Water Contact Angle of Ti and Ta

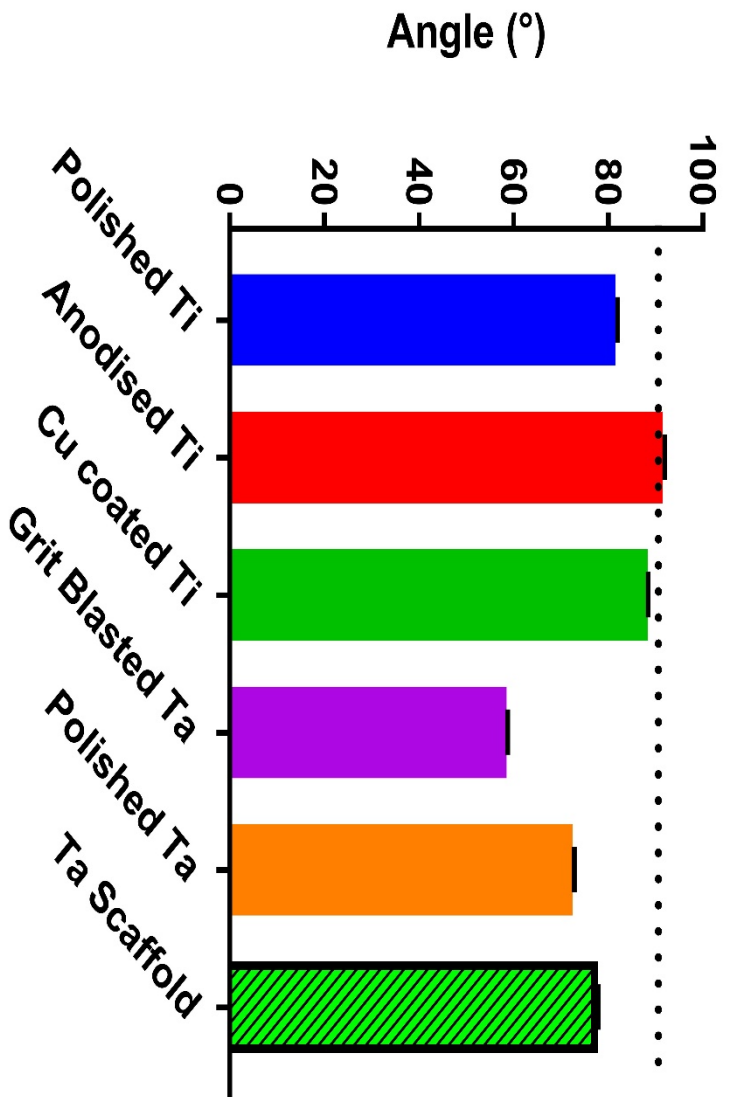


Figure 13: Water Contact Angle measurements of disk and scaffold samples. 'Polished Ti' is a polished Ti6Al4V disk sample, 'Anodised Ti' is an anodised Ti6Al4V disk sample, and 'Cu coated Ti' is a polished, cu-coated Ti6Al4V disk sample. 'Grit-blasted Ta' is a grit-blasted tantalum disk, and 'Polished-Ta' is a polished tantalum disk sample. 'Ta scaffold' is a tantalum 3D scaffold sample (Trabecular Bone). Measurement was not possible of the 3D Ti6Al4V scaffold sample due to the large size of the pores.

2.3 Discussion

2.3.1 Scanning Electron Microscopy (SEM)

Both micro- and macro-level features of a surface have been shown to affect bacterial cells [76, 246-249]. The surfaces of all types of samples are vastly different to each other. The tantalum scaffold (Figure 6A and Figure 7A), manufactured using Chemical Vapour Deposition (CVD), bears close resemblance to the geometry of trabecular bone. This may have an effect on the interaction between the implant and host cells, as suggested by Hacking *et al.* (2000). They conducted a study using subcutaneous implants in dogs and found that within 4 weeks of surgery, histologic sections showed ingrowth of soft tissue across the full-implant depth [250]. However, such a geometry may also provide a sheltered environment for the bacterial cells, due to the fact that vascularisation (which is associated with faster immune responses) takes time to become established inside the scaffold. In addition, individual immune cells also require time to penetrate the scaffold, giving bacteria time to replicate [251]. However, the macro-geometry of this scaffold is unlikely to have an effect, outside of the aforementioned sheltering, on bacterial cell behaviour. This may be due to the relatively small size of a bacterial cell (*circa* 1 μm for

S. aureus [252]) compared to the pore size of 300-400 μm for tantalum scaffolds and over 500 μm for titanium scaffolds. On the other hand, the nature of micro- and nano-level features of the surface has been shown by Rajab *et al.* (2019) [253] and others [165, 254-257] to affect bacterial cell behaviour. This has led to engineering a surface to kill bacterial cells outright, such as the sharklet design [258, 259]. The images produced by SEM show a high, irregular roughness on the surface of the struts. Similar surfaces have been observed by Shimko *et al.* [260] when assessing the fluid flow characteristics and mechanical properties of tantalum scaffolds. Both shape and size of these features is important in engineering the desired surface characteristics.

The pore size observed in the titanium scaffold is considerably larger than that of tantalum (over 500 μm and *circa* 350 μm respectively). The presence of titanium microspheres in the surface geometry would provide ample sites for bacterial cells to attach to. This is because the surface area provided at the microsphere-surface interface is larger than that of the flat surface which surrounds it. The microspheres are likely an artefact of the manufacturing process- Selective Laser Sintering. By this process, a metal powder is melted using a high-powered laser, layer by layer, to produce a 3D item. In this case some of the powder, which was not fully melted, was integrated into the surface by coming into contact with the molten material. Apart from the microspheres, the surface of these scaffold is relatively flat with small grooves present. The bacteria may again prefer attaching at the grooves as it provides more surface area for the cells to attach to.

The two scaffolds have vastly different geometries where the tantalum scaffold has no repeating pore geometry, the titanium scaffold has a highly ordered architecture. The titanium struts are roughly twice the diameter of their tantalum counterparts (*ca.* 300 μm *versus* 150 μm , respectively). The micro-features of the two scaffolds are also entirely different, with the tantalum surface displaying high roughness with low variability between the sizes of peaks, whereas the titanium surface is much more varied between areas with microspheres present and not.

The topography of titanium and tantalum grit blasted samples is similar, namely a highly rough, irregular surface strewn with high peaks and troughs. These features are the result of the grit blasting process, whereby grit is accelerated at high speed towards the sample surface, cleaving material at the impact site^[261]. There was no contamination of left-over grit apparent in the SEM micrographs in either of the sample types. The geometry of these samples results in a high surface area and then abundant sites for bacterial cells to attach. Bollenl *et al.* (1997) found that rougher titanium implant surfaces harboured 25 times more indigenous oral microbiota^[262].

The polished samples, titanium and tantalum, showed the same surface morphology as expected when assessed using SEM imaging. The surfaces are largely smooth, with slight, isolated scratches present, which are most likely to be attributed to friction between samples during transport. Polished titanium disks which were coated with copper showed identical morphology due to the small thickness of the copper coating. This was to ensure any differences seen

in bacterial presence on their surfaces were not influenced by anything but the surface chemistry. Copper was selected as a negative control due to its well documented antibacterial properties [88, 263-265], and the relative ease of coating samples with it. Copper coating was done on polished titanium discs using magnetron sputtering [266].

2.3.2 Energy-Dispersive X-Ray Spectroscopy (EDX) and X-Ray Photoelectron Spectroscopy (XPS)

EDX and XPS were used to assess the chemical composition of the surfaces. EDX allowed for deeper (up to 2 μm) [241] penetration, giving results further inside the sample, whereas XPS was utilised to test the topmost 5 - 10nm [242]. The two methods used concurrently could give an idea about the depth of the oxide layer as well as the sample surface composition. All samples showed higher oxygen contents, and therefore oxide, presence by XPS than EDX. This suggests that the oxide layer did not reach the full penetration depth of the EDX (2 μm), see Figure 8, which is in keeping with wider literature [267, 268].

Grit blasted tantalum and titanium showed higher oxygen contents compared to polished discs and scaffolds in both EDX and XPS results. This is likely due to the increased surface area of these grit blasted samples, exposing more of the surface to oxygen. XPS showed greater amounts of oxygen than EDX which might be ascribed to the presence of the oxide layer at the topmost of the samples. All samples showed a presence of small fractions of carbon.

On the whole, tantalum samples showed a greater amount of oxygen on their surfaces than that seen on the titanium samples with both EDX and XPS. This could be attributed to the fact that tantalum is more readily oxidised than titanium [269, 270], as well as their oxides differing in composition. Titanium forms titanium dioxide (TiO_2) [271], whereas tantalum forms tantalum pentoxide (Ta_2O_5) [272], therefore a tantalum pentoxide of equal depth to a titanium dioxide is expected to contain more oxygen.

The copper coated titanium samples showed predominantly copper, with small amounts of oxygen and carbon present. These are likely a result of slight sample contamination. The sample underneath the coating is the aforementioned Ti6Al4V alloy, however no titanium, aluminium nor vanadium was detected by EDX or XPS. Therefore the copper coating is expected to be at least as thick as the penetration depth of EDX ($2\ \mu\text{m}$) [241]. It is thought that copper owes this antibacterial property to its ions that are leached from its surface in aqueous solution, and as such some approaches employ copper ion complexes in an effort to further exploit its effects [273].

2.3.3 Atomic Force Microscopy (AFM) and Laser

Profilometry

AFM, in tapping mode, was used to measure the roughness of struts of the 3D scaffolds, due to the difficulty of measuring the roughness of the scaffold using laser profilometry. Therefore, the readings from these scaffolds reflect the roughness of the actual material surface excluding the pores. This is

because individual bacterial cells will be exposed to only the surface of the strut as opposed to the entire pore. The surface of tantalum scaffold displays higher roughness than that of titanium counterpart. However, the readings of the titanium scaffold were taken in areas which didn't include microspheres, due to their potential to skew the results. This is because the surface of the microspheres is smooth, and any reading taken on their surface is going to show very low roughness, whereas if only part of a microsphere was included in the reading, alongside the surface of the strut, the reading would indicate incredibly high roughness as a result of the microspheres' large size relative to the tested area.

Laser profilometry was used to measure the roughness of polished and grit-blasted samples, as it allowed for a greater area of testing on the surface, resulting in a more reliable measurement as it minimised the effect a small surface scratch would have on the final Ra reading ^[274]. Whereas the polished samples showed the lowest roughness of all sample types, with no significant difference between them. The grit blasted samples' surfaces were *circa* eight times rougher than the polished samples.

Work conducted by Aykent *et al.* (2010) suggested that increasing Ra value seems to increase bacterial cell adhesion to the surface. This study showed that a steadily decreasing roughness of the surface (from *circa* 1.5 μm to 0.7 μm) led to decrease in viable bacteria from *c.a.* 1350 to 1200. This would mean that the bacterial growth on the surface of grit blasted samples should be greater than that seen on the surface of polished samples of the same material.

Simply taking roughness into account, the bacterial presence on the scaffolds should fall somewhere between the two, however this would not take into account the additional sheltering effect of a 3D porous structure.

2.3.4 X-Ray Fluorescence Analysis (XRF)

X-Ray Fluorescence Analysis (XRF) was chosen as a method for confirmation of the presence of Iodine on treated samples due to their surface characteristics. As the Iodine was theorised by Zimmer-Biomet to have been present in its elemental state within the pores created during the Micro-Arc Oxidation (MAO) process, XPS and EDX proved to be limited in their scope to detect it. XPS has an average depth analysis of *c.a.* 5nm, meaning that it would not be able to detect Iodine present in the pores of the surface^[275]. Although EDX probes a depth of 1-2 μm ^[276], it still proved ineffective in analysing the presence of Iodine within the surface pores. XRF was chosen as it allowed for further penetration of the depth of surface, which would include more of the surface channels where Iodine was suspected to be present. This was confirmed by the fact that no Iodine was present in the EDX and XPS spectra but was indeed present in the XRF results. The amount of Iodine in the samples (0.095 wt% \pm 0.004) was small compared to other constituent elements, however its presence was detected in all Iodine-treated samples, and it was absent in testing of all other types of samples using XRF. The other constituent elements of the bulk Ti6Al4V material was similar in levels to those observed using EDX and XPS of other samples. Surface analysis of

Iodine-treated samples showed a slightly lower amount of Ti (78.245 wt% \pm 0.931) compared to the untreated grit blasted Ti6Al4V surface when analysed using EDX (80.97 wt% \pm 0.569). This is most likely due to the anodisation process through which Iodine treated samples are put, which increases the oxide layer depth on the surface. This conclusion is supported by the increased presence of O on the surface of Iodine treated samples (9.937 wt% \pm 1.002) compared to the aforementioned untreated sample with EDX (5.90 wt% \pm 0.997).

The next chapter concerns microbiological assessments of scaffolds using methods found in literature. It assesses with reference as to the reliability of such methods for acquiring quantifiable data from metal scaffolds, in pursuance of a method appropriate for adoption for this use in later parts of the work.

Chapter 3 Microbiological Assessment On Scaffolds Using Existing Methods

This chapter intends to study the reliability of existing methods in obtaining quantifiable bacterial biofouling data with the specific use-case of metal 3D scaffolds as its focus. A number of methods are analysed with a view to adopt any which prove effective in this application for the remainder of the work conducted subsequently.

There are many well documented methodologies for the microbiological assessment on the surface of solid samples^[277-281]. Methods which assess the antibacterial qualities of elutes from samples may be utilised when surfaces degrade to produce antibacterial agents such as some metal ions (Cu (II, I) and Silver (I) for instance^[282-286]) or known antibiotics which are bonded to the surface and are released during the degradation of those bonds (such as gentamicin sulfate (GS))^[287, 288].

The agar diffusion method is one such method, whereby samples are placed upon the surface of an inoculated agar plate, with the active surface in contact with the agar itself^[289]. As the elutes are released from the sample surface, they kill the bacteria in the vicinity of the sample as well as preventing bacterial cells from outside this perimeter from colonising the agar within the diameter in which the antibacterial elutes are in sufficient concentration. This creates a clearly defined ‘ring’ in the culture if the surface does indeed release antibacterial substances, and the absence of which indicates that the sample either does not release these substances (at all or in sufficient concentrations so as to affect bacterial behaviour) or that the bactericidal elutes it would release are not water-soluble^[290].

The addition of a standardised volume of sterile liquid within which samples were degraded for a given amount of time into a suspension of bacterial cells, with their number quantified (usually through Optical Density assessment) before the addition and a specific time afterwards is another way to assess the degradation products of a sample for antibacterial properties. However, this approach includes the sample as a whole as opposed to its single surface alone.

In vitro methods for the microbiological analysis of surfaces where bacterial cells are grown on the samples themselves often provide a more holistic view of the bacterial behaviour in response to the surface. This approach enables the assessment of not only water-soluble agents, such as copper ions, released from the samples, but also the effect of the surface chemistry in general and its nano-, micro- and macro-geometry on bacterial cell behaviour^[255, 291]. As a

result, methods which enable this are highly favoured in literature, where appropriate. For example, bacteria which have been genetically modified to express plasmid-borne Green Fluorescent Protein (GFP) and Chloramphenicol (Cm) resistance can be imaged using a confocal laser microscope^[292, 293].

The placement of the GFP gene into a plasmid with a Cm resistance gene allows for the preservation of the GFP gene in the bacterial colonies through selective pressure by the addition of Cm into the culture media. The bacterial strain was supplied with this GFP gene already within the plasmid by the microbiology laboratory within which this work was conducted. A confocal laser microscope is a powerful tool in such analyses as it does not require a fully flat surface to conduct testing. The confocal nature of this microscope allows it to image three-dimensional features on the surface, *ergo* it overcomes the limitations of traditional microscopy techniques.

There is also the possibility to detect a change in mass in samples where the bacterial biofilm is well-established. This is due to the fact that the biofilm formed is more dense than water and air, as it is composed of bacterial cell, and an extracellular matrix composed of extracellular polymeric substances such as polysaccharides, proteins and lipids^[294, 295]. This difference in density could theoretically allow for the quantification of biofilm formation by means of weight, both on flat samples and larger, three-dimensional scaffolds, as more biofilm formation would result in an increase in mass of the sample. Scaffolds would likely show a more pronounced mass increase, due to their large surface area compared to flat disks. If this was due only to surface area,

we may expect a 10-fold increase in mass in the scaffold samples, however as there is a finite number of bacterial cells in culture, this effect may be assumed to be lower^[296].

The recent advances in Micro-Computed Tomography (Micro-CT) have allowed the method to be used to measure features as small as $0.5\mu\text{m}$ ^[297, 298]. Micro-CT identifies the differences in density within a given volume, therefore it offers an opportunity to be an effective method for the analysis of biofilm formation and bacterial colonisation on flat disks and within scaffold samples. Computed Tomography works by the employment of X-Rays to create stacks of cross-sectional images of a physical object within a pre-defined volume^[299]. These 2D slices divide the specimen, as the edges are irradiated from the outside. As the X-Rays transverse through each slice, they are attenuated and the emergent X-Rays (now with reduced intensities) are captured using a detector array. X-Ray paths and the attenuation coefficients are calculated from these detector measurements. For each slice, a single 2D pixel map is created using these calculations, with each pixel being denoted by a threshold value (which in turn corresponds to an attenuation value measured from a corresponding location within the sample). Since the attenuation coefficient correlates to the density of material in the location, the 2D pixel maps reveal the density of the sample at the corresponding location^[197]. These stacks are then combined by an algorithm in order to create a working 3D model. The prefix of micro- is used to convey that the pixel size within the cross-sectional images are in the μm range.

The bacterial culture and approaches adopted in this work to enable suitable methodological selection are detailed in the following section.

3.1 Materials and Methods

3.1.1 Bacterial culture

All samples were sterilised by immersion in 70% ethanol for 2 hours followed by drying under UV light overnight in a sterile fume hood.

Bacteria was taken from cold storage and transferred into liquid Tryptic Soy Broth (TSB) media, in order to obtain active bacterial cells^[300]. An *S. aureus* Newman strain was used, with a green fluorescent protein (GFP) gene inserted into a plasmid containing a Chloramphenicol (Cm) resistance gene. To preserve this gene, the culture was grown on agar containing Cm (1µg/mL). In order to obtain the starting culture, a single colony of *S. aureus* was lifted from the agar plate and incubated in TSB media at 37°C and 200 RPM overnight. The overnight culture was washed twice in TSB prior to being used to inoculate the petri dishes.

Sterile samples were placed into a petri-dish, in triplicate, containing 20ml of warm (37°C) TSB media. The optical density (OD₆₀₀) of the starting culture was measured using a spectrophotometer (Jenway 6715 UV/Vis) and the suspended bacteria were placed into the petri-dishes to give a starting OD₆₀₀ of

0.1. Cm (1µg/mL) was added to the culture media in order to ensure the preservation of the GFP gene for the duration of the experiment. This starting OD₆₀₀ was chosen to ensure bacteria were not in the lag or stationary phases for the experiment. Three repeats of each sample type were not inoculated to serve as controls- they were placed in media with no bacterial inoculation. The samples were then incubated at 37°C and 60 RPM for a set amount of time, after which they were removed and washed thoroughly with deionised water (dH₂O) by vigorous agitation three times.

3.1.2 Wet weight assessment

Sterilised samples (placed in ethanol overnight and dried in a sterile hood) were placed in sterile deionised water (dH₂O) and were subsequently removed after a period of 5 minutes and placed on scales in sterile conditions, with their weight recorded. The balance used was a Nimbus® Analytical Balance NBL 124e with a 0.1 mg resolution. After this, the samples were placed in culture media and inoculated with bacteria as per the method outlined in section 3.1.1 and incubated for 24, 48, and 72 h in order to increase the bacterial presence (by attempting to take readings well within the stationary phase of the bacterial growth curve) to allow the mass of these bacteria to be sufficient in order to be measurable by weighing. Upon washing, the samples (now with bacteria- with the exception of controls which were sterile but washed nonetheless) were once again weighed using the same balance with their

weight recorded. Each sample was weighed twice, with the average taken, and each sample type was tested in triplicate. Control samples underwent the same procedure, including placing in culture medium for the length of the experiment, less the inoculation with bacteria.

3.1.3 Dry weight assessment

All samples were sterilised as per the protocol outlined in section 3.1.1, and weighed under sterile conditions using a Nimbus® Analytical Balance NBL 124e with a 0.1mg resolution, with their individual weights recorded. Once again, the samples underwent the bacterial culture protocol from section 3.1.1 (with incubation times at 24, 48 and 72 h), upon the completion of which all samples were placed in a freeze-dryer (Scanvac CoolSafe Pro 4L) running at -80°C overnight. Once the samples were dried, they were weighed again, with their weight recorded. All samples were weighed twice, with an average taken (to ensure any effect surface dust may play in the reading was minimised), and each sample type was tested in triplicate. Control samples underwent the same procedure, including placing in culture medium for the length of the experiment, less the inoculation with bacteria.

3.1.4 Micro-CT assessment

Titanium and Tantalum scaffold samples were sterilised and had half of their volume filled with a 20 wt% Agarose hydrogel in order to simulate the density of a biofilm. They were then transferred to a Micro-CT scanner (Shaw Inspection Systems Venlo H350/225 using a Tungsten Hairpin target, a IEEE SVGA Firewire Camera with a 768 x 582 pixel area, a focal spot of 5 nm and a resolution of 22 μm , running at 225 kV).

3.1.5 Confocal Laser Scanning Microscopy (CLSM)

All samples were incubated and washed as per protocol described in Section 3.1.1 and incubated for 96 h to allow for the bacterial colonisation of the entire sample surface, after which they were imaged on a Carl Zeiss L700 Confocal Laser Scanning Microscope. The biomass burden was analysed using the COMSTAT 2 plugin to ImageJ on the resulting image stacks^[301]. The scanned area was 1.2 mm².

Image stacks were combined and rendered into three-dimensional images using the ZEISS ZEN microscope software^[302].

3.1.6 Sample Selection

The samples described in this chapter are identical to those described in Chapter 2, Section 1.1.8:

“Samples for this study were supplied by Zimmer-Biomet. They included commercially available surfaces, manufactured from Tantalum and a medical-grade Titanium alloy (Ti-6Al-4V). All sample disks measured 10 x 2.5mm. A number of surfaces manufactured from these materials allowed for a simultaneous assessment of surface topography and chemistry effects on bacterial behaviour as well as the suitability of the assessment methodology.

The sample types were as follows: polished disks, grit-blasted disks, 3D additively-manufactured scaffolds (Osseo-Ti: Ti-6Al-4V scaffold manufactured using Selective Laser Sintering (SLS) and Trabecular Metal: Ta scaffold manufactured using Chemical Vapour Deposition (CVD)).

Some polished Ti disk samples were coated with elemental copper through sputtering- a Physical Vapour Deposition (PVD) process whereby a thin film is deposited using ejected materials from a target onto a substrate- in order to be used as positive control in the microbiology studies.

The Trabecular Metal is an open cell highly porous (~80% porosity^[203]) structure, similar in geometry to trabecular bone by being composed of struts ordered in dodecahedron repeats^[204]. In order to achieve this, a vitreous carbon scaffold is used as an internal matrix upon which the Tantalum is later deposited^[205]. The carbon scaffold is then placed in a sealed chamber and the

CVD process proceeds using hydrogen and chlorine gases. Evaporated tantalum (as TaCl₂) then deposits Ta molecules onto the underlying carbon scaffold^[206]. A review of available literature suggests that this material exhibits high osteoconductivity, biocompatibility, vascularisation and bone-ingrowth (as observed in *in vitro*, *in vivo* and human studies)^[176, 203, 207-210]. The Osseo-Ti scaffold is manufactured using SLS of Ti-6Al-4V powder, based directly on 3D scans of cancellous bone and exhibits ~70% porosity according to data supplied by Zimmer-Biomet.”

3.2 Results

3.2.1 Wet weight assessment

Wet weight assessments were chosen in order to ensure that any weight gain as a result of bacterial growth on/within samples was significant enough to be reliably measured by conventional laboratory weighing scales. The hypothesis was that the greater the bacterial bioburden on the sample, the higher its weight change would be as compared to the sterile control.

When flat, 2D samples were tested for the mass change (Figure 14), there was no statistically significant difference between data points up to 48 h when compared to the control (0 h). All sterile control samples showed no statistically significant mass ($p > 0.8$) change in the duration of the experiment.

After a 24 h inoculation and incubation, polished Ti, grit-blasted Ti and Iodine-treated disks had no significant mass increase (0.0002 ± 0.0014 g, 0.0005 ± 0.0008 g and 0.0005 ± 0.0062 g respectively) compared to the control samples. At the 48 h timepoint, polished Ti showed a statistically significant ($p=0.048$), albeit slight, mass increase of 0.002 ± 0.0005 g, however there was no significant change in grit-blasted Ti and Iodine-treated Ti when compared to control samples (0.0006 ± 0.0005 g and 0.0014 ± 0.0009 g respectively).

At the 72 h timepoint, all samples showed a small, statistically significant increase in mass when compared to control samples. There was no significant difference between any samples at this timepoint. Polished Ti samples showed an increase of 0.0026 ± 0.0004 g, followed by grit-blasted Ti and Iodine-treated Ti disks (0.0020 ± 0.0003 g and 0.0018 ± 0.0005 g).

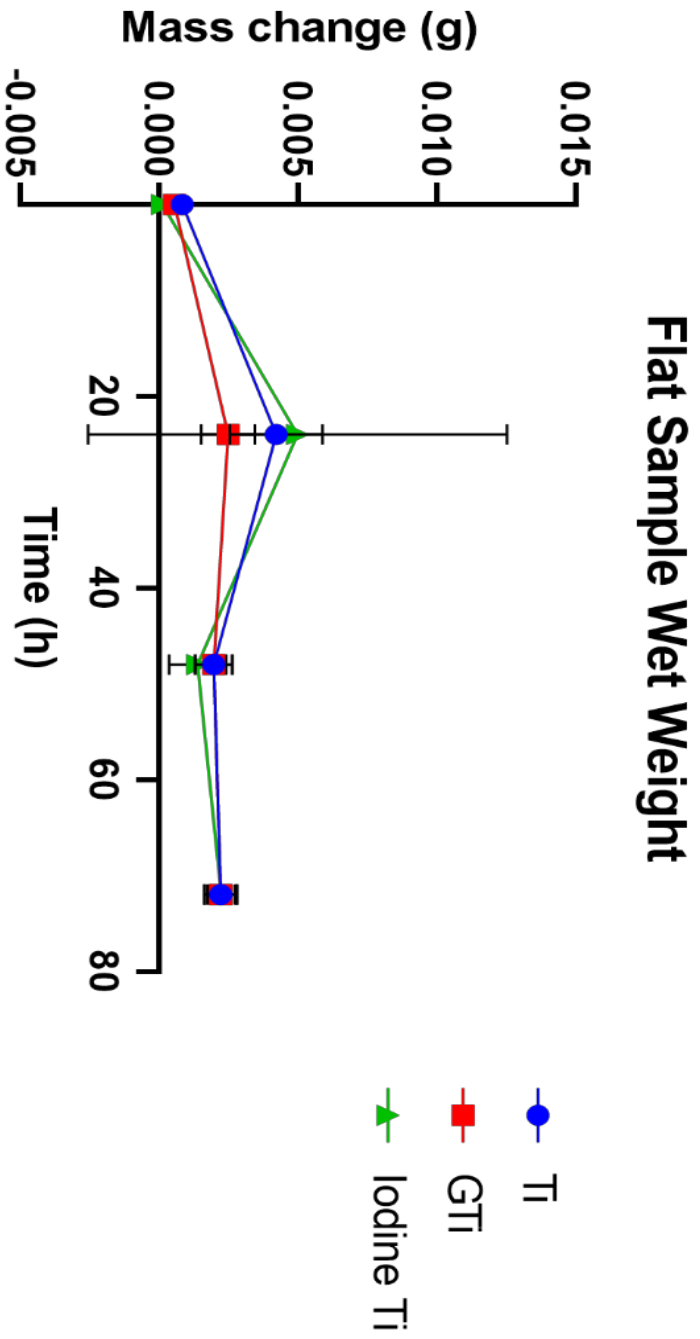


Figure 14: Weight change over time for wet samples which were incubated in TSB and inoculated with *S. aureus*. Samples at 0 h were incubated TSB, with no inoculation with bacterial culture. 'PTi' samples were flat, polished Ti-6Al-4V disks, 'GTi' samples were grit-blasted Ti-6Al-4V disks, and 'Iodine Ti' samples were iodine-treated polished Ti-6Al-4V disks.

When a three-dimensional Ti scaffold was tested using the same protocol (see Figure 15), it showed a clear upward trend in mass increase from the 24 to the 72 h timepoint. The scaffold showed the highest mass increase of all samples at all timepoints. At 0 h (the sterile control cohort), the mass of the scaffold increased by 0.016 ± 0.004 g. At 24 h there was no statistically significant ($P=0.0862$) difference to the control samples, with the weight increase at

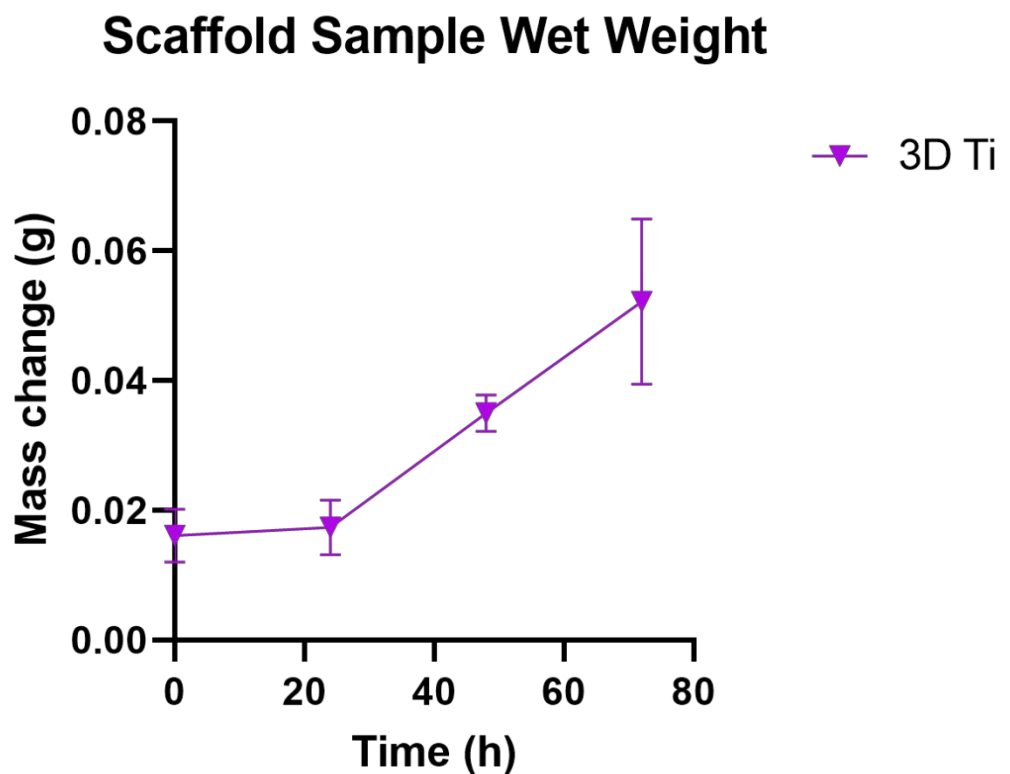


Figure 15: Weight change over time for wet scaffold samples (Ti-6Al-4V Osseo-Ti scaffolds) which were incubated in TSB and inoculated with *S. aureus*. Samples at 0 h were incubated TSB, with no inoculation with bacterial culture.

0.017 ± 0.004 g. However, at 48 h the increase in weight was 0.035 ± 0.003 g, which was significantly higher than that observed in the preceding 0 and 24 h timepoints (P=0.009). At 72 h the increase was the largest seen in this study, at 0.052 ± 0.012 g, which was statistically significantly higher than at the 48 h timepoint (P=0.0371).

3.2.2 Dry weight assessment

When freeze-dried, none of the flat samples at any time point up to and including 72 h showed any statistically significant increase in mass when compared to the control cohort (Figure 16). The polished Ti samples at 0 h showed a very slight, yet statistically significant decrease in weight of 0.0002 ± 0.0001 g. No other type of sample showed a statistically significant decrease of mass of any magnitude at any timepoint in this experiment.

The 3D Ti scaffold, on the other hand, showed a statistically significant mass increase at every time point compared to the control cohort. The control, 0 h timepoint showed an increase of 0.0006 ± 0.0003 g compared to their weight before the incubation in media and freeze-drying. At 24 h this increase in mass was 0.0011 ± 0.0002 g, with a subsequent increase of 0.0023 ± 0.0003 g at 48 h. At 72 h, however, there was no statistically significant difference between this timepoint (mass increase of 0.0024 ± 0.0002 g) and the mass increase observed at 48 h.

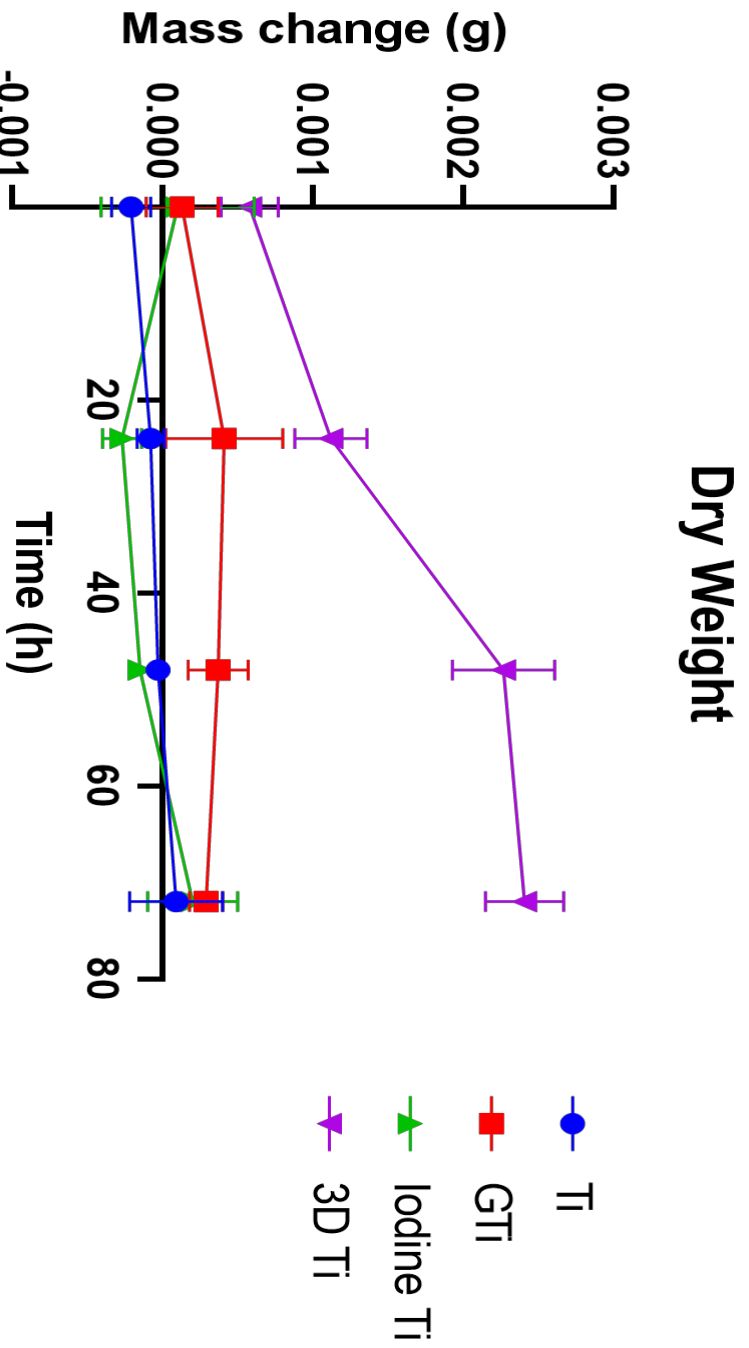


Figure 16: Weight change over time for freeze-dried samples which were incubated in TSB and inoculated with *S. aureus*. Samples at 0 h were incubated TSB, with no inoculation with bacterial culture. 'PTi' samples were flat, polished Ti-6Al-4V disks, 'GTi' samples were grit-blasted Ti-6Al-4V disks, and 'Iodine Ti' samples were iodine-treated polished Ti-6Al-4V disks. '3D Ti' samples were Osseo-Ti (Ti-6Al-4V) scaffold samples.

3.2.3 Micro-CT assessment

The micro-CT method were unable to produce viable data from either the Ta or the Ti scaffolds. Although the X-Rays were able to penetrate the structure, they were not able to do so at the required resolution (see Figure 17). The X-Rays were better able to penetrate the Ti structure, compared to the Ta scaffold, illustrated by the difference in sharpness in the two cross-sections in

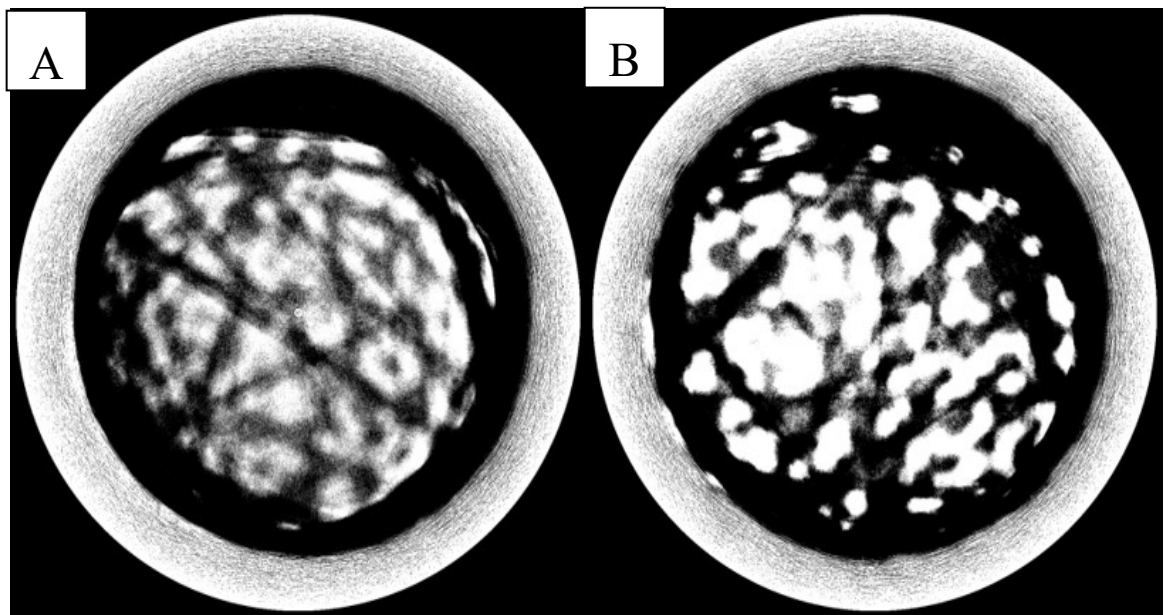


Figure 17: Micro-CT cross sectional scans of two metal scaffolds 2mm from the top surface (a hydrogel was cast in what would be the bottom half of these cross-sections, though this is not visible in the scans) ; A- Trabecular Bone scaffold (Ta), B- Osseo-Ti scaffold (Ti-6Al-4V). Typically, in CT scans, dark areas are areas of high density, lighter areas are areas of low density, with white denoting voids.

Figure 17.

3.2.4 Confocal Laser Scanning Microscopy (CLSM)

Polished Ti and Ta disks were used as a control for the ascertainment of suitability of the CLSM method in bacterial biofilm assessment in three-dimensional scaffolds (see Figure 18). Once inoculated, incubated and washed as per the protocol outlined in section 3.1.1, the samples were imaged and the resulting images analysed by combining the resulting z-stack images. After 96 h, the polished disks contained a biomass (the volume of bacteria/biofilm per unit area) of $16.2 \pm 7.1 \mu\text{m}^3/\mu\text{m}^2$ and $5.9 \pm 3.5 \mu\text{m}^3/\mu\text{m}^2$ on the Ta and Ti disks respectively. For the sterile cohort there was no biomass detected for either Ta or Ti disks.

Sterile scaffolds had a biomass reading of $0.1 \pm 0.1 \mu\text{m}^3/\mu\text{m}^2$ and $3.0 \pm 2.9 \mu\text{m}^3/\mu\text{m}^2$ for Ta and Ti respectively. Scaffolds inoculated with bacteria had a biomass presence of $92.8 \pm 27.5 \mu\text{m}^3/\mu\text{m}^2$ and $166.8 \pm 26.1 \mu\text{m}^3/\mu\text{m}^2$ for Ta and Ti scaffolds respectively.

Image stacks resulting from the CLSM testing were also combined to create three-dimensional visual renderings of the overall scanned areas, both on flat samples and on scaffolds (see Figure 19). The gradient in colour shown in Fig. 6 (from red on the lower part of the scan, through yellow and green in the

middle, to blue on the uppermost areas of the scanned area) represents the height at which the GFP signal was measured, relative to the overall scanned area. Although all scans scanned an area of 1.2 mm^2 , the true surface area scanned was significantly larger on scaffold samples compared to flat disks (see Figure 19D-F) Using a simple graphic overlay model based on the resulting 3D rendered images, the difference between a flat scanned area and a 3D area (Figure 19A and F respectively) showed that the surface area was *c.a.* 6 times greater in the case of the latter (360 mm^2 versus 2160 mm^2 respectively).

Flat disk samples show an even, uniform distribution of bacterial cells on the scanned surfaces (Figure 19A-C), with a structure resembling mature biofilm in Figure 19C. However, it is unclear if the bacterial cell distribution is even and uniform on the surface of scaffold struts, due to the irregular nature of the scanned features. Although bacterial cells entirely cover the surface of the scanned scaffold, signified by the lack of black areas on scans where no fluorescence was detected, it is unclear whether or not there were areas of greater-than-average growth as such areas would be indistinguishable from the effects of underlying surface geometry. Sharp peaks and troughs in the scaffold scans show the geometry of the underlying Ti and Ta scaffold struts and correspond to the pore structure present within the scanned area.

Biomass of Ti and Ta samples after incubation for 96h

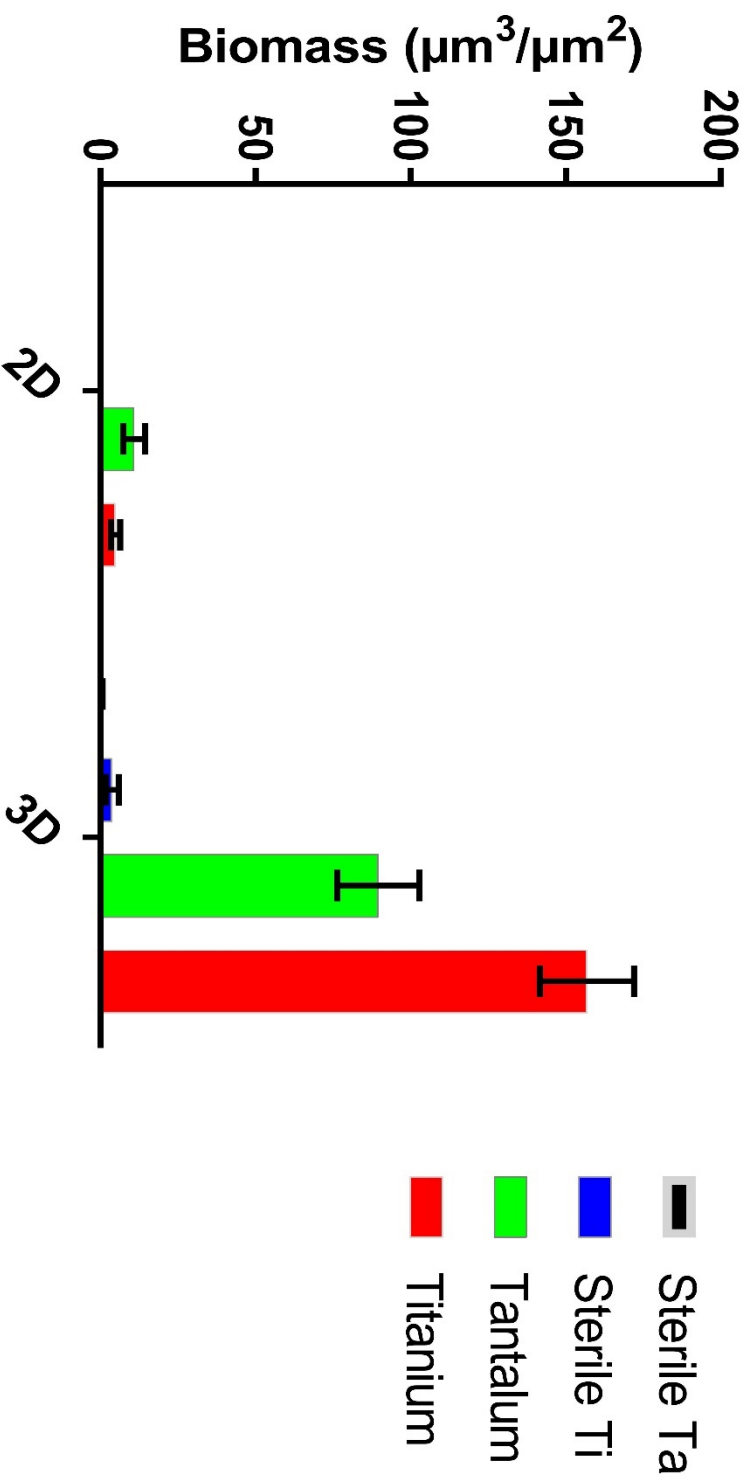


Figure 18: Biomass as measured by confocal laser microscopy after incubation for 96h in TSB media. Sterile samples were incubated in the media without inoculation with a bacterial culture, otherwise samples were inoculated with *S. aureus* prior to incubation. '2D' marks flat, polished samples of either Ti-6Al-4V or Ta, and '3D' marks scaffold samples (Osseo-Ti in the case of Titanium, and Trabecular Metal in the case of Tantalum).

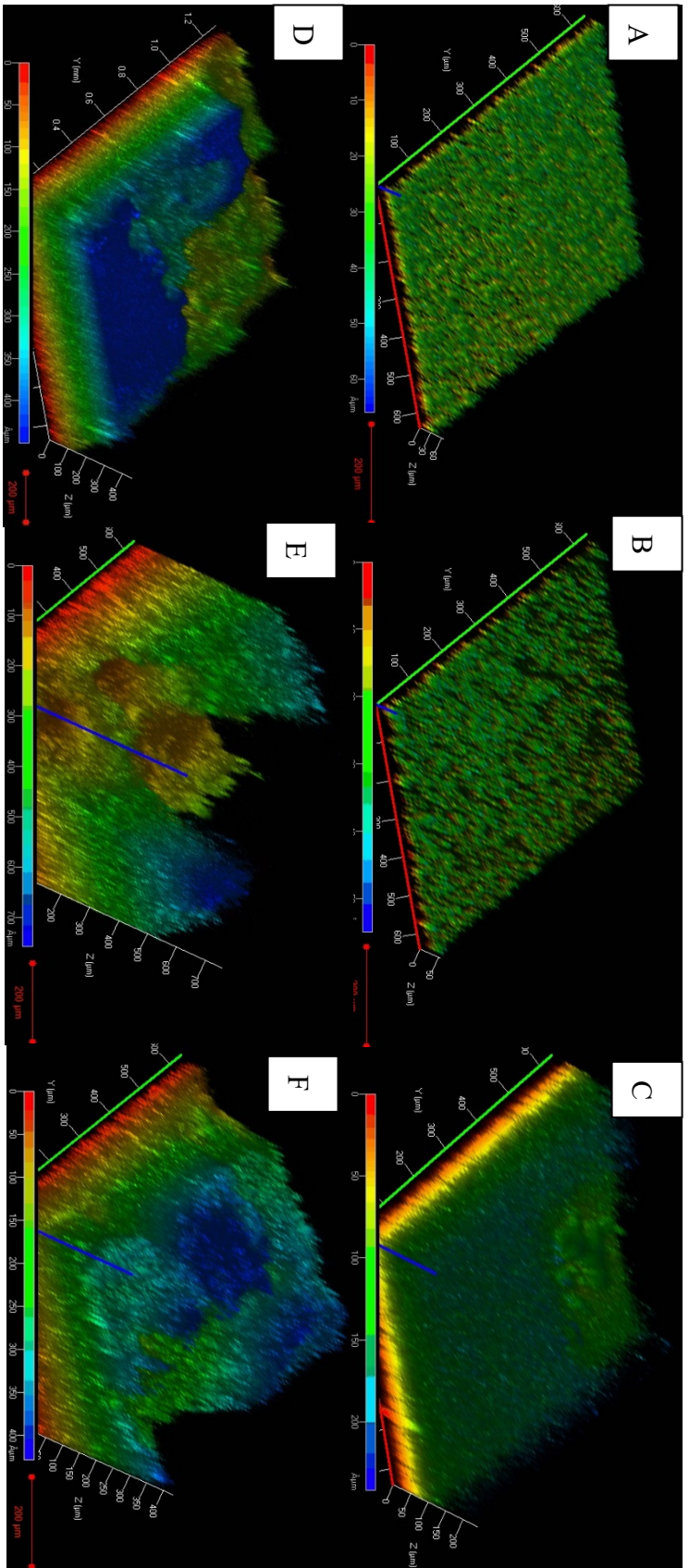


Figure 19: Example 3D rendering of confocal scans, measuring fluorescence of the GFP marker. A-D show renderings of the scanned surface of scaffolds at different, randomised locations. A-B were from a Trabecular Metal scaffold, and C-D were from an Osseo-Ti scaffold. E-F show the rendered scans of locations on flat, polished disks (Tantalum and Ti-6Al-4V respectively). Presence of GFP fluorescence is shown as a colour, and this colour changes depending on the relative height of the signal (with red being the lowest and blue being topmost).

3.3 Discussion

3.3.1 Wet weight assessment

Since bacterial biofilm has a relatively high density (1.14 g/cm^3), as outlined by the work conducted by Hermanowicz *et al.* (1983), it may be possible to quantifiably assess bacterial growth given a large enough coverage^[303].

However the density of the biofilm changes through time, with the density approaching that of water (1.0 g/cm^3) in the largest, most mature biofilm^[304]. This means that successive studies would need to take this into account and normalise any mass increases against the likely biofilm maturity stage based on the time of incubation.

The two-dimensional nature of samples results in a limited amount of surface area on which bacterial cells can proliferate and establish biofilm, relative to a three-dimensional scaffold. This means that any increase in mass resulting from bacterial presence on the surface will be smaller, and therefore require a suitably sensitive balance. However, as illustrated in Figure 14, no samples showed any statistically significant mass increase until the 72 h timepoint when compared to the control samples (with the exception of a slight increase on the polished Ti disk at 48 h). These large error bars present in this study, most pronounced at the 24 h timepoint, are indicative of the susceptibility of this method to variation resulting from random differences in the amount of water left on the sample rather than limitations of balance accuracy. Although

the samples were briefly dried, it proved difficult to ensure completely uniform removal of water from the samples when working at scales of less than 5 mg.

The largest standard error was seen in the 24 h Iodine-treated Ti cohort, where the error was 0.006 g. This may be due to the fact that water molecules had entered some surface pores on the disks resulting from the Micro-Arc Oxidation (MAO) process, but this infiltration of molecules varied in different samples. The water within the pores would most likely take a longer time to evaporate and would, therefore, still be present at the weighing stage considering all samples were initially dried for an equal amount of time. As a result, the drying times were increased at subsequent timepoints to account for this. However, despite these measures, the Iodine-treated Ti samples showed the highest standard error of all flat disk samples at all timepoints.

At 72 h, all samples showed a small, statistically significant increase in weight, relative to the control cohort. At this time, the bacterial growth seems to have reached a uniform, mature presence on the surface of all samples (as seen by the uniformity of the coverage visible with the naked eye), with the smallest standard error values of each sample type (excluding sterile controls).

All sample types' control cohorts showed a small, statistically significant increase in mass as compared to their weight before the commencement of the experiment. This is most likely due to the small residual amount of water

present on their surface after incubation, coupled with the adherence of proteins and salts from the culture media to the sample surface.

The increase in mass observed on a three-dimensional Ti scaffold (see Figure 15) is markedly more pronounced and therefore clearer to see than on flat disk samples. Although no significant increase was observed at 24 h compared to the control, there was a significant upward trend between 24 and 48 h, which was also evident at 72 h. The increase between 24 and 48 h in mass (0.018 g) is the largest increase seen in this study and is indicative of rapid biofilm formation once the bacteria have had time to attach to the surface in the first 24 h of incubation. Due to the high standard error present in the 72 h dataset, it is unclear whether the rate of weight increase between 48 - 72 h was higher, the same or lower than that seen between 24 - 48h, though the mass increase is still statistically significantly higher than at 48 h, indicating the increase didn't cease entirely. The large standard error observed in the scaffold cohort relative to flat samples is likely due to the difficulty in drying three-dimensional scaffolds sufficiently to remove effect of residual water within the structure while simultaneously ensuring that the biofilm does not dry to excess so as to preserve its weight.

3.3.2 Dry weight assessment

In order to completely remove any effects on data resulting from residual water on tested surfaces, all samples were freeze-dried by placement in a -20°C freezer overnight and subsequent transfer to a Modulyo benchtop -55°C

freeze dryer for 36 h. However, as the dry density of biofilm is markedly lower than the density of wet biofilm (between 0.0115 and 0.027 g/cm³), as outlined by the work of Timmermans *et al.* (1984), Hoehn *et al.* (1973) and Boaventura *et al.* (1988), meaning any mass increases would be significantly less pronounced^[305-307].

However, it became apparent that on flat, two-dimensional surfaces the dry weight of bacterial biofilm resulting purely from the dry polysaccharides, proteins and lipids is not sufficient to be measured by this method, up to 72 h (see Figure 16). While no flat samples showed a mass increase at any point during the study, compared to the control cohort, the sterile polished Ti disks did show a slight weight decrease of 0.0006 ± 0.0003 g. This may be due to the fact that the samples were not freeze-dried prior to the commencement of the experiment, and that some surface moisture may have been present in the first weighing. As no moisture would remain after the freeze-drying process, this would explain the slight weight decrease.

There was, however, a notable increase in the weight of the three-dimensional Ti scaffold at all time points. The statistically significant increase in the weight of the control cohort can be attributed to an adherence of salts and proteins to the scaffold surfaces. The increased surface area of the scaffolds compared to the two-dimensional surfaces of disks, mean that this effect would be more pronounced. Though this difference was estimated to be *ca.* six fold in the case of CLSM, it will likely be significantly greater when the whole structure is taken into account as opposed to a small 600 x 600 μm surface

scan example. However, the increase in the control dataset was *ca.* a third that of the increase in weight observed in sterile wet scaffolds (see Figure 15) (0.0006 ± 0.0001 g compared to 0.016 ± 0.004 g for dry and wet 3D Ti weight increase respectively) which is consistent with the fact that there was removed water weight.

Unlike in the trend seen during wet weighing, there was a mass increase in 3D Ti scaffolds between the control cohort and the inoculated samples at 24h (0.0006 ± 0.0002 g and 0.0011 ± 0.0002 g respectively). This can be attributed to some bacterial biofilm growth, though the fastest rate of mass increase was seen between 24 and 48 h with the increase doubling from 0.0011 g to 0.0023 g. This is consistent with the trend seen during wet weighing, where 3D Ti scaffolds showed a doubled increase in weight from 0.017 to 0.035 g between 24 and 48 h. Unlike the trend between 48 and 72 h in wet weight increase, where the increase was greater at 72 h than at 48 h, in the dry weight assessment there was no statistically significant difference in the mass increase of inoculated scaffolds between those timepoints.

Overall this method proved to be requiring too sensitive an apparatus, and inherently including too many sensitive variables with numerous handling steps to be a viable method for the quantification of bacterial burden on flat, polished samples. However, considering its ability to quantify mass increase in a scaffold starting from 24 h in a statistically significant manner, this method may prove useful in studies assessing scaffold samples alone. No example of this use was evident in literature.

3.3.3 Micro-CT assessment

The density of air is *ca.* 0.0012 g/cm³ at atmospheric pressure and room temperature, as described in the work conducted by El-Said *et al.* (2017); the density of wet biofilm is *ca.* 1.14 g/cm³ as studied by Hermanowicz *et al.* (1983); and the density of Ta and the Ti alloy (Ti6Al4V) is 16.6 g/cm³ and 4.30 g/cm³ respectively as shown in the work conducted by Briant *et al.* (2016) and Song *et al.* (2012)^[303, 308-310]. These differences in densities would allow for differentiation of these materials within a cross-sectional image obtained using micro-CT. Micro-CT has also been used in the study and characterisation of scaffolds, for example in work conducted by Ho *et al.* (2006) where characterisation of scaffolds was done using this technique, though only in the case of polymeric scaffolds, with a footnote describing the difficulty of using this approach for metal scaffolds due to image artefacts resulting from attenuation of X-rays by these metals^[197]. However, a more recent study by Liu *et al.* (2018) successfully characterised a 3D Ti-6Al-4V metal scaffold using micro-CT, albeit without attempting an introduction of a lower-density polymer within it^[311]. This resulted in an easily identifiable and visible strut structure which was rendered in 3D as a rendered image.

No viable results were produced using the micro-CT method. The difference in the density of the hydrogel (simulating biofilm) and the metal scaffolds was too large, as the required energy to image through the metal scaffold meant that it would not be able to distinguish between areas of air and hydrogel, and

conversely energies low enough to facilitate such differentiation were too low to produce cross-section images through the samples. Due to the increased density of elemental Ta as compared to the Ti6Al4V alloy (16.6g/cm³ and 4.30g/cm³ respectively), the cross-section images of the latter were superior than the former (see Figure 17) as a result of less pronounced attenuation of X-rays by the less-dense metal.

This approach may be better suited for investigating biofilm formation within polymeric scaffolds, where the difference between the density of the scaffold material and the biofilm is not as large. Natural and synthetic polymers have been extensively studied in literature for tissue engineering applications.

Materials such as collagen mixtures studied by Huang *et al.* (2011), Deng *et al.* (2010) and Wang *et al.* (2012), or chitosan mixtures, such as that studied by Grant *et al.* (2008)^[84, 312-314]. For instance, scaffolds like those developed by Felfel *et al.* (2019), made from chitosan and agarose would be well suited to such an assessment^[315]. This approach also showed the efficacy of micro-CT as a method of characterising scaffolds composed of two different materials, however the discrepancy between their density was significantly less significant than in the case of a metal and a hydrogel.

3.3.4 Confocal Laser Scanning Microscopy (CLSM)

The CLSM method is the most well-established method undertaken in this study^[316-322]. It is extensively used in the microbiological assessment of flat samples, due to its potential for direct quantitative analysis of biomass and

relative ease of use^[323-325]. GFP-expressing bacteria were imaged for the assessment of antibacterial properties of surfaces in studies such as those conducted by Rekha *et al.* (2018) and Ho *et al.* (2014) using CLSM^[326, 327].

In this study, designed to assess its suitability biomass measurement on metal scaffolds, a long incubation time of 96 h was chosen in order to ensure full bacterial coverage of the scanned surface- approaching the stationary phase of the growth curve. Typically, studies such as those conducted by Kim *et al.* (2018) or Abudula *et al.* (2020) focus on elution tests of scaffold and the assumption that these elutes will have the desired effect on bacteria as it would if those bacteria were simply to encounter them in solution^[328, 329]. However, these studies don't provide any data as to what occurs on the bacteria-surface interface. This, in turn, allowed for the evaluation of the biomass while fully considering the effects of sample geometry. If bacterial cells did not cover the full extent of the surface, the underlying surface geometry could not be fully considered, as such an eventuality would result in an absence of fluorescence in areas with no bacterial cells.

Flat disks were tested alongside three-dimensional scaffolds. Flat samples were used as part of the control cohort in order to validate results of the scaffold analysis. After 96 h, the polished tantalum disks had a larger biomass burden on their surface than polished titanium disks ($16.2 \pm 7.1 \mu\text{m}^3/\mu\text{m}^2$ and $5.9 \pm 3.5 \mu\text{m}^3/\mu\text{m}^2$ respectively) which will be the result of surface chemistry affecting bacterial cell behaviour due to the fact that both surfaces had identical surface geometries. This is a measure of the volume of cells per unit

area, and the mass can be obtained by multiplying the volume by the density of the bacterial cells ($1.1\text{g}/\text{cm}^3$) by the volume given[330]. These results served as benchmarks against which the scaffolds would be compared to. Sterile disks were also imaged using the confocal laser microscope in order to ensure no auto-fluorescence occurred. This would occur if the surface produced a signal when imaged with the laser without the presence of GFP. It could be a result of the surface chemistry or, more likely, any proteins or salts adhered to the surface from the culture media. However, no such autofluorescence was observed on any disk samples.

Biomass values obtained from scaffold sample analysis seemingly demonstrate an over five-fold increase in biomass on the Ta scaffold compared to its polished counterpart (scaffold biomass of $92.8\ \mu\text{m}^3/\mu\text{m}^2$), and an almost thirty-fold increase of biomass on the Ti scaffold (scaffold biomass of $166.8\ \mu\text{m}^3/\mu\text{m}^2$). In this instance, the trend is reversed relative to the flat disks, namely: the Ti scaffold has a significantly greater biomass burden compared to Ta. This suggests the overall geometry of the structure has a stronger influence.

Once again sterile control samples were incubated for the full duration of the experiment in culture media but were not inoculated with bacteria. Once imaged, there was no biomass burden on the Ta scaffold, however there was a slight, yet statistically significant, biomass reading on the Ti scaffold ($3.0 \pm 2.9\ \mu\text{m}^3/\mu\text{m}^2$). This may be the result of sample contamination, either during

the duration of the experiment or, more likely considering the small biomass value, a contamination during sample handling for imaging purposes.

Owing to the large increase in biomass burden between two- and three-dimensional samples, the image stacks resulting from the CLSM study were compiled into a 3D-rendering of the scan (see Figure 19). It was hoped that this would explain the magnitude of the discrepancy. Upon examination of rendered images, it became clear that the scanned surface areas of scaffold samples were significantly greater (~6 times greater) than the scanned surface areas of the flat disks.

As seen in Figure 19A-C, the imaged disk surfaces are predictably flat, with the bacteria spread uniformly. No large peaks or troughs are observed, with the maximum imaged height (distance from underlying metal surface) of 40 μm . This is the result of the underlying geometry. Likewise, the presence of what visually appears to be a mature biofilm (as seen in Figure 19C) shows a similar order in terms of the scanned maximum height.

This, however, is not the case when the rendered images of scaffolds are analysed (Figure 19D-F). In this instance, there is considerable variation in the topography of the scanned surface, with areas of peaks reaching heights of up to 600 μm higher than the areas of troughs (Figure 19E). Due to the underlying tomography of sample surfaces, the actual scanned surface area varies greatly. As the bacterial cells will attach to and cover this surface, this

increased surface area gives an impression of a significant biomass burden increase, when in real terms this is not the case.

It would, theoretically, be possible to negate this effect by modelling the underlying sample geometry and normalising the results against the true surface area. This approach, however, would require a considerable effort for each data point, with each timepoint and each sample type (in triplicate) being imaged in three positions. The modelling effort in this case would not be viable for a reliable study of any size over two data points, and more data points would be required to make the data more meaningful.

3.4 Conclusion

Considering the limitations of some of the aforementioned analysis methods, which would render them ineffective in the study of bioburden in a way which would allow for a quantitative comparison between 3D structures against flat samples, the need for a new approach became apparent. This new approach is detailed in the following chapter.

The scaffold samples proved too dense for analysis using micro-CT which would otherwise be able to penetrate the depth of the sample and yield results as to the volume of any structure within. The weight-difference methods were only sensitive enough to measure the most extreme bacterial growth, but not growth at earlier stages/ on samples such as flat samples where the volume of bacterial bioburden wasn't as great in terms simple volume.

CLSM, despite being widely used for biomass assessment on the surfaces of flat samples proved to be unreliable in assessment of scaffold samples due to the large scan area capturing large variation in sample topography and its inability to target singular struts during measurements.

The following chapter describes the development of a novel analysis method for quantifiable analysis of bacterial biofouling using SEM imaging in the wake of the lack of appropriate existing methods in the context of metal scaffolds.

Chapter 4 Scanning Electron Microscopy (SEM) Biofilm Formation Analysis Method Development

This chapter intends to describe the development of a novel SEM image analysis method to measure bacterial coverage. The method is validated against a well-established analysis method- CLSM- in an application it's well-suited for- flat surfaces. It's then used to conduct proof-of-concept studies using 3D scaffolds.

In light of the limitations of the analysis methods considered in Chapter 2, a method utilising Scanning Electron Microscopy (SEM) was developed for the quantification of bacterial burden on sample surfaces. The imaging of bacterial cells using SEM is well studied and explored in literature^[331, 332]. The method allows for imaging at a resolution suitable for identifying individual bacterial cells and is comparable to cell counting in tissue culture samples.

Cell counting provides a process to acquire quantifiable data from an optical source, i.e. an image, and although manual counting is rare (for bacterial cells), similar methods ascertaining Colony-Forming Units (CFU) of bacteria are still undertaken. This can be done, for instance, using a protocol like that outlined in standard ASTM D5465 which relies on the growth of bacteria on agar plates from spreads of a suspension, though other methods for CFU counting are documented^[333, 334]. However, a significant drawback of cell counting is that it is prone to human error, as it relies entirely upon the operator to not miscount the cells present in the optical medium.

To overcome this problem, each SEM micrograph was converted into a binary image, containing pixels of only 2 values: 1 and 0. Values of 1 corresponded to areas on the original micrograph where a bacterial cell was present, and values of 0 where areas with no bacterial cell coverage.

This approach allowed for the quantification of bacterial cell coverage via pixel area coverage, using SEM images. Due to the fact that in order to complete the conversion, each image has to be studied at high magnification, manually selecting each bacterial cell, which in itself takes some time, the likelihood of operator error is significantly reduced.

As this method is novel, with no precedence in literature, it had to be evaluated against a known and tested analysis method. As the microbiological assessment of flat samples is well documented, and the confocal laser scanning microscopy (CLSM) method widely used, it was chosen as a

benchmark against which the SEM method would be compared^[171, 292, 293, 316, 318-321, 323, 325, 335].

Only once there was sufficient evidence that the trends observed using CLSM correlated closely to those obtained using SEM image analysis, could the subsequent study of samples begin.

4.1 Materials and Methods

4.1.1 Sample Selection

Samples for this study were supplied by Zimmer-Biomet. They included commercially available surfaces, manufactured from Tantalum and a medical-grade Titanium alloy (Ti-6Al-4V). All sample disks measured 10 x 2.5mm. A number of surfaces manufactured from these materials allowed for a simultaneous assessment of surface topography and chemistry effects on bacterial behaviour as well as the suitability of the assessment methodology. The sample types were as follows: polished disks, grit-blasted disks, 3D additively-manufactured scaffolds (Osseo-Ti: Ti-6Al-4V scaffold manufactured using Selective Laser Sintering (SLS) and Trabecular Metal: Ta scaffold manufactured using Chemical Vapour Deposition (CVD)).

Some polished Ti disk samples were coated with elemental copper through sputtering- a Physical Vapour Deposition (PVD) process whereby a thin film

is deposited using ejected materials from a target onto a substrate- in order to be used as positive control in the microbiology studies.

The Trabecular Metal is an open cell highly porous (~80% porosity^[203]) structure, similar in geometry to trabecular bone by being composed of struts ordered in dodecahedron repeats^[204]. In order to achieve this, a vitreous carbon scaffold is used as an internal matrix upon which the Tantalum is later deposited^[205]. The carbon scaffold is then placed in a sealed chamber and the CVD process proceeds using hydrogen and chlorine gases. Evaporated tantalum (as TaCl₅) then deposits Ta molecules onto the underlying carbon scaffold^[206]. A review of available literature suggests that this material exhibits high osteoconductivity, biocompatibility, vascularisation and bone-ingrowth (as observed in *in vitro*, *in vivo* and human studies)^[176, 203, 207-210].

The Osseo-Ti scaffold is manufactured using SLS of Ti-6Al-4V powder, based directly on 3D scans of cancellous bone and exhibits ~70% porosity according to data supplied by Zimmer-Biomet.

4.1.2 Bacterial seeding and incubation

All samples were sterilised by immersion in 70% ethanol for 2 hours followed by drying under UV light overnight in a sterile fume hood.

Bacteria was taken from cold storage and transferred into Tryptic Soy Broth (TSB) media, in order to obtain active bacterial cells. The *S. aureus* Newman

strain containing a plasmid conferring Chloramphenicol (Cm) resistance and expressing green fluorescent protein (GFP) [336, 337] and was grown in Cm (1µg/ml) to apply sufficient selective pressure to ensure that the plasmid was stably maintained in the population. In order to obtain the starting culture, a single colony of *S. aureus* was lifted from the agar plate and used to inoculate 20 ml TSB media which was incubated overnight at 37°C (200 RPM). The overnight culture was washed twice in TSB and the optical density (OD₆₀₀) measured using a spectrophotometer (Jenway 6715 UV/Vis). The bacteria were then added to the petri-dishes containing the sterile disks immersed in 20 ml of warm (37°C) TSB media to give a starting OD₆₀₀ of 0.1. Samples were prepared in triplicate with uninoculated samples as negative controls. The samples were then incubated at 37°C and 60 RPM for the appropriate time, after which they were removed and washed with deionised water (dH₂O) three times. 60 RPM was suggested as the standard by the microbiology lab within which the work was conducted.

There were three different methods of introducing protein in the experiment: the samples were either incubated in pure TSB media (denoted as ‘TSB’ in results) with no protein present^[338]; were incubated in TSB media with added Foetal Bovine Serum (FBS) to produce *circa* 2.5 g/dL of protein in solution (levels similar to those seen in wound fluid) [339, 340] (denoted as ‘FBS’ in results). The concentration was created by obtaining the particular FBS batch protein content provided by the manufacturer (ThermoFischer).

Some samples were left in pure FBS for 2h in order to produce a protein conditioning film on their surface- these are shown as 'PRE' in results.

4.1.3 SEM bacterial growth analysis

Samples were incubated and washed as per protocol outlined in Section 4.1.2, and fixation for SEM was done following a modified human cell fixing protocol using 3% Glutaraldehyde to result in longer dehydration times using ethanol. In this protocol, the samples were placed sequentially in 10%, 20%, 30%, 40%, 50%, 60%, 70%, 90% and 100% ethanol for 20 minutes at a time^[341]. Micrographs were obtained using a FEI XL30 Scanning Electron Microscope, in the Secondary Electron (SE) detection setting. A working distance was maintained between 10.0 and 11.0mm, utilising a beam energy of 20kV and magnification of x2500. Three images were taken from the surface of each triplicate sample.

False colouring and conversion to binary images was done using a modified version of open source software GIMP 2.8.14^[342, 343]. The modified version inserted a line of code in the software to enable more accurate masking over bacterial cells. Due to their geometries, any sudden change in brightness was assumed by the code to be the edge of a cell and would therefore not mask over the edge of this threshold. This could be overridden if the user decided that this assumption was not correct in any case.

This method involved taking SEM images at fixed magnification and working distance, and through a series of steps converting them into binary images, showing bacterial cells white in a black background. The white pixels were then counted, and a percentage area was calculated to quantify the bacterial cell coverage in a given image.

$$\text{Bacterial area coverage} = \frac{a}{a + b}$$

Where a = number of white pixels, and b = number of black pixels.

4.1.4 Confocal Laser Scanning Microscopy (CLSM)

The method used for CLSM is identical to that employed during the work in Chapter 3.

Samples were incubated and washed as per protocol described in Section 3.1.1 and incubated for 96h to allow for the bacterial colonisation of the entire sample surface, after which they were imaged on a Carl Zeiss L700 Confocal Laser Scanning Microscope. The biomass burden was analysed using the COMSTAT 2 plugin to ImageJ on the resulting image stacks^[301]. The scanned area was 1.2mm².

4.2 Results

4.2.1 Image Processing

Once the surfaces were imaged using SEM, in triplicate, the resultant micrographs were saved as TIFF images (in order to preserve the quality of the image and not risk compression degradation) and transferred into the GIMP software for the masking and measurement process. The original image (Figure 20A) had its brightness reduced in order to ensure no original pixels are at their maximum value (255), but instead a maximum of 225 (i.e. no pixels of value 255 remained in the image). A value of 255 is then applied to pixels corresponding to individual bacterial cells (Figure 20B) through image masking, after which thresholding can be applied to select only pixels with the value of 255, with all others being reduced to 0. This is done to ensure that no areas of the original image are converted automatically into ‘bacterial cell’ areas, and that such areas can only be designated manually. This process converts the image to a binary format (Figure 20C), and the number of pixels of each value can be ascertained. No features from the original image are present in the final binary images, as seen in Figure 20.

Although the bacterial cell areas require manual selection, the remaining process can be, and was, automated. This includes steps such as the initial pixel devaluation, thresholding and pixel counting. All of these steps were automated successfully, hastening an otherwise time-consuming process. This

was done by a custom automated program which selected the desired image, entered the editing functionality of the GIMP software, devalued pixels to remove extremes, applied a binary threshold as described above and produced a pixel count. All of these are core functionalities of the GIMP software.

During the masking process images were edited at high magnifications so as to ensure that all bacterial cells were accounted for. The images were taken at magnifications of 2500x at a Working Distance of 10.5mm, meaning the magnification was still great enough to facilitate easy identification of individual bacterial cells in resulting micrographs.

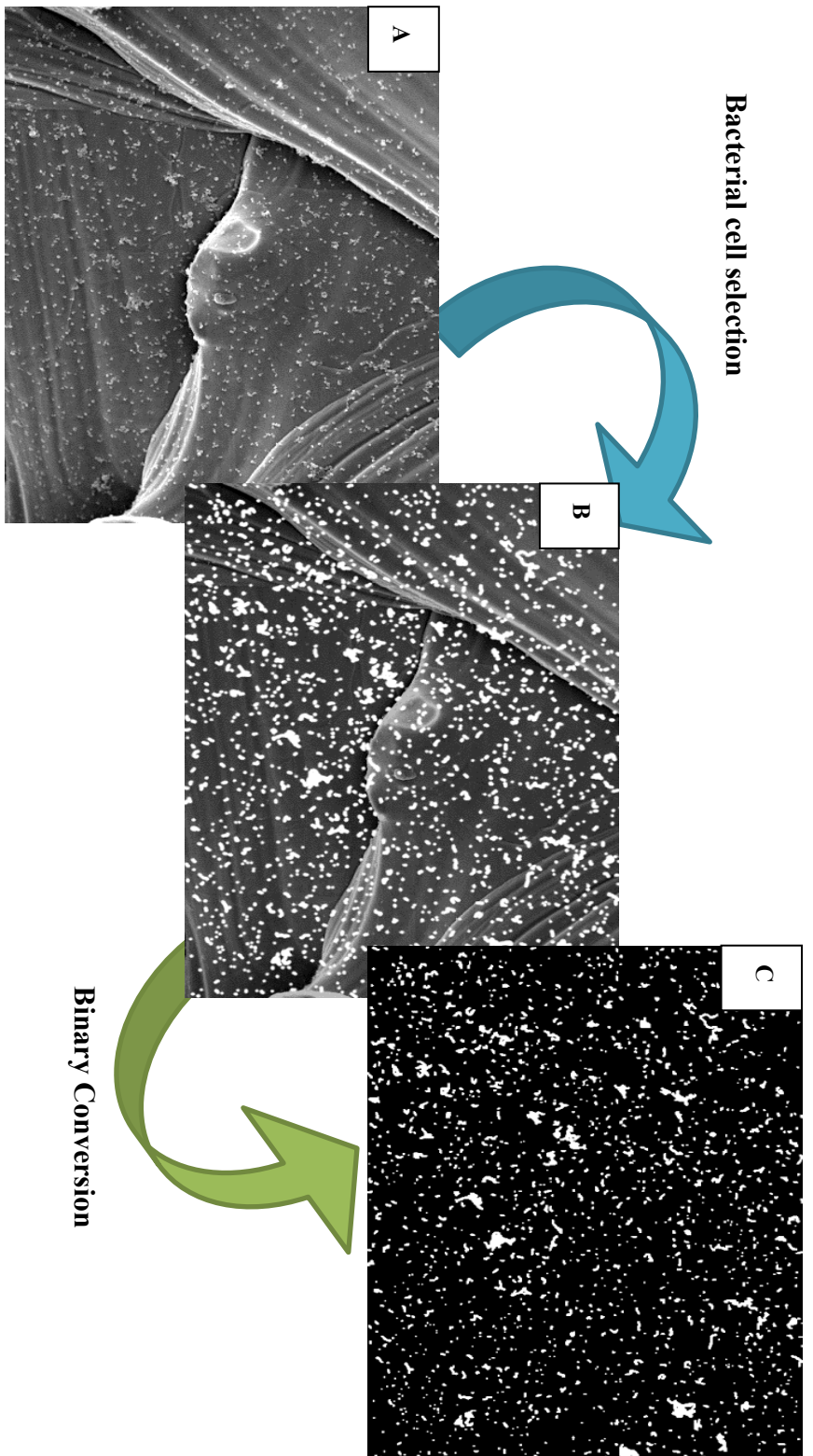


Figure 20: The main image processing steps to achieve a binary image. A shows a raw micrograph as taken using SEM imaging. B shows an image which has had its brightness reduced (pixel devaluation) and subsequently had a mask of bright pixels applied over any location where bacterial cells were present in the image (masking). Image C shows the binary picture which was used to count pixels, once the image has gone through thresholding which left only 2 types of pixels – black and white (values of 0 and 255 respectively).

4.2.2 Method validation

4.2.2.1 24 hour Confocal Laser Scanning Microscopy (CLSM) and Scanning Electron Microscope (SEM) comparison

In order to establish whether or not binary image area coverage analysis was a viable alternative to CLSM, a study was undertaken on polished titanium samples (Figure 21) over a period of 24h. The same samples were first imaged using CLSM, and then prepared and imaged in SEM.

The CLSM results show no statistically significant ($P=0.372$) increase in biomass between the initial 3 and 6h (0.33 ± 0.13 and $0.75\pm 0.40\mu\text{m}^3/\mu\text{m}^2$ respectively), then rapidly rising from 6h, through 9h ($P=0.0404$) and to 12h ($P=0.0127$) (1.88 ± 0.48 and $3.17\pm 0.33\mu\text{m}^3/\mu\text{m}^2$ respectively), and beginning to plateau from 12h to 24h ($4.46\pm 0.65\mu\text{m}^3/\mu\text{m}^2$) ($P=0.1101$). This growth pattern is similar to that observed during work by Ceri *et al.* (1999), which studied the growth curves of bacterial strains, including *S. aureus*. The results showed a little growth in the initial 4 hours of testing, with a rapid growth phase between 4h and 10h, and either a markedly lower growth rate between 10h and 25h, or a plateau between those time points^[104].

The SEM analysis results show how a similar growth pattern, with no statistically significant increase in pixel area coverage from the initial 3 to 6h ($P=0.345$) (0.14 ± 0.06 and $0.31\pm 0.16\%$ respectively), followed by a steady

increase from 6h, through 9h (0.0377) and to 12h (P=0.0188) ($0.66 \pm 0.14\%$ and $1.24 \pm 0.20\%$ respectively). However, unlike in the CLSM assessment, there is no statistically significant ($p > 0.05$) difference between the pixel area coverage between 12h and 24h ($1.51 \pm 0.23\%$).

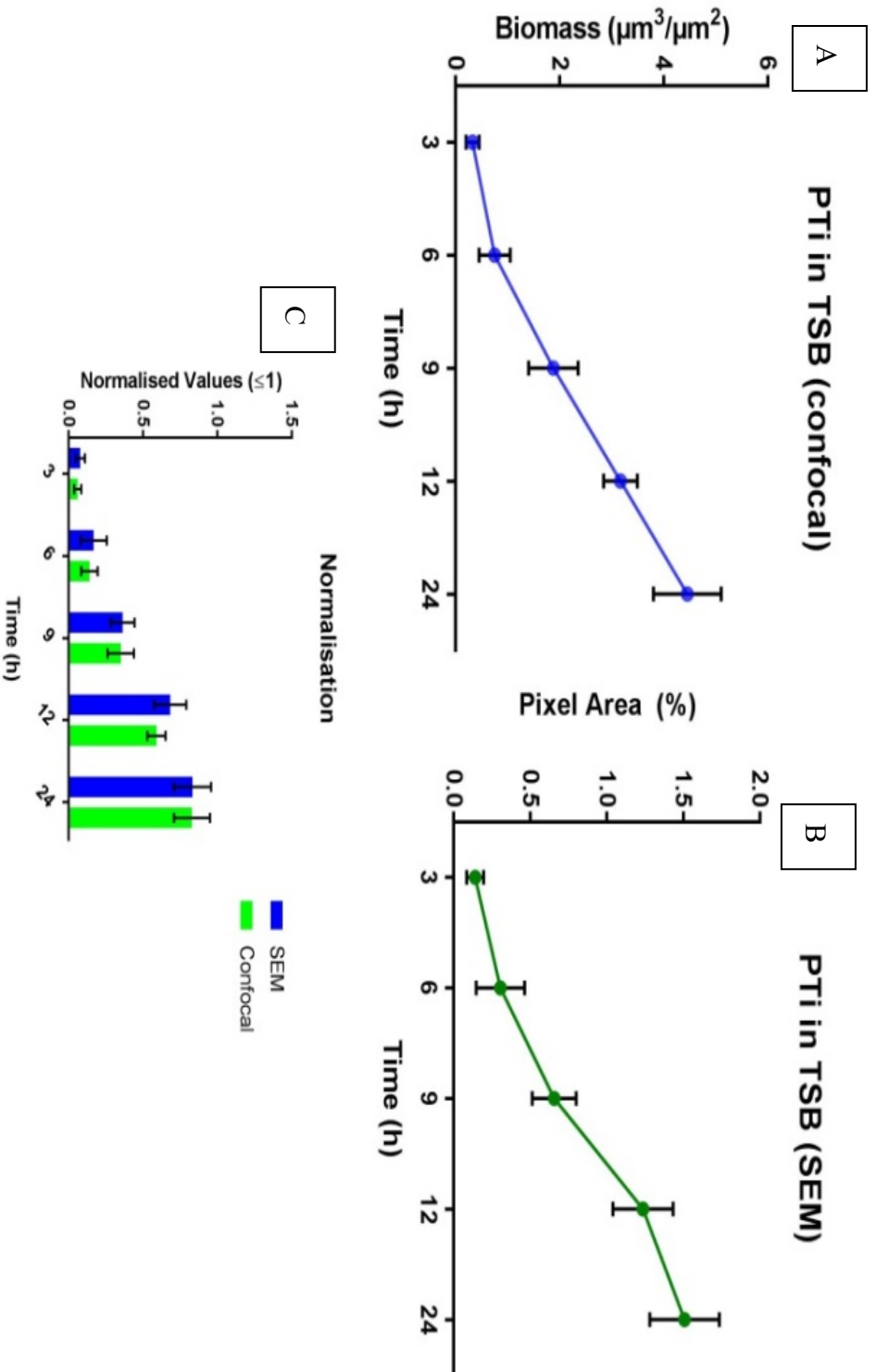


Figure 21: Validation of the SEM method against confocal laser scanning microscopy (CLSM) on polished Ti6Al4V disks. *S. aureus* was used to inoculate the media, and the samples were incubated for up to 24h. Graph A shows the biomass as measured by CLSM at 3, 6, 9, 12 and 24h. Graph B shows pixel counts as measured by the SEM method. Graph C shows how the normalised values from both methods (values were divided by the maximum seen in the cohort) compared at each time point. No statistically significant difference is seen between different methods in graph C at any time point ($p > 0.005$).

The results from the two methods were then normalised (Figure 21, graph C), by dividing each value in a dataset by the maximum value in the cohort. At 3h the SEM and CLSM results show $6.2 \pm 2.2\%$ and $7.8 \pm 1.8\%$ of the highest cohort value respectively, resulting in an adjusted P value of 0.9959. At 6h the SEM and CLSM values represent $16.5 \pm 8.1\%$ and $14.0 \pm 4.9\%$ of the maximum cohort value respectively, with an adjusted P value of 0.9634. At 9h the SEM and CLSM values were $36.3 \pm 7.4\%$ and $35.0 \pm 8.3\%$ of the maximum corresponding values, with the adjusted P value of 0.9992. The two methods showed greatest discrepancies in data at the 12h timepoint, where the SEM method yielded values of $68.3 \pm 10.6\%$ of the maximum, and the CLSM's values were $59.1 \pm 6.8\%$, however those differences were still not statistically significantly different from one another, with an adjusted P value of 0.1174. At 24h, the means of results from SEM and CLSM analysis were $83.3 \pm 12.1\%$ and $82.9 \pm 11.9\%$ of the maximum value, with an adjusted P value of $p > 0.9999$.

There was no statistically significant difference between the normalised values of CLSM and SEM analysis results at any timepoint ($P \geq 0.1174$ in all cases).

4.2.2.2 3 hour Bioburden Protein Study

In an attempt to further validate the SEM image analysis method against CLSM results, a study was conducted over 3h, which also aimed to concurrently assess bacterial cell attachment to orthopaedic surfaces in the presence of protein (Figure 23). 3h was chosen to ensure the bacteria were before the log phase, and therefore bacterial cells on the surface were likely present due to attachment rather than any replication. The protein was introduced either to the media in the form of Foetal Bovine Serum (FBS) which was added to TSB to result in 2.5g/dL of protein in the media (an amount of protein akin to that seen in wound fluid [339, 340]), or as a protein conditioning layer, which was introduced to the sample surfaces by exposing the surface to FBS for 3h prior to inoculation with bacteria. Pure TSB media acted as a control, and copper-coated titanium disks acted as negative sample controls due to the well-established antibacterial properties of copper [88, 263-265].

CLSM (Data given as $\mu\text{m}^3/\mu\text{m}^2$)			
	FBS	TSB	PRE
CuTi	0.12 ± 0.03	0.11 ± 0.03	0.26 ± 0.03
PTa	0.18 ± 0.07	0.19 ± 0.06	0.52 ± 0.07
PTi	0.37 ± 0.06	0.30 ± 0.09	0.53 ± 0.08
GTa	0.78 ± 0.15	0.67 ± 0.15	1.28 ± 0.18
GTi	0.78 ± 0.16	0.67 ± 0.15	1.28 ± 0.18

Table 1: Bacterial presence on the surface of flat samples as measured by Confocal Laser Scanning Microscopy (CLSM). CuTi is a Copper-coated, polished Ti6Al4V disk, PTa and PTi are polished Tantalum and Ti6Al4V disks respectively, and GTa and GTi are grit-blased Tantalum and Ti6Al4V disks respectively. FBS is a cohort of samples incubated in media with added Foetal-Bovine Serum, and inoculated with *S. aureus*. TSB samples were incubated in Tryptic Soy Borth media, and PRE samples were left in pure Foetal Bovine Serum prior to transfer into Tryptic Soy Broth media for inoculation and incubation

SEM (Data given as % coverage)			
	FBS	TSB	PRE
CuTi	0.036 ± 0.01	0.045 ± 0.01	0.114 ± 0.01
PTa	0.108 ± 0.012	0.066 ± 0.050	0.206 ± 0.024
PTi	0.146 ± 0.027	0.164 ± 0.020	0.228 ± 0.018
GTa	0.291 ± 0.019	0.278 ± 0.024	0.536 ± 0.029
GTi	0.404 ± 0.034	0.411 ± 0.036	0.520 ± 0.029

Table 2: Bacterial presence on the surface of flat samples as measured by Scanning Electron Microscopy (SEM) micrograph coverage analysis. CuTi is a Copper-coated, polished Ti6Al4V disk, PTa and PTi are polished Tantalum and Ti6Al4V disks respectively, and GTa and GTi are grit-blased Tantalum and Ti6Al4V disks respectively. FBS is a cohort of samples incubated in media with added Foetal-Bovine Serum, and inoculated with *S. aureus*. TSB samples were incubated in Tryptic Soy Borth media, and PRE samples were left in pure Foetal Bovine Serum prior to transfer into Tryptic Soy Broth media for inoculation and incubation.

There was no statistically significant difference between the pure TSB and FBS+TSB media cohorts in either the CLSM (Table 1) or the SEM analysis (Table 2) results (lowest p value is $p>0.5$); however the protein conditioning film cohort had higher values than those seen in either of the aforementioned data sets across all sample types. In both CLSM and SEM analysis results the copper-coated titanium disks showed the lowest values (Table 1 and Table 2), followed by polished titanium and tantalum, which were all significantly lower than the grit blasted samples.

Both methods (SEM analysis and CLSM assessment) showed the greatest standard error values in the grit-blasted Ti and Ta datasets.

There is no statistically significant difference between pre-conditioned copper-coated titanium disks and polished tantalum and titanium disks incubated in TSB+FBS media.

The results were normalised much like in the 24h study- namely by the division by the maximum value, and the normalised results were then compared between each analysis methods for each data set.

	Normalised Values											
	FBS						TSB					
	SEM	CLSM	p	SEM	CLSM	p	SEM	CLSM	p	SEM	CLSM	p
CuTi	0.062 ± 0.010	0.076 ± 0.008	P>0.999	0.077 ± 0.006	0.072 ± 0.009	P>0.999	0.197 ± 0.012	0.171 ± 0.019	P=0.9952			
PTa	0.185 ± 0.019	0.116 ± 0.020	P=0.0979	0.114 ± 0.029	0.128 ± 0.045	P>0.999	0.354 ± 0.071	0.348 ± 0.083	P>0.999			
PTi	0.251 ± 0.074	0.246 ± 0.081	P>0.999	0.282 ± 0.013	0.203 ± 0.031	P=0.0180	0.391 ± 0.042	0.353 ± 0.030	P=0.8420			
GTa	0.500 ± 0.102	0.521 ± 0.116	P=0.9992	0.477 ± 0.099	0.458 ± 0.158	P=0.9766	0.921 ± 0.123	0.850 ± 0.210	P=0.567			
GTi	0.695 ± 0.087	0.627 ± 0.074	P=0.0826	0.706 ± 0.069	0.606 ± 0.041	P=0.0008	0.894 ± 0.148	0.879 ± 0.121	P>0.999			

Table 3: Bacterial presence on the surface of flat samples as measured by Scanning Electron Microscopy (SEM) micrograph coverage analysis and Confocal Laser Scanning Microscopy (CLSM) normalised (value in each subset is divided by the maximum value in the subset). CuTi is a Copper-coated, polished Ti6Al4V disk, PTa and PTi are polished Tantalum and Ti6Al4V disks respectively, and GTa and GTi are grit-bladed Tantalum and Ti6Al4V disks respectively. FBS is a cohort of samples incubated in media with added Foetal-Bovine Serum, and inoculated with *S. aureus*. TSB samples were incubated in Tryptic Soy Borth media, and PRE samples were left in pure Foetal Bovine Serum prior to transfer into Tryptic Soy Broth media for inoculation and incubation.

There was a statistically significant difference between the analysis methods in the pure TSB-incubated, grit blasted titanium ($P=0.0008$) and polished titanium disks ($P=0.0180$), however there was no statistically significant difference between the two methods in the remaining 13 data sets.

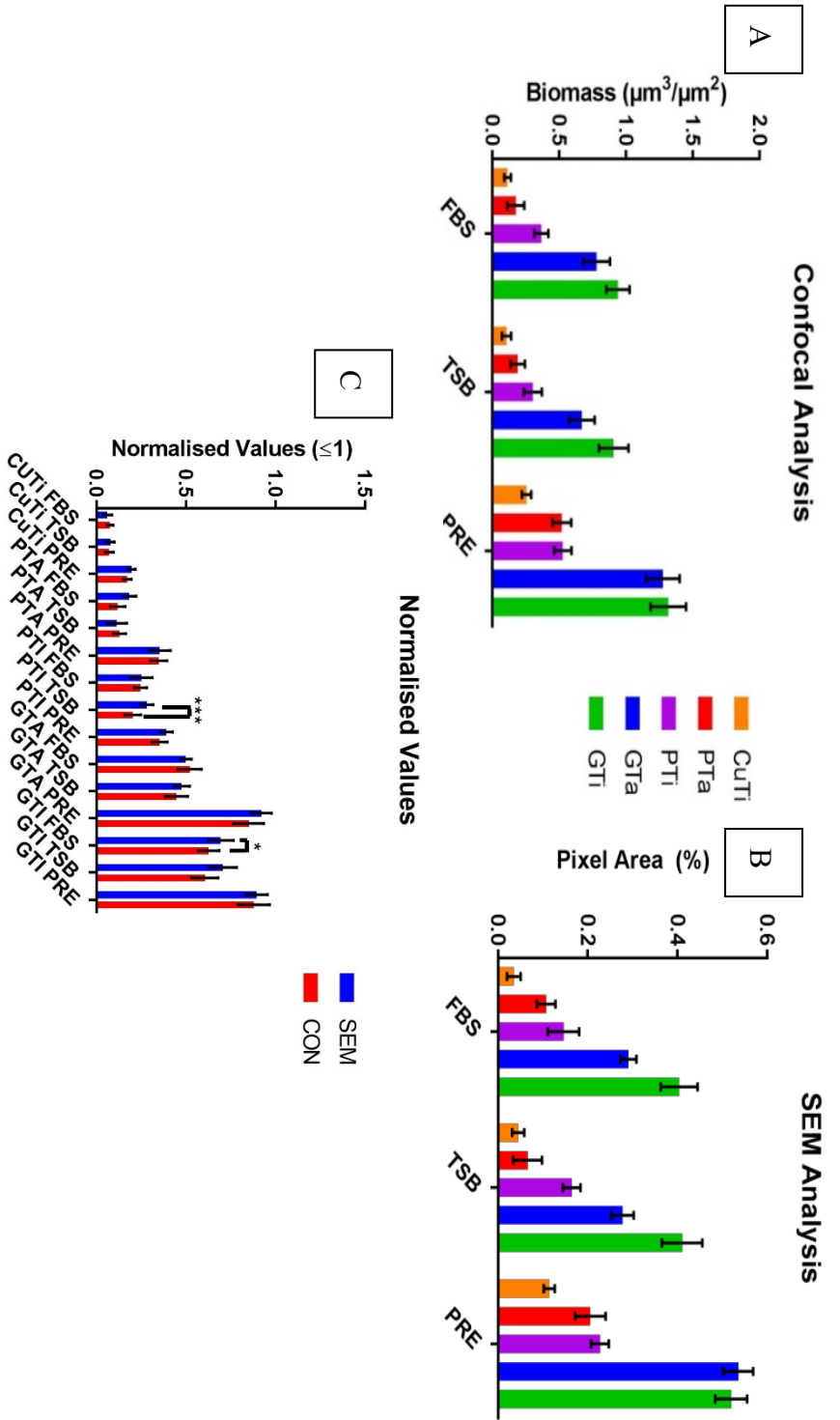


Figure 22: Validation of the SEM method against confocal laser scanning microscopy (CLSM) on polished Ti6Al4V disks. *S. aureus* was used to inoculate the media, and the samples were incubated for 3h in different media. Samples in the FBS cohort were incubated in TSB media with added FBS. Samples in the TSB cohort were incubated in pure TSB media. Samples in the PRE cohort were left in FBS media to obtain a protein conditioning film, then incubated in TSB media. CuTi were copper-coated Ti disks, PTa and PTi were polished Tantalum and Titanium disks respectively. GTa and GTi were grit-blasted Tantalum and Titanium disks respectively. Graph A shows the biomass as measured by CLSM at 3h. Graph B shows pixel counts as measured by the SEM method. Graph C shows how the normalised values from both methods (values were divided by the maximum seen in the cohort) compared at each time point. No statistically significant difference is seen between different methods in graph C at any time point ($p > 0.005$) apart from PTi TSB cohorts and GTi FBS cohorts.

4.2.3 Qualitative Scanning Electron Microscope (SEM)

micrograph analysis

In order to clearly illustrate the limitations of the SEM image analysis method, seen in Figure 21 at the 24h time point, micrographs were obtained of samples which have been incubated for 48h (Figure 24). Whereas the CLSM method allows for quantification of biomass as volume per unit area, the SEM method is a simple coverage area analysis method. As a result, it does not account for multiple layers of bacterial cells; a feature of advanced bacterial growth on the surface, as those would increase in volume without necessarily increasing the area of the sample surface which they occupy. In Figure 24, micrographs A, B and C show what visually appear to be biofilms on the surface of the samples, which boast several layers of bacterial cells, without occupying the whole surface in a uniform manner. In these cases, SEM image analysis of the pixel area coverage would not be reliable. However, Figure 24D, in which the micrograph shows a location where single layers of bacterial cells spread across the surface are visible, could be reliably analysed using this method.

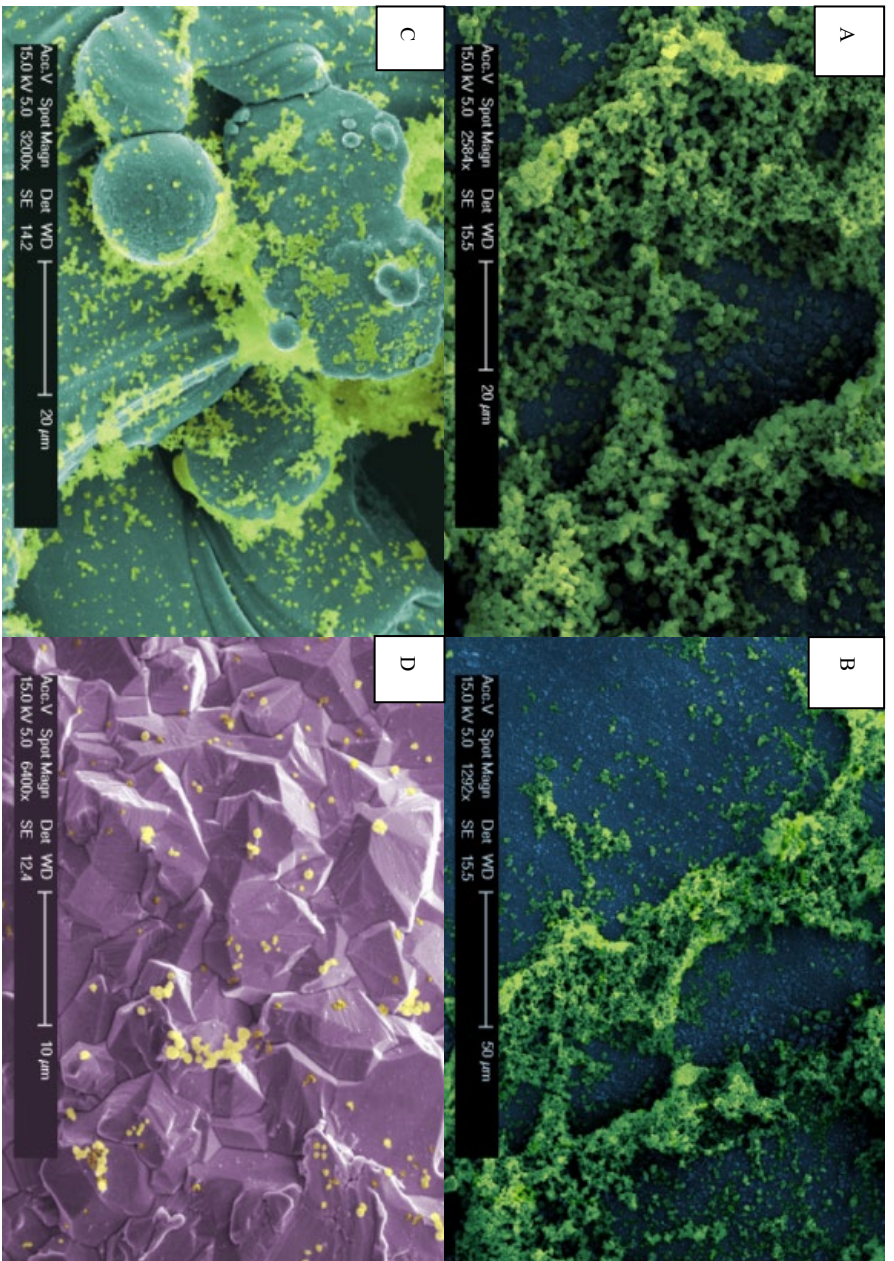


Figure 23: False-coloured SEM images of multi-layered colonies and single-layered *S. aureus* colonies on surfaces of samples. A is a colony which was incubated for 24h on a polished Ti6Al4V disk surface. The area in blue is the sample surface, and the area in green is the bacterial colony at a magnification of x2584. Image C is the same colony at a magnification of x1292. C is an image of a surface inside a 3D Ti6Al4V scaffold (Osseo-Ti) at a magnification of x3200. The blue area is the sample surface and the bacterial cells are coloured in green. D shows a surface of a strut inside a 3D Tantalum scaffold (Trabecular Metal) at a magnification of x6400. The surface is coloured in purple, and the *S. aureus* cells are coloured in yellow.

4.3 Discussion

4.3.1 Image processing

A novel image analysis of SEM micrographs (not seen in literature) was utilised to measure bacterial cell coverage on the surface of samples.

Despite the fact that this process is relatively labour-intensive, in that each bacterial cell has to be manually masked over using a highly magnified image, the steps preceding and following the masking are easily automated, and require no manual input.

The initial manual masking exposes the process to the risk of human error, as any bacterial cell that isn't masked will not be counted in later steps, affecting the results. However, conducting this vital step at high zoom of the original micrograph minimises this risk, as individual cells are obvious and difficult to miss. Care also needs to be taken to mask only the cell within its boundaries, as masking outside these will increase the number of pixels corresponding to bacterial cells and, again, affect the end result. The process, however, doesn't differentiate between live and dead cells.

Following the masking step, the images are converted to a binary version of themselves through thresholding, whereby anything below a certain pixel value is reduced to 0, leaving only the pixel value used during the masking process. The resulting image can be analysed using any image processing tool

to give the total number of pixels of each value, and a percentage can be obtained from these numbers.

As illustrated in Figure 24, assessment of samples containing extensive, mature bacterial biofilm growth may prove problematic. As the SEM image analysis method is suited to bacterial cell coverage, it converts each image into a two-dimensional map unto which the positions of cells are plotted. Since biofilms are inherently three-dimensional structures, such a method of assessment would likely result in an under-estimation of bacterial burden present upon the tested surface in reality.

This limitation could be overcome in two ways, depending on the parameters of a given study. If the study was concerned about the biofilm fouling exclusively, with no focus on individual bacterial cells, the biofilm areas could be masked over by the operator while treating individual cells as though they were the underlying surface. This approach could then be used to ascertain the number, average size and distribution of biofilm on the surface in question. However, as this approach would intrinsically disregard the individual cell presence, which is of equal importance to biofilm presence in most microbiological assessments of biomaterials, this method would be suitable to only a few scenarios.

Alternatively, an approach yielding results similar to that of CLSM analysis could be undertaken. As the magnification and scale are known variables, as are the dimensions of commonplace features of the imaged surface (size of the

struts/ pores in scaffolds, or the size of an average bacterial cell from a strain studied), the dimensions of the biofilm structure could be estimated. The height could be calculated by using known reference points in the image, such as struts. This estimate would allow for the calculation of a volume, and as the volume of individual cells could also be ascertained, the overall volume of bacterial burden present in an image could be established. This would allow for results to be given in biomass per image and would take into account individual cells as well as mature biofilm. This approach, however, would be the considerably time consuming, as the biofilm in each image would require measuring individually by the operator. An average volume could be given to each bacterial cell, and those counted to give an estimate volume of individual cells on the surface, however despite this the labour-intensive nature of this method would likely result in its limited viability in general microbiological studies of biomaterials. The increased risk of operator error in this method would act to further limit the efficacy of this approach.

Another notable limitation of the SEM image analysis method is the fact that it is unable to distinguish between live and dead bacterial cells. Although dead bacterial cells which have not reached the irreversible stage of attachment would be removed during the washing phase of the analysis process, any cells which had undergone this attachment and were subsequently killed (by the surface or otherwise) would be indistinguishable from live cells in an SEM micrograph.

This may be overcome by the study of the samples using a LIVE/DEAD assay in order to ascertain the average (mean) ratio of alive and dead bacterial cells upon the tested surface, upon the conclusion of which the sample would undergo preparation for SEM imaging^[344, 345]. As this assay is well documented in the analysis of bacterial cell viability, such an approach could prove effective, however care would have to be taken to limit the time the samples are out of incubation before preparation for SEM imaging, as this could affect results^[346-348].

4.3.2 Method Validation

4.3.2.1 24 Hour Bioburden SEM and CLSM comparison study

A study was conducted over a 24h period, with 5 time points (3, 6, 9, 12, 24h), using only one flat sample type (polished titanium disks) in order to ascertain whether the SEM image analysis method could be validated against a standard common analysis method, CLSM. The same samples were used for both analysis methods, meaning samples were removed from media at each time point, imaged under the confocal microscope and then fixed for SEM imaging. This removed any potential for variation caused by external factors during

inoculation and incubation between the two methods. The confocal imaging showed that there was a slow increase in bacterial presence on the surface of the samples between 3 and 6h, with a steady increase from 6 to 24h. The subsequent SEM imaging of these samples showed a similar slow increase between 3 and 6h, with a steady increase between 6 and 12h, and a slight slowdown from 12 to 24h.

Due to the fact that the role of the culture medium and the protein conditioning film are often overlooked in the microbiological assessment of biomaterial surfaces, this study aimed to be a preliminary assessment of these effects within the parameters of this work^[349]. The research conducted by Lorite *et al.* (2011) indicated that the presence of phosphate groups upon the substrate (present on the protein conditioning film) was more relevant in the facilitation of bacterial cell adhesion than surface roughness or hydrophobic surface properties^[349]. These findings are consistent with the work conducted by Monds *et al.* (2009) and Wolfe *et al.* (2003) which investigated the role of phosphate groups as a regulator during the secretion of surface proteins by bacterial cells, which are essential for adhesion and biofilm formation^[350, 351].

It is also possible to utilise proteins bound to a surface to induce an antibacterial effect. This can be done through the utilisation of a network of sensory transduction proteins, such as in the case studied by Ruiz *et al.* (2019). In this work, proteins discovered to be involved in the control of the bacterial transition from an unattached into a sessile state, were utilised to control the bacterial attachment decision. A potent developmental inhibitor (HfiA) of a

secreted adhesin which enables permanent bacterial cell attachment to surfaces was successfully utilised to limit this attachment upon a substrate^[352].

Another approach to use of proteins to elicit antibacterial properties on a substrate surface was studied by Solanki *et al.* (2013), where enzymes (*Listeria* bacteriophage endolysin Ply500) immobilised on a surface of silica nanoparticles. These surfaces, upon subsequent investigation, were found to be effective in killing of bacterial cells^[353]. Further work by Li *et al.* (2019) confirms the possible efficacy of such an approach in biomaterials^[354].

The generated results from both tests were normalised (see Figure 21C) and no statistically significant difference between CLSM and SEM image analysis at any time point was seen. This proved the validity of SEM approach for quantifying the bacterial growth on flat surfaces. However, at the SEM approach has a limitation in that once bacterial cells begin to multiply, and form colonies that are more than one cell deep, this method begins to undervalue the bacterial coverage. This is because it analyses the coverage in a 2D manner, not accounting for 3D structures on the surface.

The bacterial growth curve is extensively studied^[104]. The growth begins slowly in the initial stages, followed by relatively fast growth as the bacteria begin to replicate followed by a plateau as the incubation time progressed. In this study, the stationary phase of the growth curve was reached to avoid the limitation of the SEM approach. The results seen in this study, by both methods of analysis, fit this pattern of general bacterial colony growth^[355].

Importantly, this study provided the first confirmation that SEM image analysis could indeed be used in the bacterial burden analysis of flat surfaces. Further to this, it provided initial data to which any subsequent results could be referred to in order to verify the method's results' reproducibility since polished Ti samples will be included in all consequent studies.

The positive growth trend in bacterial presence on polished Ti samples between 3h and 24h confirms that studies up to 24 hours will give relevant results, and that judging by the slow growth between 0h and 3h, that studies under 3h may not hold much value in this case.

The difference in patterns seen between the two methods at the 12-24h timepoints (in that the SEM method showed no statistically significant increase between these two datapoints, whereas the CLSM assessment did indeed show such increase) is most likely due to the fact that biofilm was forming on the surfaces between the two timepoints. The SEM method was not able to account for this, whereas the CLSM analysis was able to measure this more accurately. For this reason, future assessments using SEM image analysis do not go beyond 12h. After this time, in the tested set-up of the SEM method, CLSM may prove to be a more reliable method of bioburden quantification, until such time that the SEM method is modified so as to account for the 3D nature of biofilms or multi-layer bacterial colonies..

4.3.2.2 3 Hour Bioburden SEM and CLSM comparison study

The SEM image analysis method was further validated by conducting a 3h study into the bacterial cell attachment to treated surfaces in three different incubation media (FBS, TSB and protein pre-conditioned samples in TSB). This study was conducted at a single time point (3h) on polished and grit blasted tantalum and titanium discs, and copper coated titanium discs was used as a control group.

This experiment was performed, in addition for the need of further validation of the SEM image analysis method, due to the fact that biomaterials, and bacteria therein, are likely to encounter levels of protein in their environment upon implantation in a patient, and thereafter ^[340].

Across all sample types, when measured with both analysis methods, there was no statistically significant difference between the FBS and TSB media. The “PRE” cohort, on the other hand, allows for assessment of the bacterial presence once a protein layer is already present of the sample.

Both methods of analysis showed increased bacterial presence on surfaces of all sample types in the preconditioned cohort (PRE), compared to both “FBS” and “TSB” media. This effect was also seen in the negative control sample-copper coated titanium disks, most likely due to the fact that the antibacterial effect of copper is due to its release of copper ions ^[273]. The deposited protein

layer would be anticipated to create a physical barrier between the copper surface, its environment and bacterial cells. It was hypothesised that this protein layer may affect the antibacterial effects of copper in four ways; firstly, the film may act as a simple barrier preventing direct contact between bacterial cells and the antibacterial surface and allowing them to attach unhindered. Secondly, the protein may provide bacterial cells with recognisable attachment sites, allowing for faster attachment to a familiar “biological” surface. Thirdly, the protein film may prevent the aqueous media from coming into contact with the copper surface, thus preventing the production and subsequent leaching of copper ions from it. Lastly, the film may act as a diffusion barrier, slowing the rate of copper ion release from the surface into the surrounding environment. A combination of the aforementioned factors is likely to be responsible for the significant increase in the preconditioned copper coated samples.

All other sample types have also shown a marked increase in the preconditioned cohort, compared to their “FBS” and “TSB” counterparts. This trend suggests that the familiarity of the protein film on the surface plays an important role in bacterial cell attachment on these surfaces, as none of these sample types release bactericidal ions ^[356].

Overall, the trends seen in this study, with use of both analysis methods, show that the copper-coated titanium disks have the lowest bacterial presence on their surface after 3h, followed by polished tantalum, then polished titanium, which in turn is succeeded by grit blasted tantalum, with grit blasted titanium

showing the highest presence, in both “FBS” and “TSB” media. All differences are statistically significant ($P < 0.0152$). However, in the “PRE” cohort, while the trend between surface treatments (Cu-coating, polishing and grit-blasting) remain, there is no statistically significant difference between titanium and tantalum counterparts from each surface type. There is one exception to this, namely- polished tantalum disks and copper coated titanium showing no statistically significant difference between them in the “TSB” cohort when analysed using SEM image analysis. However, the error of the polished tantalum data set in this instance is significant ($p < 0.5$), therefore no conclusions shall be drawn from this.

The trends observed in the pre-conditioned data, with both analysis methods, set show that copper coated titanium still has the lowest bacterial presence on its surface from all sample types in this cohort, followed by both polished tantalum and titanium, with grit blasted tantalum and titanium showing the highest presence. In this cohort, there is no statistically significant difference between respective tantalum and titanium samples.

The difference in bacterial burden on the surfaces of polished and grit-blasted disks (Ti and Ta alike) is likely due to the combination of increased surface of grit-blasted samples, as well as the fact that a rough surface provides more secure attachment sites for bacteria. The former variable (increased surface area) simply increases the amount of surface on to which a bacterial cell may

attach, and the amount of surface imaged. These would inherently increase the results from these samples in both the SEM and CLSM analyses.

The latter variable would become more prominent in a dynamic fluid culture medium scenario, such as the one present in this study, where bacterial cells are subjected to fluid turbulence of their environment due to the movement of the culture medium during incubation. Rough areas provide more surface on to which a single cell can attach, such as a crevice or an angled surface, therefore preventing itself from being detached by the fluid turbulence during the initial attachment to the surface- similar to the effect of turbulence on bacterial adhesion described by Mikkelsen *et al.* (2001)^[357].

The SEM image analysis method was again validated against the CLSM method, see Figure 23. The results show that out of 15 data sets, only two were statistically significantly different between the two methods. Namely; the grit blasted titanium samples incubated in “TSB” media and imaged by CLSM show lower bacterial presence on their surface than when analysed using SEM. Polished titanium disks incubated in “TSB” media also show a slightly lower bacterial presence when imaged using CLSM, as opposed to SEM image analysis.

There was no statistically significant difference between the normalised values resulting from CLSM and SEM image analysis methods. This, alongside the 24h study, confirmed that SEM image analysis would be a viable alternative to

CLSM when assessing bacterial cell presence on the surface of flat samples at short time points (up to 12h).

The next chapter builds on the SEM image analysis method, and concerns studies of the effect of a protein conditioning film on bacterial coverage, both on flat and scaffold samples.

Chapter 5 Effect Of A Protein Conditioning Film Upon Substrate Surface On Bacterial Cell Presence

This chapter describes studies conducted to investigate the effect of protein presence on bacterial coverage and growth upon flat and three-dimensional samples. All microbiological results described herein are obtained using the SEM image analysis method.

There has been work conducted to investigate the effect of protein on bacterial behaviour^[358-361]. Despite this, the sheer number of different proteins and species of bacteria, mean there are inevitable gaps in our understanding of this effect. Molecule dynamics dictate that upon *in vivo* placement of devices, they are exposed to considerable concentrations of protein^[362, 363], these are assessed in this study. As is the effect this conditioning film would have on the efficacy of proven antibacterial agents upon the sample surface.

Copper has widely documented antibacterial and bactericidal properties, as does iodine^[264, 364-368]. The former works by the release of copper (II) ions in solution, and the latter works by a similar mechanism of releasing Iodine ions^[369-371].

Magnesium has shown some initial promise in numerous biomedical application studies^[372-375], due to its low corrosion resistance and the fact that it occurs naturally in bone^[376-378]. An *in vivo* investigation conducted by Witte *et al.* (2005) showed that, when compared with a biodegradable polymer (self-reinforced poly-96L/4D-lactide), magnesium alloy devices showed greater osseointegration with an increased bone mass surrounding the devices^[379]. As magnesium provides an opportunity for a bioresorbable metallic device, and its mixture with calcium has also shown potential in osseointegration, as reported by Stroganov (1972), both a pure Mg coating, and an MgCa coating are assessed in this study^[380].

Samples for the following studies have been chosen to result in a cross-sectional investigation of surface chemistries and topographies which are used as metallic orthopaedic devices, and how adsorption of proteins to them may affect bacterial cell presence. A protein-rich media was used for the process of protein conditioning, in order to ensure the surfaces would be subjected to a variety of proteins, of differing sizes, as an analogue for the nature of an environment the devices would encounter *in vivo*. Many of the sample types in both studies are identical to the ones used in Chapter 4, in order to provide a

continuous evaluation of the repeatability of results obtained by use of the SEM image analysis method.

Work such as that conducted by Yu *et al.* (2019), Wang *et al.* (2019) and Wang *et al.* (2015) describes the considerable efficacy of using copper (both as substrate or coating) in a clinical, orthopaedic application^[381-383]. The lattermost study, for instance, showed an increase in antibacterial properties of a surface at *c.a.* 70% after coating with copper.

Studies undertaken by Inoue *et al.* (2019) and Wu *et al.* (2019) show that the Iodine presence upon tested samples did indeed significantly limit the bacterial cell attachment to the devices tested^[384, 385]. In these cases, the Iodine existed as a coating.

Ti6Al4V and Tantalum were investigated by Shi *et al.* (2017), Das *et al.* (2020) and Olmos *et al.* (2020) and were found to have no inherent antibacterial properties^[386-388].

5.1 Materials and Methods

The samples used in this study include the disks studied in previous chapters, as well as disks coated with Magnesium, PPS Iodine and Magnesium with Calcium additive (Figure 25). These were made by coating Ti6Al4V disks. These disk samples were coated with elemental copper through sputtering- a Physical Vapour Deposition (PVD) process whereby a thin film is deposited

using ejected materials from a target onto a substrate. They were supplied by Dr. Reda Felfel, a supervisor to this work, and were selected due to the potential antibacterial properties of magnesium^[389-391]. Calcium was added to the fact that it encourages bone formation, and as such it would be likely to be present in a clinical setting if magnesium was present as a coating^[392-394].

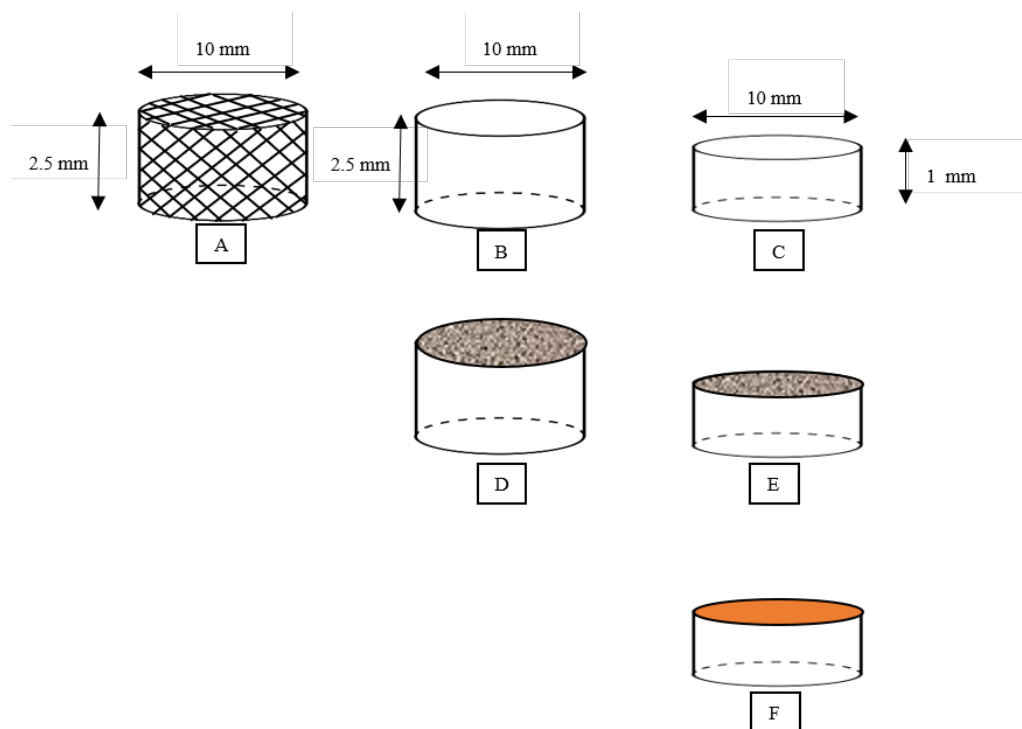


Figure 24: Schematic outline diagrams of sample types. A. shows Ti6Al4V and Tantalum 3D scaffolds (Osseo-Ti and Trabecular Bone respectively). B. shows polished Tantalum and Ti6Al4V disks. C shows Ti6Al4V disks coated with Magnesium and Magnesium-Calcium. D shows grit-blasted Tantalum and Ti6Al4V disks. E shows anodised and Iodine-treated Ti6Al4V disks. F shows copper-coated Ti6Al4V disks.

5.1.1 Characterisation

5.1.1.1 SEM surface topography assessment

SEM imaging of sterile samples was conducted using an identical protocol to that outlined in Chapter 2:

“Surface topography was assessed using SEM imaging in the Secondary Electron (SE) detection setting. Micrographs were obtained using a FEI XL30 Scanning Electron Microscope. A working distance was maintained between 10.0 and 11.0mm utilising a beam energy of 20kV.”

5.1.1.2 XPS surface analysis

XPS analysis was conducted on polished samples (copper-coated Ti, Ti and Ta disks) which had been left in FBS media for 2h, in order to allow ample time for protein adsorption, and subsequently washed in deionised water to remove any remaining liquid media. The testing was done in triplicate. The XPS analysis protocol is identical to that utilised in Chapter 2:

“X-ray Photoelectron Spectroscopy (XPS) analysis was done using a VGESCALab Mark II X-ray photoelectron spectrometer with a monochromatic Al K α X-ray source incident to the sample surface at 30°. Survey and high-resolution scans were conducted. A measurement of adventitious C 1s was taken for calibration, and consequently the charge was

corrected to 284.8 eV. The parameters during acquisition were: number of scans set at 5, step size of 1.0; dwell time 0.2 s (survey scans), and 0.4 s (high-resolution scans). Binding energies were measured over a range of 0–1200 eV. Casa XPS was used for spectrum analysis, constraining the Full Width at Half Maximum to the same value for all de-convoluted spectral peaks of the same element.”

5.1.2 Protein conditioning film establishment

The protein conditioning film was established on the surface of samples prior to inoculation with bacteria, but after sterilisation. Samples were placed in pure Foetal Bovine Serum for 2 hours, after which they were transferred into their respective petri dishes ready for inoculation and incubation. It was a working assumption of this work that the film was established, though the presence of protein was confirmed using XPS on the surface of protein-conditioned samples.

5.1.3 Bacterial seeding and incubation

The bacterial seeding and incubation process followed the same protocol as outlined in Chapter 3:

All samples were sterilised by immersion in 70% ethanol for 2 hours followed by drying under UV light overnight in a sterile fume hood.

Bacteria was taken from cold storage and transferred into liquid Tryptic Soy Broth (TSB) media, in order to obtain active bacterial cells. An *S. aureus* Newman strain was used, with a green fluorescent protein (GFP) gene inserted into a plasmid containing a Chloramphenicol (Cm) resistance gene. To preserve this gene, the culture was grown on agar containing Cm. In order to obtain the starting culture, a single colony of *S. aureus* was lifted from the agar plate and incubated in TSB media at 37°C and 200 RPM overnight. The overnight culture was washed twice in TSB prior to being used to inoculate the petri dishes.

Sterile samples were placed into a petri-dish, in triplicate, containing 20 ml of warm (37°C) TSB media. The optical density (OD₆₀₀) of the starting culture was measured using a spectrophotometer (Jenway 6715 UV/Vis) and the suspended bacteria were placed into the petri-dishes to give a starting OD₆₀₀ of 0.1. 1 µg/mL of Cm was added to the culture media in order to ensure the preservation of the GFP gene for the duration of the experiment. Three repeats of each sample type were not inoculated to serve as controls. The samples were then incubated at 37°C and 60 RPM for a set amount of time, after which they were removed and washed thoroughly with deionised water (dH₂O) by vigorous agitation three times.”

5.1.4 SEM microbiological assessment

The SEM bacterial presence analysis procedure was the same as that used in Chapter 4:

Samples were incubated and washed as per protocol outlined in Section 4.1.2, and fixed for SEM using a modified human cell fixation protocol using 3% Glutaraldehyde to result in longer dehydration times using ethanol.

Micrographs were obtained using a FEI XL30 Scanning Electron Microscope, in the Secondary Electron (SE) detection setting. A working distance was maintained between 10.0 and 11.0 mm, utilising a beam energy of 20 kV and magnification of x2500. Three measurements were taken from the surface of each triplicate sample.

False colouring and conversion to binary images was done using a modified version of open source software GIMP 2.8.14.

This method involved taking SEM images at fixed magnification and working distance, and through a series of steps which created a pixel map over the location of bacterial cells, converting them into binary images, as white bacterial cells in a black background. The white pixels were then counted, and a percentage area was calculated to quantify the bacterial cell coverage in a given image.

$$\text{Bacterial area coverage} = \frac{a}{a + b}$$

Where a = number of white pixels, and b = number of black pixels.”

5.2 Results

5.2.1 XPS analysis

The presence of nitrogen, which was used as the indicator of protein surface adsorption, was detected on all three tested samples (Figure 26). The nitrogen composition values ranged from 10.25wt% on Ta, to *circa* 13.0wt% on CuTi and Ti samples. The two most abundant elements in the conditioning film composition were carbon and oxygen; on CuTi the values were 35.4wt% and 33.8wt% respectively, on Ta they were 31.6wt% and 31.1wt% respectively and Ti had 32.1wt% and 46.8wt% respectively.

Chlorine was also detected on all samples, with 6.1wt%, 30.0wt% and 5.1wt% on CuTi, Ta and Ti disks respectively, as was sodium (3.7wt%, 4.4wt% and 3.0wt% respectively) (Figure 26). Sulphur was present in on the surfaces of CuTi and Ta (1.1wt% and 0.8wt% respectively), though it was not present on Ti. The surface composition of the film upon a Ta substrate contained 0.9wt% Co; and 6.6wt% of copper was detected on the CuTi surface.

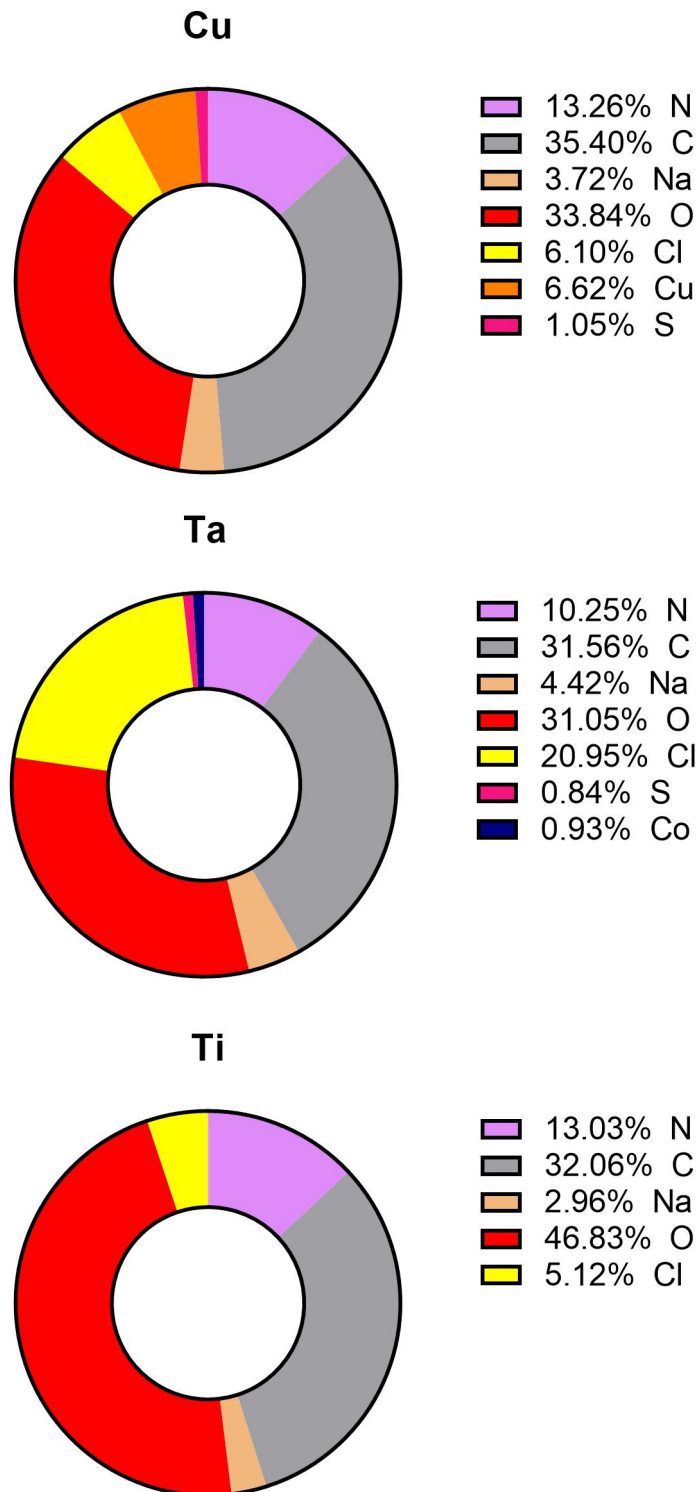


Figure 25: Chemical composition as measured by XPS and taken from the surface of disk samples which have been conditioned with protein by immersion in Foetal Bovine Serum. 'Cu' is a polished, Cu-coated Ti6Al4V disk. 'Ta' is a polished tantalum disk sample. 'Ti' is a polished Ti6Al4V disk.

5.2.2 12 hour Bioburden SEM Study

Once the SEM image analysis method had been validated, a 12h-long study was conducted to compare the effect of a protein conditioning film on 3D scaffolds against flat disks, the results of which were obtained using SEM. Readings were taken at 3h, 9h and 12h (Figure 27). 12h was chosen to attempt to conclude the experiment in the log phase of the bacterial growth curve. The time points of 3h, 9h, and 12h were chosen to attempt to take readings at the lag phase, the beginning of the log phase and further in the log phase respectively.

Although the copper-coated titanium disks showed the lowest bacterial cell coverage at every time point (Table 4), this effect was markedly more significant in the samples which were not pre-conditioned with protein. The pre-conditioned copper coated samples, although still displaying lower bacterial cell presence on their surface when compared to other pre-conditioned samples, had a reading similar to those observed on non-pre-conditioned polished tantalum.

TSB									
	CuTi	PTi	PTa	Gta	Gti	3DTa	3DTi		
3h	0.042% ± 0.004	0.154% ± 0.064	0.125% ± 0.043	0.258% ± 0.039	0.372% ± 0.068	0.507% ± 0.065	0.539% ± 0.072		
9h	0.240% ± 0.051	0.559% ± 0.114	0.450% ± 0.102	1.006% ± 0.090	0.992% ± 0.217	1.491% ± 0.098	1.480% ± 0.342		
12h	0.709% ± 0.199	1.280% ± 0.321	1.141% ± 0.309	2.478% ± 0.410	2.546% ± 0.394	3.348% ± 0.444	3.514% ± 0.429		
PRE									
	CuTi	PTi	PTa	Gta	Gti	3DTa	3DTi		
3h	0.108% ± 0.026	0.223% ± 0.080	0.204% ± 0.071	0.532% ± 0.054	0.553% ± 0.056	0.684% ± 0.031	0.696% ± 0.047		
9h	0.476% ± 0.060	0.560% ± 0.116	0.450% ± 0.092	1.511% ± 0.207	1.407% ± 0.156	2.110% ± 0.254	2.036% ± 0.200		
12h	1.391% ± 0.099	0.210% ± 0.201	1.342% ± 0.192	3.098% ± 0.338	3.213% ± 0.519	4.079% ± 0.315	4.395% ± 0.366		

Table 4: Bacterial presence on the surface of flat samples as measured by Scanning Electron Microscopy (SEM) micrograph coverage analysis. CuTi is a Copper-coated, polished Ti6Al4V disk, PTa and PTi are polished Tantalum and Ti6Al4V disks respectively, and Gta and GTi are grit-biased Tantalum and Ti6Al4V disks respectively. 3DTa and 3DTi are Trabecular Metal (Tantalum scaffold) and OsseoTi (Ti6Al4V scaffold) respectively. TSB samples were incubated in Tryptic Soy Borth media, and inoculated with *S. aureus*; and PRE samples were left in pure Foetal Bovine Serum prior to transfer into Tryptic Soy Broth media for inoculation and incubation.

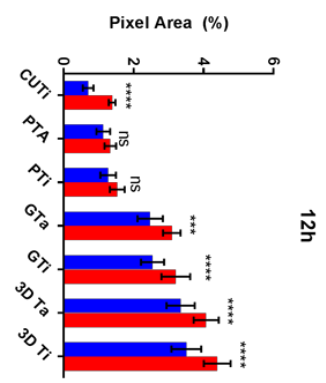
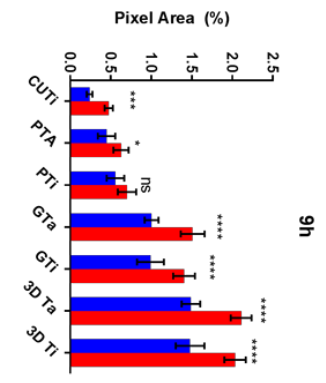
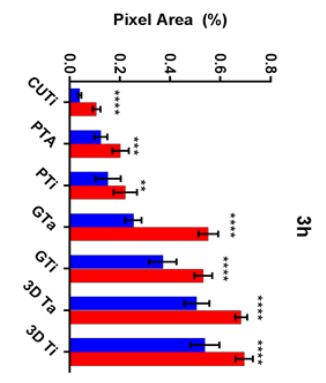
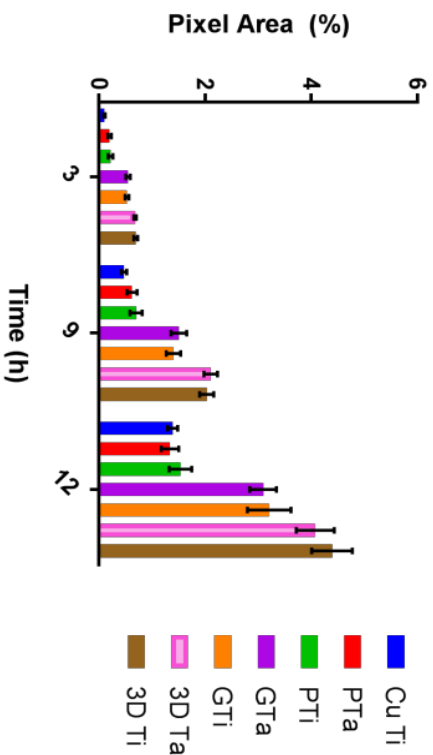
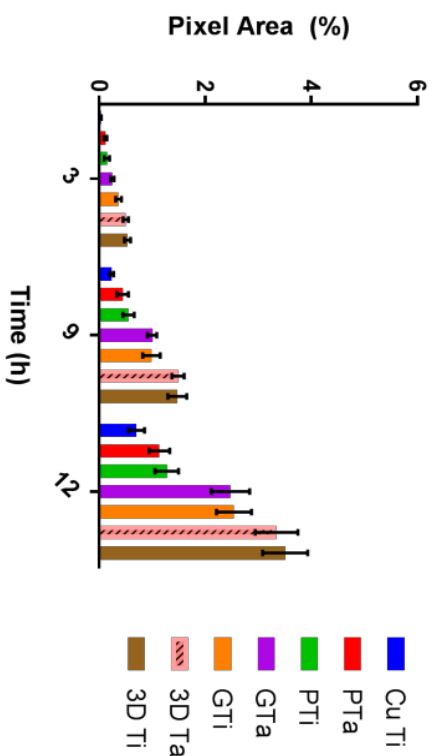
The polished samples showed the lowest pixel area coverage, followed by grit-blasted samples, with scaffolds showing the highest values in both pure TSB and pre-treated cohorts (Table 4), however there was no statistically significant difference between the titanium and tantalum samples in corresponding surface topography and treatment data sets.

The pre-treated cohort showed statistically significantly higher values at every time point and sample type, compared to pure TSB, except in the cases of polished titanium at 9h and 12h, and polished tantalum at 12h.

At the 3h timepoint, all samples with a protein conditioning layer (PRE group) had statistically significantly higher pixel area coverage values compared to the equivalent TSB samples.

This trend continued in the 9h timepoint, with the exception of polished Ti disks samples, where no statistically significant difference was present between the PRE and TSB cohorts.

At 12h 2 groups of samples (polished Ta and polished Ti) showed no significant difference between their PRE and TSB groups, however all other sample types did.



Effect Of A Protein Conditioning Film Upon Substrate Surface On Bacterial Cell Presence

Figure 26: Bacterial surface coverage as measured by the SEM analysis method at 3, 9 and 12h timepoints. 'TSB' shows the cohort of samples which was incubated in pure TSB media after inoculation with *S. aureus*. 'PRE' is a cohort of samples which has been pre-conditioned with protein by immersion in Foetal Bovine Serum prior to inoculation. 'Cu-Ti' are polished, Cu-coated Ti6Al4V disks, 'PTa' and 'PTi' are polished tantalum and Ti6Al4V disks respectively. 'GTa' and 'GTi' are grit-blasted tantalum and Ti6Al4V disk samples respectively. '3DTi' is a 3D Ti6Al4V scaffold sample (Osseo-Ti). '3DTa' is a 3D tantalum scaffold (Trabecular Bone). The topmost graphs show segmentation by incubation method. The bottom graphs show the bacterial coverage by timepoint.

5.2.3 Iodine Bioburden SEM Study

The effect of a protein conditioning film on bacterial adhesion to the samples, including those with those potential antibacterial properties, was investigated with a 12h-long study. Timepoints were taken at 3h, 6h, 9h and 12h (Figure 28). These were selected to provide readings at the lag phase, and the progress into the log phase respectively.

The full results from this study, in the TSB and PRE cohorts can be seen in Tables 1 and 2 respectively. The pixel area coverage increased with time in all sample types.

In the TSB cohort (Table 5), at 3h, there was no statistically significant difference in the pixel area coverage values of copper-coated Ti disks and grit-blasted Iodine-treated Ti samples (Figure 31)($p>0.7$). These disks did, however, have significantly lower coverage values than MgCa and Mg samples ($p<0.3$), as well as polished Ta and Ti ($p<0.1$). There was no difference between the coverage on the lattermost two aforementioned samples and PPS Iodine disks ($p>0.7$). Grit-blasted Ta had a higher bacterial presence than PPS ($p<0.2$), but lower than grit-blasted Ti disks ($p<0.05$). Apart from these samples, no other sample type had a significant difference between the Ta and Ti samples. Three-dimensional Ta and Ti scaffolds had higher coverage values than any other sample type at this timepoint ($p<0.005$) (Figure 31).

At 6h, there was no difference between the CuTi and grit-blasted Iodine disks ($p>0.05$) (Figure 31). These did, however, had lower coverage values than MgCa and Mg ($p<0.1$), between which there was also no statistically significant difference ($p>0.6$). Polished Ta samples had a higher coverage than the aforementioned surfaces ($p<0.05$), but significantly lower than that observed on polished Ti ($p<0.01$). There was no difference between grit-blasted samples ($p>0.5$); and those were higher than PPS Iodine samples ($p<0.01$) and higher than lower than 3D scaffolds ($p<0.01$) (Figure 31).

CuTi samples at 9h had significantly lower pixel area coverage than grit-blasted Iodine samples ($p<0.2$) (Figure 32). There was no difference between the latter disks and MgCa and Mg samples ($p<0.6$), while the polished Ta and Ti had higher coverage values than these disks ($p<0.05$). Grit-blasted Ta surfaces had values higher than PPS Iodine samples ($p<0.005$), though there was no difference between them and grit-blasted Ti ($p>0.5$) (Figure 32).

At 12h, CuTi had the lowest coverage value ($p<0.1$), with grit-blasted Iodine having significantly higher values than Mg, MgCa and polished Ti and Ta ($p<0.2$) (Figure 32). There was no difference between PPS Iodine samples and grit-blasted Ta and Ti.

In the PRE cohort (Table 6), at 3h, there was no statistically significant difference between copper-coated Ti disks and grit-blasted iodine-treated Ti disks ($p>0.5$) (Figure 29), though these two samples had significantly lower coverage than polished Ti, Ta, Mg and MgCa disks ($p<0.05$). PPS Iodine disks

had significantly higher coverage than polished samples ($p < 0.02$), though lower values than grit-blasted Ti and Ta disks ($p < 0.01$). There was no statistically significant difference between Ti and Ta of a given surface type at this time point ($p > 0.6$) (Figure 29).

At 6h there was no difference between the coverage on CuTi, GB I, MgCa and Mg disks ($p > 0.8$), though these had values statistically significantly lower than those of polished Ta and Ti ($p < 0.4$) (Figure 29). PPS I disks had a higher value than polished samples ($p < 0.2$), but lower than grit blasted Ti and Ta ($p < 0.3$). There was no difference between Ta and Ti samples of the same type at this timepoint ($p > 0.6$).

At the 9h timepoint there was no difference in the coverage on CuTi and GB I surfaces ($p > 0.7$), and these samples had statistically significantly lower values than polished Ti, Ta, Mg and MgCa samples (highest p value was: $p < 0.3$) (Figure 30). PPS I samples had a lower bacterial presence than grit-blasted Ta and Ti ($p < 0.05$), but higher than polished samples ($p < 0.05$). Once again, there was no difference between Ta and Ti samples of the same surface type ($p > 0.7$).

There was no statistically significant difference between the pixel area coverage at 12h on CuTi, GB I, MgCa, Mg, PTa and PTi samples ($p > 0.7$).

There was also no significant difference in the values of PPS I, GTa and GTa ($p > 0.6$), though these were lower than the coverage on three-dimensional Ta

and Ti scaffolds ($p < 0.1$). There was no difference between Ta and Ti samples of a given surface type at this timepoint.

At 3h, all samples had a statistically significantly higher pixel area coverage in the PRE cohort compared to corresponding sample type in the TSB group (highest p value: $p < 0.3$) (Figure 28). This trend held true at the 6h timepoint, where all samples showed an increased coverage in the PRE dataset (highest p value: $p < 0.3$), with the exception of polished Ti disks, where there was no statistically significant difference between the two groups ($p = 0.7815$). At 9h, only one sample type had no increase between TSB and PRE cohorts- polished Ti disks ($P = 0.7044$), other types had a highest p value of $p < 0.1$. Two sample types at 12 hours showed no significant difference between the TSB and PRE cohorts (grit-blasted Iodine treated Ti disks ($P > 0.9999$) and polished Ta disks ($P = 0.6398$), with all other sample types showing an increased pixel area coverage in the PRE group (highest p value: $p < 0.3$).

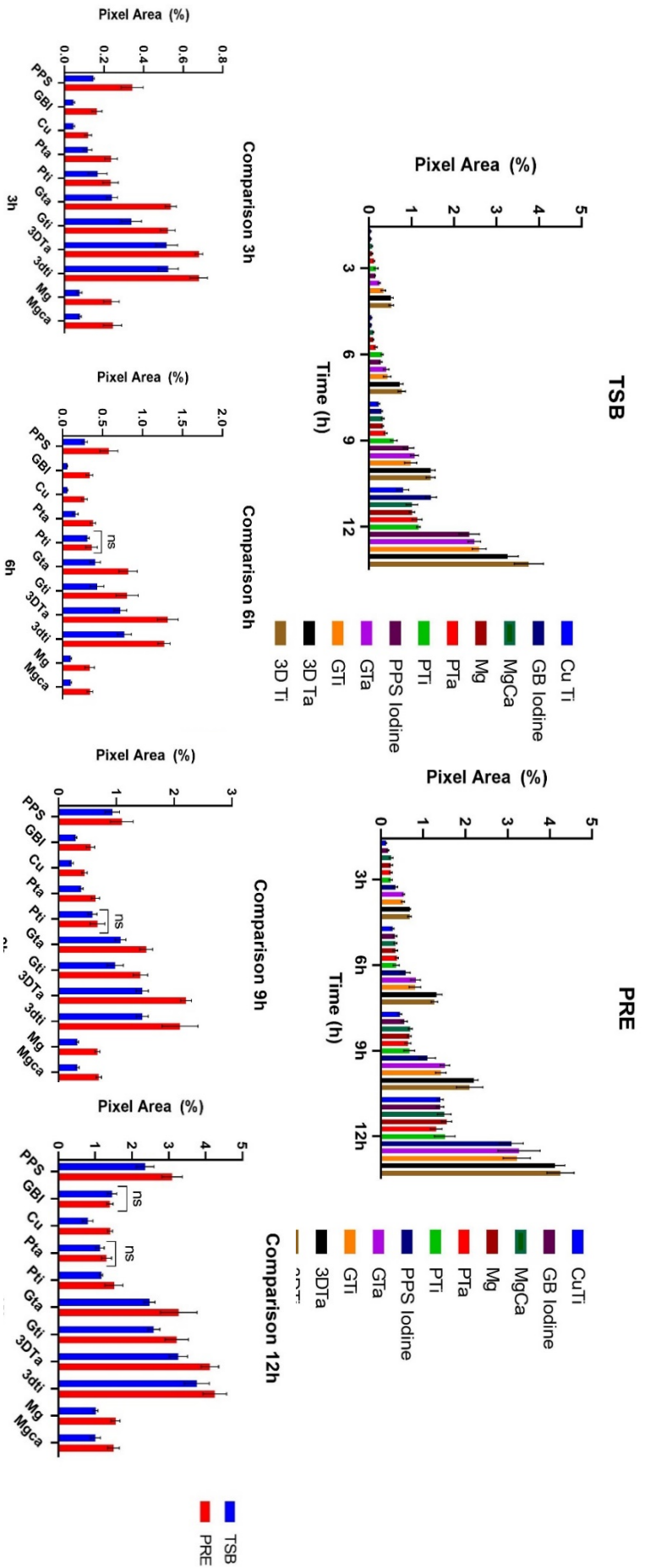


Figure 27: Bacterial surface coverage as measured by the SEM analysis method at 3, 6, 9 and 12h timepoints. 'TSB' shows the cohort of samples which was incubated in pure TSB media after inoculation with *S. aureus*. 'PRE' is a cohort of samples which has been pre-conditioned with protein by immersion in Foetal Bovine Serum prior to inoculation. 'Cu-Ti' are polished, Cu-coated Ti6Al4V disks, 'PTa' and 'PTi' are polished tantalum and Ti6Al4V disks respectively. 'GB Iodine' are grit-blasted disks which have been treated with Iodine. 'MgCa' and 'Mg' samples are Ti6Al4V samples coated with a magnesium-calcium compound and magnesium only, respectively. 'PPS Iodine' are disks which have undergone PPS treatment with iodine. 'GTa' and 'GTi' are grit-blasted tantalum and Ti6Al4V disk samples respectively. '3DTi' is a 3D Ti6Al4V scaffold sample (Osseo-Ti). '3DTa' is a 3D tantalum scaffold (Trabecular Bone). The topmost graphs show segmentation by incubation method. The bottom graphs show the bacterial coverage by timepoint.

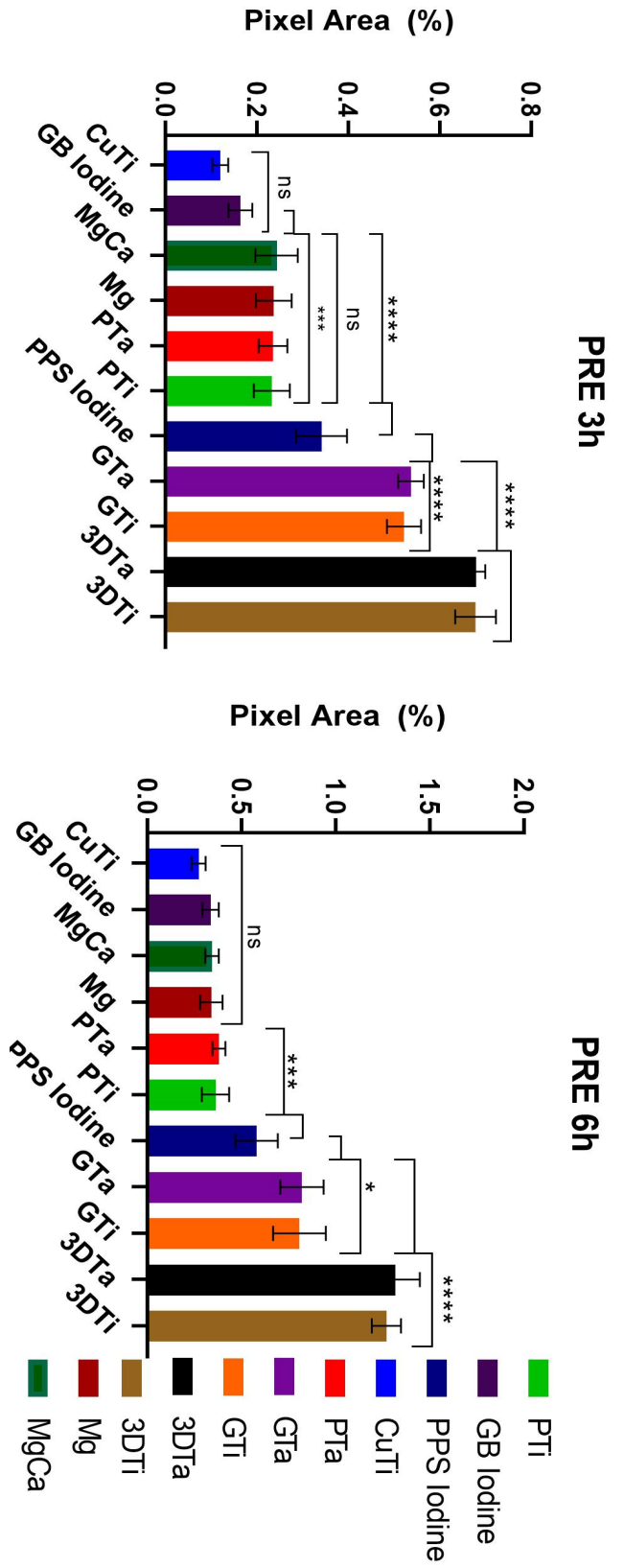


Figure 28: Bacterial surface coverage as measured by the SEM analysis method at 3 and 6h timepoints. 'PRE' is a cohort of samples which has been pre-conditioned with protein by immersion in Foetal Bovine Serum prior to inoculation. 'Cu-Ti' are polished, Cu-coated Ti6Al4V disks, 'PTa' and 'PTi' are polished tantalum and Ti6Al4V disks respectively. 'GB Iodine' are grit-blasted disks which have been treated with Iodine. 'MgCa' and 'Mg' samples are Ti6Al4V samples coated with a magnesium-calcium compound and magnesium only, respectively. 'PPS Iodine' are disks which have undergone PPS treatment with iodine. 'GTa' and 'GTi' are grit-blasted tantalum and Ti6Al4V disk samples respectively. '3DTi' is a 3D Ti6Al4V scaffold sample (Osseo-Ti), '3DTa' is a 3D tantalum scaffold (Trabecular Bone).

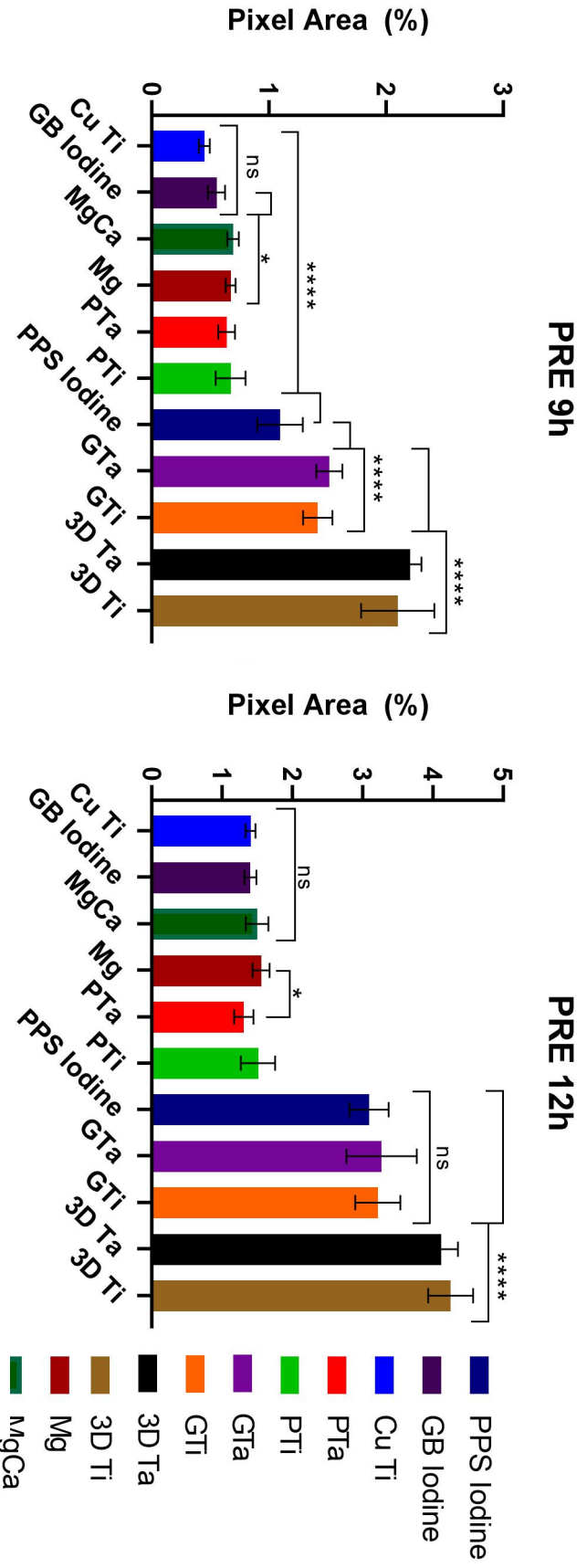


Figure 29: Bacterial surface coverage as measured by the SEM analysis method at 9 and 12h timepoints. 'PRE' is a cohort of samples which has been pre-conditioned with protein by immersion in Foetal Bovine Serum prior to inoculation. 'Cu-Ti' are polished, Cu-coated Ti6Al4V disks, 'PTa' and 'PTi' are polished tantalum and Ti6Al4V disks respectively. 'GB Iodine' are grit-blasted disks which have been treated with Iodine. 'MgCa' and 'Mg' samples are Ti6Al4V samples coated with a magnesium-calcium compound and magnesium only, respectively. 'PPS Iodine' are disks which have undergone PPS treatment with iodine. 'GTa' and 'GTi' are grit-blasted tantalum and Ti6Al4V disk samples respectively. '3DTi' is a 3D Ti6Al4V scaffold sample (Osseo-Ti). '3DTa' is a 3D tantalum scaffold (Trabecular Bone).

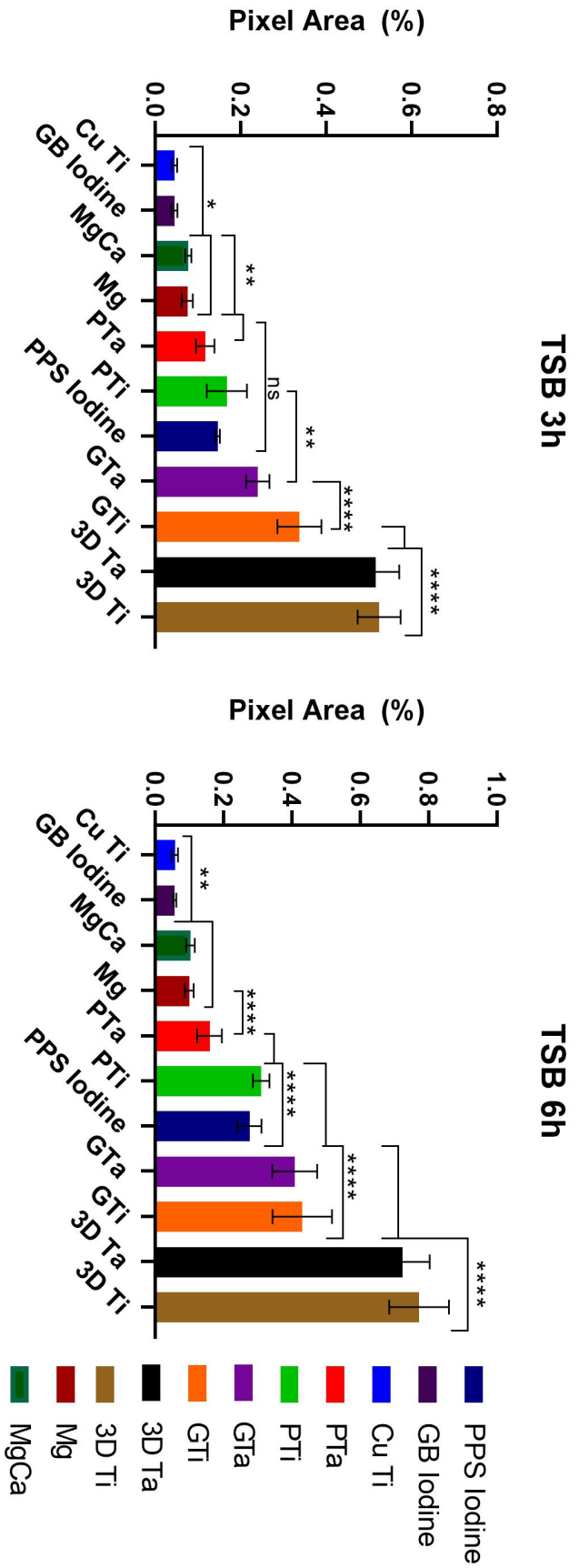


Figure 30: Bacterial surface coverage as measured by the SEM analysis method at 3 and 6h timepoints. 'TSB' is a cohort of samples which has not been pre-conditioned with protein, instead being inoculated with bacteria in pure TSB media. 'Cu-Ti' are polished, Cu-coated Ti6Al4V disks, 'PTa' and 'PTi' are polished tantalum and Ti6Al4V disks respectively. 'GB Iodine' are grit-blasted disks which have been treated with Iodine. 'MgCa' and 'Mg' samples are Ti6Al4V samples coated with a magnesium-calcium compound and magnesium only, respectively. 'PPS Iodine' are disks which have undergone PPS treatment with iodine. 'GTa' and 'GTi' are grit-blasted tantalum and Ti6Al4V disk samples respectively. '3DTi' is a 3D Ti6Al4V scaffold sample (Osseo-Ti). '3DTa' is a 3D tantalum scaffold (Trabecular Bone).

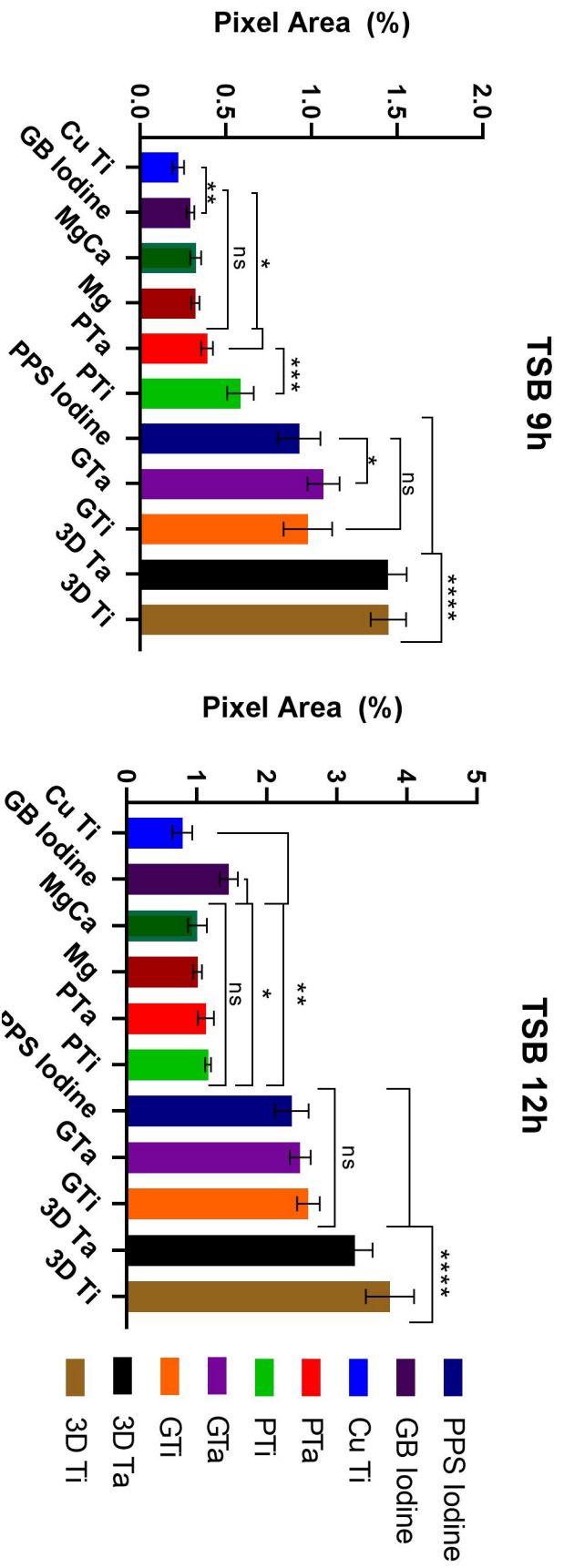


Figure 3.1: Bacterial surface coverage as measured by the SEM analysis method at 9 and 12h timepoints. 'TSB' is a cohort of samples which has not been pre-conditioned with protein, instead being inoculated with bacteria in pure TSB media. 'Cu-Ti' are polished, Cu-coated Ti6Al4V disks, 'PTa' and 'PTi' are polished tantalum and Ti6Al4V disks respectively. 'GB Iodine' are grit-blasted disks which have been treated with Iodine. 'MgCa' and 'Mg' samples are Ti6Al4V samples coated with a magnesium-calcium compound and magnesium only, respectively. 'PPS Iodine' are disks which have undergone PPS treatment with Iodine. 'GTa' and 'GTi' are grit-blasted tantalum and Ti6Al4V disk samples respectively. '3DTi' is a 3D Ti6Al4V scaffold sample (Osseo-Ti). '3DTa' is a 3D tantalum scaffold (Trabecular Bone).

TSB

	CuTi	GB Iodine	MgCa	Mg	PTa	PTi	PPS Iodine	GTa	GTi	3D Ta	3D Ti
3h	0.046% ±0.011	0.045% ±0.014	0.078% ±0.009	0.076% ±0.017	0.117% ±0.022	0.168% ±0.064	0.146% ±0.010	0.240% ±0.035	0.338% ±0.079	0.517% ±0.069	0.525% ±0.067
6h	0.058% ±0.011	0.057% ±0.008	0.104% ±0.020	0.100% ±0.017	0.159% ±0.048	0.310% ±0.040	0.276% ±0.046	0.409% ±0.087	0.431% ±0.102	0.723% ±0.097	0.773% ±0.120
9h	0.224% ±0.043	0.294% ±0.034	0.326% ±0.044	0.323% ±0.029	0.392% ±0.037	0.587% ±0.098	0.930% ±0.141	1.08% ±0.110	0.981% ±0.154	1.449% ±0.118	1.451% ±0.115
12h	0.798% ±0.223	1.460% ±0.184	1.012% ±0.206	1.016% ±0.100	1.132% ±0.199	1.165% ±0.053	2.361% ±0.307	2.481% ±0.238	2.599% ±0.250	3.265% ±0.311	3.762% ±0.374

Table 5: Table of bacterial surface coverage as measured by the SEM analysis method at 3, 6, 9 and 12h timepoints. 'TSB' is a cohort of samples which has not been pre-conditioned with protein, instead being inoculated with bacteria in pure TSB media. 'Cu-Ti' are polished, Cu-coated Ti6Al4V disks, 'PTa' and 'PTi' are polished tantalum and Ti6Al4V disks respectively. 'GB Iodine' are grit-blasted disks which have been treated with Iodine. 'MgCa' and 'Mg' samples are Ti6Al4V samples coated with a magnesium-calcium compound and magnesium only, respectively. 'PPS Iodine' are disks which have undergone PPS treatment with iodine. 'GTa' and 'GTi' are grit-blasted tantalum and Ti6Al4V disk samples respectively. '3DTi' is a 3D Ti6Al4V scaffold sample (Osseo-Ti). '3DTa' is a 3D tantalum scaffold (Trabecular Bone).

	<u>CuTi</u>	GB Iodine	<u>MgCa</u>	Mg	<u>PTa</u>	<u>PTi</u>	PPS Iodine	<u>GTA</u>	<u>GTI</u>	3D Ta	3D <u>Ti</u>
3h	0.120% ±0.021	0.165% ±0.030	0.243% ±0.063	0.237% ±0.057	0.236% ±0.041	0.233% ±0.059	0.342% ±0.081	0.538% ±0.035	0.522% ±0.062	0.681% ±0.038	0.679% ±0.079
6h	0.272% ±0.048	0.336% ±0.052	0.343% ±0.045	0.340% ±0.061	0.380% ±0.039	0.362% ±0.079	0.580% ±0.100	0.821% ±0.107	0.807% ±0.124	1.316% ±0.099	1.270% ±0.085
9h	0.450% ±0.039	0.553% ±0.049	0.695% ±0.035	0.673% ±0.033	0.641% ±0.051	0.674% ±0.074	1.097% ±0.148	1.517% ±0.058	1.419% ±0.072	2.208% ±0.061	2.101% ±0.286
12h	1.407% ±0.042	1.403% ±0.051	1.500% ±0.185	1.155% ±0.110	1.311% ±0.138	1.514% ±0.257	3.094% ±0.264	3.272% ±0.502	3.219% ±0.317	4.121% ±0.241	4.257% ±0.325

Table 6: Table of bacterial surface coverage as measured by the SEM analysis method at 3, 6, 9 and 12h timepoints. 'PRE' is a cohort of samples which has been pre-conditioned with protein by immersion in Foetal Bovine Serum prior to inoculation. 'Cu-Ti' are polished, Cu-coated Ti6Al4V disks, 'PTa' and 'PTi' are polished tantalum and Ti6Al4V disks respectively. 'GB Iodine' are grit-blasted disks which have been treated with Iodine. 'MgCa' and 'Mg' samples are Ti6Al4V samples coated with a magnesium-calcium compound and magnesium only, respectively. 'PPS Iodine' are disks which have undergone PPS treatment with iodine. 'GTA' and 'GTi' are grit-blasted tantalum and Ti6Al4V disk samples respectively. '3DTi' is a 3D Ti6Al4V scaffold sample (Osseo-Ti). '3DTa' is a 3D tantalum scaffold (Trabecular Bone).

5.3 Discussion

5.3.1 XPS analysis

The XPS analysis of these samples was conducted chiefly in order to confirm the presence of protein on the substrate surfaces. To this end, since all detected elements are found in various proteins, this was achieved. The absence of detection of elements present in the substrate chemistry (as ascertained in Chapter 2) on Ta and Ti disks suggests that the thickness of the protein conditioning film is greater than the depth resolution of XPS, and that this film is continuous since 3 measurements were taken on each surface.

The presence of copper on the CuTi sample, and considering it was present in all three scans, means that the protein film thickness on these samples was thinner, or not entirely continuous as it was on the aforementioned samples' surfaces. This will likely be due to the surface chemistry.

5.3.2 12 hour Bioburden SEM Study

Since the validity of SEM approach for the purposes of investigation bacterial presence upon surfaces was established, a 12h study was conducted on 2D flat and 3D scaffold samples. The effect a protein conditioning film on bacterial presence on the surfaces was also investigated. This is a subject present in literature, finding that surfaces pre-treated with protein did indeed display higher bacterial growth rates than those without^[395-398].

Bacterial cell coverage on the pre-conditioned samples with protein showed a significant increase when compared to the non-treated samples (the smallest increase was seen in CuTi samples between PRE and TSB cohorts at the 3 hour time point- 160% increase (0.046% to 0.120%, $p < 0.2$), with all other samples showing higher differences). This suggests that the greatest impact of the protein conditioning film was in the initial bacterial cell attachment, with diminished (yet still significant) with time effects. This suggests that this effect is most pronounced in initial bacterial attachment.

Similar to the 3h study, the copper coated titanium disks showed the lowest bacterial cell presence across all time points on the samples with no protein conditioning film, however this trend was not apparent in the preconditioned samples (in the PRE cohort, the coverage increased from $0.120 \pm 0.021\%$ at 3h to $0.272 \pm 0.0048\%$, $0.450 \pm 0.39\%$ and $1.407 \pm 0.042\%$ at 6h, 9h and 12h respectively, whereas the Polished Ti6Al4V disks had a coverage of $0.233 \pm 0.059\%$, $0.362 \pm 0.079\%$, $0.674 \pm 0.074\%$ and $1.514 \pm 0.257\%$ at those time points).

At all time points, the 3D scaffold samples displayed the greatest bacterial cell presence, compared to the disk samples (the coverage increase from the next highest sample type is an average (mean) of 87.2% in the TSB cohort and 35.9% in the PRE cohort). Considering the fact that grit blasted samples displayed the highest roughness, and thus surface area, the scaffold samples' increased bacterial presence may be due to the sheltering effect their structure provide ^[251]. The area of the scaffold where two or more struts meet also

provide the bacteria with an increased surface area to which they can attach, meaning they may find it easier to attach to.

Polished samples had the lowest bacterial cell presence on their surfaces, followed by grit blasted samples, in both the pre conditioned and pure FBS cohorts (Table 5 and Table 6), suggesting that the topography of the surface plays an important role as expected [399].

This study suggests that the roughness of the sample directly impacts the bacterial presence observed using the SEM image analysis method, and a similar relationship was documented by both Lu *et al.* (2020) and Chen *et al.* (2020), whereby the samples with higher roughness values contained more bacteria after inoculation and incubation^[400, 401]. The reason for this could be due to two possibilities, though is likely a combination of both working concurrently. Firstly, the surface area imaged upon analysis of grit blasted samples is inherently greater than that of polished samples. This is one of the limitations of this method outlined in Chapter 4. Secondly, the rough surface may be creating areas with reduced fluid turbulence which could aid in initial bacterial cell attachment.

At all cohorts the copper-coated Ti disks had the lowest bacterial presence on them, with the exception of the 12h PRE group, where the results were not statistically significantly different to those of polished Ta and Ti disks (1.407%± 0.042, 1.311%± 0.138 and 1.514%± 0.257 respectively) (p>0.8).

This suggests that the antibacterial effect owing to copper ions is indeed

pronounced in these samples, apart from scenarios where bacterial cells have had time to establish themselves on the protein conditioning film.

The protein adsorption resulted in significantly higher bacterial cell presence at every time point and sample type, with the exception of 3 (polished Ti at 9h, and polished Ta and Ti at 12h) (Table 5 and Table 6). This suggests that the bacteria do indeed find this conditioning film beneficial for either attachment or proliferation, with the former hypothesis being more likely since this effect is seen as early as in the initial 3h (coverage in PRE at $0.120\% \pm 0.021$, and in TSB at $0.046\% \pm 0.011$). This is supported by the literature^[395].

Scaffold samples have the highest coverage values of all samples, which may be due to the fact that the 3D structure provides ample attachment sites and protection from shear forces resulting from fluid media movement.

There was no difference between Ti and Ta samples of any type at any timepoint in this study (lowest p value of $p > 0.6$), insinuating that there is no inherent antibacterial effect in either of these substrate chemistries.

5.3.3 Iodine Bioburden SEM Study

A large cohort of samples was chosen for this study in order to observe any effect on surface chemistries with documented antibacterial properties. These samples include Iodine-treated samples, polished Ti samples coated with

copper, magnesium and a magnesium-calcium mixture. Iodine has well documented antibacterial properties^[384, 402, 403].

Likewise, copper has been widely observed to display antibacterial properties^[264, 364-368].

The results in this study which have also been reported in the aforementioned 12h investigation followed the same trends, in that in the TSB cohort CuTi samples had the lowest bacterial coverage at all timepoints when compared to polished, grit-blasted and tree-dimensional samples, with that trend continuing in the PRE cohort up to and including the 9h timepoint (highest p value: $p < 0.3$). At the 12h timepoint, much like in the previous study, the pixel area coverage values are not statistically significantly different between CuTi and polished Ti and Ta ($p > 0.6$).

Work conducted by Mauerer *et al.* (2017) supports these findings, as they reported a reduction in infected devices from 88% to *circa* 35% (total of 36 rabbits) when the device was coated with copper (statistically significant difference)^[404]. All of the devices in this study were inoculated with *S. aureus* prior to implantation.

Grit blasted Iodine samples, despite having a roughness comparable to the Ta and Ti grit-blasted samples, had a bacterial area coverage that was lower than polished samples' (up to and including 9h in the TSB group and 9h in the PRE group) (highest p value: $p < 0.3$). Their bacterial cell coverage was also equal to

that to the coverage observed on CuTi surfaces at all timepoints in the PRE cohort and up to and including 9h in the TSB cohort (lowest p value: $p>0.6$). In the TSB group at 9h, the GB Iodine samples had a higher coverage value than CuTi ($p<0.3$), but at 12h its bacterial coverage was significantly higher than all polished samples ($p<0.1$), and approaching the values seen on grit-blasted Ta and Ti.

The results of GB Iodine could be due to the rate of dissolution of Iodine from the samples' surfaces. The initial antibacterial properties of Iodine were most pronounced in the first half of the experiment in the TSB group, as the iodine was released from the sample in solution. However, as the amount of Iodine on these samples is finite, and confined to the inside of small pores, this effect showed signs of exhaustion at the 12h timepoint in this cohort. However, even after 12h, these samples had a significantly lower bacterial cell presence ($p<0.2$) than that observed on samples with comparable surface roughness (grit-blasted Ti and Ta). Over time it would be expected that although the initial effect is noted, viable bacteria still on the surface, albeit in lower numbers, would eventually proliferate (once the Iodine presence is exhausted) to the same levels as seen on other samples given enough time. As such, this may simply be a delaying characteristic.

The effect of Iodine in the GB-I samples is also apparent in the PRE cohort, where there is no statistically significant difference between CuTi and GB-I at any timepoint ($p>0.6$), which is noteworthy as the former has a lower surface

roughness. However, the relative release rates weren't measured, so no conclusions can be taken based on this fact alone.

A similar outcome of iodine treatment was evident in the PPS iodine samples. At 3h and 6h in the TSB group, these samples had the same bacterial cell coverage as polished Ti ($p>0.6$) (PPS Iodine at $0.146\% \pm 0.010$ and $0.276\% \pm 0.046$ at 3h and 6h respectively, whereas PTi was at $0.168\% \pm 0.064$ and $0.310\% \pm 0.040$), which is significant as PPS iodine samples had a surface roughness higher than grit-blasted samples. At 9h these had equal coverage to grit-blasted Ti ($p<0.8$), and slightly lower than grit-blasted Ta ($p<0.4$), and at 12h there was no statistically significant difference between PPS iodine and grit blasted Ti and Ta samples ($p>0.7$).

In the PRE cohort, PPS iodine samples higher coverage values than polished samples, but lower than grit blasted Ti and Ta, at 3h, 6h and 9h timepoints. At 12h, however, there was no statistically significant difference between the PPS iodine samples and grit-blasted Ta and Ti.

The fact that the iodine samples (both grit-blasted and PPS) have lower pixel area coverage than samples of equivalent surface roughness, signifies that this treatment does indeed exhibit some antibacterial properties. This effect is less pronounced but prolonged when tested with a protein conditioning layer. The limited aspect of it could be as a result of the reduced release rate due to the presence of protein providing a physical barrier to diffusion. However, this same protein film is likely responsible for the prolonged presence of this

effect, as it likely decreases the release of iodine into solution, *ergo* spreading this release over a longer period of time. An elution study to measure the Iodine release rates would be required to confirm this hypothesis. In both cases, with and without protein conditioning, this effect seems to reduce bacterial presence before 12h, after which the bacterial coverage increases rapidly.

Work conducted by Shirai *et al.* (2014) concluded that iodine treatment of devices reduced the Periprosthetic Joint Infection (PJI) incidence from 11.4%-14.8% to 0%-5% in a clinical setting^[405]. This is a significant reduction of infections. These findings were supported by results reported by Kabata *et al.* (2015), who found no incidence of infection in 30 patients with iodine-treated devices in the short term^[406]. Though they too concluded that the Iodine did likely provide most protection in the early stages of the device lifecycle^[406]. Since these were *in vivo* studies, meaning the samples would be subjected to protein adsorption, it is likely that the antibacterial properties of these devices was prolonged, based on the results seen in Section 5.2.3.

Magnesium-coated disks (both Mg and MgCa) with a protein conditioning film (PRE) had the same bacterial coverage as polished Ti and Ta disks at all timepoints ($p > 0.6$ in all cases). This suggests that these surfaces don't provide any innate antibacterial properties with adsorbed surface proteins.

In the TSB cohort, the magnesium-coated disks had a lower pixel area coverage than polished Ti and Ta samples up to and including the 9h timepoint (highest p value: $p < 0.3$), though statistically significantly higher than the grit-blasted Iodine-treated samples and copper-coated disks (highest p value: $p < 0.3$). At 12h, however, the bacterial cell coverage on the surface of these samples was the same as the values observed on the polished Ti and Ta disks ($p > 0.8$). This suggests that the magnesium-coated samples may indeed either prevent bacterial cell attachment or slow their proliferation on the surface, but that any such effect is limited to low bacterial growth and becomes negligible when the bacterial presence becomes well established.

In keeping with the results of the 12h study, all samples which were pre-conditioned with protein at the 3h timepoint had significantly higher bacterial coverage than they did without the protein film (highest p value: $p < 0.3$). In the case of CuTi, magnesium-coated Ti (Mg and MgCa) and grit-blasted Ta, the PRE cohort had more than double the TSB coverage values (the PRE cohort had coverages of $0.237\% \pm 0.057$, $0.243\% \pm 0.063$ and $0.538\% \pm 0.035$, for Mg, MgCa and GTa respectively, whereas the TSB cohort had coverages of $0.076\% \pm 0.017$, $0.078\% \pm 0.009$ and $0.240\% \pm 0.035$ respectively).

At 6h and 9h, all samples with the exception of polished Ti disks, had statistically significantly greater bacterial coverage in the PRE group than in the TSB cohort (highest p value: $p < 0.3$), and at 12h grit-blasted Iodine

samples and polished Ta disks showed no difference between these two groups ($p>0.6$).

This suggests that the positive effect of adsorbed protein on bacterial behaviour is most pronounced at the initial stages of a bacterial growth curve, with the effect diminishing (though still present) at later timepoints, hinting at a mechanism of enhancing bacterial cell coverage through facilitating a more beneficial surface for bacterial cell attachment.

The following chapter describes novel hybrid-scaffolds and their potential in the pursuance of obtaining antimicrobial characteristics within orthopaedic three-dimensional scaffolds without compromising the original scaffold's mechanical or bioactive properties. It then progresses to conclusions for the whole body of work, as well as the future work suggestions to follow.

Chapter 6 Metal-Polymer Hybrid Scaffolds

This chapter contains proof-of-concept studies concerning hybrid scaffolds (metal-polymer) and their potential in endowing orthopaedic devices with antibacterial properties without compromising their long-term bioactive or mechanical properties.

The interlinked porosity of metallic orthopaedic scaffolds used in this study presents an opportunity to utilise synergies originating in the use of such scaffold in conjunction with weaker, more bioactive or antibacterial polymer scaffolds. A device resulting from such an approach would benefit from the mechanical properties of an underlying metal “skeleton” scaffold, while taking advantage of properties lent to it by the polymer scaffold. Such a polymer scaffold could be modified to provide bioactivity (for example by addition of growth factors or substances such as hydroxyapatite to aid bone formation^{[407,}
^{408]}) or antibacterial properties (by addition of Cu or Ag ion complexes, or antibiotics), while the resorbable nature of materials like chitosan or poly-l-

lactic acid (PLLA) would ensure that the device *in vivo* after a period of time wouldn't have any larger a footprint than the original metal scaffold.

A proof of concept, therefore, was undertaken using commercially available Ti and Ta scaffolds which were tested throughout this piece of work. Chitosan was selected due to numerous studies reporting on its antibacterial properties and the relative ease with which it is formed into a scaffold^[409-413]. In addition to these studies, chitosan was found by Aksel et al. (2020) to be a viable platform to host antibiotics without losing their antibacterial properties^[335]. This approach would be able to enhance any inherent antibacterial properties of chitosan itself.

This study was conducted in order to determine if casting a chitosan scaffold within a metal scaffold is feasible and identify any limiting factors of such an approach. The effect of the metal scaffolds' pore size on the internal chitosan scaffold casting, as well as the interface of the two materials (where delamination was a possibility) were investigated. The study also aimed to investigate the effect of an added nanoparticle with known antibacterial properties into the chitosan scaffold would have on the synthesis of the hybrid scaffold.

Therefore, a chitosan scaffold was cast within each of the two commercially available metal scaffolds (Trabecular metal (tantalum) and Osseo-Ti (Ti6Al4V)), and the resulting sample investigated using SEM imaging to

ascertain the topography and the physical interface between the two constituent materials.

6.1 Materials and methods

6.1.1 Sample preparation

Samples were prepared by casting of chitosan scaffolds within the metallic scaffolds. Ti and Ta scaffolds were sonically cleaned in deionised water in order to remove any contaminants, after which they were placed in a chitosan solution and subjected to a vacuum within a syringe with manual force in order to remove any air from the sample and ensure full penetration of the solution.

The chitosan solution was prepared using a chitosan powder (Mw of 471 kDa) of 84% deacetylation (Weifeng Kenai Ltd, China), and glacial acetic acid from Sigma Aldrich (United Kingdom). A 2wt% chitosan solution was produced by dissolving 1.0g of chitosan powder in 50ml deionised water containing 1.25ml of acetic acid (at room temperature, with vigorous stirring of 500 RPM) for 15min. The solution containing 1wt% Ag nanoparticles was prepared using the same aforementioned process, with the addition of 1wt% Ag nanoparticles during the stirring phase. The resulting solution was covered with cling film

and left overnight in order to allow for the escape of any air bubbles trapped within during the dissolution process^[315].

Ti and Ta scaffolds placed in the solution and subjected to a vacuum, after which they were placed in a PTFE mould (10mm height, 10mm diameter) and topped up with the chitosan solution to result in full submersion of a metal scaffold, and subsequently transferred to a freezer (-20°C) and left overnight.

Once frozen, the samples were removed from the PTFE moulds and freeze-dried for 48h at -55°C using a Modulyo benchtop freeze dryer.

6.1.2 SEM imaging

The samples were imaged as per the protocol outlined in Chapter 2. The surface topography was assessed using SEM imaging in the Secondary Electron (SE) detection setting. Micrographs were obtained using a FEI XL30 Scanning Electron Microscope. A working distance was maintained between 10.0 and 11.0mm utilising a beam energy of 20kV.

6.2 Results

Both pure chitosan and chitosan-Ag scaffolds were successfully cast within both Ta and Ti scaffolds (see Figure 33 and Figure 34). The pure chitosan polymer scaffold was coloured purple, and the underlying metal scaffold is denoted by the colour blue. Chitosan-Ag polymer scaffolds were coloured

golden, with the underlying metal scaffolds represented by green, in order to support in the distinction between polymer and metal components.

There was uniform distribution of the polymer scaffold, with no areas visible without its presence. The polymer scaffolds had large, interconnected pores within the metal scaffolds, though this was not the case when the polymer scaffolds were cast by themselves (Figure 33A and Figure 34A). Polymer scaffolds not cast within metal constructs showed a distinctly layered geometry, with few constructs which could be labelled as pores. The scaffolds with added Ag nanoparticles displayed this trait more overtly than those with no nanoparticle addition (Figure 33 and Figure 34).

The interface between two materials, such as that between the metal scaffold and the polymer within these hybrid scaffolds. Poor integration can affect mechanical and degradation properties^[414-416]. In SEM micrographs at higher magnifications (Figure 33 (C-G) and Figure 34(C-G)) it is clear that there is little or no distance between the polymer and metal surfaces at their interface, with the polymer matrix seemingly becoming well integrated within the metal structure. Further studies to confirm this would be required.

Figure 35 shows both scaffolds at high magnifications, with no visible delamination between the substrate metal scaffold and the polymer scaffold.

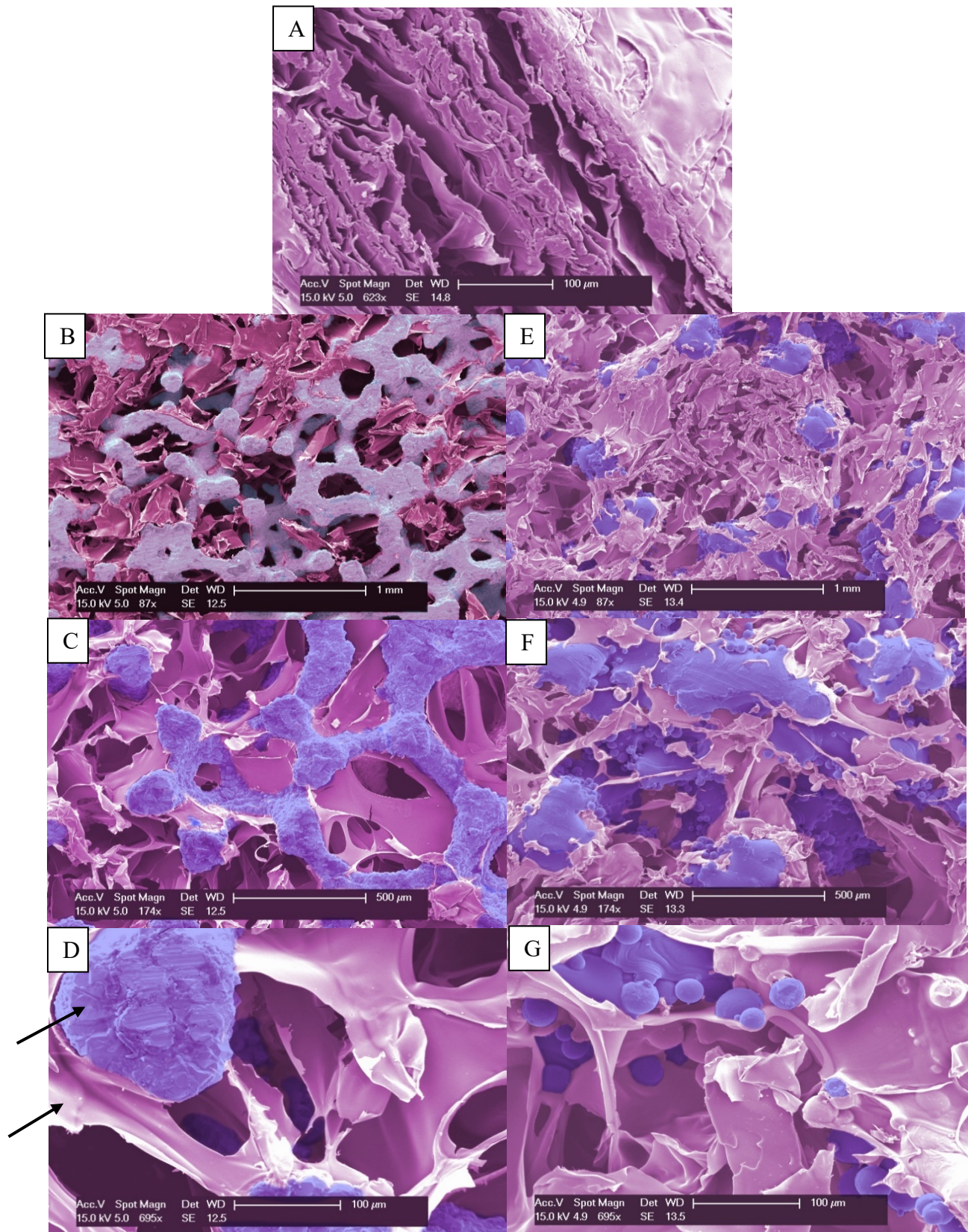


Figure 32: False-colour SEM micrographs of chitosan scaffolds which were created within metal scaffolds. Chitosan is coloured in purple and the metal is blue. A is a chitosan scaffold with no metal scaffold. B, C and D are images of chitosan cast within a tantalum scaffold (Trabecular Metal), at 87x, 174x and 695x magnifications respectively. E, F and G are images of chitosan scaffolds within Ti6Al4V scaffolds (Osseo-Ti) at 87x, 174x and 695x magnifications respectively.

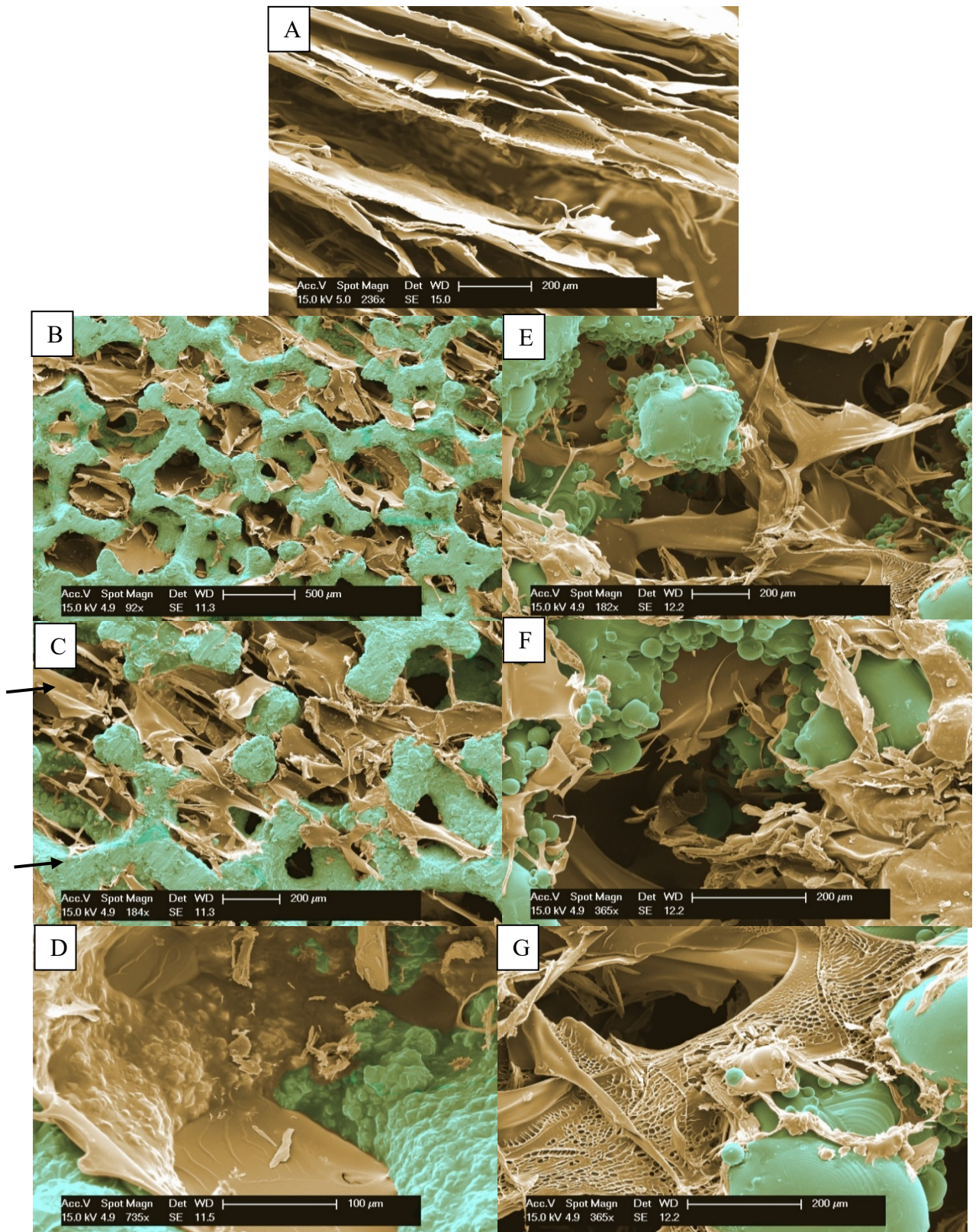


Figure 33: False-colour SEM micrographs of chitosan scaffolds with Ag nanoparticles which were cast within metal scaffolds. Ag- Chitosan is coloured in yellow and the metal is blue. A is an Ag-chitosan scaffold with no metal scaffold. B, C and D are images of Ag-chitosan cast within a tantalum scaffold (Trabecular Metal), at 92x, 184x and 735x magnifications respectively. E, F and G are images of Ag-chitosan scaffolds within Ti6Al4V scaffolds (Osseo-Ti) at 182x and 365x magnifications respectively.

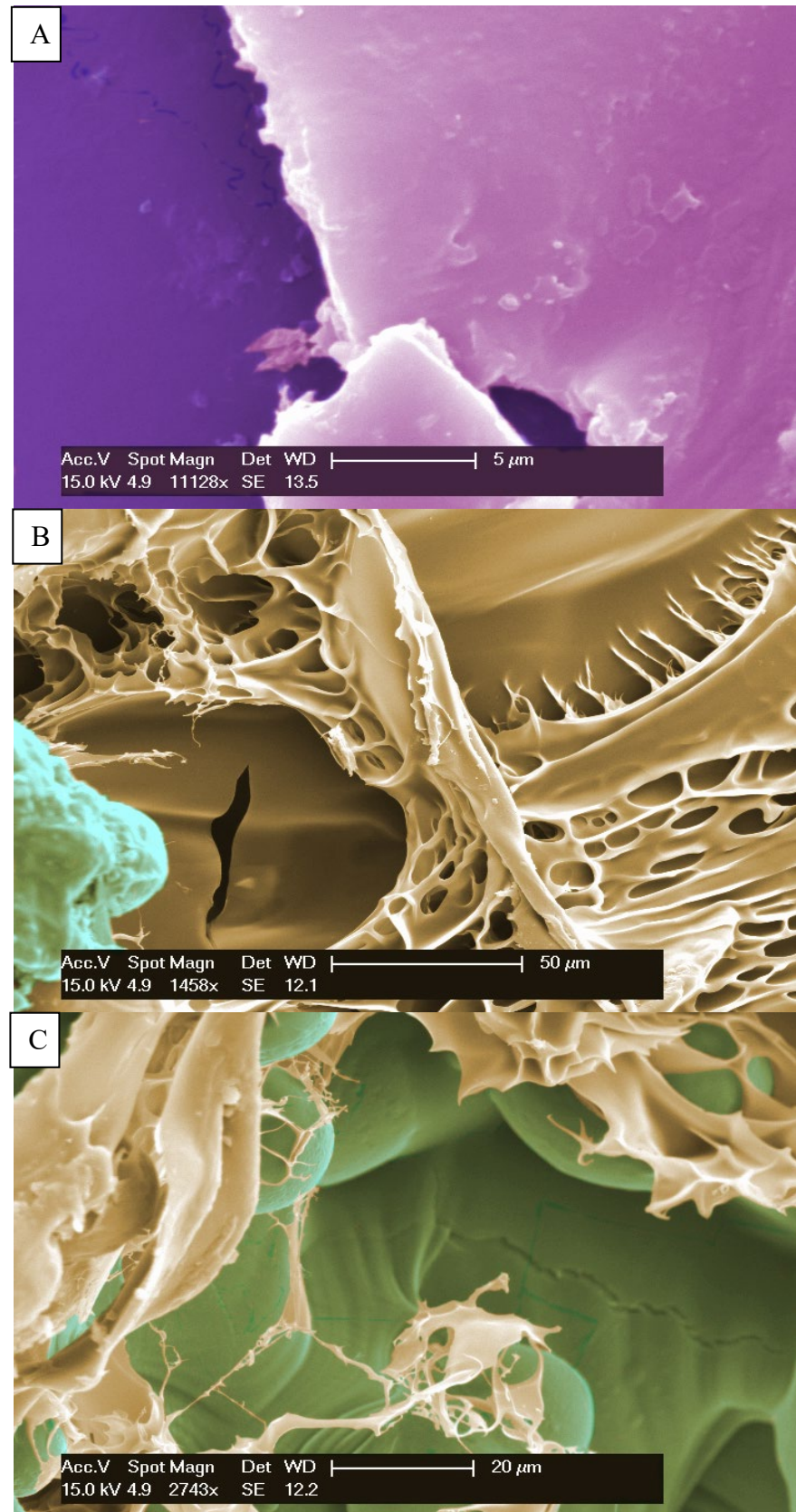


Figure 34: High magnification false-colour SEM images of the chitosan-metal scaffold material interface. Chitosan is purple, Ag-Chitosan is coloured in yellow and the metal is blue. A is a Chitosan-Tantalum material interface at a magnification of 11128x. B and C are Ag-Chitosan-Ti6Al4V material interface at magnifications of 1458x and 2743x respectively.

6.3 Discussion

The proof of concept of combining a polymeric scaffold within a metal ‘skeleton’ scaffold, creating a hybrid device, was substantiated by this work, as shown in Figure 33, Figure 34 and Figure 35

Chitosan scaffolds, with and without Ag nanoparticle additions, had a morphology more resembling a layered structure rather than a porous scaffold required for biomedical applications^[417-421]. The confinement of the Chitosan scaffolds within a metal scaffold resulted in significantly more pronounced porosity of the Chitosan scaffold, with pores being created within the metal scaffolds’ pores. These pores increase the surface area of the chitosan, compared to solid chitosan, exposing it and its antibacterial properties to any bacterial cells, or being expected to result in increasing its degradation and subsequent release of any chemical agents (antibiotics or compounds which promote human cell growth) to induce characteristics to the scaffold which would either promote healing or reduce the chance of bacterial infection.

The polymer-metal interface showed good integration with no visible delamination between the two materials. This can be seen in Figure 33 and Figure 35. This good interface means that any bacterial cells will have less of the metal surface to attach to, instead being faced with the antibacterial chitosan surface chemistry. If delamination was present, this would expose more of the metal scaffolds’ surface to the environment.

Such devices were foreseen by researchers such as Tomsia *et al.* (2005), who in their review of devices available at the time mused about the potential of “hybrid” devices, which would take advantage of the bioactive potential of polymers and the high strength of metals or ceramics to result in implants which would change over time, with the polymer portion becoming resorbed by the surrounding tissue and the metal/ceramic providing the required mechanical strength^[422]. Later on, Zhao *et al.* (2011) described such hybrid constructs as one of the areas with the most potential in orthopaedic devices [423].

Hybrid scaffolds have been recently assessed for their benefits, where a combination of a metal and polymer is used. Those prepared by Tsai *et al.* (2019) studied both Chitosan and Magnesium-Calcium polymers cast within a 3D printed Ti6Al4V scaffold. They found the bioactivity of such constructs, in the case of both polymer-hybrids, significantly increased^[424]. While the proliferation rate of osteoblast cells cultured on these samples was almost double the rate observed on metal scaffolds without the polymer at the 7-day culture timepoint (0.81 and 0.45 absorbance values respectively), the Alkaline phosphatase (ALP) expression was *circa* 4 times greater in the polymer-hybrid cohort when compared to metal only scaffolds (0.17 and 0.59 ALP activity respectively). ALP expression is used as a mark of cell differentiation^[424].

Similarly, a study conducted by Yang *et al.* (2018) investigated the potential of such hybrid scaffolds in imparting antibacterial properties upon metal scaffolds *in vivo*. Using a composite chitosan (HACC)-grafted polylactide-co-

glycolide (PLGA)/hydroxyapatite (HA) resulted in a bacterial burden (of *S. aureus*) of these devices being *c.a.* 1.0×10^4 lower than the control scaffold after 8 weeks^[425].

The relative ease with which substances such as nanoparticles, chemical signalling molecules, growth factors, antibiotics or metal-ion complexes can be added to an internal chitosan structure, coupled with its biodegradable characteristic, makes this substance an appealing candidate when assessing methods for increasing metal scaffold bioactivity while providing bacterial resistance to the structure.

As chitosan is prepared in aqueous solution, water-soluble antibiotics or other substances may be added during the preparation phase with relative ease, thus endowing the resultant scaffold with desired properties^[426]. Work conducted by Raftery *et al.* (2016) showed that addition of chitosan into collagen scaffolds increased their mechanical and biological functionality^[426]. Xia *et al.* (2018) showed that addition of calcium phosphate and oxide nanoparticles increased osteogenesis by a factor of 3^[427]. Perli *et al.* (2017) showed that Ag nanoparticles were well integrated within chitosan scaffolds, with uniform distribution, and that their addition significantly increased the antibacterial properties of the structure^[428]. Doty *et al.* (2015) showed that two antibiotics (amikacin and vancomycin) can be incorporated within a calcium sulfate and chitosan hybrid scaffold and that these antibiotics can be eluted from the structure in an aqueous solution during the degradation of the polymer^[429].

Casting such a polymer scaffold within an orthopaedic Ti or Ta device allows for the exploitation of characteristics introduced by the polymer matrix, while simultaneously benefiting from the metals' mechanical properties, pore geometries, and surface chemistries^[430-433]. For example, polymers such as chitosan are flexibly biodegradable (parameters can be altered to provide shorter or longer degradation times^[434, 435]) allowing the overall polymeric structure to degrade over time *in vivo* in one phase, while leaving the metal device in place provide strength and mechanical strength to the hybrid.

Such scaffolds have significant potential to advance the field of orthopaedic devices, however their microbiological studies need to be appropriate to the nature of these samples so as to provide sufficiently reliable data *in vitro* prior to *in vivo* performance analysis. Currently studies focus on the measurement of elutes from these scaffolds when any antimicrobial characteristics are required, operating with the assumption that these will have the same effect on bacterial cells as they would in a solution. However, this approach doesn't account for the complexities of 3D structures and the formation of biofilms, nor does it provide insight into the bacteria-substrate interaction- either for the initial attachment or subsequent growth. It's this that this work aims to address, and forms a basis for subsequent work for this use.

Chapter 7 Conclusions, and Future Work

This chapter contains the conclusions for the entire body of work hitherto described in previous chapters and recommendations for future work.

7.1 Conclusions

The aim of this study is to develop and validate a new analysis method to provide quantifiable, accurate and reliable results for the measurement of bacterial biofouling on flat and three-dimensional porous samples alike.

The objectives of this work were to evaluate currently-available approaches for quantifiable biofouling/ bioburden assessments and their potential use to measure biofilm formation within a metal scaffold and if no such method was transferable to the assessment of metal scaffolds- to develop and validate a novel methodology for this purpose. Further, the objectives were to evaluate bacterial biofilm growth within orthopaedic scaffolds currently present in clinic in clean media as well as an environment such scaffolds would likely be subjected to *in situ*- protein rich media; to ascertain what, if any, surface

treatments to the aforementioned samples may limit any bacterial biofilm formation and to conduct a proof-of-concept evaluation of novel metal-polymer hybrid scaffolds against samples available in clinic in terms of bacterial biofilm formation.

Two existing analysis methods for the quantitative analysis of bacterial growth on orthopaedic devices proved effective and viable in the testing of only a subset of sample types:

1. CLSM for flat sample testing
2. Micro-CT for analysis of polymeric three-dimensional scaffolds

Neither of these two methods allow for the assessment of bacterial growth throughout the full spectrum of surface features and macro-geometries.

The CLSM method proved inaccurate when measuring biofouling in 3D scaffold samples, and the 3D image rendering showed this to be due to the fact that the scanned surface area was too inconsistent. Micro-CT analysis failed to provide results for metal samples due to the shielding effect of metal and the X-Rays' inability to penetrate the structure with low enough energy to also map biofilm.

However, SEM micrograph coverage analysis proved effective in facilitating full-spectrum analysis, delivering results comparable to those obtained by conventional testing on appropriate sample types, and repeatable across a number of studies and timepoints. SEM micrograph coverage analysis also allows for data to be comparable between different surface geometries, crucially including three-dimensional metallic scaffold samples, as long as it doesn't attempt to measure biofilm structures in its current form.

Once the initial polymer selection had taken place, the hybrid scaffolds could then be assessed using the SEM image analysis method to study the bacterial presence across both the polymer-metal interfaces and exposed metal surfaces.

In order to limit any effect of variation of bacterial presence upon the surface of a sample, with some areas exhibiting higher coverage than others, a set of 3 standardised location coordinates was taken at every sample, and each sample type was tested in triplicate. This resulted in 9 data-points at each timepoint, preventing any high- or low-outlier's ability to significantly affect the results.

The SEM method was assessed against the standard of CLSM on flat samples to ensure that it returned accurate and reliable data. The comparison returned a mean p-value of $p > 0.05$ which means that there was no statistically significant difference between the results of these two methods as they were similar.

SEM micrograph analysis method was then further utilised to assess the effect of a protein conditioning film upon the surface of samples - an aspect often overlooked in *in vitro* analysis of orthopaedic devices. The presence of protein on the substrate surface increased the bacterial presence on the samples in all cases, diminishing and minimising the effect of any antibacterial surface chemistries. This effect was most pronounced at the early timepoints, suggesting that the bacterial cells find it somewhat easier to attach themselves to a substrate covered in protein, and that any bactericidal effects of the sample surface may be limited by the proteins atop.

This effect was observed on samples of all geometries tested, however it is recognised that the number of surface topographies (3) is not a large sample size, therefore the conclusions taken from this are limited.

It must be noted that SEM micrograph coverage analysis has three significant drawbacks:

1. It relies heavily on operator input during the conversion of images into a binary format rendering it susceptible to human error
2. Results are liable to skewing by variations in surface area scanned in each image
3. The technique is not reliable once bacterial cells begin to establish more mature biofilms due to its focus on simple coverage values (biofilms are three-dimensional features upon the surface)

These can be mitigated as follows:

1. High magnifications required during image editing serve to limit human error as the bacterial cells are easily identifiable.
2. Although a surface area limitation is inherent to a method such as this, the best mitigating factor is high magnification which limits the likelihood of imaging a whole strut. Images are seen by the operator, and as such if the resulting micrograph only captures a part of a strut, the sample can be slightly repositioned to mitigate this. The ability of the operator to image each surface at the correct Working Distance/magnification values so as to ensure comparable images is also of paramount importance to the successful application of this method.
3. This limitation can be overcome by the superimposition of each image onto a three-dimensional model of the imaged surface and normalisation against the actual surface area in each micrograph. In addition, a quantification of real volume of bacterial cells/ biofilm in each image would allow for the analysis of samples with a bacterial biofilm burden. This could be within the scope of future work.

On balance the SEM image analysis method presents a new tool, which has previously not been used for this purpose in literature, to investigate bacterial

bioburden within 3D scaffold samples. Limitations of existing analysis methods, such as CLSM's inability to reliably calculate biomass in 3D structures, are addressed and complemented by the SEM method. With this method, the bacteria-substrate interface can begin to be studied within the highly-complex environment of a 3D scaffold, which can provide an as-yet-overlooked aspect of in vitro testing of these samples within a microbiological context. However, its high reliance on the operator mean that is significantly less time-efficient and more prone to human error than the highly-automated process of CLSM analysis. For this reason, though it has proved useful for 3D samples, it's unlikely to be appropriate for use on flat samples where alternatives are available. Further development of this method could achieve higher time efficiency and lower the probability of human error through increased automation.

7.2 Future Work

The analysis method described above requires further refinement and validation through repeat studies.

Subsequent analysis of the effect of a protein conditioning film on bacterial behaviour upon orthopaedic substrate surfaces is required, as well as study of any variation in the effects based upon the specific characteristics of such a film (such as roughness, hydrophilic properties or the particular chemical

profile). Investigations into the nature of protein conditioning films on surfaces with different chemistries and surface topographies could be conducted to ascertain how particular devices would present their surface chemistries to bacterial cells *in vivo* upon implantation. This could be done by quantitative methods such as time-of-flight secondary ion mass spectrometry or Liquid Chromatography Coupled with Mass Spectrometry^[436-438].

Further investigation into the effect of a protein conditioning film on a wider number of surface topographies would also allow for increasing the understanding of how best to combine surface topography and chemistry in order to limit bacterial adhesion/ presence, in a similar effort to that seen in platelet adhesion to heart valve implant devices ^[439-441].

The synthesis of hybrid scaffolds, utilising different materials' properties to their full effect while mitigating their limiting factors should be studied further. This field of prospective orthopaedic devices presents a significant potential for improvement of device performance in a clinical setting, possibly contributing to significant reduction of patient suffering and cost associated with treatment.

The utilisation of 3D printing, together with the ability to cast highly porous polymer scaffolds, allows for exploitation of substances which rely on release into solution for their effects, while not compromising the structural integrity of the overall device.

It is imperative that methods are developed and advanced for the assessment of bacterial growth within three-dimensional structures composed of materials with wide-ranging densities as such devices become more widely researched and implemented. Bacterial cell behaviour, survival and biofilm formation, and the effects of the device upon these characteristics need to be fully understood and studied within such structures, in order to fully exploit desirable material attributes, while simultaneously working to eliminate undesirable device effects.

It should be noted that three-dimensional constructs will behave differently to flat substrate surfaces of the same chemistry - increasing surface area would cause effects such as: providing more attachment sites for bacteria, creating an opportunity for faster antibacterial substance release, providing shelter for bacterial from environmental mechanical forces created by turbulence, and increasing the time an immune response would be initiated against any bacterial cells deeper within the structure. Because of this, testing of flat constructs cannot be used as a substitute for testing of three-dimensional substrates, simply on the basis of a similar chemical profile.

References

1. Trust, N.H.N.F., *Trust implements interventions to reduce surgical morbidity stemming out of post-operative infections in joint replacement, reducing readmission rates and patient length of stay*, in *HSJ Solutions*. 2019.
2. Morin, C.D. and E. Deziel, *Use of Alternative Gelling Agents Reveals the Role of Rhamnolipids in Pseudomonas aeruginosa Surface Motility*. *Biomolecules*, 2021. **11**(10).
3. DeHart, T.G., et al., *The unusual cell wall of the Lyme disease spirochaete Borrelia burgdorferi is shaped by a tick sugar*. *Nature Microbiology*, 2021. **6**(12): p. 1583-+.
4. Zayed, A., et al., *Rediscovering bacterial exopolysaccharides of terrestrial and marine origins: novel insights on their distribution, biosynthesis, biotechnological production, and future perspectives*. *Critical Reviews in Biotechnology*.
5. Thairu, Y., I. Nasir, and Y. Usman, *Laboratory perspective of gram staining and its significance in investigations of infectious diseases*. *Sub-Saharan African Journal of Medicine*, 2014. **1**(4): p. 168-174.
6. Hamada, S., et al., *The importance of fimbriae in the virulence and ecology of some oral bacteria*. *Oral Microbiology and Immunology*, 1998. **13**(3): p. 129-138.
7. Mizuno, K., et al., *Fimbriae and lipopolysaccharides are necessary for co-aggregation between Lactobacilli and Escherichia coli*. *Bioscience, Biotechnology, and Biochemistry*, 2014. **78**(9): p. 1626-1628.
8. Hammond, S.M., P. Lambert, and A. Rycroft, *The Bacterial Cell Surface*. 2012: Springer Netherlands.
9. Tolstorukov, M.Y., et al., *Organization of DNA in a bacterial nucleoid*. *BMC Microbiology*, 2016. **16**(1): p. 22.
10. Egan, E.S., M.A. Fogel, and M.K. Waldor, *MicroReview: Divided genomes: negotiating the cell cycle in prokaryotes with multiple chromosomes*. *Molecular Microbiology*, 2005. **56**(5): p. 1129-1138.

11. Mackenzie, C., et al., *The home stretch, a first analysis of the nearly completed genome of Rhodobacter sphaeroides 2.4.1*. Photosynthesis Research, 2001. **70**(1): p. 19-41.
12. Wood, D.W., et al., *The Genome of the Natural Genetic Engineer Agrobacterium tumefaciens C58*. Science, 2001. **294**(5550): p. 2317.
13. Xiong, W., et al., *Responses of plasmid-mediated quinolone resistance genes and bacterial taxa to (fluoro)quinolones-containing manure in arable soil*. Chemosphere, 2015. **119**: p. 473-478.
14. Dionisio, F., et al., *The evolution of a conjugative plasmid and its ability to increase bacterial fitness*. Biology Letters, 2005. **1**(2): p. 250.
15. Svara, F. and D.J. Rankin, *The evolution of plasmid-carried antibiotic resistance*. BMC Evolutionary Biology, 2011. **11**(1): p. 130.
16. Barth, S. and R. Bauerfeind, [*Virulence plasmids of Salmonella enterica--incidence and properties*]. Berliner und Munchener tierarztliche Wochenschrift, 2005. **118**(1-2): p. 8-23.
17. Prozorov, A.A., *Conjugation in Bacilli*. Microbiology, 2003. **72**(5): p. 517-527.
18. Abriouel, H., et al., *Bacteriocin production, plasmid content and plasmid location of enterocin P structural gene in enterococci isolated from food sources*. Letters in Applied Microbiology, 2006. **42**(4): p. 331-337.
19. Labbe, R.G. and T.H. Huang, *Generation Times and Modeling of Enterotoxin-Positive and Enterotoxin-Negative Strains of Clostridium perfringens in Laboratory Media and Ground Beef*. Journal of Food Protection, 1995. **58**(12): p. 1303-1306.
20. apos, et al., *Mapping the fitness of Mycobacterium tuberculosis strains: a complex picture*. Journal of Medical Microbiology, 2010. **59**(12): p. 1533-1535.
21. Whiting, R.C. and L.K. Bagi, *Modeling the lag phase of Listeria monocytogenes*. International Journal of Food Microbiology, 2002. **73**(2-3): p. 291-295.
22. Silva, C.D., et al., *Effect of Moxifloxacin plus Pretomanid against Mycobacterium tuberculosis in Log Phase, Acid Phase, and Nonreplicating-Persister Phase in an In Vitro Assay*. Antimicrobial Agents and Chemotherapy, 2019. **63**(1).
23. Llorens, J.M.N., A. Tormo, and E. Martinez-Garcia, *Stationary phase in gram-negative bacteria*. Fems Microbiology Reviews, 2010. **34**(4): p. 476-495.

24. Navarre, W.W. and O. Schneewind, *Surface proteins of gram-positive bacteria and mechanisms of their targeting to the cell wall envelope*. Microbiology and Molecular Biology Reviews, 1999. **63**(1): p. 174-+.
25. Armstrong, J.J., et al., *NUCLEOTIDES AND THE BACTERIAL CELL WALL*. Nature, 1958. **181**(4625): p. 1692-1693.
26. Hughes, A.H., I.C. Hancock, and J. Baddiley, *The function of teichoic acids in cation control in bacterial membranes*. Biochemical Journal, 1973. **132**(1): p. 83.
27. Preston, N.W. and A. Morrell, *Reproducible results with the gram stain*. The Journal of Pathology and Bacteriology, 1962. **84**(1): p. 241-243.
28. Beveridge, T.J., *Structures of Gram-Negative Cell Walls and Their Derived Membrane Vesicles*. Journal of Bacteriology, 1999. **181**(16): p. 4725-4733.
29. Plésiat, P. and H. Nikaido, *Outer membranes of Gram-negative bacteria are permeable to steroid probes*. Molecular Microbiology, 1992. **6**(10): p. 1323-1333.
30. Tapia-Rodriguez, M.R., et al., *Carvacrol as potential quorum sensing inhibitor of Pseudomonas aeruginosa and biofilm production on stainless steel surfaces*. Food Control, 2017. **75**: p. 255-261.
31. Majumdar, S. and S. Mondal, *Conversation game: talking bacteria*. J Cell Commun Signal, 2016. **10**(4): p. 331-335.
32. Koul, S. and V.C. Kalia, *Multiplicity of Quorum Quenching Enzymes: A Potential Mechanism to Limit Quorum Sensing Bacterial Population*. Indian Journal of Microbiology, 2017. **57**(1): p. 100-108.
33. Shapiro, J.A., *Thinking about bacterial populations as multicellular organisms*. Annu Rev Microbiol, 1998. **52**: p. 81-104.
34. Rosenberg, E. and M. Varon, *Antibiotics and Lytic Enzymes*, in *Myxobacteria: Development and Cell Interactions*, E. Rosenberg, Editor. 1984, Springer New York: New York, NY. p. 109-125.
35. Kleerebezem, M., et al., *Quorum sensing by peptide pheromones and two-component signal-transduction systems in Gram-positive bacteria*. Mol Microbiol, 1997. **24**(5): p. 895-904.
36. Novick, R.P. and T.W. Muir, *Virulence gene regulation by peptides in staphylococci and other Gram-positive bacteria*. Curr Opin Microbiol, 1999. **2**(1): p. 40-5.
37. Bassler, B.L., *How bacteria talk to each other: regulation of gene expression by quorum sensing*. Curr Opin Microbiol, 1999. **2**(6): p. 582-7.

38. Fuqua, W.C., S.C. Winans, and E.P. Greenberg, *Quorum sensing in bacteria: the LuxR-LuxI family of cell density-responsive transcriptional regulators*. J Bacteriol, 1994. **176**(2): p. 269-75.
39. Schell, M.A., *To be or not to be: how Pseudomonas solanacearum decides whether or not to express virulence genes*. European Journal of Plant Pathology, 1996. **102**(5): p. 459-469.
40. Flavier, A.B., et al., *Hierarchical autoinduction in Ralstonia solanacearum: control of acyl-homoserine lactone production by a novel autoregulatory system responsive to 3-hydroxypalmitic acid methyl ester*. J Bacteriol, 1997. **179**(22): p. 7089-97.
41. Sprecher, K.S., et al., *Cohesive Properties of the Caulobacter crescentus Holdfast Adhesin Are Regulated by a Novel c-di-GMP Effector Protein*. mBio, 2017. **8**(2): p. e00294-17.
42. Ramage, G., et al., *Inhibition of Candida albicans Biofilm Formation by Farnesol, a Quorum-Sensing Molecule*. Applied and Environmental Microbiology, 2002. **68**(11): p. 5459-5463.
43. Jabra-Rizk, M.A., et al., *Effect of farnesol on Candida dubliniensis biofilm formation and fluconazole resistance*. FEMS Yeast Res, 2006. **6**(7): p. 1063-73.
44. Koczan, J.M., et al., *Cell Surface Attachment Structures Contribute to Biofilm Formation and Xylem Colonization by Erwinia amylovora*. Applied and Environmental Microbiology, 2011. **77**(19): p. 7031-7039.
45. Pizarro-Cerda, J. and P. Cossart, *Bacterial adhesion and entry into host cells*. Cell, 2006. **124**(4): p. 715-27.
46. Kim, T.J., B.M. Young, and G.M. Young, *Effect of flagellar mutations on Yersinia enterocolitica biofilm formation*. Appl Environ Microbiol, 2008. **74**(17): p. 5466-74.
47. Kline, K.A., et al., *Bacterial adhesins in host-microbe interactions*. Cell Host Microbe, 2009. **5**(6): p. 580-92.
48. Davey, M.E. and A. O'Toole G, *Microbial biofilms: from ecology to molecular genetics*. Microbiol Mol Biol Rev, 2000. **64**(4): p. 847-67.
49. Kang, Y., et al., *Ralstonia solanacearum requires type 4 pili to adhere to multiple surfaces and for natural transformation and virulence*. Mol Microbiol, 2002. **46**(2): p. 427-37.
50. Bahar, O., T. Goffer, and S. Burdman, *Type IV Pili are required for virulence, twitching motility, and biofilm formation of acidovorax avenae subsp. Citrulli*. Mol Plant Microbe Interact, 2009. **22**(8): p. 909-20.

51. Feil, H., W.S. Feil, and S.E. Lindow, *Contribution of Fimbrial and Afimbrial Adhesins of Xylella fastidiosa to Attachment to Surfaces and Virulence to Grape*. *Phytopathology*, 2007. **97**(3): p. 318-24.
52. Stewart, P.S., *Diffusion in biofilms*. *J Bacteriol*, 2003. **185**(5): p. 1485-91.
53. Costerton, J.W., P.S. Stewart, and E.P. Greenberg, *Bacterial biofilms: a common cause of persistent infections*. *Science*, 1999. **284**(5418): p. 1318-22.
54. Cao, Y.X., et al., *Non-antibiotic antimicrobial agents to combat biofilm-forming bacteria*. *Journal of Global Antimicrobial Resistance*, 2020. **21**: p. 445-451.
55. de Beer, D., P. Stoodley, and Z. Lewandowski, *Liquid flow in heterogeneous biofilms*. *Biotechnol Bioeng*, 1994. **44**(5): p. 636-41.
56. Davies, D.G., A.M. Chakrabarty, and G.G. Geesey, *Exopolysaccharide production in biofilms: substratum activation of alginate gene expression by Pseudomonas aeruginosa*. *Applied and Environmental Microbiology*, 1993. **59**(4): p. 1181-1186.
57. Ward, K.H., et al., *Mechanism of persistent infection associated with peritoneal implants*. *J Med Microbiol*, 1992. **36**(6): p. 406-13.
58. Fux, C.A., et al., *Survival strategies of infectious biofilms*. *Trends Microbiol*, 2005. **13**(1): p. 34-40.
59. *Microbial Biofilms*. *Biotechnology Research*. 1995, Cambridge: Cambridge University Press.
60. Singh, P.K., et al., *Quorum-sensing signals indicate that cystic fibrosis lungs are infected with bacterial biofilms*. *Nature*, 2000. **407**(6805): p. 762-764.
61. Darveau, R.P., A. Tanner, and R.C. Page, *The microbial challenge in periodontitis*. *Periodontol 2000*, 1997. **14**: p. 12-32.
62. Høiby, N., et al., *ESCMID* guideline for the diagnosis and treatment of biofilm infections 2014*. *Clinical Microbiology and Infection*, 2015. **21**, **Supplement 1**: p. S1-S25.
63. Francolini, I. and G. Donelli, *Prevention and control of biofilm-based medical-device-related infections*. *FEMS Immunology & Medical Microbiology*, 2010. **59**(3): p. 227-238.
64. http://ecdc.europa.eu/en/healthtopics/Healthcare-associated_infections/Pages/index.aspx.
65. Klevens, R.M., et al., *Estimating health care-associated infections and deaths in U.S. hospitals, 2002*. *Public Health Rep*, 2007. **122**(2): p. 160-6.
66. NICE, *Costing statement: Surgical site infection: prevention and treatment of surgical site infection 2008*.

67. Jamkhande, P.G., et al., *Metal nanoparticles synthesis: An overview on methods of preparation, advantages and disadvantages, and applications*. Journal of Drug Delivery Science and Technology, 2019. **53**.
68. van der Mei, H.C., et al., *Surface properties of Streptococcus salivarius HB and nonfibrillar mutants: measurement of zeta potential and elemental composition with X-ray photoelectron spectroscopy*. J Bacteriol, 1988. **170**(6): p. 2462-6.
69. Liu, L.X., et al., *Flexible and Multifunctional Silk Textiles with Biomimetic Leaf-Like MXene/Silver Nanowire Nanostructures for Electromagnetic Interference Shielding, Humidity Monitoring, and Self-Derived Hydrophobicity*. Advanced Functional Materials, 2019. **29**(44).
70. Boelens, J.J., et al., *Antibacterial activity of antibiotic-soaked polyvinylpyrrolidone-grafted silicon elastomer hydrocephalus shunts*. Journal of Antimicrobial Chemotherapy, 2000. **45**(2): p. 221-224.
71. Cassinelli, C., et al., *Evaluation of interfacial properties of hyaluronan coated poly(methylmethacrylate) intraocular lenses*. Journal of Biomaterials Science, Polymer Edition, 2000. **11**(9): p. 961-977.
72. John, T., et al., *Antibiotic pretreatment of hydrogel ureteral stent*. J Endourol, 2007. **21**(10): p. 1211-6.
73. Russell, P.B., et al., *Staphylococcal adherence to polyvinyl chloride and heparin-bonded polyurethane catheters is species dependent and enhanced by fibronectin*. J Clin Microbiol, 1987. **25**(6): p. 1083-7.
74. Appelgren, P., et al., *Surface heparinization of central venous catheters reduces microbial colonization in vitro and in vivo: results from a prospective, randomized trial*. Crit Care Med, 1996. **24**(9): p. 1482-9.
75. Abdelkefi, A., et al., *Use of heparin-coated central venous lines to prevent catheter-related bloodstream infection*. J Support Oncol, 2007. **5**(6): p. 273-8.
76. Ivanova, E.P., et al., *Bactericidal activity of black silicon*. Nature Communications, 2013. **4**: p. 2838.
77. Gon, S., et al., *How Bacteria Adhere to Brushy PEG Surfaces: Clinging to Flaws and Compressing the Brush*. Macromolecules, 2012. **45**(20): p. 8373-8381.
78. Kingshott, P., et al., *Covalent Attachment of Poly(ethylene glycol) to Surfaces, Critical for Reducing Bacterial Adhesion*. Langmuir, 2003. **19**(17): p. 6912-6921.
79. Antonelli, P.J., E.M. Sampson, and C. Ojano-Dirain, *Biofilm formation on silicone tympanostomy tubes with polyvinylpyrrolidone coating*. Arch Otolaryngol Head Neck Surg, 2011. **137**(1): p. 19-23.

80. Tunney, M.M. and S.P. Gorman, *Evaluation of a poly(vinyl pyrrolidone)-coated biomaterial for urological use*. *Biomaterials*, 2002. **23**(23): p. 4601-8.
81. Kaper, H.J., H.J. Busscher, and W. Norde, *Characterization of poly(ethylene oxide) brushes on glass surfaces and adhesion of Staphylococcus epidermidis*. *J Biomater Sci Polym Ed*, 2003. **14**(4): p. 313-24.
82. Shukla, A., et al., *Release of vancomycin from multilayer coated absorbent gelatin sponges*. *Journal of Controlled Release*, 2012. **157**(1): p. 64-71.
83. Rossi, S., A.O. Azghani, and A. Omri, *Antimicrobial efficacy of a new antibiotic-loaded poly(hydroxybutyric-co-hydroxyvaleric acid) controlled release system*. *Journal of Antimicrobial Chemotherapy*, 2004. **54**(6): p. 1013-1018.
84. Wang, B.-L., et al., *Fast and long-acting antibacterial properties of chitosan-Ag/polyvinylpyrrolidone nanocomposite films*. *Carbohydrate Polymers*, 2012. **90**(1): p. 8-15.
85. Fu, J., et al., *Construction of antibacterial multilayer films containing nanosilver via layer-by-layer assembly of heparin and chitosan-silver ions complex*. *Journal of Biomedical Materials Research Part A*, 2006. **79A**(3): p. 665-674.
86. Valappil, S.P., et al., *Antimicrobial Gallium-Doped Phosphate-Based Glasses*. *Advanced Functional Materials*, 2008. **18**(5): p. 732-741.
87. Valappil, S.P., et al., *Controlled delivery of antimicrobial gallium ions from phosphate-based glasses*. *Acta Biomaterialia*, 2009. **5**(4): p. 1198-1210.
88. Grass, G., C. Rensing, and M. Solioz, *Metallic Copper as an Antimicrobial Surface*. *Applied and Environmental Microbiology*, 2011. **77**(5): p. 1541-1547.
89. Du, W.-L., et al., *Antibacterial activity of chitosan tripolyphosphate nanoparticles loaded with various metal ions*. *Carbohydrate Polymers*, 2009. **75**(3): p. 385-389.
90. Donlan, R.M. and J.W. Costerton, *Biofilms: Survival Mechanisms of Clinically Relevant Microorganisms*. *Clinical Microbiology Reviews*, 2002. **15**(2): p. 167-193.
91. Kim, J.S., et al., *Antimicrobial effects of silver nanoparticles*. *Nanomedicine: Nanotechnology, Biology and Medicine*, 2007. **3**(1): p. 95-101.
92. El-Rafie, M.H., et al., *Antimicrobial effect of silver nanoparticles produced by fungal process on cotton fabrics*. *Carbohydrate Polymers*, 2010. **80**(3): p. 779-782.

93. Kenawy, E.-R., S.D. Worley, and R. Broughton, *The Chemistry and Applications of Antimicrobial Polymers: A State-of-the-Art Review*. *Biomacromolecules*, 2007. **8**(5): p. 1359-1384.
94. Sambhy, V., B.R. Peterson, and A. Sen, *Multifunctional Silane Polymers for Persistent Surface Derivatization and Their Antimicrobial Properties*. *Langmuir*, 2008. **24**(14): p. 7549-7558.
95. Yang, W.J., et al., *Biomimetic Anchors for Antifouling and Antibacterial Polymer Brushes on Stainless Steel*. *Langmuir*, 2011. **27**(11): p. 7065-7076.
96. Roy, D., et al., *Antibacterial Cellulose Fiber via RAFT Surface Graft Polymerization*. *Biomacromolecules*, 2008. **9**(1): p. 91-99.
97. Fu, J., et al., *Construction of anti-adhesive and antibacterial multilayer films via layer-by-layer assembly of heparin and chitosan*. *Biomaterials*, 2005. **26**(33): p. 6684-92.
98. Cheng, G., et al., *A Switchable Biocompatible Polymer Surface with Self-Sterilizing and Nonfouling Capabilities*. *Angewandte Chemie International Edition*, 2008. **47**(46): p. 8831-8834.
99. Mi, L. and S. Jiang, *Synchronizing nonfouling and antimicrobial properties in a zwitterionic hydrogel*. *Biomaterials*, 2012. **33**(35): p. 8928-8933.
100. Stewart, P.S. and J. William Costerton, *Antibiotic resistance of bacteria in biofilms*. *The Lancet*, 2001. **358**(9276): p. 135-138.
101. Levy, S.B., *Factors impacting on the problem of antibiotic resistance*. *Journal of Antimicrobial Chemotherapy*, 2002. **49**(1): p. 25-30.
102. Livermore, D.M., *Minimising antibiotic resistance*. *The Lancet Infectious Diseases*, 2005. **5**(7): p. 450-459.
103. Jefferson, K.K., *What drives bacteria to produce a biofilm?* *Fems Microbiology Letters*, 2004. **236**(2): p. 163-173.
104. Ceri, H., et al., *The Calgary Biofilm Device: New technology for rapid determination of antibiotic susceptibilities of bacterial biofilms*. *Journal of Clinical Microbiology*, 1999. **37**(6): p. 1771-1776.
105. Anderl, J.N., M.J. Franklin, and P.S. Stewart, *Role of antibiotic penetration limitation in *Klebsiella pneumoniae* biofilm resistance to ampicillin and ciprofloxacin*. *Antimicrobial Agents and Chemotherapy*, 2000. **44**(7): p. 1818-1824.
106. Correa, C., et al., *Eigenstrain simulation of residual stresses induced by laser shock processing in a Ti6Al4V hip replacement*. *Materials & Design*, 2015. **79**: p. 106-114.
107. Stirbu, I., et al., *Electrochemical Deposition of Hydroxyapatite (HA) on Titanium Alloys for the Implant Surface Bio-functionalization*. 2013 E-Health and Bioengineering Conference (Ehb), 2013.

108. Ramesh, G.V. and T.P. Radhakrishnan, *A Universal Sensor for Mercury (Hg, HgI, HgII) Based on Silver Nanoparticle-Embedded Polymer Thin Film*. ACS Applied Materials & Interfaces, 2011. **3**(4): p. 988-994.
109. Geringer, J., B. Forest, and P. Combrade, *Wear analysis of materials used as orthopaedic implants*. Wear, 2006. **261**(9): p. 971-979.
110. Zhang, J.Y., *Effects of Ti, Ti6Al4V, and Ti6Al7Nb on Osteoblast Bioactivity*, in *Proceedings of the 2014 International Conference on Mechatronics, Electronic, Industrial and Control Engineering*, L. Chang, C. Guiran, and L. Zhen, Editors. 2014. p. 1424-1427.
111. Steegmueller, R., et al., *Gold coating of nitinol devices for medical applications*, in *Shape Memory Materials and Its Applications*, Y.Y. Chu and L.C. Zhao, Editors. 2001. p. 161-164.
112. CARTER, D.R. and D.M. SPENGLER, *Mechanical Properties and Composition of Cortical Bone*. Clinical Orthopaedics and Related Research®, 1978(135): p. 192-217.
113. Niinomi, M., *Mechanical properties of biomedical titanium alloys*. Materials Science and Engineering: A, 1998. **243**(1): p. 231-236.
114. Prakasam, M., et al., *Biodegradable Materials and Metallic Implants-A Review*. J Funct Biomater, 2017. **8**(4).
115. Weinans, H., R. Huiskes, and H.J. Grootenboer, *Effects of material properties of femoral hip components on bone remodeling*. J Orthop Res, 1992. **10**(6): p. 845-53.
116. Maistrelli, G.L., et al., *Effect of stem modulus in a total hip arthroplasty model*. The Journal of Bone and Joint Surgery. British volume, 1991. **73-B**(1): p. 43-46.
117. Zysset, P.K., et al., *Elastic modulus and hardness of cortical and trabecular bone lamellae measured by nanoindentation in the human femur*. Journal of Biomechanics, 1999. **32**(10): p. 1005-1012.
118. CA, E., B. JD, and G. AH, *Porous-coated hip replacement. The factors governing bone ingrowth, stress shielding, and clinical results*. The Journal of Bone and Joint Surgery. British volume, 1987. **69-B**(1): p. 45-55.
119. Huiskes, R., H. Weinans, and B. van Rietbergen, *The relationship between stress shielding and bone resorption around total hip stems and the effects of flexible materials*. Clinical Orthopaedics and Related Research, 1992: p. 124-134.
120. Soylemez, S., et al., *Development of a novel biosensor based on a conducting polymer*. Talanta, 2014. **118**: p. 84-89.
121. Katti, K.S., *Biomaterials in total joint replacement*. Colloids and Surfaces B-Biointerfaces, 2004. **39**(3): p. 133-142.

122. Thein-Han, W.W., Y. Kitiyanant, and R.D.K. Misra, *Chitosan as scaffold matrix for tissue engineering*. Materials Science and Technology, 2008. **24**(9): p. 1062-1075.
123. Pina, S. and J.M.F. Ferreira, *Bioresorbable Plates and Screws for Clinical Applications: A Review*. Journal of Healthcare Engineering, 2012. **3**(2): p. 243-260.
124. Jalali-Vahid, D., et al., *Prediction of lubricating film thickness in UHMWPE hip joint replacements*. Journal of Biomechanics, 2001. **34**(2): p. 261-266.
125. Santoro, M. and G. Perale, *Using synthetic bioresorbable polymers for orthopedic tissue regeneration, in Durability and Reliability of Medical Polymers*, M. Jenkins and A. Stamboulis, Editors. 2012. p. 119-139.
126. Hoshiba, T., et al., *Decellularized matrices for tissue engineering*. Expert Opinion on Biological Therapy, 2010. **10**(12): p. 1717-1728.
127. Kim, T.G., H. Shin, and D.W. Lim, *Biomimetic Scaffolds for Tissue Engineering*. Advanced Functional Materials, 2012. **22**(12): p. 2446-2468.
128. Davis, H.E., et al., *Biomimetic scaffolds fabricated from apatite-coated polymer microspheres*. Journal of Biomedical Materials Research Part A, 2009. **90A**(4): p. 1021-1031.
129. Catledge, S.A., et al., *Nanostructured ceramics for biomedical implants*. Journal of Nanoscience and Nanotechnology, 2002. **2**(3-4): p. 293-312.
130. Affatato, S. and P. Taddei, *Wear phenomena of ceramic joints, in Wear of Orthopaedic Implants and Artificial Joints*, S. Affatato, Editor. 2012. p. 278-297.
131. Benzaid, R., et al., *Fracture toughness, strength and slow crack growth in a ceria stabilized zirconia-alumina nanocomposite for medical applications*. Biomaterials, 2008. **29**(27): p. 3636-3641.
132. Bartolome, J.F., et al., *Alumina/zirconia micro/nanocomposites: A new material for biomedical applications with superior sliding wear resistance*. Journal of the American Ceramic Society, 2007. **90**(10): p. 3177-3184.
133. Turon, P., et al., *Biodegradable and Biocompatible Systems Based on Hydroxyapatite Nanoparticles*. Applied Sciences-Basel, 2017. **7**(1).
134. Dedourkova, T., et al., *Synthesis of sphere-like nanoparticles of hydroxyapatite, in Chisa 2012*, P. Kluson, Editor. 2012. p. 1816-1821.
135. Sopyan, I., et al., *Porous hydroxyapatite for artificial bone applications*. Science and Technology of Advanced Materials, 2007. **8**(1-2): p. 116-123.

136. Albrektsson, T. and C. Johansson, *Osteoinduction, osteoconduction and osseointegration*. European spine journal : official publication of the European Spine Society, the European Spinal Deformity Society, and the European Section of the Cervical Spine Research Society, 2001. **10 Suppl 2**(Suppl 2): p. S96-S101.
137. Hench, L.L., *BIOCERAMICS - FROM CONCEPT TO CLINIC*. Journal of the American Ceramic Society, 1991. **74**(7): p. 1487-1510.
138. !!! INVALID CITATION !!! [].
139. Kim, S.S., et al., *Poly(lactide-co-glycolide)/hydroxyapatite composite scaffolds for bone tissue engineering*. Biomaterials, 2006. **27**(8): p. 1399-1409.
140. Zhang, Y.Z., et al., *Electrospun biomimetic nanocomposite nanofibers of hydroxyapatite/chitosan for bone tissue engineering*. Biomaterials, 2008. **29**(32): p. 4314-4322.
141. Anitha, A., et al., *Chitin and chitosan in selected biomedical applications*. Progress in Polymer Science, 2014. **39**(9): p. 1644-1667.
142. Armentano, I., et al., *Biodegradable polymer matrix nanocomposites for tissue engineering: A review*. Polymer Degradation and Stability, 2010. **95**(11): p. 2126-2146.
143. Fabi, D. and B. Levine, *Porous coatings on metallic implant materials*. ASM Handbook, 2012. **23**: p. 307-319.
144. Tsaras, G., et al., *Incidence, secular trends, and outcomes of prosthetic joint infection: a population-based study, Olmsted county, Minnesota, 1969–2007*. Infection Control & Hospital Epidemiology, 2012. **33**(12): p. 1207-1212.
145. Poultsides, L.A., L.L. Liarpoulos, and K.N. Malizos, *The socioeconomic impact of musculoskeletal infections*. JBJS, 2010. **92**(11): p. e13.
146. Bauer, T.W. and J. Schils, *The pathology of total joint arthroplasty. I. Mechanisms of implant fixation*. Skeletal radiology, 1999. **28**(8): p. 423-432.
147. Kurtz, S.M., et al., *Infection burden for hip and knee arthroplasty in the United States*. The Journal of arthroplasty, 2008. **23**(7): p. 984-991.
148. Zimmerli, W., A. Trampuz, and P.E. Ochsner, *Prosthetic-joint infections*. New England Journal of Medicine, 2004. **351**(16): p. 1645-1654.
149. Sugarman, B. and E. Young, *Infections associated with prosthetic devices: magnitude of the problem*. Infectious disease clinics of North America, 1989. **3**(2): p. 187-198.
150. Bauer, T.W. and J. Schils, *The pathology of total joint arthroplasty*. Skeletal radiology, 1999. **28**(9): p. 483-497.

151. Patzakis, M.J. and J. Wilkins, *Factors influencing infection rate in open fracture wounds*. *Clinical orthopaedics and related research*, 1989(243): p. 36-40.
152. Boxma, H., et al., *Randomised controlled trial of single-dose antibiotic prophylaxis in surgical treatment of closed fractures: the Dutch Trauma Trial*. *The Lancet*, 1996. **347**(9009): p. 1133-1137.
153. Teterycz, D., et al., *Outcome of orthopedic implant infections due to different staphylococci*. *International Journal of Infectious Diseases*, 2010. **14**(10): p. e913-e918.
154. Beswick, A.D., et al., *What is the evidence base to guide surgical treatment of infected hip prostheses? Systematic review of longitudinal studies in unselected patients*. *BMC medicine*, 2012. **10**(1): p. 18.
155. Kapadia, B.H., et al., *Periprosthetic joint infection*. *The Lancet*, 2016. **387**(10016): p. 386-394.
156. Moriarty, T.F., et al., *Orthopaedic device-related infection: current and future interventions for improved prevention and treatment*. *EFORT open reviews*, 2017. **1**(4): p. 89-99.
157. Corvec, S., et al., *Epidemiology and new developments in the diagnosis of prosthetic joint infection*. *The International journal of artificial organs*, 2012. **35**(10): p. 923-934.
158. Del Pozo, J.L. and R. Patel, *Infection associated with prosthetic joints*. *New England Journal of Medicine*, 2009. **361**(8): p. 787-794.
159. Montanaro, L., et al., *Scenery of Staphylococcus implant infections in orthopedics*. *Future microbiology*, 2011. **6**(11): p. 1329-1349.
160. Trampuz, A. and W. Zimmerli, *Diagnosis and treatment of infections associated with fracture-fixation devices*. *Injury*, 2006. **37**(2): p. S59-S66.
161. Tande, A.J. and R. Patel, *Prosthetic joint infection*. *Clinical microbiology reviews*, 2014. **27**(2): p. 302-345.
162. Matinyi, S., et al., *Contamination of microbial pathogens and their antimicrobial pattern in operating theatres of peri-urban eastern Uganda: a cross-sectional study*. *BMC Infectious Diseases*, 2018. **18**(1): p. 460.
163. Pasteur, L.E.H.C., *"Germ theory and its applications to medicine and surgery"/"La théorie des germes et ses applications à la médecine et à la chirurgie : lecture faite à l'Académie de médecine"*. Paris : G. Masson, 1878.
164. Kuijper, R., et al., *Assessing infection risk in implanted tissue-engineered devices*. *Biomaterials*, 2007. **28**(34): p. 5148-54.

165. Puckett, S.D., et al., *The relationship between the nanostructure of titanium surfaces and bacterial attachment*. *Biomaterials*, 2010. **31**(4): p. 706-713.
166. Chua, P.H., et al., *Surface functionalization of titanium with hyaluronic acid/chitosan polyelectrolyte multilayers and RGD for promoting osteoblast functions and inhibiting bacterial adhesion*. *Biomaterials*, 2008. **29**(10): p. 1412-1421.
167. Neoh, K.G., et al., *Balancing osteoblast functions and bacterial adhesion on functionalized titanium surfaces*. *Biomaterials*, 2012. **33**(10): p. 2813-2822.
168. Veerachamy, S., et al., *Bacterial adherence and biofilm formation on medical implants: A review*. *Proceedings of the Institution of Mechanical Engineers Part H-Journal of Engineering in Medicine*, 2014. **228**(10): p. 1083-1099.
169. Balouiri, M., M. Sadiki, and S.K. Ibnsouda, *Methods for in vitro evaluating antimicrobial activity: A review*. *Journal of Pharmaceutical Analysis*, 2016. **6**(2): p. 71-79.
170. Minoura, K., et al., *Antibacterial effects of the artificial surface of nanoimprinted moth-eye film*. *PLoS ONE*, 2017. **12**(9): p. e0185366.
171. Stiefel, P., et al., *Critical aspects of using bacterial cell viability assays with the fluorophores SYTO9 and propidium iodide*. *BMC Microbiology*, 2015. **15**(1): p. 36.
172. Lachica, R., C. Genigeorgis, and P. Hoeprich, *Metachromatic agar-diffusion methods for detecting staphylococcal nuclease activity*. *Appl. Environ. Microbiol.*, 1971. **21**(4): p. 585-587.
173. Boorn, K.L., et al., *Antimicrobial activity of honey from the stingless bee *Trigona carbonaria* determined by agar diffusion, agar dilution, broth microdilution and time-kill methodology*. *Journal of Applied Microbiology*, 2010. **108**(5): p. 1534-1543.
174. Mullineaux, C.W., *Localization and mobility of bacterial proteins by confocal microscopy and fluorescence recovery after photobleaching*. *Methods Mol Biol*, 2007. **390**: p. 3-15.
175. Poelstra, K.A., et al., *A novel spinal implant infection model in rabbits*. *Spine (Phila Pa 1976)*, 2000. **25**(4): p. 406-10.
176. Boby, J., et al., *Characteristics of bone ingrowth and interface mechanics of a new porous tantalum biomaterial*. *The Journal of bone and joint surgery. British volume*, 1999. **81**(5): p. 907-914.
177. Zhang, Y., et al., *INTERFACIAL FRICTIONAL BEHAVIOR: CANCELLOUS BONE, CORTICAL BONE, AND A NOVEL POROUS TANTALUM BIOMATERIAL*. *Journal of Musculoskeletal Research*, 1999. **03**(04): p. 245-251.

178. Li, Q.T., et al., *Three-dimensional technology assisted trabecular metal cup and augments positioning in revision total hip arthroplasty with complex acetabular defects*. Journal of Orthopaedic Surgery and Research, 2019. **14**(1): p. 9.
179. Han, Q., et al., *Porous Tantalum and Titanium in Orthopedics: A Review*. ACS Biomaterials Science & Engineering, 2019. **5**(11): p. 5798-5824.
180. Peng, Q., et al., *Facile fabrication of boronized Ti6Al4V/HA composites for load-bearing applications*. Journal of Alloys and Compounds, 2020. **825**.
181. Parthasarathy, J., et al., *Mechanical evaluation of porous titanium (Ti6Al4V) structures with electron beam melting (EBM)*. Journal of the Mechanical Behavior of Biomedical Materials, 2010. **3**(3): p. 249-259.
182. Van Bael, S., et al., *The effect of pore geometry on the in vitro biological behavior of human periosteum-derived cells seeded on selective laser-melted Ti6Al4V bone scaffolds*. Acta Biomaterialia, 2012. **8**(7): p. 2824-2834.
183. Rafi, H.K., et al., *Microstructures and Mechanical Properties of Ti6Al4V Parts Fabricated by Selective Laser Melting and Electron Beam Melting*. Journal of Materials Engineering and Performance, 2013. **22**(12): p. 3872-3883.
184. Li, J.P., et al., *Bone ingrowth in porous titanium implants produced by 3D fiber deposition*. Biomaterials, 2007. **28**(18): p. 2810-2820.
185. Vrancken, B., et al., *Heat treatment of Ti6Al4V produced by Selective Laser Melting: Microstructure and mechanical properties*. Journal of Alloys and Compounds, 2012. **541**: p. 177-185.
186. Gallardo-Moreno, A.M., et al., *In vitro biocompatibility and bacterial adhesion of physico-chemically modified Ti6Al4V surface by means of UV irradiation*. Acta Biomaterialia, 2009. **5**(1): p. 181-192.
187. Shah, F.A., et al., *Commercially pure titanium (cp-Ti) versus titanium alloy (Ti6Al4V) materials as bone anchored implants - Is one truly better than the other?* Materials Science & Engineering C-Materials for Biological Applications, 2016. **62**: p. 960-966.
188. Heidenau, F., et al., *A novel antibacterial titania coating: Metal ion toxicity and in vitro surface colonization*. Journal of Materials Science-Materials in Medicine, 2005. **16**(10): p. 883-888.
189. Choi, J.Y., et al., *Photocatalytic antibacterial effect of TiO₂ film formed on ti and TiAg exposed to Lactobacillus acidophilus*. Journal of Biomedical Materials Research Part B-Applied Biomaterials, 2007. **80B**(2): p. 353-359.

190. Kotharu, V., et al., *Fabrication of corrosion resistant, bioactive and antibacterial silver substituted hydroxyapatite/titania composite coating on Cp Ti*. *Ceramics International*, 2012. **38**(1): p. 731-740.
191. Cunha, A., et al., *Femto second laser surface texturing of titanium as a method to reduce the adhesion of Staphylococcus aureus and biofilm formation*. *Applied Surface Science*, 2016. **360**: p. 485-493.
192. Tashiro, T., *Antibacterial and bacterium adsorbing macromolecules*. *Macromolecular Materials and Engineering*, 2001. **286**(2): p. 63-87.
193. Burkhardt, B.R. and E. Eades, *THE EFFECT OF BIOCELL TEXTURING AND POVIDONE-IODINE IRRIGATION ON CAPSULAR CONTRACTURE AROUND SALINE-INFLATABLE BREAST IMPLANTS*. *Plastic and Reconstructive Surgery*, 1995. **96**(6): p. 1317-1325.
194. Portenier, I., et al., *Inactivation of the antibacterial activity of iodine potassium iodide and chlorhexidine digluconate against Enterococcus faecalis by dentin, dentin matrix, type-I collagen, and heat-killed microbial whole cells*. *Journal of Endodontics*, 2002. **28**(9): p. 634-637.
195. Shirai, T., et al., *Antibacterial iodine-supported titanium implants*. *Acta Biomaterialia*, 2011. **7**(4): p. 1928-1933.
196. Tsuchiya, H., et al., *Innovative antimicrobial coating of titanium implants with iodine*. *Journal of Orthopaedic Science*, 2012. **17**(5): p. 595-604.
197. Ho, S.T. and D.W. Hutmacher, *A comparison of micro CT with other techniques used in the characterization of scaffolds*. *Biomaterials*, 2006. **27**(8): p. 1362-1376.
198. Jones, A.C., et al., *Assessment of bone ingrowth into porous biomaterials using MICRO-CT*. *Biomaterials*, 2007. **28**(15): p. 2491-2504.
199. Holdsworth, D.W. and M.M. Thornton, *Micro-CT in small animal and specimen imaging*. *Trends in Biotechnology*, 2002. **20**(8): p. S34-S39.
200. Norman, C., et al., *Visualisation of the mechanosensitive channel of large conductance in bacteria using confocal microscopy*. *European Biophysics Journal with Biophysics Letters*, 2005. **34**(5): p. 396-402.
201. Bohorquez, D., et al., *Correlative Confocal and 3D Electron Microscopy of a Specific Sensory Cell*. *Jove-Journal of Visualized Experiments*, 2015(101): p. 8.
202. Yu, Y.H., et al., *GFP fluorescence imaging with laser confocal scanning microscope*, in *1999 International Conference on Biomedical Optics*, Q. Luo, et al., Editors. 1999, Spie-Int Soc Optical Engineering: Bellingham. p. 337-340.

203. Levine, B.R., et al., *Experimental and clinical performance of porous tantalum in orthopedic surgery*. Biomaterials, 2006. **27**(27): p. 4671-4681.
204. Bencharit, S., et al., *Development and applications of porous tantalum trabecular metal-enhanced titanium dental implants*. Clinical implant dentistry and related research, 2014. **16**(6): p. 817-826.
205. Cohen, R., *A porous tantalum trabecular metal: basic science*. American journal of orthopedics (Belle Mead, NJ), 2002. **31**(4): p. 216-217.
206. Zardiackas, L.D., et al., *Structure, metallurgy, and mechanical properties of a porous tantalum foam*. Journal of Biomedical Materials Research: An Official Journal of The Society for Biomaterials, The Japanese Society for Biomaterials, and The Australian Society for Biomaterials and the Korean Society for Biomaterials, 2001. **58**(2): p. 180-187.
207. Miyazaki, T., et al., *Mechanism of bonelike apatite formation on bioactive tantalum metal in a simulated body fluid*. Biomaterials, 2002. **23**(3): p. 827-832.
208. Bobyn, J.D., et al., *Clinical validation of a structural porous tantalum biomaterial for adult reconstruction*. JBJS, 2004. **86**(suppl_2): p. 123-129.
209. Heiner, A., *Structural efficacy of a novel porous tantalum implant for osteonecrosis grafting*. Trans. Orthop. Res. Soc., 2001. **26**: p. 280.
210. Christie, M.J., *Clinical applications of Trabecular Metal*. American journal of orthopedics (Belle Mead, NJ), 2002. **31**(4): p. 219-220.
211. Bayan, E.M., et al., *Zn-F co-doped TiO₂ nanomaterials: Synthesis, structure and photocatalytic activity*. Journal of Alloys and Compounds, 2020. **822**.
212. Labanni, A., et al., *Size controlled synthesis of well-distributed nano-silver on hydroxyapatite using alkanolamine compounds*. Ceramics International, 2020. **46**(5): p. 5850-5855.
213. Imanzadeh, H., et al., *A sensitive nanocomposite design via carbon nanotube and silver nanoparticles: Selective probing of Emedastine Difumarate*. Journal of Pharmaceutical and Biomedical Analysis, 2020. **181**.
214. Lv, H., et al., *Preparation and characterization of SiO₂ nanowires using a SnO₂ catalyst*. Physics Letters A, 2020. **384**(8).
215. Zhou, Q., D.D. Duan, and J.W. Feng, *Preparation of Ni-Co/RuO₂ Composite Electrode and Electrocatalytic Activity for Hydrogen Evolution*. Chinese Journal of Inorganic Chemistry, 2020. **35**(12): p. 2301-2310.

216. Bekx-Schurmann, S., et al., *Morphology, microstructure, coordinative unsaturation, and hydrogenation activity of unsupported MoS₂: How idealized models fail to describe a real sulfide material*. Applied Catalysis B-Environmental, 2020. **266**.
217. Parsafard, N., et al., *Activity Evaluation of CoMo Nanoparticles Supported on Meso-microporous Composites in Dibenzothiophene Hydrodesulphurization*. Bulletin of Chemical Reaction Engineering and Catalysis, 2020. **15**(1): p. 112-118.
218. Goncalves, A.H.A., et al., *Surface investigation by X-ray photoelectron spectroscopy of Ru-Zn catalysts for the partial hydrogenation of benzene*. Molecular Catalysis, 2020. **483**.
219. Hermann, R. and M. Muller, *Limits in high-resolution scanning electron microscopy: Natural surfaces?* Scanning, 1997. **19**(5): p. 337-342.
220. Hermann, R. and M. Muller, *PREREQUISITES OF HIGH-RESOLUTION SCANNING ELECTRON-MICROSCOPY*. Scanning Microscopy, 1991. **5**(3): p. 653-664.
221. Goldstein, J.I., et al., *Scanning electron microscopy and X-ray microanalysis*. 2017: Springer.
222. Flegler, S.L. and S.L. Flegler, *Scanning & Transmission Electron Microscopy*. 1997: Oxford University Press.
223. Cardenas, G., et al., *SEM-EDX studies of chitosan derivatives-metal adducts*. Journal of the Chilean Chemical Society, 2003. **48**(4): p. 49-53.
224. Echlin, P., et al., *Advanced scanning electron microscopy and X-ray microanalysis*. 2013: Springer Science & Business Media.
225. Shallenberger, J.R. and N. Hellgren, *Zinc selenide analyzed by XPS*. Surface Science Spectra, 2020. **27**(1).
226. Seah, M., *A review of the analysis of surfaces and thin films by AES and XPS*. Vacuum, 1984. **34**(3-4): p. 463-478.
227. Demri, B. and D. Muster, *XPS study of some calcium compounds*. Journal of materials processing technology, 1995. **55**(3-4): p. 311-314.
228. Li, C.C., et al., *Superhydrophobic surface containing cerium salt and organosilane for corrosion protection of galvanized steel*. Journal of Alloys and Compounds, 2020. **825**.
229. Acquafredda, P., *XRF technique*. Physical Sciences Reviews, 2019. **4**(8).
230. Giumlia-Mair, A., *On surface analysis and archaeometallurgy*. Nuclear Instruments and Methods in Physics Research Section B: Beam Interactions with Materials and Atoms, 2005. **239**(1-2): p. 35-43.

231. del Hoyo-Meléndez, J.M., et al., *Micro-XRF analysis of silver coins from medieval Poland*. Nuclear Instruments and Methods in Physics Research Section B: Beam Interactions with Materials and Atoms, 2015. **349**: p. 6-16.
232. Makhlof, A.S.H. and A. Barhoum, *Emerging Applications of Nanoparticles and Architectural Nanostructures: Current Prospects and Future Trends*. 2018: William Andrew.
233. Gheno, S.M., H.L. Hasegawa, and P.I. Paulin, *AFM characterization of barium titanate*. Ferroelectrics, 2006. **334**: p. 43-48.
234. Mullan, F., et al., *Precision of 655 nm Confocal Laser Profilometry for 3D surface texture characterisation of natural human enamel undergoing dietary acid mediated erosive wear*. Dental Materials, 2018. **34**(3): p. 531-537.
235. Montani, I., et al., *Analysis of Roman pottery graffiti by high resolution capture and 3D laser profilometry*. Journal of Archaeological Science, 2012. **39**(11): p. 3349-3353.
236. Samyn, P., J. Van Erps, and H. Thienpont, *Relation between optical non-contact profilometry and AFM roughness parameters on coated papers with oil-filled nanoparticles*. Measurement, 2016. **82**: p. 75-93.
237. Henry, K.S. and S. Patton, *Measurement of the contact angle of water on geotextile fibers*. Geotechnical Testing Journal, 1998. **21**(1): p. 11-17.
238. Nishikiori, H., et al., *Water retentivity of allophane-titania nanocomposite films*. Applied Catalysis B-Environmental, 2020. **266**.
239. El-Sayed, N.M. and N.A. Eid, *Surface Modification of Cu/PS Nanocomposite Films: A Comparative Study of DC N-2 Plasma and Gamma Radiation and their Effects on the Films' Antibacterial Activity*. Arab Journal of Nuclear Sciences and Applications, 2020. **53**(1): p. 88-96.
240. Moon, H.S., et al., *The three-dimensional microstructure of the trabecular bone in the mandible*. Surgical and Radiologic Anatomy, 2004. **26**(6): p. 466-473.
241. Ehrich, H., et al., *SEM-EDX and SAM-AES Investigations on Rochow Contact Masses*. Applied Organometallic Chemistry, 1997. **11**(3): p. 237-247.
242. McArthur, S.L., *Applications of XPS in bioengineering*. Surface and Interface Analysis, 2006. **38**(11): p. 1380-1385.
243. Magsipoc, E., Q. Zhao, and G. Grasselli, *2D and 3D Roughness Characterization*. Rock Mechanics and Rock Engineering, 2020. **53**(3): p. 1495-1519.

244. Duan, D.X. and C.G. Lin. *Effect of Surface Free Energy and Electrochemical Polarization on Attachment of Sulfate Reducing Bacteria*. in *2nd International Conference on Manufacturing Science and Engineering*. 2011. Guilin, PEOPLES R CHINA.
245. Good, R.J., *Contact angle, wetting, and adhesion: a critical review*. *Journal of Adhesion Science and Technology*, 1992. **6**(12): p. 1269-1302.
246. Tiller, J.C., et al., *Designing surfaces that kill bacteria on contact*. *Proceedings of the National Academy of Sciences*, 2001. **98**(11): p. 5981.
247. Ivanova, E.P., et al., *Differential attraction and repulsion of Staphylococcus aureus and Pseudomonas aeruginosa on molecularly smooth titanium films*. *Scientific Reports*, 2011. **1**: p. 165.
248. Mrabet, B., et al., *Anti-fouling poly(2-hydroxyethyl methacrylate) surface coatings with specific bacteria recognition capabilities*. *Surface Science*, 2009. **603**(16): p. 2422-2429.
249. Ivanova, E.P., et al., *Natural Bactericidal Surfaces: Mechanical Rupture of Pseudomonas aeruginosa Cells by Cicada Wings*. *Small*, 2012. **8**(16): p. 2489-2494.
250. Hacking, S., et al., *Fibrous tissue ingrowth and attachment to porous tantalum*. *Journal of biomedical materials research*, 2000. **52**(4): p. 631-638.
251. Ghanaati, S., et al., *Scaffold vascularization in vivo driven by primary human osteoblasts in concert with host inflammatory cells*. *Biomaterials*, 2011. **32**(32): p. 8150-8160.
252. Huang, Z., et al., *Toxicological Effect of ZnO Nanoparticles Based on Bacteria*. *Langmuir*, 2008. **24**(8): p. 4140-4144.
253. Rajab, F.H., et al., *Controlling bacteria retention on polymer via replication of laser micro/nano textured metal mould*. *Optics & Laser Technology*, 2019. **111**: p. 530-536.
254. Cheng, Y., G. Feng, and C.I. Moraru, *Micro- and Nanotopography Sensitive Bacterial Attachment Mechanisms: A Review*. *Frontiers in microbiology*, 2019. **10**: p. 191-191.
255. Teughels, W., et al., *Effect of material characteristics and/or surface topography on biofilm development*. *Clinical Oral Implants Research*, 2006. **17**: p. 68-81.
256. Anselme, K., et al., *The interaction of cells and bacteria with surfaces structured at the nanometre scale*. *Acta Biomaterialia*, 2010. **6**(10): p. 3824-3846.

257. Hasan, J., R.J. Crawford, and E.P. Lvanova, *Antibacterial surfaces: the quest for a new generation of biomaterials*. Trends in Biotechnology, 2013. **31**(5): p. 31-40.
258. Arthanareeswaran, V.K.A., et al., *EVALUATION OF SURFACE MICROPATTERN (SHARKLET) ON FOLEYS SILICON CATHETER IN REDUCING URINARY TRACT INFECTIONS*. Journal of Urology, 2017. **197**(4): p. E270-E270.
259. Mann, E.E., et al., *Surface micropattern limits bacterial contamination*. Antimicrobial resistance and infection control, 2014. **3**: p. 28-28.
260. Shimko, D.A., et al., *Effect of porosity on the fluid flow characteristics and mechanical properties of tantalum scaffolds*. Journal of Biomedical Materials Research Part B: Applied Biomaterials, 2005. **73B**(2): p. 315-324.
261. Avcu, E., et al., *Tailoring the surface characteristics of electrophoretically deposited chitosan-based bioactive glass composite coatings on titanium implants via grit blasting*. Progress in Organic Coatings, 2018. **123**: p. 362-373.
262. Bollenl, C.M.L., P. Lambrechts, and M. Quirynen, *Comparison of surface roughness of oral hard materials to the threshold surface roughness for bacterial plaque retention: A review of the literature*. Dental Materials, 1997. **13**(4): p. 258-269.
263. Hajipour, M.J., et al., *Antibacterial properties of nanoparticles*. Trends in Biotechnology, 2012. **30**(10): p. 499-511.
264. Borkow, G. and J. Gabbay, *Copper as a biocidal tool*. Current Medicinal Chemistry, 2005. **12**(18): p. 2163-2175.
265. Borkow, G. and J. Gabbay, *Putting copper into action: copper-impregnated products with potent biocidal activities*. Faseb Journal, 2004. **18**(12): p. 1728-+.
266. Kelly, P.J. and R.D. Arnell, *Magnetron sputtering: a review of recent developments and applications*. Vacuum, 2000. **56**(3): p. 159-172.
267. Rokosz, K. and T. Hryniewicz, *COMPARATIVE SEM AND EDX ANALYSIS OF SURFACE COATINGS CREATED ON NIOBIUM AND TITANIUM ALLOYS AFTER PLASMA ELECTROLYTIC OXIDATION (PEO)*. Tehnicki Vjesnik-Technical Gazette, 2017. **24**(2): p. 465-472.
268. Luo, D.F., et al., *Hydrothermal calcification surface modification of biomedical tantalum*. Rare Metals, 2021. **40**(4): p. 928-933.
269. Barnett, R., K.T. Kilby, and D.J. Fray, *Reduction of Tantalum Pentoxide Using Graphite and Tin-Oxide-Based Anodes via the FFC-Cambridge Process*. Metallurgical and Materials Transactions B-Process Metallurgy and Materials Processing Science, 2009. **40**(2): p. 150-157.

270. Chen, G.Z., D.J. Fray, and T.W. Farthing, *Direct electrochemical reduction of titanium dioxide to titanium in molten calcium chloride*. Nature, 2000. **407**: p. 361.
271. Diebold, U., *The surface science of titanium dioxide*. Surface Science Reports, 2003. **48**(5-8): p. 53-229.
272. Chaneliere, C., et al., *Tantalum pentoxide (Ta₂O₅) thin films for advanced dielectric applications*. Materials Science and Engineering: R: Reports, 1998. **22**(6): p. 269-322.
273. Robinson, N.J. and D.R. Winge, *Copper Metallochaperones*. Annual Review of Biochemistry, 2010. **79**(1): p. 537-562.
274. Ståhl, J.E., F. Schultheiss, and S. Hägglund, *Analytical and Experimental Determination of the Ra Surface Roughness during Turning*. Procedia Engineering, 2011. **19**: p. 349-356.
275. Cumpson, P.J., *Angle-resolved XPS depth-profiling strategies*. Applied Surface Science, 1999. **144-145**: p. 16-20.
276. Ebnesajjad, S., *Chapter 4 - Surface and Material Characterization Techniques*, in *Surface Treatment of Materials for Adhesive Bonding (Second Edition)*, S. Ebnesajjad, Editor. 2014, William Andrew Publishing: Oxford. p. 39-75.
277. Mishra, A.H. and D. Mishra, *Evidences of Biomimetic and Nonantibiotic Characteristics of the Zinc-Carboxymethyl Chitosan-Genipin Organometallic Complex and Its Biocompatibility Aspects*. Biomacromolecules, 2020. **21**(2): p. 688-700.
278. Jaskiewicz, M., et al., *Methods Used for the Eradication of Staphylococcal Biofilms*. Antibiotics-Basel, 2019. **8**(4).
279. Kheiri, S., X.Y. Liu, and M. Thompson, *Nanoparticles at biointerfaces: Antibacterial activity and nanotoxicology*. Colloids and Surfaces B-Biointerfaces, 2019. **184**.
280. Zhu, Y.L., et al., *3D printed zirconia ceramic hip joint with precise structure and broad-spectrum antibacterial properties*. International Journal of Nanomedicine, 2019. **14**: p. 5977-5987.
281. Khadar, Y.A.S., et al., *Synthesis, characterization and antibacterial activity of cobalt doped cerium oxide (CeO₂:Co) nanoparticles by using hydrothermal method*. Journal of Materials Research and Technology-Jmr&T, 2019. **8**(1): p. 267-274.
282. Ketikidis, I., et al., *Conjugation of Penicillin-G with Silver(I) Ions Expands Its Antimicrobial Activity against Gram Negative Bacteria*. Antibiotics-Basel, 2020. **9**(1).
283. Orabi, A.S., et al., *Novel and highly effective composites of silver and zinc oxide nanoparticles with some transition metal complexes against*

- different microorganisms*. Arabian Journal of Chemistry, 2020. **13**(1): p. 2628-2648.
284. Shankar, S. and J.W. Rhim, *Eco-friendly antimicrobial nanoparticles of keratin-metal ion complex*. Materials Science & Engineering C- Materials for Biological Applications, 2019. **105**.
285. Petrik, I.S., et al., *Effect of silver and copper nanoparticles on adsorption and fluorescence of tryptophan on the surface of bactericidal textile*. Applied Nanoscience.
286. Hassoon, A.A., et al., *Synthesis, single crystal X-ray, spectroscopic characterization and biological activities of Mn²⁺, Co²⁺, Ni²⁺ and Fe³⁺ complexes*. Journal of Molecular Structure, 2020. **1203**.
287. Li, M., et al., *Chemical grafting of antibiotics into multilayer films through Schiff base reaction for self-defensive response to bacterial infections*. Chemical Engineering Journal, 2020. **382**.
288. Costa, F., et al., *Covalent immobilization of antimicrobial peptides (AMPs) onto biomaterial surfaces*. Acta Biomaterialia, 2011. **7**(4): p. 1431-1440.
289. Uwizeyimana, J.D., et al., *Determination of Colistin Resistance by Simple Disk Diffusion Test Using Modified Mueller-Hinton Agar*. Annals of Laboratory Medicine, 2020. **40**(4): p. 306-+.
290. Ismayil, K.M.M., A. Varghese, and R. Antony, *Silver-doped polyaniline-polyvinyl chloride nanocomposite films for photocatalytic and antibacterial applications*. Journal of Elastomers and Plastics, 2020. **52**(2): p. 103-116.
291. Pavithra, D. and M. Doble, *Biofilm formation, bacterial adhesion and host response on polymeric implants - issues and prevention*. Biomedical Materials, 2008. **3**(3).
292. Kleine, D., et al., *Monitoring of biofilms grown on differentially structured metallic surfaces using confocal laser scanning microscopy*. Engineering in Life Sciences, 2019. **19**(7): p. 513-521.
293. Rybkin, I., et al., *Thickness of Polyelectrolyte Layers of Separately Confined Bacteria Alters Key Physiological Parameters on a Single Cell Level*. Frontiers in Bioengineering and Biotechnology, 2019. **7**.
294. López, D., H. Vlamakis, and R. Kolter, *Biofilms*. Cold Spring Harbor perspectives in biology, 2010. **2**(7): p. a000398-a000398.
295. Hall-Stoodley, L., J.W. Costerton, and P. Stoodley, *Bacterial biofilms: from the Natural environment to infectious diseases*. Nature Reviews Microbiology, 2004. **2**(2): p. 95-108.
296. Kumar, P., B.S. Dehiya, and A. Sindhu, *Ibuprofen-Loaded CTS/nHA/nBG Scaffolds for the Applications of Hard Tissue Engineering*. Iran Biomed J, 2019. **23**(3): p. 190-9.

297. Tao, W.B., et al., *Machining accuracy detection of PCB hole by X-ray micro-CT*. Micron, 2020. **131**.
298. Shen, B.N., et al., *Influence of laser post-processing on pore evolution of Ti-6Al-4V alloy by laser powder bed fusion*. Journal of Alloys and Compounds, 2020. **818**.
299. Dewanckele, J., et al., *Innovations in laboratory-based dynamic micro-CT to accelerate in situ research*. Journal of Microscopy.
300. Fioretto, F., et al., *Inactivation of Staphylococcus aureus and Salmonella enteritidis in tryptic soy broth and caviar samples by high pressure processing*. Brazilian Journal of Medical and Biological Research, 2005. **38**(8): p. 1259-1265.
301. Heydorn, A., et al., *Quantification of biofilm structures by the novel computer program comstat*. Microbiology, 2000. **146**(10): p. 2395-2407.
302. Uslu, Y.S. and N. Donmez, *The effects on dentin tubules of two desensitising agents in combination with Nd:YAG laser: An in vitro analysis (CLSM and SEM)*. Optics and Laser Technology, 2020. **129**.
303. Hermanowicz, S.W. and J.J. Ganczarczyk, *Some fluidization characteristics of biological beds*. Biotechnology and Bioengineering, 1983. **25**(5): p. 1321-1330.
304. Ro, K.S. and J.B. Neethling, *Biofilm Density for Biological Fluidized Beds*. Research Journal of the Water Pollution Control Federation, 1991. **63**(5): p. 815-818.
305. Boaventura, R.A. and A.E. Rodrigues, *Consecutive reactions in fluidized-bed biological reactors: Modeling and experimental study of wastewater denitrification*. Chemical Engineering Science, 1988. **43**(10): p. 2715-2728.
306. Hoehn, R.C. and A.D. Ray, *Effects of Thickness on Bacterial Film*. Journal (Water Pollution Control Federation), 1973. **45**(11): p. 2302-2320.
307. Timmermans, P. and A. Van Haute, *Influence of the type of organisms on the biomass hold-up in a fluidized-bed reactor*. Applied Microbiology and Biotechnology, 1984. **19**(1): p. 36-43.
308. El-Said, M., V. Bhuse, and A. Arendsen, *An Empirical Study to Investigate the Effect of Air Density Changes on the DSRC Performance*. Procedia Computer Science, 2017. **114**: p. 523-530.
309. Briant, C.L. and M.K. Banerjee, *Refractory Metals and Alloys*, in *Reference Module in Materials Science and Materials Engineering*. 2016, Elsevier.

310. Song, B., et al., *Effects of processing parameters on microstructure and mechanical property of selective laser melted Ti6Al4V*. *Materials & Design*, 2012. **35**: p. 120-125.
311. Liu, F., et al., *Functionally graded porous scaffolds in multiple patterns: New design method, physical and mechanical properties*. *Materials & Design*, 2018. **160**: p. 849-860.
312. Huang, C., et al., *Electrospun collagen–chitosan–TPU nanofibrous scaffolds for tissue engineered tubular grafts*. *Colloids and Surfaces B: Biointerfaces*, 2011. **82**(2): p. 307-315.
313. Deng, C., et al., *A collagen–chitosan hydrogel for endothelial differentiation and angiogenesis*. *Tissue Engineering Part A*, 2010. **16**(10): p. 3099-3109.
314. Grant, J., et al., *Influence of molecular organization and interactions on drug release for an injectable polymer-lipid blend*. *International Journal of Pharmaceutics*, 2008. **360**(1): p. 83-90.
315. Felfel, R.M., et al., *Structural, mechanical and swelling characteristics of 3D scaffolds from chitosan-agarose blends*. *Carbohydrate Polymers*, 2019. **204**: p. 59-67.
316. Divya, M., et al., *Isolation of beta-glucan from Eleusine coracana and its antibiofilm, antidiabetic, antioxidant, and biocompatible activities*. *Microbial Pathogenesis*, 2020. **140**.
317. Giardino, L., et al., *Antimicrobial effectiveness of etidronate powder (Dual Rinse(R) HEDP) and two EDTA preparations against Enterococcus faecalis: a preliminary laboratory study*. *Odontology*.
318. Tkhilaishvili, T., et al., *Antibacterial Efficacy of Two Commercially Available Bacteriophage Formulations, Staphylococcal Bacteriophage and PYO Bacteriophage, Against Methicillin-Resistant Staphylococcus aureus: Prevention and Eradication of Biofilm Formation and Control of a Systemic Infection of Galleria mellonella Larvae*. *Frontiers in Microbiology*, 2020. **11**.
319. Chien, H.W., et al., *Inhibition of biofilm formation by rough shark skin-patterned surfaces*. *Colloids and Surfaces B-Biointerfaces*, 2020. **186**.
320. Moron-Lopez, J. and S. Molina, *Optimization of Recycled-Membrane Biofilm Reactor (R-MBfR) as a sustainable biological treatment for microcystins removal*. *Biochemical Engineering Journal*, 2020. **153**.
321. Astorga, S.E., et al., *Ordered micropillar array gold electrode increases electrochemical signature of early biofilm attachment*. *Materials & Design*, 2020. **185**.
322. Swain, S., R.N. Padhy, and T.R. Rautray, *Polarized piezoelectric bioceramic composites exhibit antibacterial activity*. *Materials Chemistry and Physics*, 2020. **239**.

323. Tian, Z., et al., *Evaluation of laser cleaning for defouling of marine biofilm contamination on aluminum alloys*. Applied Surface Science, 2020. **499**.
324. Liu, B.Y., et al., *Effect of Silver Fluoride in Preventing the Formation of Artificial Dentinal Caries Lesions in vitro*. Chinese Journal of Dental Research, 2019. **22**(4): p. 273-280.
325. Park, J.W., et al., *Microbial changes in biofilms on composite resins with different surface roughness: An in vitro study with a multispecies biofilm model*. Journal of Prosthetic Dentistry, 2019. **122**(5).
326. Rekha, R., et al., *Searching for crab-borne antimicrobial peptides: Crustin from *Portunus pelagicus* triggers biofilm inhibition and immune responses of *Artemia salina* against GFP tagged *Vibrio parahaemolyticus* Dahv2*. Molecular Immunology, 2018. **101**: p. 396-408.
327. Ho, K.K.K., et al., *Quorum sensing inhibitory activities of surface immobilized antibacterial dihydropyrrolones via click chemistry*. Biomaterials, 2014. **35**(7): p. 2336-2345.
328. Kim, J.Y., et al., *In vitro study of three-dimensional printed metal-polymer hybrid scaffold incorporated dual antibiotics for treatment of periprosthetic joint infection*. Materials Letters, 2018. **212**: p. 263-266.
329. Abudula, T., et al., *3D Printing of Metal/Metal Oxide Incorporated Thermoplastic Nanocomposites With Antimicrobial Properties*. Frontiers in Bioengineering and Biotechnology, 2020. **8**.
330. Loferer-Krössbacher, M., J. Klima, and R. Psenner, *Determination of bacterial cell dry mass by transmission electron microscopy and densitometric image analysis*. Appl Environ Microbiol, 1998. **64**(2): p. 688-94.
331. Ma, Y., et al., *Antimicrobial mechanism of strictinin isomers extracted from the root of *Rosa roxburghii* Tratt (*Ci Li Gen*)*. Journal of Ethnopharmacology, 2020. **250**: p. 112498.
332. Sondi, I. and B. Salopek-Sondi, *Silver nanoparticles as antimicrobial agent: a case study on *E. coli* as a model for Gram-negative bacteria*. Journal of Colloid and Interface Science, 2004. **275**(1): p. 177-182.
333. Hanaor, D., et al., *The effects of firing conditions on the properties of electrophoretically deposited titanium dioxide films on graphite substrates*. Journal of the European Ceramic Society, 2011. **31**(15): p. 2877-2885.
334. Hazan, R., et al., *A method for high throughput determination of viable bacteria cell counts in 96-well plates*. BMC Microbiology, 2012. **12**(1): p. 259.
335. Aksel, H., et al., *Antimicrobial Activity and Biocompatibility of Antibiotic-Loaded Chitosan Hydrogels as a Potential Scaffold in*

- Regenerative Endodontic Treatment*. Journal of Endodontics, 2020. **46**(12): p. 1867-1875.
336. Gao, T., et al., *Is intracellular Staphylococcus aureus associated with recurrent infection in a rat model of open fracture?* Bone & Joint Research, 2020. **9**(2): p. 71-76.
337. Li, Z.R., et al., *Impact of negative-pressure wound therapy on bacterial behaviour and bioburden in a contaminated full-thickness wound*. International Wound Journal, 2019. **16**(5): p. 1214-1221.
338. Choi, G.H., et al., *Growth and antioxidant production of Bacillus polyfermenticus SCD in whey protein concentrate (WPC)-based medium*. Korean Journal for Food Science of Animal Resources, 2008. **28**(1): p. 105-108.
339. Cutting, K.F., *Wound exudate: composition and functions*. British Journal of Community Nursing, 2003. **8**(Sup3): p. S4-S9.
340. Wade, C., et al., *Loss of Protein, Immunoglobulins, and Electrolytes in Exudates From Negative Pressure Wound Therapy*. Nutrition in Clinical Practice, 2010. **25**(5): p. 510-516.
341. Allan-Wojtas, P., L.T. Hansen, and A.T. Paulson, *Microstructural studies of probiotic bacteria-loaded alginate microcapsules using standard electron microscopy techniques and anhydrous fixation*. Lwt-Food Science and Technology, 2008. **41**(1): p. 101-108.
342. Castro, A.M., et al., *Application of the GIMP software in the analysis of birefringence images obtained in a multipass rheometer*. Rheologica Acta, 2018. **57**(2): p. 113-126.
343. Czarnul, P., A. Cierieszko, and M. Fraczak, *Towards efficient parallel image processing on cluster grids using GIMP*, in *Computational Science - Iccs 2004, Pt 2, Proceedings*, M. Bubak, et al., Editors. 2004. p. 451-458.
344. Gottenbos, B., et al., *In vitro and in vivo antimicrobial activity of covalently coupled quaternary ammonium silane coatings on silicone rubber*. Biomaterials, 2002. **23**(6): p. 1417-1423.
345. Guggenheim, B., et al., *Validation of an in vitro biofilm model of supragingival plaque*. Journal of Dental Research, 2001. **80**(1): p. 363-370.
346. Shi, Z.L., et al., *Antibacterial and mechanical properties of bone cement impregnated with chitosan nanoparticles*. Biomaterials, 2006. **27**(11): p. 2440-2449.
347. Choi, O., et al., *The inhibitory effects of silver nanoparticles, silver ions, and silver chloride colloids on microbial growth*. Water Research, 2008. **42**(12): p. 3066-3074.

348. Suresh, A.K., et al., *Silver Nanocrystallites: Biofabrication using Shewanella oneidensis, and an Evaluation of Their Comparative Toxicity on Gram-negative and Gram-positive Bacteria*. Environmental Science & Technology, 2010. **44**(13): p. 5210-5215.
349. Lorite, G.S., et al., *The role of conditioning film formation and surface chemical changes on Xylella fastidiosa adhesion and biofilm evolution*. Journal of Colloid and Interface Science, 2011. **359**(1): p. 289-295.
350. Monds, R.D. and G.A. O'Toole, *The developmental model of microbial biofilms: ten years of a paradigm up for review*. Trends in Microbiology, 2009. **17**(2): p. 73-87.
351. Wolfe, A.J., et al., *Evidence that acetyl phosphate functions as a global signal during biofilm development*. Molecular Microbiology, 2003. **48**(4): p. 977-988.
352. Ruiz, L.M.R., A. Fiebig, and S. Crosson, *Regulation of bacterial surface attachment by a network of sensory transduction proteins*. PLoS genetics, 2019. **15**(5): p. e1008022.
353. Solanki, K., et al., *Enzyme-Based Listericidal Nanocomposites*. Scientific Reports, 2013. **3**.
354. Li, R., et al., *In vivo immobilization of an organophosphorus hydrolyzing enzyme on bacterial polyhydroxyalkanoate nano-granules*. Microbial Cell Factories, 2019. **18**(1).
355. Kreft, J.-U., G. Booth, and J.W.T. Wimpenny, *BacSim, a simulator for individual-based modelling of bacterial colony growth*. Microbiology, 1998. **144**(12): p. 3275-3287.
356. Yeung, K.W.K., et al., *Antimicrobial effects of oxygen plasma modified medical grade Ti-6Al-4V alloy*. Vacuum, 2013. **89**: p. 271-279.
357. Mikkelsen, L.H. and P.H. Nielsen, *Quantification of the bond energy of bacteria attached to activated sludge floc surfaces*. Water Science and Technology, 2001. **43**(6): p. 67-75.
358. Yuan, H.H., et al., *The influence of conditioning film on antifouling properties of the polyurethane film modified by chondroitin sulfate in urine*. Applied Surface Science, 2017. **426**: p. 587-596.
359. Loza-Correa, M., et al., *Comparison of bacterial attachment to platelet bags with and without preconditioning with plasma*. Vox Sanguinis, 2017. **112**(5): p. 401-407.
360. Bracic, M., et al., *Protein-repellent and antimicrobial nanoparticle coatings from hyaluronic acid and a lysine-derived biocompatible surfactant*. Journal of Materials Chemistry B, 2017. **5**(21): p. 3888-3897.

361. Sunarintyas, S., *Bioadhesion of Biomaterials*, in *Biomaterials and Medical Devices: A Perspective from an Emerging Country*, F. Mahyudin and H. Hermawan, Editors. 2016. p. 103-125.
362. Krajewski, S., et al., *Bacterial interactions with proteins and cells relevant to the development of life-threatening endocarditis studied by use of a quartz-crystal microbalance*. Analytical and Bioanalytical Chemistry, 2014. **406**(14): p. 3395-3406.
363. Rochford, E.T.J., et al., *Bacterial adhesion to orthopaedic implant materials and a novel oxygen plasma modified PEEK surface*. Colloids and Surfaces B-Biointerfaces, 2014. **113**: p. 213-222.
364. Ruparelia, J.P., et al., *Strain specificity in antimicrobial activity of silver and copper nanoparticles*. Acta Biomaterialia, 2008. **4**(3): p. 707-716.
365. Wu, C.T., et al., *Copper-containing mesoporous bioactive glass scaffolds with multifunctional properties of angiogenesis capacity, osteostimulation and antibacterial activity*. Biomaterials, 2013. **34**(2): p. 422-433.
366. Golcu, A., et al., *Cd(II) and Cu(II) complexes of polydentate Schiff base ligands: synthesis, characterization, properties and biological activity*. Inorganica Chimica Acta, 2005. **358**(6): p. 1785-1797.
367. Eley, B.M., *Antibacterial agents in the control of supragingival plaque - a review*. British Dental Journal, 1999. **186**(6): p. 286-296.
368. Punyani, S. and H. Singh, *Preparation of iodine containing quaternary amine methacrylate copolymers and their contact killing antimicrobial properties*. Journal of Applied Polymer Science, 2006. **102**(2): p. 1038-1044.
369. Tang, Y., et al., *Preparation and antibacterial activity of quaternized chitosan with iodine*. Materials Science & Engineering C-Materials for Biological Applications, 2015. **48**: p. 1-4.
370. Chatterjee, A.K., R. Chakraborty, and T. Basu, *Mechanism of antibacterial activity of copper nanoparticles*. Nanotechnology, 2014. **25**(13).
371. Top, A. and S. Ulku, *Silver, zinc, and copper exchange in a Na-clinoptilolite and resulting effect on antibacterial activity*. Applied Clay Science, 2004. **27**(1-2): p. 13-19.
372. Gu, X.N., et al., *In vitro corrosion and biocompatibility of binary magnesium alloys*. Biomaterials, 2009. **30**(4): p. 484-498.
373. Zhang, S.X., et al., *Research on an Mg-Zn alloy as a degradable biomaterial*. Acta Biomaterialia, 2010. **6**(2): p. 626-640.

374. Hornberger, H., S. Virtanen, and A.R. Boccaccini, *Biomedical coatings on magnesium alloys - A review*. Acta Biomaterialia, 2012. **8**(7): p. 2442-2455.
375. Niinomi, M., M. Nakai, and J. Hieda, *Development of new metallic alloys for biomedical applications*. Acta Biomaterialia, 2012. **8**(11): p. 3888-3903.
376. Okuma, T., *Magnesium and bone strength*. Nutrition, 2001. **17**(7): p. 679-680.
377. Vormann, J., *Magnesium: nutrition and metabolism*. Molecular Aspects of Medicine, 2003. **24**(1): p. 27-37.
378. Witte, F., et al., *Degradable biomaterials based on magnesium corrosion*. Current Opinion in Solid State and Materials Science, 2008. **12**(5): p. 63-72.
379. Witte, F., et al., *In vivo corrosion of four magnesium alloys and the associated bone response*. Biomaterials, 2005. **26**(17): p. 3557-3563.
380. Stroganov, G.B., et al., *Magnesium-base alloy for use in bone surgery*. 1972, Google Patents.
381. Wang, M.Q. and T.T. Tang, *Surface treatment strategies to combat implant-related infection from the beginning*. Journal of Orthopaedic Translation, 2019. **17**: p. 42-54.
382. Wang, S., et al., *Antibacterial nanostructured copper coatings deposited on tantalum by magnetron sputtering*. Materials Technology, 2015. **30**(B2): p. B120-B125.
383. Yu, B., et al., *Antibacterial Activity of a Novel Titanium-Copper (Ti - Cu) Sintered Alloy in Preventing Periprosthetic Joint Infection in Rabbit Model*. Journal of Biomaterials and Tissue Engineering, 2019. **9**(5): p. 607-614.
384. Inoue, D., et al., *Iodine-supported titanium implants have good antimicrobial attachment effects*. Journal of Orthopaedic Science, 2019. **24**(3): p. 548-551.
385. Wu, S.X., et al., *Preparation and characterization of TiO₂ nanotubes antimicrobial coating of iodine-supported titanium implants*, in *2nd International Workshop on Materials Science and Mechanical Engineering*, H.J. Fan, Editor. 2019.
386. Shi, J.Y., et al., *Enhanced osteointegration of tantalum-modified titanium implants with micro/nano-topography*. Rsc Advances, 2017. **7**(73): p. 46472-46479.
387. Das, A. and M. Shukla, *New generation hopeite coating on Ti6Al4V (TC4) by radio frequency magnetron sputtering for prosthetic-orthopaedic implant applications: synthesis and characterisation*. Transactions of the Institute of Metal Finishing, 2020. **98**(2): p. 88-96.

388. Olmos, L., et al., *Synthesis and characterisation of Ti6Al4V/xTa alloy processed by solid state sintering*. Powder Metallurgy, 2020. **63**(1): p. 64-74.
389. Chen, M., et al., *Visual and antibacterial magnesium implants with low biocorrosion and bioactive surface for in vivo tracking and treating MRSA infection*. Chemical Engineering Journal, 2021. **417**.
390. Jenifer, A., et al., *Investigation on antibacterial and hemolytic properties of magnesium-doped hydroxyapatite nanocomposite*. Chemical Physics Letters, 2021. **771**.
391. Wang, X., et al., *Enhanced anticorrosive and antibacterial performances of silver nanoparticles/ polyethyleneimine/MAO composite coating on magnesium alloys*. Journal of Materials Research and Technology-Jmr&T, 2021. **11**: p. 2354-2364.
392. Bose, S. and S. Tarafder, *Calcium phosphate ceramic systems in growth factor and drug delivery for bone tissue engineering: A review*. Acta Biomaterialia, 2012. **8**(4): p. 1401-1421.
393. Surmenev, R.A., M.A. Surmeneva, and A.A. Ivanova, *Significance of calcium phosphate coatings for the enhancement of new bone osteogenesis - A review*. Acta Biomaterialia, 2014. **10**(2): p. 557-579.
394. Barrere, F., C.A. van Blitterswijk, and K. de Groot, *Bone regeneration: molecular and cellular interactions with calcium phosphate ceramics*. International Journal of Nanomedicine, 2006. **1**(3): p. 317-332.
395. Statz, A.R., A.E. Barron, and P.B. Messersmith, *Protein, cell and bacterial fouling resistance of polypeptoid-modified surfaces: effect of side-chain chemistry*. Soft Matter, 2008. **4**(1): p. 131-139.
396. Wagner, V.E., J.T. Koberstein, and J.D. Bryers, *Protein and bacterial fouling characteristics of peptide and antibody decorated surfaces of PEG-poly(acrylic acid) co-polymers*. Biomaterials, 2004. **25**(12): p. 2247-2263.
397. Huang, G.B., Y. Chen, and J. Zhang, *Nanocomposited coatings produced by laser-assisted process to prevent silicone hydrogels from protein fouling and bacterial contamination*. Applied Surface Science, 2016. **360**: p. 383-388.
398. Zouaghi, S., et al., *Graphite-based composites for whey protein fouling and bacterial adhesion management*. International Dairy Journal, 2018. **86**: p. 69-75.
399. Crawford, R.J., et al., *Surface topographical factors influencing bacterial attachment*. Advances in Colloid and Interface Science, 2012. **179-182**: p. 142-149.
400. Lu, A.G., et al., *Effects of surface roughness and texture on the bacterial adhesion on the bearing surface of bio-ceramic joint*

- implants: An in vitro study*. Ceramics International, 2020. **46**(5): p. 6550-6559.
401. Chen, L.Y., et al., *Comparison of bacterial adhesion and biofilm formation on zirconia fabricated by two different approaches: an in vitro and in vivo study*. Advances in Applied Ceramics.
 402. Jin, Y.B., et al., *Synthesis of caged iodine-modified ZnO nanomaterials and study on their visible light photocatalytic antibacterial properties*. Applied Catalysis B-Environmental, 2019. **256**.
 403. Borjihan, Q., et al., *Povidone-iodine-functionalized fluorinated copolymers with dual-functional antibacterial and antifouling activities*. Biomaterials Science, 2019. **7**(8): p. 3334-3347.
 404. Mauerer, A., et al., *Antibacterial effect of a 4x Cu-TiO₂ coating simulating acute periprosthetic infection—An animal model*. Molecules, 2017. **22**(7): p. 1042.
 405. Shirai, T., et al., *Antimicrobial megaprotheses supported with iodine*. Journal of Biomaterials Applications, 2014. **29**(4): p. 617-623.
 406. Kabata, T., et al., *Iodine-supported hip implants: short term clinical results*. BioMed research international, 2015. **2015**.
 407. Zhou, Y.L., et al., *Nanoparticle-coated sutures providing sustained growth factor delivery to improve the healing strength of injured tendons*. Acta Biomaterialia, 2021. **124**: p. 301-314.
 408. Nuswantoro, N.F., et al., *Hydroxyapatite coating on titanium alloy TNTZ for increasing osseointegration and reducing inflammatory response in vivo on Rattus norvegicus Wistar rats*. Ceramics International, 2021. **47**(11): p. 16094-16100.
 409. Tiplea, R.E., et al., *Antimicrobial Films based on Chitosan, Collagen, and ZnO for Skin Tissue Regeneration*. Biointerface Research in Applied Chemistry, 2021. **11**(4): p. 11985-11995.
 410. Mallick, S.P., et al., *Chitosan Oligosaccharide Based Hydrogel: an Insight into the Mechanical, Drug Delivery, and Antimicrobial Studies*. Biointerface Research in Applied Chemistry, 2021. **11**(3): p. 10293-10300.
 411. Boominathan, T. and A. Sivaramakrishna, *Recent Advances in the Synthesis, Properties, and Applications of Modified Chitosan Derivatives: Challenges and Opportunities*. Topics in Current Chemistry, 2021. **379**(3).
 412. Irastorza, A., et al., *The versatility of collagen and chitosan: From food to biomedical applications*. Food Hydrocolloids, 2021. **116**.
 413. Liang, C.Y., et al., *Construction of novel antimicrobial peptide-modified extracellular matrix biologic scaffold material*. Biochemical and Biophysical Research Communications, 2021. **546**: p. 162-168.

414. Kang, Z., et al., *Preparation of polymer/calcium phosphate porous composite as bone tissue scaffolds*. *Materials Science & Engineering C-Materials for Biological Applications*, 2017. **70**: p. 1125-1131.
415. Lu, H.H., et al., *Development of controlled heterogeneity on a polymer-ceramic hydrogel scaffold for osteochondral repair*, in *Bioceramics 17*, P. Li, K. Zhang, and C.W. Colwell, Editors. 2005. p. 607-610.
416. Dubey, K.A., et al., *Polymers, Blends and Nanocomposites for Implants, Scaffolds and Controlled Drug Release Applications*, in *Advances in Biomaterials for Biomedical Applications*, A. Tripathi and J.S. Melo, Editors. 2017. p. 1-44.
417. Dong, X.Z., et al., *A chitosan based scaffold with enhanced mechanical and biocompatible performance for biomedical applications*. *Polymer Degradation and Stability*, 2020. **181**.
418. Kulkarni, N., et al., *Peptide-Chitosan Engineered Scaffolds for Biomedical Applications*. *Bioconjugate Chemistry*, 2021. **32**(3): p. 448-465.
419. Shishkovsky, I.V. and V.I. Scherbakov, *Additive manufacturing of polymer composites with nano-titania inclusions*. *Laser Physics Letters*, 2021. **18**(6).
420. Sikhosana, S.T., et al., *Poly(lactic acid) and its composites as functional materials for 3-D scaffolds in biomedical applications: A mini-review of recent trends*. *Express Polymer Letters*, 2021. **15**(6): p. 568-580.
421. Puertas-Bartolome, M., A. Mora-Boza, and L. Garcia-Fernandez, *Emerging Biofabrication Techniques: A Review on Natural Polymers for Biomedical Applications*. *Polymers*, 2021. **13**(8).
422. Tomsia, A.P., et al., *Biomimetic bonelike composites and novel bioactive glass coatings*. *Advanced Engineering Materials*, 2005. **7**(11): p. 999-1004.
423. Zhao, X., *Bioactive materials in orthopaedics*. *Bioactive Materials in Medicine: Design and Applications*, ed. X. Zhao, J.M. Courtney, and H. Qian. 2011. 124-154.
424. Tsai, C.H., et al., *Improved Bioactivity of 3D Printed Porous Titanium Alloy Scaffold with Chitosan/Magnesium-Calcium Silicate Composite for Orthopaedic Applications*. *Materials*, 2019. **12**(2).
425. Yang, Y., et al., *Dual-functional 3D-printed composite scaffold for inhibiting bacterial infection and promoting bone regeneration in infected bone defect models*. *Acta Biomaterialia*, 2018. **79**: p. 265-275.
426. Raftery, R.M., et al., *Multifunctional biomaterials from the sea: Assessing the effects of chitosan incorporation into collagen scaffolds*

- on mechanical and biological functionality*. Acta Biomaterialia, 2016. **43**: p. 160-169.
427. Xia, Y., et al., *Injectable calcium phosphate scaffold with iron oxide nanoparticles to enhance osteogenesis via dental pulp stem cells*. Artificial Cells Nanomedicine and Biotechnology, 2018. **46**: p. S423-S433.
428. Perli, M.D., et al., *Synthesis and Characterization of Ag Nanoparticles for Orthopaedic applications*. Materials Today: Proceedings, 2017. **4**(7, Part 1): p. 6889-6900.
429. Doty, H.A., et al., *Elution of amikacin and vancomycin from a calcium sulfate/chitosan bone scaffold*. Biomaterials and Biomechanics in Bioengineering, 2015. **2**(3): p. 159-172.
430. Eldesouky, I. and H. El-Hofy, *Design and prototyping of a novel low stiffness cementless hip stem*. International Journal of Biomedical Engineering and Technology, 2020. **32**(3): p. 229-244.
431. Li, C.M., et al., *Design of biodegradable, implantable devices towards clinical translation*. Nature Reviews Materials, 2020. **5**(1): p. 61-81.
432. Parai, R. and S. Bandyopadhyay-Ghosh, *Engineered bio-nanocomposite magnesium scaffold for bone tissue regeneration*. Journal of the Mechanical Behavior of Biomedical Materials, 2019. **96**: p. 45-52.
433. Ranjan, N., R. Singh, and I.P.S. Ahuja, *Investigations on joining of orthopaedic scaffold with rapid tooling*. Proceedings of the Institution of Mechanical Engineers Part H-Journal of Engineering in Medicine, 2019. **233**(7): p. 754-760.
434. Soundhar, A. and K. Jayakrishna, *Investigations on mechanical and morphological characterization of chitosan reinforced polymer nanocomposites*. Materials Research Express, 2019. **6**(7).
435. Acevedo, C.A., et al., *Design of a biodegradable UV-irradiated gelatin-chitosan/nanocomposed membrane with osteogenic ability for application in bone regeneration*. Materials Science & Engineering C-Materials for Biological Applications, 2019. **99**: p. 875-886.
436. Morsbach, S., et al., *Engineering Proteins at Interfaces: From Complementary Characterization to Material Surfaces with Designed Functions*. Angewandte Chemie-International Edition, 2018. **57**(39): p. 12626-12648.
437. Snopok, B.A. and E.V. Kostyukevich, *Kinetic studies of protein-surface interactions: A two-stage model of surface-induced protein transitions in adsorbed biofilms*. Analytical Biochemistry, 2006. **348**(2): p. 222-231.

438. Wagner, M.S., et al., *Quantitative time-of-flight secondary ion mass spectrometry for the characterization of multicomponent adsorbed protein films*. Applied Surface Science, 2003. **203**: p. 704-709.
439. Liu, C.G., et al., *A riboflavin-ultraviolet light A-crosslinked decellularized heart valve for improved biomechanical properties, stability, and biocompatibility*. Biomaterials Science, 2020. **8**(9): p. 2549-2563.
440. Khoffi, F., et al., *Surface modification of polymer textile biomaterials by N-2 supercritical jet: Preliminary mechanical and biological performance assessment*. Journal of the Mechanical Behavior of Biomedical Materials, 2020. **107**: p. 10.
441. Ataei, B., et al., *Plasma modification of heparinised CNT/PU nanocomposite and measuring of mechanical, calcification and platelet adhesion properties for application in heart valve*. Plastics Rubber and Composites, 2020. **49**(7): p. 289-299.

